INVESTIGATION INTO THE APPLICABILITY OF AVO TECHNIQUES TO COAL MINE EXPLORATION

Romaric Davy LIMACHER

Submitted for the degree of Doctor of Philosophy

Heriot-Watt University

Petroleum Engineering Institute

Edinburgh

United Kingdom

May 2011

ABSTRACT

AVO (for Amplitude Versus Offset) is a seismic technology known in the oil industry for its ability to differentiate gas sands (over oil producing reservoirs) from wet sands (over non-producing reservoirs) in the Gulf of Mexico. Its applicability to a broad range of exploration fields has led to its potential application within the ADEMA (Advances in Exploration Methods and Applications) project being considered. Within the frame of this project, this PhD thesis assesses the ability of AVO to detect a difference between Mudstone and Sandstone roofs over a 6 meters thick coal seam, in the region of Daw Mill (UK). It moreover presents a modification of a triaxial cell aimed at calibrating AVO in the laboratory, and thereby improving the quality of AVO analysis in general.

The analysis presented in this PhD thesis leads to the conclusion that in this region, the particular rock properties can lead to a signal difference detectable by AVO. However, analysis of seismic data confirmed that tuning effect interferes with these distinct signals, and prevents AVO technology to differentiate mudstone from sandstone roofs.

Finally, this thesis proposes different technical recommendations for successfully running a test with the modified triaxial cell in future.

AKNOWLEDGEMENTS

To Sophie,

To my parents,

ACADEMIC REGISTRY
Research Thesis Submission

Name*:*	Romaric Davy LIMACHER		
School/PGI:	Petroleum Engineering Institute		
Version: *(i.e. First, Resubmission, Final)*	Resubmission	Degree Sought (Award **and** Subject area)	PhD

Declaration

In accordance with the appropriate regulations I hereby submit my thesis and I declare that:

1) the thesis embodies the results of my own work and has been composed by myself
2) where appropriate, I have made acknowledgement of the work of others and have made reference to work carried out in collaboration with other persons
3) the thesis is the correct version of the thesis for submission and is the same version as any electronic versions submitted*.
4) my thesis for the award referred to, deposited in the Heriot-Watt University Library, should be made available for loan or photocopying and be available via the Institutional Repository, subject to such conditions as the Librarian may require
5) I understand that as a student of the University I am required to abide by the Regulations of the University and to conform to its discipline.

* *Please note that it is the responsibility of the candidate to ensure that the correct version of the thesis is submitted.*

Signature of Candidate*:*	Romaric LIMACHER	Date:	

Submission

Submitted By *(name in capitals):*	ROMARIC DAVY LIMACHER
Signature of Individual Submitting:	
Date Submitted:	

For Completion in Academic Registry

Received in the Academic Registry by *(name in capitals):*			
Method of Submission *(Handed in to Academic Registry; posted through internal/external mail):*			
*E-thesis Submitted (**mandatory for final theses from January 2009)***			
Signature:		Date:	

Contents

List of Tables

List of Figures

List of Abbreviations

AVO : Amplitude Versus Offset
AVA: Amplitude Versus Angle
CMP: Common Mid Point
V_P: P-wave velocity
V_S: S-wave velocity
E: Young's modulus
ν: Poisson's ratio
ρ: density
(λ, μ): Lame's parameters
σ: stress
ε: strain
R_0: Reflection coefficient at zero incidence
T: Traveltime
X: Offset
i: incidence angle

Chapter 1.INTRODUCTION

The need to determine the strength of a coal seam's roof in Daw Mill Colliery (UK), prior to its exploitation, led to the investigation of the applicability of Amplitude Versus Offset (AVO) in mine planning. This PhD was motivated by the application of this technology in a different context to oil industry. A brief review of AVO's principles precedes a more detailed description of the problems linked to the Daw Mill site (UK), the formation of this PhD's subject, and the content of this thesis' chapters.

1.1. AVO PRINCIPLE

The principle of this commercially successful technology relies on the observation detailed below: consider a seismic survey performed on a simple two layers case, with their respective impendance, as depicted in Figure 1.

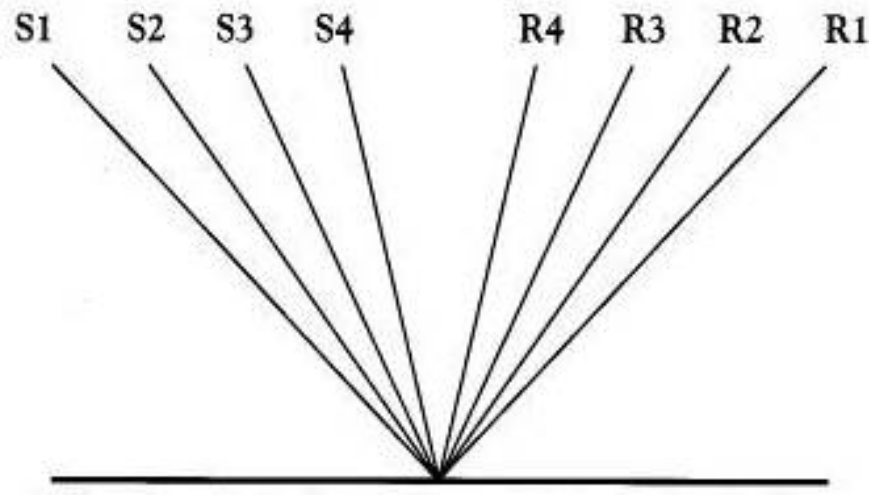

Figure 1 - Raypaths imaging a common midpoint in the subsurface at increasing angles of incidence, for sources S1-4 and receivers R1-4. During seismic processing, these traces formed into a CMP gather, the input to AVO analysis. (Allen & Peddy ,1993)

At normal incidence, if an important change in impedance can directly be quantified from reflected amplitudes, it will also be technically impossible to determine which layer displays the physical parameter with the higher numerical value. In oil industry, a common and pragmatic application of the use of physics to solve this problem is bright spots (as shown in Figure 2 2). A high amplitude reflection can be evenly generated by: a high impedance bottom layer (igneous intrusions, carbonates, hard streaks, lignites or wet sands) , or a low impedance bottom layer (e.g. gas sands on top of economically interesting reservoirs)

In the gulf of Mexico, drilling in the location of this specific feature only leads to a 20% probability of discovering a new oil producing reservoir (Allen & Peddy, 1993).

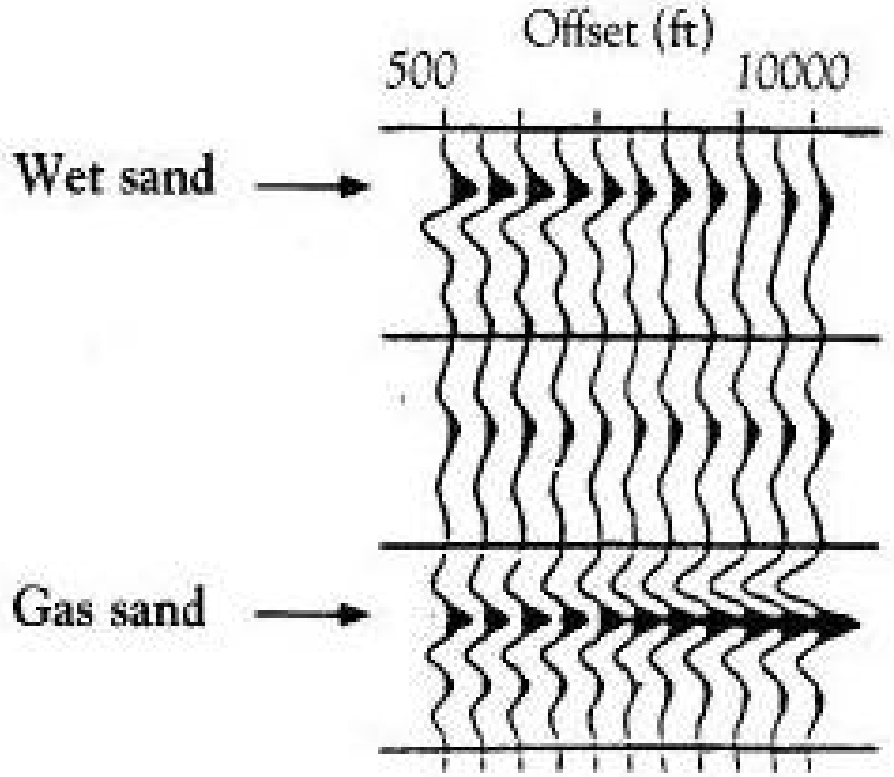

Figure 2 - Model CMP gather contrasting the expected AVO repsonse of a typical wet sand and gas sand. The increasing amplitudes at the far offsets for the gas sand are anomalous with respect to most other reflections, such as the wet sand reflection. (Allen, J.L. & Peddy, C.P., 1993)

Ostrander (1984) defined the principle of AVO. In summary, in a 2 layer case, if the upper layer has a weaker impedance the reflection coefficient will decrease with increasing offset. However, if the bottom layer has a weaker impedance the same reflection coefficient will increase with offset. The pragmatic application of this simple observation reversed the situation in the gulf of Mexico with 80% of the drillings leading to a new discovery (Allen & Peddy, 1993).

1.2. POTENTIAL APPLICATION OF AVO IN MINE PLANNING

Daw Mill colliery, located near Arley in the Warwickshire (UK), is Britain's biggest coal producer. It exploits a 6 meters thick coal seam section, at an average of 600 meters underground. With such depth characteristics, a 3D seismic survey (for defining the geometry of the seam) was more economical than drilling and logging techniques classically used in coal industry.

Advances in Exploration Methods and Applications (ADEMA), an EC funded project, was initiated in response to problems identified with the exploitation of the data. The primary aim was to check the capability of different oil exploration technologies in order to improve mine planning. It involved a number of companies and public organsiations from different European countries, detailed below:

1. **UK Coal Mining Ltd** - Harwort Park, Harworth, Doncaster DN11 8DB, UK
2. **Geocontrol SA** - Cristobal Bordiu 19-21 5, 28003 Madrid, SPAIN

3. **Glowny Instytut Gornictwa** - Jednostka Badawczo-Rozwojna, Plac Gwarkow 1, 40 166 Katowice, POLAND

4. **Heriot-Watt University**, Riccarton, Edinburgh EH14 4AS, UK

5. **Mines Rescue Service Ltd - Leeming Lane South**, Mansfield Woodhouse, Mansfield NG19 9AQ, UK

6. **Seismic Image Processing** - Crossways, 28-30 High Street, Guilford GU1 3EL, UK

7. **Nederlandse Organisatie voor Toegepast Natuurwetenschappelijk Onderzoek (TNO)** - Princetonlann 6, 3584 CB Utrecht, NETHERLANDS

This thesis focuses on my work within the Heriot-Watt University examining the capability of AVO to differentiate mudstone from sandstone layers overlying a coal seem. On this site, sandstones are considered suitable roofs for mine galleries whereas mudstones, with weak mechanical properties, pose a threat. Exploiting a mudstone roof area endangers miners and collapses induce production delays, which involve providing financial compensation to customers. Therefore, mine planners are willing to only exploit sandstone roof areas. The oil exploration technique AVO, having proven the ability to differentiate these two different lithologies, was viewed as a potential solution to this problem.

1.3. OBJECTIVES

Although the use of AVO resulted in a great improvement in the Gulf of Mexico (see 1.1) it has not always demonstrated the same efficiency in exploration areas with distinct geologies. Therefore a need is recognised to refine the technique by including a mandatory reconnaissance step. Prior to the ADEMA project, AVO had not been used in the coal industry; therefore this thesis is the first to address this question:

1. Can AVO differentiate between a sandstone and a mudstone roof overlying a coal seam?

Furthermore, depending on the method of determination, many numerical values can be attributed to the same mechanical property. This discrepancy raised the problem of AVO calibration from the laboratory for matching geotechnically (used by mine planners) and geophysically (provided by seismic data) determined parameters. This formed the basis of the second question;

2. Could an AVO calibration be performed in laboratory by adding an extra step based on a triaxial cell modification?

The triaxial cell modification consisted of an array of piezo-components placed along the perimeter of the equipment's section (hence the name of sensitive sleeve), allowing the recording of reflection coefficients at different angles (hence the idea of calibrating AVO from the laboratory).

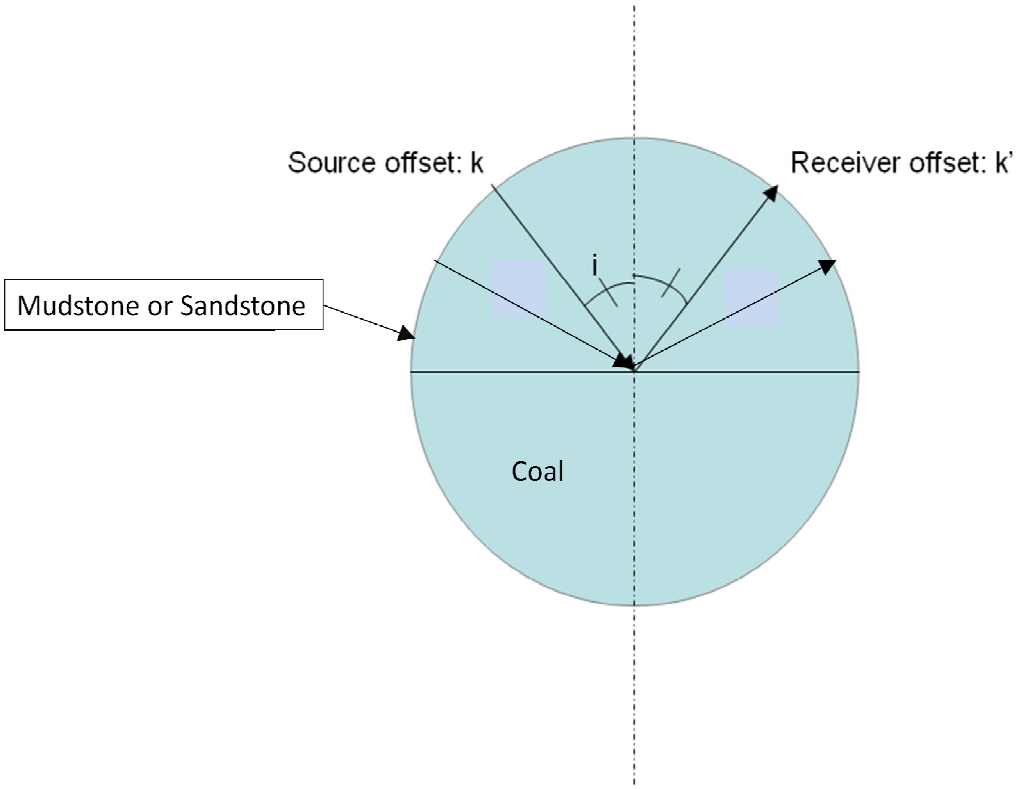

Figure 3 - Principle of AVO record in the laboratory, on a bilithic sample. Like in a seismic survey, the reflection coefficient would be recorded at different incidence angles.

The principle, illustrated in figure 3, would consist of collecting, on a bilithic sample, different reflection coefficients at different angles. A direct comparison between data from laboratory to seismic shot gathers (like infigure 3) was thought, at the beginning of the project, to be potentially helpul in improving AVO from the laboratory. For example, an inversion algorithm could be tested on these data for checking the capability of an inversion algorithm to determine rock mechanical properties from the reflection coefficients.

1.4. THESIS STRUCTURE

This thesis addresses two distinct problems: AVO reconnaissance and triaxial cell's modifications.

In doing so, the physical impossiblity (in the scientific sense of the term) to carry out a task would not impede the realization and delivery of the second. It is organised into the 6 chapters detailed below:

1. Introduction
2. Theoretical Review
3. Laboratory Testing : Collection of rock mechanical properties
4. Modelling : Application of these mechanical properties in modelling
5. Seismic: Comparison between modelling and real seismic data
6. Conclusion

Chapter 1: Introduction

Chapter 2: Literature Review.
This chapter primarily describes the basics of AVO, defined by the combination of elastic wave propagation and Zoeppritz's (1907) boundary conditions between two elastic layers. The second part of this chapter is dedicated to the direct link between wave propagation/reflection and rock mechanical properties and seismic processing related problems. Finally it focuses on the discrepancies betwen the initial hypothesises and:

1. the finely layered media observed at seismic and ultrasonic scales;
2. the potentialy different boundary conditions at ultrasonic scale.

Chapter 3: Laboratory Testing.

While the initial roof and floor's geotechnical database provided a useful dataset, the data for the mechanical properities of the coal seams were sparse and incomplete. This necessitated the collection of the data in the rock laboratory facility of the Petroleum Engineering Institute (within the Heriot-Watt University). Although initially problematic, it led to the definition of a probability distribution for each mechanical property. The first part of the chapter describes this process in detail. The second part of the chapter focuses on the tests conducted with the modified triaxial cell's prototype (also referred to as Sensitive Sleeve). The first tests using coal samples were promising however, attenuation within the sandstone samples hindered the detection of any transmitted or reflected wave.

Chapter 4: Application of the laboratory data in modelling.

The fourth chapter uses the probability distributions defined in Chapter 3, through Aki and Richard's solutions (2002) to the Zoeppritz equations, to statistically prove the ability of AVO to discriminate mudroofs from sandroofs. In addition mean values were used in synthetic acquisitions within a sensitive sleeve model, in order to allow comparisons with the real tests.

Chapter 5: AVO analysis of seismic data.

The fifth chapter builds on the work presented in Chapter 4 with the modelling demonstrating an ability to differentiate the two different roofs by checking the real applicability of AVO in mine planning.

Chapter 6: Conclusion.

This chapter firstly reviews the data collection in the laboratory, the definition of their probability distribution and application in modelling. Theoretically, it was

proven that in Daw Mill, AVO can be used to differentiate sandroofs from mudroofs over a coalseam. However, a practical application is compromised by the presence of cyclothems which induce:

1. a tuning effect within (between) a (different) coal seam(s)
2. a limited roofs thickness (compared to the main seismic wavelength) leading to a potential inability to perform any characterisation

Secondly, the conclusion focuses on the triaxial cell's modification which has led to:

1. the discovery of potentially different boundary conditions at ultrasonic frequencies (theory)
2. the developement of a graphical user interface for modelling synthetic acquisitions (modelling)
3. a successful attempt for improving the signal to noise ratio (experimental effort)

Chapter 2. THEORETICAL REVIEW

2.1. BRIEF SYNOPSIS

This chapter is a literature review detailing the theoretical basis of this thesis. It describes the basis of the data required to describe the rock mechanical phenomena encountered in seismic data analysis, the data to be measured in the laboratory (Chapter 3), and presents the Aki and Richards' solutions to the Zoeppritz's equations. This forms the basis for the theoretical comparison of an AVO signal recorded on a Mudstone/Coal interface with that recorded on a Sandstone/Coal interface. The final part reviews the applicability of these formulas in the laboratory and in the field (Daw Mill mine).

The theoretical review is organised into three parts:

1. AVO Theory
2. Link between AVO and Rock Physics
3. Apparent Contradiction with AVO Hypothesises

Introduction to AVO theory: this section describes elastic plane-wave propagation and reflection in non-attenuating, isotropic, homogeneous and semi-infinite media. The theory of amplitude variation with offset is a combination of:

- waves propagation
- reflection boundary conditions

This part summarises the solutions to the wave equation, and their application in the Zoeppritz's boundary conditions (1919), which leads to the four equations solved by Aki and Richards (2002). It can be clearly determined from the analytical solutions (used for modelling AVO responses) that the following parameters have to be measured in the laboratory:

- P-wave velocity (V_P)
- S-wave velocity (V_S)
- density

Link between AVO and Rock Physics: this part starts by introducing Poisson's ratio, Young's modulus, their link to V_P and V_S, and raises the problem of parameters' extraction. Shuey's approximation illustrates the concept of AVO classes for different conditions and provides a simplified formula used in Chapter 5 for inverting and interpreting the seismic data. Finally, a new AVO class has been proposed in this thesis to describe the specific conditions found in coal exploration.

Different AVO Hypotheses: if AVO theory describes wave propagation in non-attenuating, isotropic and semi-infinite media its direct application may not be relevant in:

- attenuating media
- finite media
- anisotropic media

This section introduces the origin of attenuation with thermoelasticty, before presenting the general case developed by Zener (1948). This review of the physical phenomena introduces the velocity difference observed, in the same propagating media, between seismic (30~60 Hz) and ultrasonic (1 MHz) waves; a theoretical or

empirical formula is then required to upscale laboratory data to seismic surveys' scale (upscaling will be used in the chapter dedicated to the data collection (Chapter 3)).

These additional physical phenomena have an impact on wave reflection by introducing a different set of boundary conditions between the two observed propagating media and AVO theory may not be relevant for describing ultrasonic wave reflection and transmission. A simple calibration of AVO from the laboratory may not be possible.

Finally, the potential consequences of the layer finite thickness are:

- dispersivity (wave's velocity varying with frequency)
- anisotropy
- converted modes
- tuning effect
- wave shape distortion

The observation of seismic data in Chapter 5 will show that tuning effect and wave shape distortion have an important role in the practical applicability of AVO in Daw Mill mine.

2.2. AVO THEORY

2.2.1. Objectives and organization of part 2.2

Aki and Richards' reference, Quantitative Seismology, second edition (2002), is the basis of this section. This reference is used extensively to review:

- The application of potentials in the wave equation solution. This approach, described by Aki and Richards, will be used in paragraph 2.4 (Contradiction of AVO Hypotheses) for assessing the influence of thermoelasticity on V_P and V_S at ultrasonic scales.
- A comparison of thermoelastic and Zoeppritz's respective boundary conditions.
- The determination of which parameters to determine in the laboratory (in chapter 3).
- The use of the Aki and Richards' solutions in numerical applications (in chapter 4).

This section is structured as follows:

1. A presentation of AVO's hypothesises
2. A presentation of the analogy between light and acoustic wave propagation
3. A presentation of Knott's equations
4. Resolution of wave equations with potentials
5. A presentation of Zoeppritz's boundary conditions
6. An application of potentials in these boundary conditions, which leads to a set of four equations known as the Zoeppritz's equations.
7. Analytical resolution of these equations by Aki and Richards

2.2.2. AVO theory hypotheses

Hypotheses for the:

- two propagating media

•boundary separating the two media

define the physical system representative of an acoustic wave's reflection/transmission problem.

Hypotheses state that the two media are:

- Homogeneous
- Isotropic
- Elastic
- Semi-infinite

The boundary separating the two media is:

- Plane
- Welded

The propagating wave is:

- Homogeneous
- Plane

Knott defined a set of four equations in acoustics, based on this physical system. This set of equations is solved by using potentials. These analytical expressions, applied as boundary conditions on stresses and strains (Zoeppritz (1919)), lead to a new system of four equations known as the Zoeppritz Equations. Aki and Richards have analytically solved this last set of equations.

2.2.3. Analogy between light and acoustic wave propagation

Using the hypotheses cited in the preceding paragraph, an analogy can be undertaken using optics, and the reflection and Snell's laws define the path followed by a seismic wave in propagating media.

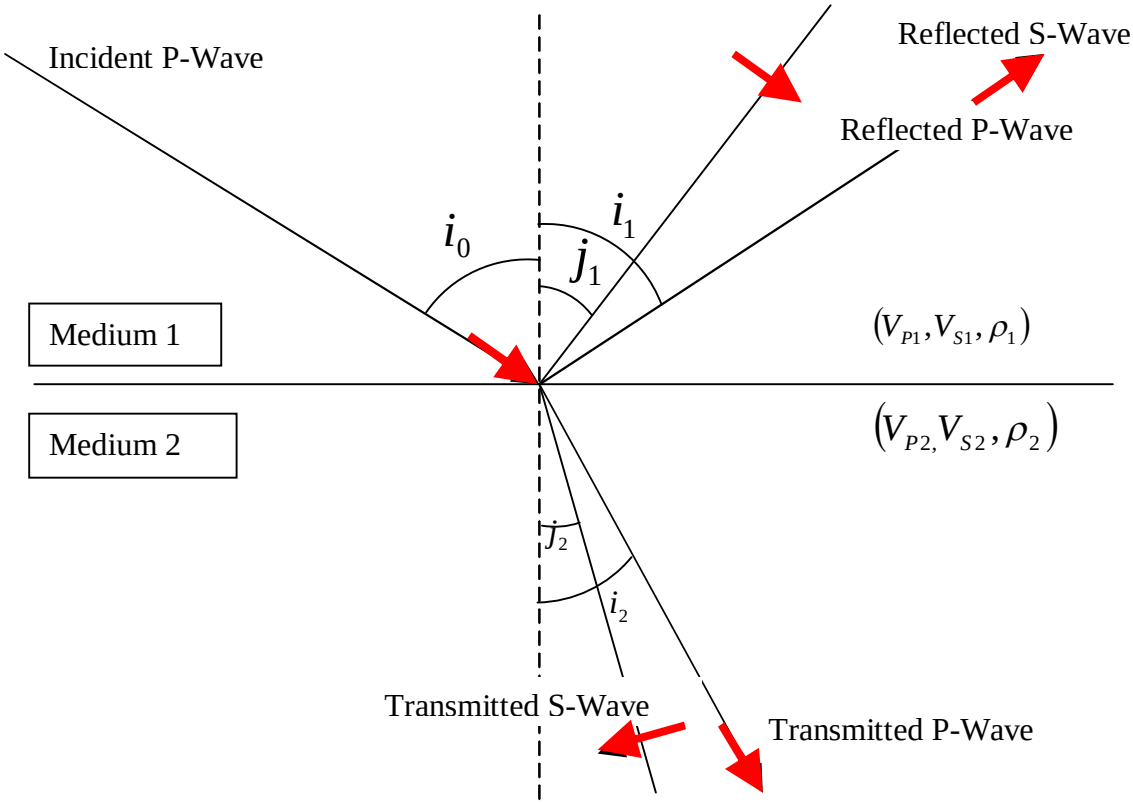

Figure 4 –A plane boundary separating two elastic media separates the energy of an incident P-wave into reflected and transmitted waves, with P and S- polarities. Black lines represent the different trajectories (also called ray paths) related to wave trend, while red arrows stand for their polarization. The dotted line represents the normal to the interface.

For an incident ray reaching a solid/solid plane interface separating two elastic, isotropic and homogeneous media the laws of reflection are:

1. The incident and reflected waves are in the same plane as the reflector surface's normal.
2. The angle of the incident ray to the normal (dotted line in Figure 4) is equal to the angle of the reflected ray to the same normal (consequence in Figure 4; $i_0 = i_1$).

The analytical expression of the Snell's law is (referring to Figure 4) :

$$p = \frac{\sin(i_1)}{V_{P1}} = \frac{\sin(i_2)}{V_{P2}} = \frac{\sin(j_1)}{V_{S1}} = \frac{\sin(j_2)}{V_{S2}} \qquad \textbf{Equation 1}$$

With:

- p: constant called the ray parameter
- V_{Pi} : P-wave velocity in the ith propagating medium
- V_{Si} : S-wave velocity in the ith propagating medium

Beyond a certain angle of incidence, waves are refracted: they travel along the boundary separating the two media (Figure 5). The critical angle i_c, beyond which all waves are refracted, is given by:

$$i_c = \sin^{-1}\left(\frac{V_{P1}}{V_{P2}}\right) \qquad \textbf{Equation 2}$$

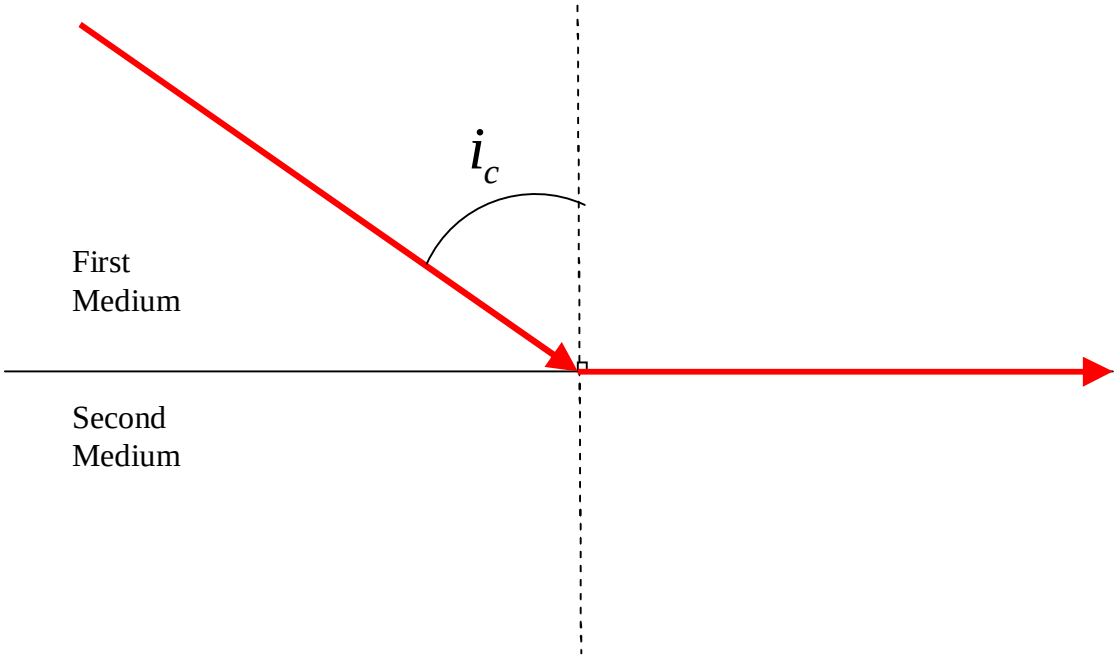

Figure 5 – Ray path followed by a refracted ray

2.2.4. Wave propagation in elastic media: Wave Equation

By citing Knott, Aki and Richards (2002) shows that if the displacement field $\vec{u} = \vec{u}\left(\vec{x},t\right)$ satisfies the Newton's second law of motion:

$$\rho\ddot{\vec{u}} = \vec{f} + (\lambda + 2\mu)\vec{\nabla}\left(\vec{\nabla}.\vec{u}\right) - \mu\vec{\nabla}\times\left(\vec{\nabla}\times\vec{u}\right) \qquad \textbf{Equation 3}$$

- $\boldsymbol{\rho}$**:** density
- $(\boldsymbol{\lambda},\boldsymbol{\mu})$**:** Lame's parameters
- $\vec{\boldsymbol{f}}$**:** Source (depicted here as a force)
- $\vec{u}$ **:** Displacement field
- $\ddot{\vec{u}}$: second time derivative of $\vec{u}$ (acceleration)
- $\vec{\nabla}.$: divergence in the Cartesian (x,y,z) space
- $\vec{\nabla}\times$: rotational in the Cartesian (x,y,z) space

And if the body force and initial values of $\ddot{\vec{u}}$ and $\vec{u}$ are expressed in terms of Helmholtz potentials (A,B,C,D, Φ and Ψ) via:

$$\vec{f} = \vec{\nabla}\Phi + \vec{\nabla}\times\Psi \qquad \textbf{Equation 4}$$

$$\ddot{u}\left(\vec{x},0\right) = \vec{\nabla}\vec{A} + \vec{\nabla}\times\vec{B} \qquad \textbf{Equation 5}$$

$$u\left(\vec{x},0\right) = \vec{\nabla}\vec{C} + \vec{\nabla}\times\vec{D} \qquad \textbf{Equations 6}$$

With:

$$\vec{\nabla}.\vec{\Psi} = 0 \qquad \textbf{Equation 7}$$

$$\vec{\nabla}.\vec{B} = 0 \qquad \textbf{Equation 8}$$

$$\vec{\nabla}.\vec{D} = 0 \qquad \textbf{Equation 9}$$

Then $\vec{u}$ can be defined by its potentials Φ and Ψ .

$$\vec{u} = \vec{\nabla}\Phi + \vec{\nabla} \times \Psi \qquad \textbf{Equation 10}$$

$$\vec{\nabla}.\Psi = 0 \qquad \textbf{Equation 11}$$

$$\ddot{\Phi} = \frac{\Phi}{\rho} + V_P^2 \nabla^2 \Phi \qquad \textbf{Equation 12}$$

$$\ddot{\Psi} = \frac{\Psi}{\rho} + V_S^2 \nabla^2 \Psi \qquad \textbf{Equation 13}$$

Where $\frac{\phi}{\rho}$ and $\frac{\psi}{\rho}$ are the source terms.

Euqation 11 denotes the continuity of the strain at the interface separating the two propagating media.

The driven harmonic oscillator equations 12 and 13 depict respectively the P-(longitudinal polarization) and S-wave (transversal polarization) motions in a propagating medium. The terms $\frac{\phi}{\rho}$ and $\frac{\psi}{\rho}$ are neglected due to the transient nature of the sources of a seismic survey; the driven harmonic oscillator equations become the equations of a simple harmonic oscillator.

Finally, equation 10 is the link between potentials and strain.

2.2.5. Wave propagation in elastic media: wave equation solutions

In a 2D medium with no internal forces, equations 12 and 13 have, in a Cartesian coordinate system, the following expressions:

$$\frac{1}{V_P^2}\frac{\partial^2 \phi}{\partial t^2} = \frac{\partial^2 \phi}{\partial x^2} + \frac{\partial^2 \phi}{\partial z^2} \qquad \textbf{Equation 14}$$

$$\frac{1}{V_S^2}\frac{\partial^2 \psi}{\partial t^2} = \frac{\partial^2 \psi}{\partial x^2} + \frac{\partial^2 \psi}{\partial z^2} \qquad \textbf{Equation 15}$$

In the notation used by Yilmaz(2001), the solutions of these equations are:

1. Incident P-wave:

$$\phi_i = A_0 \exp\left(i\frac{\omega}{V_{P1}}\sin(i_0)x + i\frac{\omega}{V_{P1}}\cos(i_0)z - i\omega t \right) \quad \textbf{Equation 16}$$

2. Reflected P-Wave:

$$\phi_r = A_1 \exp\left(i\frac{\omega}{V_{P1}}\sin(i_1)x - i\frac{\omega}{V_{P1}}\cos(i_1)z - i\omega t \right) \quad \textbf{Equation 17}$$

3. Reflected S-wave:

$$\psi_r = B_1 \exp\left(i\frac{\omega}{V_{S1}}\sin(j_1)x - i\frac{\omega}{V_{S1}}\cos(j_1)z - i\omega t \right) \quad \textbf{Equation 18}$$

4. Transmitted P-Wave:

$$\phi_t = A_2 \exp\left(i\frac{\omega}{V_{P2}}\sin(i_2)x + i\frac{\omega}{V_{P2}}\cos(i_2)z - i\omega t \right) \quad \textbf{Equation 19}$$

5. Transmitted S-wave:

$$\psi_t = B_2 \exp\left(i\frac{\omega}{V_{S2}}\sin(j_2)x + i\frac{\omega}{V_{S2}}\cos(j_2)z - i\omega t \right) \quad \textbf{Equation 20}$$

With:

- **ω**: angular frequency (in radians) **($\omega = 2\Pi f$, Equation 21)**
- A_0: Incident P-wave amplitude
- A_1: Reflected P-wave amplitude
- A_2: Transmitted P-wave amplitude
- B_1: Reflected S-wave amplitude
- B_2: Transmitted S-wave amplitude

These solutions describe the separation of incident wave energy (as depicted in Figure 4) into:

- P reflected and transmitted waves
- S reflected and transmitted waves

The P- and S-wave displacement potentials in the first media are respectively:

$$\phi_1 = \phi_i + \phi_r \quad \textbf{Equation 22}$$

$$\psi_1 = \psi_r \quad \textbf{Equation 23}$$

And;

$$\phi_2 = \phi_t \quad \textbf{Equation 24}$$

$$\psi_2 = \psi_t \quad \textbf{Equation 25}$$

in the second media.

The substitution of potentials by their expressions leads to:

$$\phi_1 = A_0 \exp\left(i\frac{\omega}{V_{P1}}\sin(i_0)x + i\frac{\omega}{V_{P1}}\cos(i_0)z - i\omega t \right) + A_1 \exp\left(i\frac{\omega}{V_{P1}}\sin(i_1)x - i\frac{\omega}{V_{P1}}\cos(i_1)z - i\omega t \right) \quad \textbf{Equation 26}$$

$$\phi_2 = A_2 \exp\left(i\frac{\omega}{V_{P2}}\sin(i_2)x + i\frac{\omega}{V_{P2}}\cos(i_2)z - i\omega t \right)$$ **Equation 27**

$$\psi_1 = B_1 \exp\left(i\frac{\omega}{V_{S1}}\sin(j_1)x - i\frac{\omega}{V_{S1}}\cos(j_1)z - i\omega t \right)$$ **Equation 28**

$$\psi_2 = B_2 \exp\left(i\frac{\omega}{V_{S2}}\sin(j_2)x + i\frac{\omega}{V_{S2}}\cos(j_2)z - i\omega t \right)$$ **Equation 29**

These expressions are different from the solutions (computed in section 2.5) of the thermoelastic wave equations.

2.2.6. Boundary conditions

Four conditions of stress and strain define a continuous solid/solid plane interface separating two elastic and isotropic media:

1. displacement component tangential to the interface: $u_1 = u_2$ **Equation 30**
2. displacement component normal to the interface: $w_1 = w_2$ **Equation 31**
3. stress component tangential to the interface: $(\sigma_{xz})_1 = (\sigma_{xz})_2$ **Equation 32**
4. stress component normal to the interface: $(\sigma_{zz})_1 = (\sigma_{zz})_2$ **Equation 33**

Subscripts 1 and 2 refer to the media 1 and 2 defined in Figure 4.

In this chapter (e.g. paragraph 2.5), the analysis based on the analogy between Zoeppritz and thermoelastic boundary conditions ends at this stage. The analytical expressions of thermoelastic boundary conditions in a cartesian coordinate system are not determined in this thesis.

However, a method for computing the cartesian expressions of equations 31 to 33 can be found in Yilmaz, Seismic Data Analysis, Volume 2 (2001) (respectively equations L-65 and L-67 (in page 2016), L-75 (in page 2018) and L-70 (in page 2017) and named equations 34, 35, 36 and 37 are in this PhD thesis).

$$u_1 = u_2 \quad \Leftrightarrow \quad \frac{\partial\phi_1}{\partial x} + \frac{\partial\psi_1}{\partial z} = \frac{\partial\phi_2}{\partial x} + \frac{\partial\psi_2}{\partial z}$$ **Equation 34**

$$w_1 = w_2 \quad \Leftrightarrow \quad \frac{\partial\phi_1}{\partial z} - \frac{\partial\psi_1}{\partial x} = \frac{\partial\phi_2}{\partial z} - \frac{\partial\psi_2}{\partial z}$$ **Equation 35**

$$\mu_1\left(2\frac{\partial^2\phi_1}{\partial x\partial z} + \frac{\partial^2\psi_1}{\partial z^2} - \frac{\partial^2\psi_1}{\partial x^2} \right) = \mu_2\left(2\frac{\partial^2\phi_2}{\partial x\partial z} + \frac{\partial^2\psi_2}{\partial z^2} - \frac{\partial^2\psi_2}{\partial x^2} \right)$$ **Equation 36**

$$\rho_1\frac{\partial^2\phi_1}{\partial t^2} - 2\rho_1 V_{S1}^2\left(\frac{\partial^2\phi_1}{\partial x^2} - \frac{\partial^2\psi_1}{\partial x\partial z} \right) = \rho_2\frac{\partial^2\phi_2}{\partial t^2} - 2\rho_2 V_{S2}^2\left(\frac{\partial^2\phi_2}{\partial x^2} - \frac{\partial^2\psi_2}{\partial x\partial z} \right)$$ **Equation 37**

2.2.7. Zoeppritz's equations

Zoeppritz's equations are the application of the potential equations 26 to 29 in the cartesian expressions of boundary conditions. The mathematical demonstration of this application can be found in Yilmaz's reference, Seismic Data Analysis (2001), second volume, Appendix L (respectively equations L-66 and L-68 in page 2016, equation L-73 in page 2017 and L-77 in page 2018).:

1. $$\frac{\sin(i_1)}{V_{P1}}A_0 + \frac{\sin(i_1)}{V_{P1}}A_1 - \frac{\cos(i_1)}{V_{S1}}B_1 = \frac{\sin(i_2)}{V_{P2}}A_2 + \frac{\cos(j_2)}{V_{S2}}B_2$$

Equation 38

2. $$\frac{\cos(i_1)}{V_{P1}}A_0 - \frac{\cos(i_1)}{V_{P1}}A_1 - \frac{\sin(i_1)}{V_{S1}}B_1 = \frac{\cos(i_2)}{V_{P2}}A_2 - \frac{\sin(j_2)}{V_{S2}}B_2$$

Equation 39

3. $$-A_0\cos(2j_1) - A_1\cos(2j_1) - B_1\sin(2j_1) = -\frac{\rho_2}{\rho_1}A_2\cos(2j_2) + \frac{\rho_2}{\rho_1}B_2\sin(2j_2)$$

Equation 40

4. $$-A_0\sin(2i_1) + A_1\sin(2i_1) - B_1\frac{V_{P1}^2}{V_{S1}^2}\cos(2j_1) = -A_2\frac{\rho_2 V_{S2}^2 V_{P1}^2}{\rho_1 V_{S1}^2 V_{P2}^2}\sin(2i_2) - B_2\frac{\rho_2 V_{P1}^2}{\rho_1 V_{S1}^2}\cos(2j_2)$$

Equation 41

2.2.8. Aki and Richards' solutions

The fifth chapter of "Quantitative Seismology", second edition (Aki and Richards (2002)) proposes a method for solving the equations of Zoeppritz. The solutions are the analytical expressions of reflection or transmission coefficients. Their numerical application, in the fourth chapter of this thesis, assesses the AVO response of different roof layers over a coal seam.

This numerical assessment requires a set of six parameters, three in each layer:

- V_{P1}: roof P-wave velocity
- V_{S1}: roof S-wave velocity
- ρ_1: roof density
- V_{P2}: coal seam P-wave velocity
- V_{S2}: coal seam S-wave velocity
- ρ_2: coal seam density

In the laboratory, the set (V_P, V_S,) shall be collected for each rock.

The different solutions are:

- Incident-P wave, reflected P-wave:

$$\overset{\backslash}{P}\overset{/}{P} = \frac{\left[\left(b\frac{\cos(i_1)}{V_{P1}} - c\frac{\cos(i_2)}{V_{P2}}\right)F - \left(a + d\frac{\cos(i_1)}{V_{P1}}\frac{\cos(j_2)}{V_{S2}}\right)Hp^2\right]}{D}$$

Equation 42

- Incident P-wave, reflected S-wave

$$\overset{\backslash}{P}\overset{/}{S} = -2\frac{\cos(i_1)}{V_{S1}D}\left(ab + cd\frac{\cos(i_2)}{V_{P2}}\frac{\cos(j_2)}{V_{S2}}\right)p$$

Equation 43

- Incident P-wave, transmitted P-wave

$$\overset{\backslash}{P}\overset{\backslash}{P} = 2\rho_1\frac{\cos(i_1)}{V_{P2}D}F$$

Equation 44

- Incident P-wave, transmitted S-wave

$$\overset{\backslash}{P}\overset{\backslash}{S} = 2\rho_1\frac{\cos(i_1)}{V_{S2}D}Hp$$

Equation 45

- Incident S-wave, reflected P-wave

$$\overset{\backslash}{S}\overset{/}{P} = -2p\frac{\cos(j_1)}{V_{P1}D}\left(ab + cd\frac{\cos(i_2)}{V_{P2}}\frac{\cos(j_2)}{V_{S2}}\right)$$

Equation 46

- Incident S-wave, reflected S-wave

$$\overset{\backslash}{S}\overset{/}{S} = -\frac{\left[\left(b\frac{\cos(j_1)}{V_{S1}} - c\frac{\cos(j_2)}{V_{S2}}\right)E - \left(a + d\frac{\cos(i_2)}{V_{P2}}\frac{\cos(j_1)}{V_{S1}}\right)Gp^2\right]}{D}$$

Equation 47

- Incident S-wave, transmitted P-wave

$$\overset{\backslash}{S}\overset{\backslash}{P} = -2\rho_1\frac{\cos(j_1)}{V_{P2}D}Gp$$

Equation 48

- Incident S-wave, transmitted S-wave

$$\overset{\backslash}{S}\overset{\backslash}{S} = 2\rho_1\frac{\cos(j_1)}{V_{S2}D}E$$

Equation 49

Where a, b, c, d, D, E, F, G and H terms are:

- $a = \rho_2\left(1-2V_{S2}^2 p^2\right)-\rho_1\left(1-2V_{S1}^2 p^2\right)$ **Equation 50**
- $b = \rho_2\left(1-2V_{S2}^2 p^2\right)+2\rho_1 V_{S1}^2 p^2$ **Equation 51**
- $c = \rho_1\left(1-2V_{S1}^2 p^2\right)+2\rho_2 V_{S2}^2 p^2$ **Equation 52**
- $d = 2\left(\rho_2 V_{S2}^2 - \rho_1 V_{S1}^2\right)$ **Equation 53**
- $E = b\dfrac{\cos(i_1)}{V_{P1}} + c\dfrac{\cos(i_2)}{V_{P2}}$ **Equation 54**
- $F = b\dfrac{\cos(j_1)}{V_{S1}} + c\dfrac{\cos(j_2)}{V_{S2}}$ **Equation 55**
- $G = a - d\dfrac{\cos(i_1)}{V_{P1}}\dfrac{\cos(j_2)}{V_{S2}}$ **Equation 56**
- $H = a - d\dfrac{\cos(i_2)}{V_{P2}}\dfrac{\cos(j_1)}{V_{S1}}$ **Equation 57**
- $D = EF + GHp^2 = \dfrac{\det(M)}{V_{P1}V_{P2}V_{S1}V_{S2}}$ **Equation 58**

2.2.9. Discussion

The objectives were to:

- Introduce the application of potentials for solving the wave equation.
- Present the boundary conditions separating two homogeneous, isotropic and elastic media.
- Determine that the set of parameters (V_P, V_S,) which have to be collected for each rock in the laboratory (Chapter 3).
- Present the Aki and Richards' solutions to the Zoeppritz's equations. The formulas of these solutions will be used equations solutions in numerical applications (in chapter 4).

The first two objectives aim to prove theoretically, in this chapter, that due to non-negligible physical phenomena at ultrasonic scales, a direct calibration of AVO from the laboratory may not be straightforward.

2.3. LINK BETWEEN AVO AND ROCK PHYSICS

2.3.1. Objectives and organization of part 2.3

In 2.2.8, Equation 42 to Equation 49 relate a link between rock properties and recorded signals; from the knowledge of densities, P- and S-wave velocities, these formulas compute the variations of the reflection amplitude with the incidence angle of a wave.

This numerical application initially requires the knowledge of six parameters, while seismic exploration consists in deducing the properties of a system from its response to a signal. Shuey developed a solution to this inverse problem with the simplified set of equations 42 to 58; in the process, he introduced the concept of AVO classes.

If these AVO classes are representative of different cases met in the oil industry, none of them describes cases from coal exploration, hence the potential need to develop one or more additional classes.

The following sections introduce:

1. Young's modulus
2. Poisson's ratio
3. Lame's parameters
4. Links between Poisson's ratio, Young's Modulus, V_P and V_S
5. Approximation of Aki and Richards
6. Approximation of Shuey
7. AVO Classes
8. AVO Classes and Coal
9. Discussion

2.3.2. Young's Modulus

Figure 6 shows that a material sustains a deformation under a compressive or tensile force.

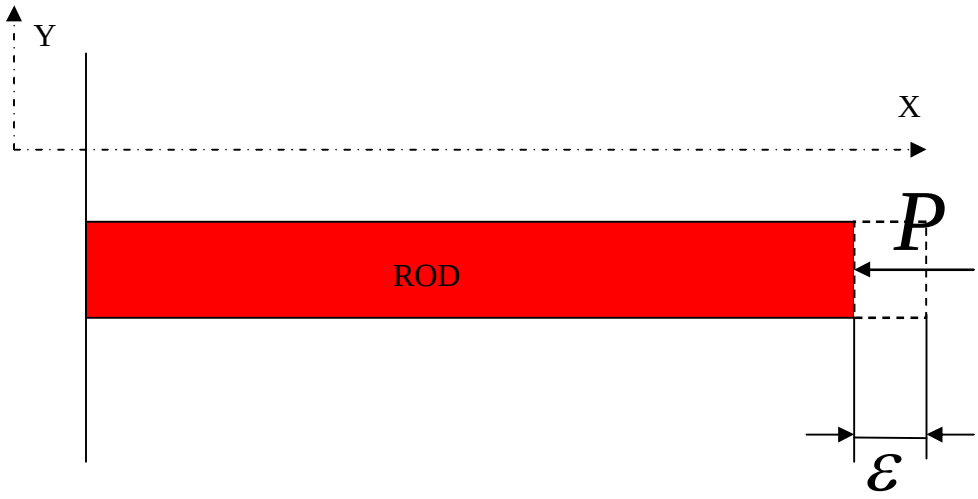

Figure 6 - The application of a force F generates a strain ε

The degree of deformation depends on the Young's modulus, a measure of the stiffness of an isotropic elastic material. It determines a material's ability to maintain its atoms at a constant distance; the bigger the value of E, the more rigid the material. The link between stress, strain and Young's modulus is an analogy with Hooke's law, which states that in the elastic limit, the extension of a spring is in direct proportion with the load added to it. In the elastic region (see Figure 7), for small strains, a similar law approximates the linear relation between stress and strain:

$$\sigma = E\varepsilon \qquad \textbf{Equation 59}$$

Where:

- σ : tensile or compressive stress (in Pascal, or N/m^2)
- ε : strain (dimensionless)
- E: Young's Modulus (in Pascal, or N/m^2).

With the stress:

$$\sigma = \frac{F}{S_0}$$ **Equation 60**

- F: force applied to the object
- S_0: original cross-sectional area through which the force is applied

And the strain:

$$\varepsilon = \frac{l - l_0}{l_0}$$ **Equation 61**

- l_0: initial length of the object
- l: object's length under stress

The linear equation 56 describes a material's property in the elastic zone. Section 2.4 shows how Young's Modulus determined dynamically (with ultrasonic waves, where strains in the elastic region) varies from its static determination (in the plastic region, if directly measured in a coalmine where the deformation of the rock exceeds the elastic limit).

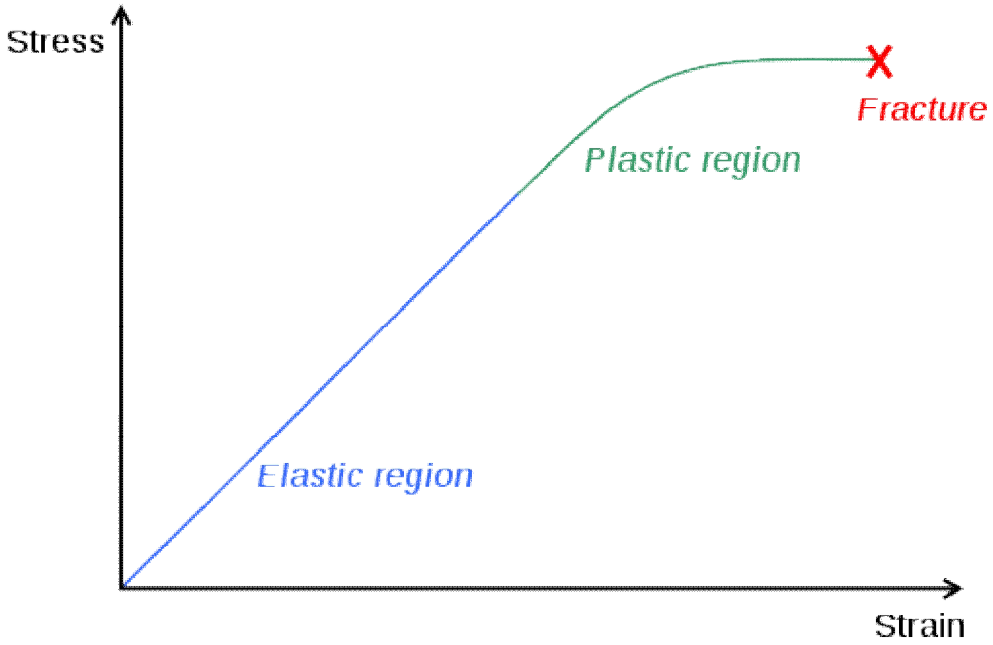

Figure 7 - Diagram of a stress-strain curve, showing the relationship between stress (force applied) and strain (deformation) of a ductile metal.

2.3.3. Poisson's Ratio

Poisson's ratio is the ratio, when a sample object is stretched, of the contraction or transverse strain (perpendicular to the applied load) to the extension or axial strain (in the direction of the applied load). It relates a material's physical ability to keep its volume under compression or extension. The Poisson's ratio mathematical expression, based on a stretched cylindrical rod depicted in Figure 8, is:

$$\nu = \frac{transversalContraction}{axialExtension} = \frac{(l_0 - l)/l_0}{(L - L_0)/L_0} = -\frac{\varepsilon_{trans}}{\varepsilon_{axial}}$$ **Equation 62**

With:

- ν: Poisson's ratio
- l_0: initial diameter of the rod
- l: diameter of the stretched rod
- L_0: initial length of the rod
- L: length of the stretched rod
- ε_{trans}: transversal strain
- ε_{axial}: axial strain

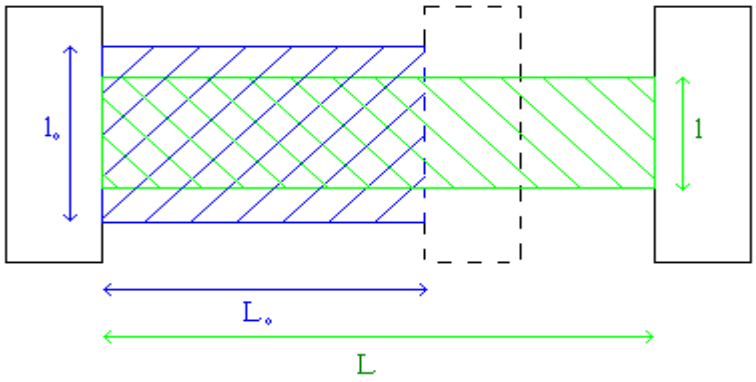

Figure 8 - Poisson's ratio is a material's ability to keep its section under extension of compression

The Poisson's ratio has no unit, its value is theoretically between -1 and 0.5 for an isotropic material (a theoretical demonstration is presented by Sadd, 2005), and generally ranges from 0 (like cork, showing no contraction under load) to nearly 0.5 (like rubber, unable to keep its volume under load). For coal, the average Poisson's ratio is 0.354 (Szabo (1981), Van Krevelen (1993), Gercek (2007)), but varies with the presence of cleats and cracks (Barton(2008), and Figure 9).

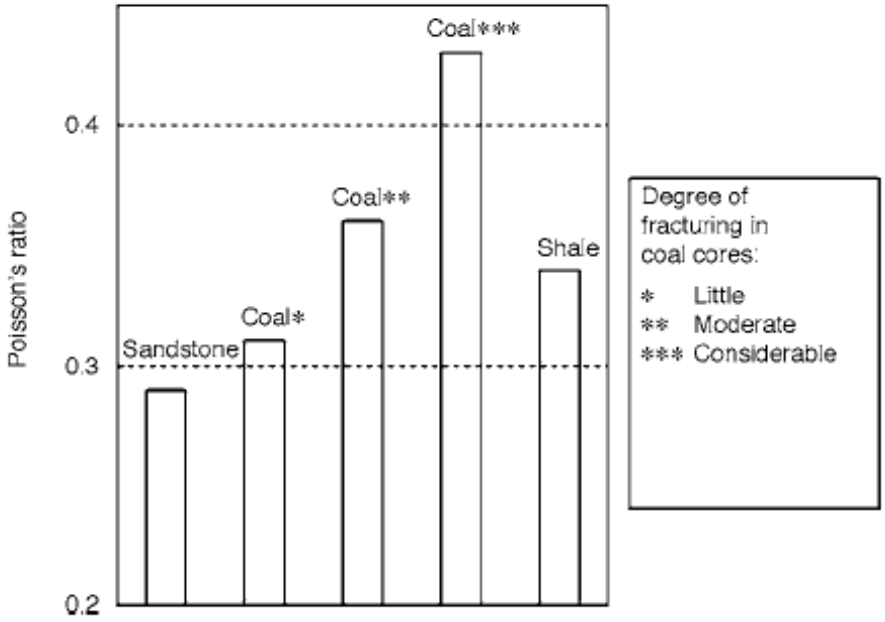

Figure 9 – Lab Measurements for Poisson's ratio in vertical coal core from Cedar Hill Field, New Mexico (Peng (2006)).

2.3.4. Lame's parameters

Jaeger & Cook, Fundamentals of Rock Mechanics, third edition (1979), state that for homogenous, isotropic and linear elastic materials:

$$\lambda = \frac{\nu E}{(1+\nu)(1-2\nu)}$$ **Equation 63**

$$\mu = \frac{E}{2(1+\nu)}$$ **Equation 64**

Where:

- λ: Lamé's first parameter
- μ: shear modulus or Lamé's second parameter
- E: Young's modulus
- ν: Poisson's ratio

In this thesis, λ and μ are used as intermediate parameters for establishing a link between Young's modulus, Poisson's ratio, V_P and V_S.

2.3.5. Link between Young's Modulus, Poisson's ratio, Vp and Vs

Jaeger & Cook, Fundamentals of Rock Mechanics, third edition (1979), also prove for homogenous, isotropic and linear elastic materials that:

$$V_P = \sqrt{\frac{\lambda + 2\mu}{\rho}}$$ **Equation 65**

$$V_S = \sqrt{\frac{\mu}{\rho}}$$ **Equation 66**

A direct link between Poisson's ratio, Young's modulus and velocities being:

$$V_P = \sqrt{\frac{E(1-\nu)}{(1+\nu)(1-2\nu)\rho}}$$ **Equation 67**

$$V_S = \sqrt{\frac{E}{2(1+\nu)\rho}}$$ **Equation 68**

And vice-versa:

$$E = \rho V_S^2 \left(\frac{3V_P^2 - 4V_S^2}{V_P^2 - V_S^2} \right)$$ **Equation 69**

$$\nu = \frac{V_P^2 - 2V_S^2}{2(V_P^2 - V_S^2)}$$ **Equation 70**

2.3.6. Aki and Richards' approximation

AVO analysis seeks to extract rock parameters, and to identify lithologies, by analysing seismic amplitudes as a function of offset, or more correctly, as a function of angle (Avseth, Mukerji & Mavko, 2005). This inversion is done with a simplified version of Equation 42, based on a weak layer contrasts assumption:

$$\overset{\backslash}{P}\overset{/}{P} = \frac{1}{2}(1 - 4V_S^2)\frac{\Delta\rho}{\rho} + \frac{1}{2\cos^2(i)}\frac{\Delta V_P}{V_P} - 4V_S^2 p^2 \frac{\Delta V_S}{V_S}$$ **Equation 71**

With:

- $\Delta\rho = \rho_2 - \rho_1$ **Equation 72**
- $\rho = \frac{(\rho_1 + \rho_2)}{2}$ **Equation 73**
- $\Delta V_P = V_{P2} - V_{P1}$ **Equation 74**
- $V_P = \frac{(V_{P1} + V_{P2})}{2}$ **Equation 75**
- $\Delta V_S = V_{S2} - V_{S1}$ **Equation 76**
- $V_S = \frac{(V_{S1} + V_{S2})}{2}$ **Equation 77**

Including the following terms linked to different scattering angles:

- $i = \frac{(i_1 + i_2)}{2}$ **Equation 78**
- $\Delta i = i_2 - i_1 \approx \left(\frac{\Delta V_P}{V_P} \right) \tan(i)$ **Equation 79**
- $j = \frac{(j_1 + j_2)}{2}$ **Equation 80**
- $\Delta j = j_2 - j_1 \approx \left(\frac{\Delta V_S}{V_S} \right) \tan(j)$ **Equation 81**

2.3.7. Shuey Approximation

Shuey made a further approximation:

$R(i) = R_0 + G \sin^2(i) + F\left(\tan^2(i) - \sin^2(i)\right)$ **Equation 82**

With:

- $R_0 \approx \frac{1}{2}\left(\frac{\Delta V_P}{V_P} + \frac{\Delta \rho}{\rho} \right)$ **Equation 83**
- $i = \frac{i_1 + i_2}{2} \approx i_1$ **Equation 84**
- $G = \frac{1}{2}\frac{\Delta V_P}{V_P} - 2\frac{V_S^2}{V_P^2}\left(\frac{\Delta \rho}{\rho} + 2\frac{\Delta V_S}{V_S} \right) = R(0) - \frac{\Delta \rho}{\rho}\left(\frac{1}{2} + \frac{2V_S^2}{V_P^2} \right) - \frac{4V_S^2}{V_P^2}\frac{\Delta V_S}{V_S}$ **Equation 85**
- $F = \frac{1}{2}\frac{\Delta V_P}{V_P}$ **Equation 86**

- Ro: reflection amplitude at normal incidence, also called intercept
- i: mean incidence angle
- G: gradient, related to near offsets
- F: curvature, related to amplitude variations at far offsets

Chapter 5 presents the results of an inversion process of a seismic shot recorded in Daw Mill mine having a 28 degrees average aperture. Neglecting the last term of expression equation 82 leads to:

$R(i) \approx R(0) + G \sin^2(i)$ **Equation 87**

This two-terms approximation is accurate for angles of incidences up to 30 degrees, but may not be valid for the thin-bed geology met in Daw Mill.

2.3.8. AVO classes

The outputs of an inversion conducted with equation 87 are, respectively, the reflection amplitude at normal incidence, and the gradient. The cross-plot of these two extracted parameters gives a new insight to the analysis, by establishing a link between geology and variations of amplitude. To do so, Rutherford and Williams

(1984) proposed a classification scheme for different AVO classes, presented in Figure 10.

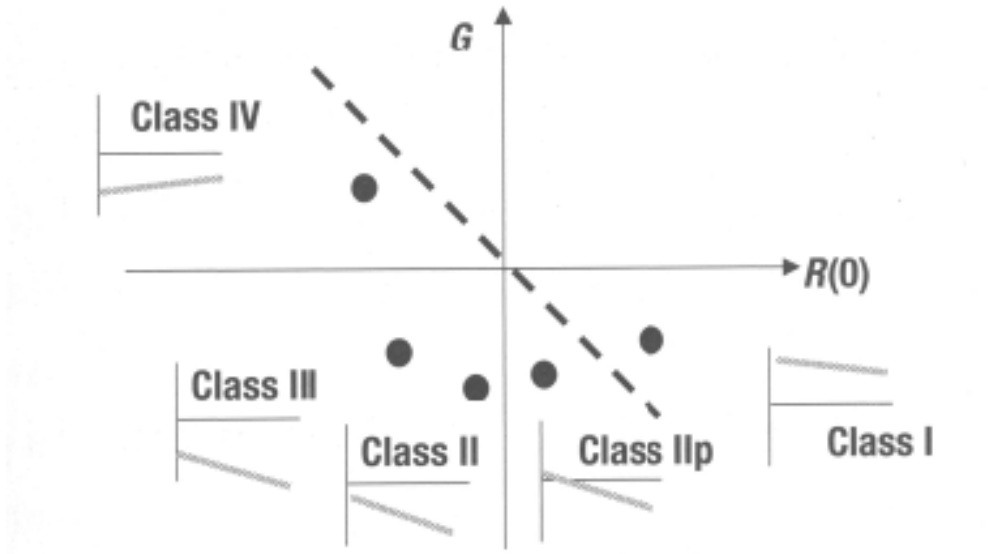

Figure 10 - Rutherford and Williams AVO Classes. (Asveth, Mukerji and Mavko (2005))

Asveth, Mukerji and Mavko (2005) summarize these four classes as follow;

Class 1: The reflection coefficient at normal incidence is positive, and the gradient is negative. The product of these terms, referred as the AVO product in Table 1, is negative. It means that the reflected amplitude will decrease with offset (as in Figure 11). AVO class I are generally associated to relatively hard sands with hydrocarbons.

Class 2: generally describes transparent sands (i.e, these sands are not seen on a seismic section due to their impendance). If not compensated by a strong gradient, the weak value of Ro generates dim spots on a seismic section

Class 3: is the classical AVO anomaly with negative intercept and negative gradient, like the gas sand example in Figure 2.

Class 4: is rare, and occurs when a stiff-cap rock-shale caps soft-sands with gas.

Class	Relative Impedance	Quadrant	R(0)	G	AVO product
I	High-impedance sand	4th	+	-	Negative
II	No or low contrast	4th	+	-	Negative
IIp		3rd	-	-	Positive
III	Low Impedance	3rd	-	-	Positive
IV	Low Impedance	2nd	-	+	Negative

Table 1 – AVO classes, after Rutherford and Williams (1989), extended by Castagna and Smith (1994), and Ross and Kinman (1995).

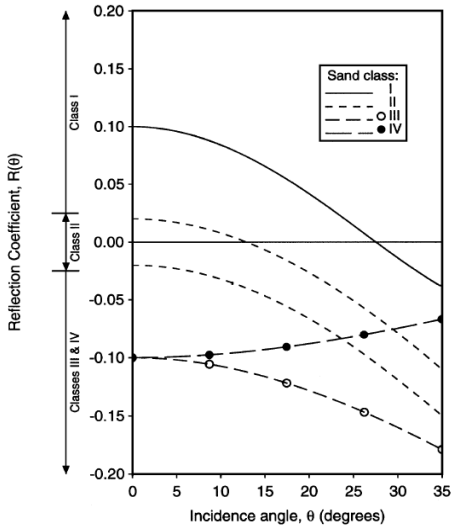

Figure 11 – Representative P-wave amplitude variation with angle of incidence of the Rutherford and Williams classes (Castagna, Swan and Foster (1998)).

2.3.9. AVO classes and Coal

The application of equations 83 and 85 (with average mechanical properties of coal, mudstone and sandstone samples collected in Daw Mill) establishes a class difference between mud-roofs and sand-roofs (see figure 12); these classes are also different from the initial classification of Rutherford and Williams (comparison between figures 10 and 12).

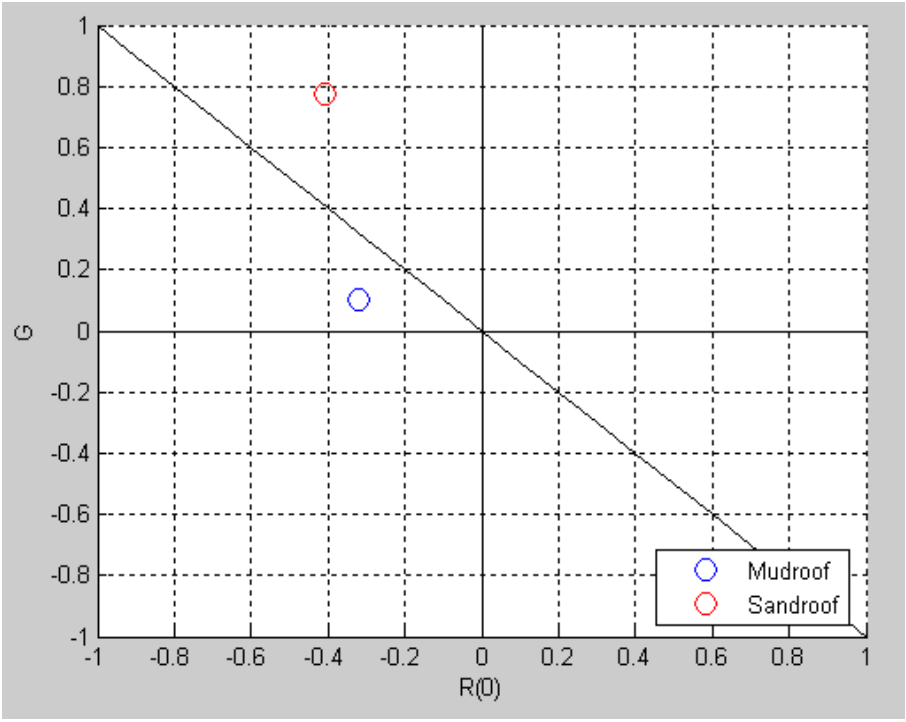

Figure 12 - Application of equations 80 and 82 (with average properties of coal, mudstone and sandstone collected in Daw Mill).

From this class difference, the expected outcome, described in chapter 4, is that AVO can theoretically detect a difference between mud- and sand-roofed coal seams. However, this raises a new problem in that if a new practical application is

established in Chapter 5 the adaptation of AVO to coal exploration may require the definition of at least one new class.

2.3.10. Discussion

The overall aim of this section is to establish a direct link between rocks and AVO theory.

Firstly, Equation 42 to Equation 48 provided formulas, which are used in chapter 4, to assess the variation of amplitude with the angle of incidence. A careful examination of these expressions has led to the conclusion that a numerical implementation requires the following parameters:

- P-wave velocity
- S-wave velocity
- density

As the coalmine industry does not provide velocities, but Young's modulus and Poisson's ratio, the second part of the chapter has presented the theoretical link between these geotechnical parameters and the velocities (with equations 65, 66, 69 and 70).

Section 2.3 also shows that part of AVO's ability to make a distinction between mud- and sand-roofs relies on an inversion, done with a simplified version of formula Equation 42: the Shuey approximation. If cross-plotted, the parameters extracted from this inversion enter into different classes, each one being directly linked to a type of lithology met in oil exploration. A first assessment has shown a class difference between a coal seam with a mudstone and a sandstone roof, and underlined the need to define at least one new class for describing events related to coal geology. Finally, in a multi-layered geology, the results of this inversion may not be accurate in the presence of two close consecutive and interfering reflections; the final part of this chapter introduces this case, known as tuning-effect.

2.4. DIFFERENCES WITH AVO HYPOTHESISES

2.4.1. Objectives and organization of part 2.4

The first two parts of this chapter have presented the link between rock properties and reflection amplitudes of a wave. The solutions of this physical problem describe a model representative of a seismic survey, with plane wave propagation in elastic, isotropic, homogeneous and semi-infinite media. This standard model has proven results in oil exploration, but after some failures (Allen, J.L. & Peddy, C.P., 1993), a reconnaissance step became part of the analysis (cf Figure 13). The reconnaissance consists of checking if:

- the trends of AVO curves provide distinctive signals
- the hypotheses describe the geology of an area

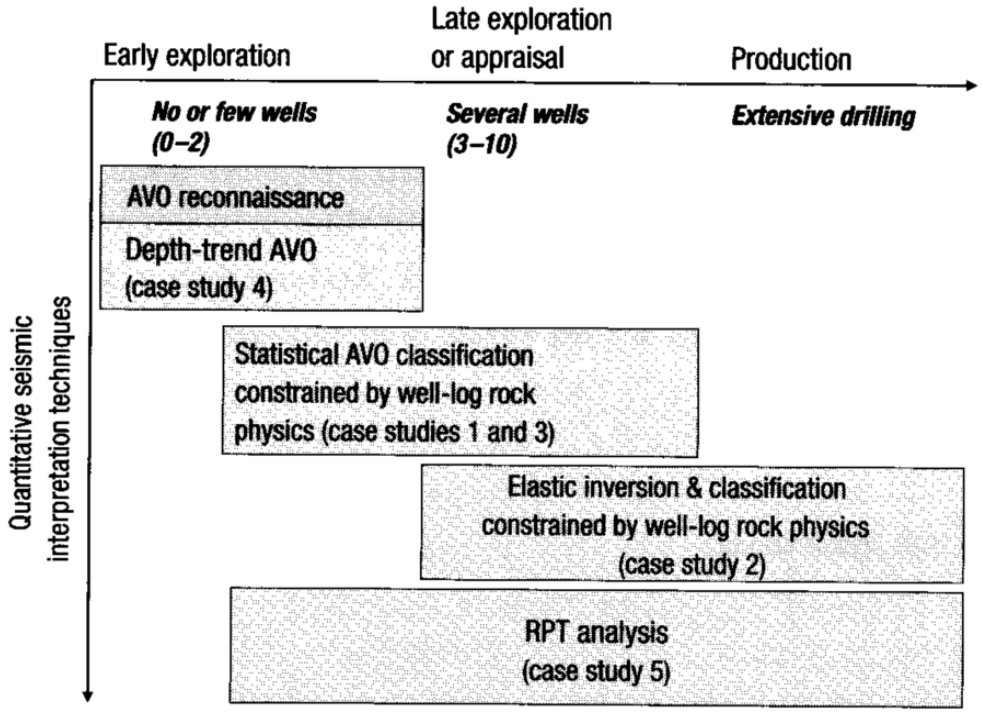

Figure 13 – Typical Quantitative Interpretation techniques performed at different stages of development of an oil field. (Source Asveth, Mukerji, Mavko (2005))

By introducing a class difference, which may exist between AVO signals recorded on mudstone and sandstone roofs deposited over coal seams, section 2.3.9 has indirectly mentioned the existence of distinct AVO curves. The last part of this chapter completes the theoretical aspect of this reconnaissance, by describing the most significant discrepancies between AVO hypotheses and the structure of coal, and by assessing their consequences. The following sections show that aspects related to multi-layering are the most problematic, and concludes that AVO calibration in the laboratory may not be possible with ultrasonic waves. It describes:

1. Coal's structure
2. Cyclothems
3. Tuning effect
4. Wave propagation in finely layered media
5. Thermoelasticity and attenuation
6. Zener

2.4.2. Coal's structure

In a note for the Kentucky Geological Survey, Ariffin (2003) gave the following definition:

"Coal is a compact stratified mass of metamorphosed plants which have, in part, suffered arrested decay to varying degrees of completeness."

This layered structure, shown in Figure 14, induces anisotropic mechanical properties (depicted in Figure 15 and Figure 16). Part 2.4.5 will show, with the work of Hovem (1992), how this fine stratification could also affect wave propagation, and prevent any correlation between anisotropy at ultrasonic scale, and anisotropy observed at seismic scale.

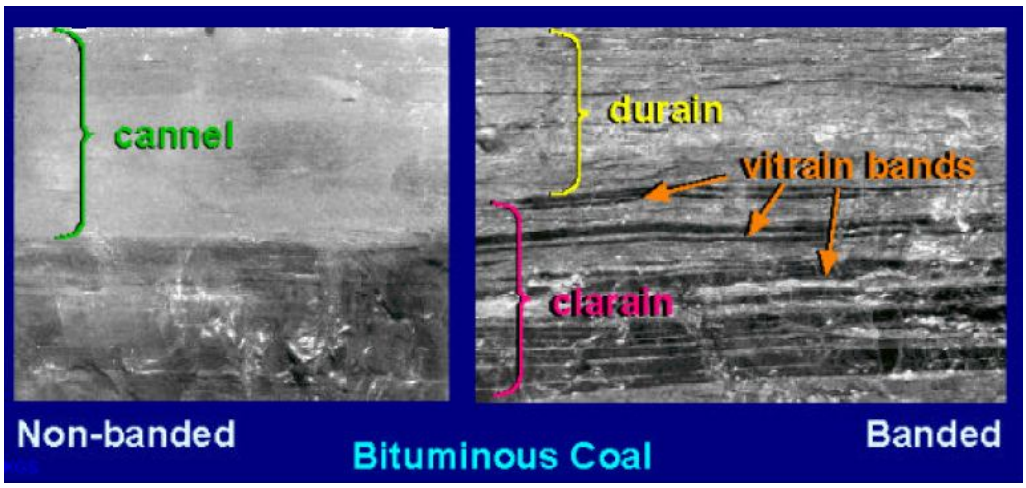

Figure 14 - Comparison between a banded and non banded coal (Ariffin (2003) , courtesy of KGS). The layered structure induces anisotropic mechanical properties.

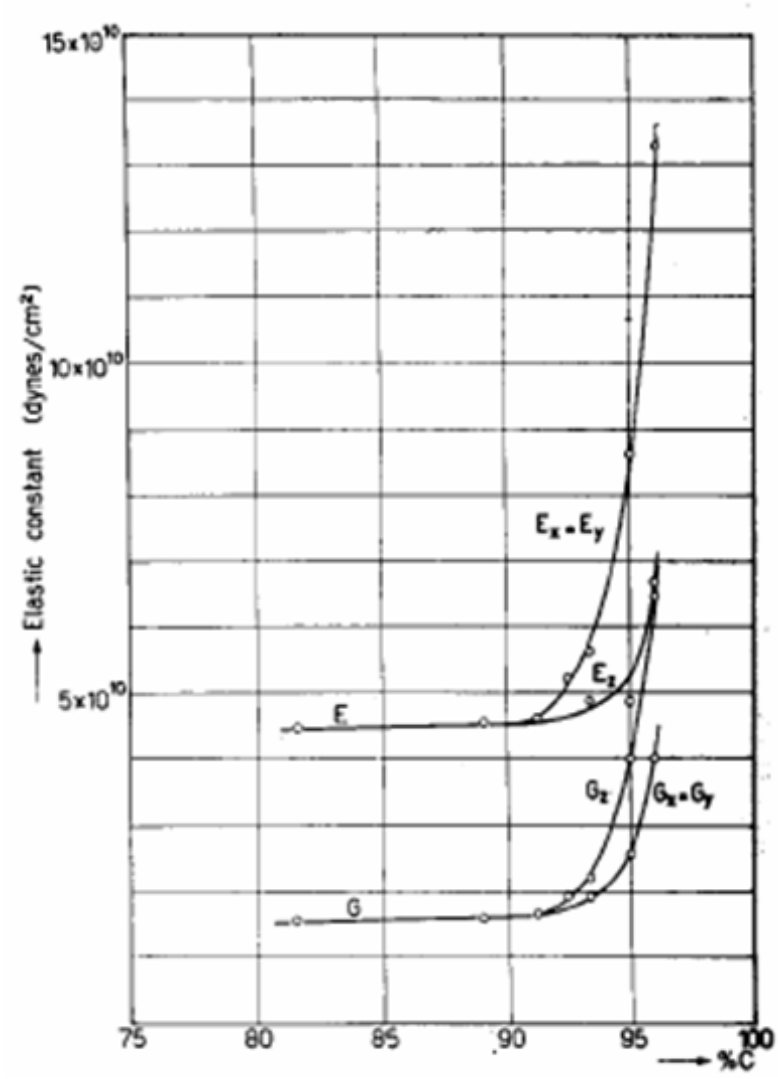

Figure 15 – Variations of the Young and Shear moduli of coal with carbon content. High carbon content is possible with organized carbon chains, which corollary is micro layering. (Schuyer, Dijkstra and Van Krevelen (1954)).

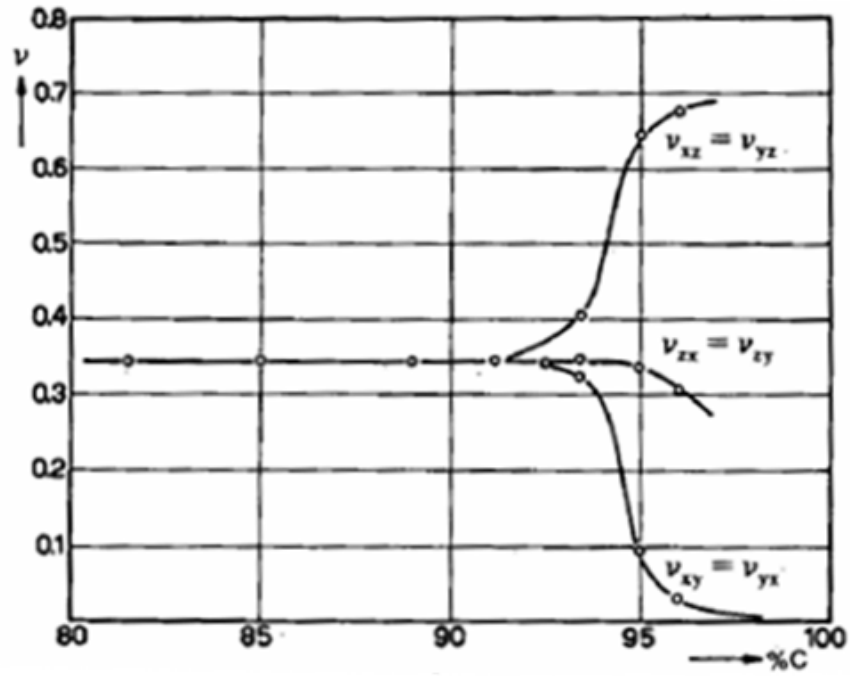

Figure 16 - Variation of the Poisson's ratio of Coal with carbon content. High carbon content is possible with organized carbon chains, which corollary is micro layering.
(Schuyer, Dijkstra and Van Krevelen (1954)).

2.4.3. Cyclothems

Stanley (1999) gave the following definition of a geological feature presented in Figure 17: "In geology, cyclothems are alternating stratigraphic sequences of marine and non-marine sediments, sometimes interbedded with coal seams. Unique to the Carboniferous and earliest Permian periods, they apparently formed as a result of marine transgressions and regressions related to decay and growth of ice sheets, respectively, as the Carboniferous was a time of widespread glaciation."

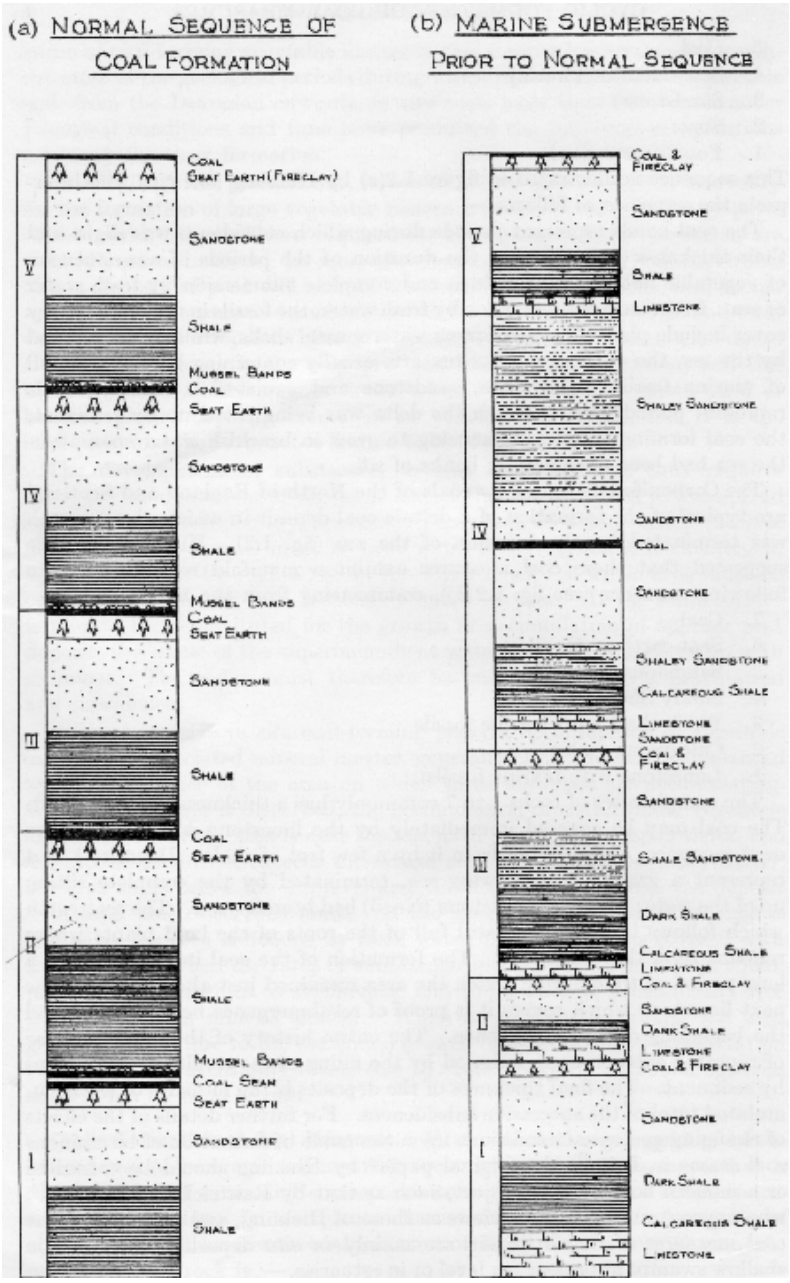

Figure 17 – Example of cyclothems (Wilfrid (1961))

The Daw Mill mine site, for example, has cyclothems composed of alternating mudstone/sandstone sequences, interbedded with three main coal seams and, sometimes, siltstone layers. In this area, a careful analysis of the data provided by UK coal led to the conclusion that the maximum thickness of these layers doesn't exceed more than a few metres; the seismic resolution may not allow an interpreter to distinguish these layers.

With collected data showing approximately a 4200 meters/second average velocity (at a depth of 600 meters), and with a dominant frequency of 60 Hz, the seismic wavelength is 4200/60 = 70 meters; a stratigraphic layer can be resolved with seismic if the layer thickness is larger than a quarter of the dominant wavelength (Avseth, Mukerji, Mavko (2005)). In this case, a layer of 15 meters can be resolved. Section 2.3.9 has shown that theoretically, a distinction could be expected between amplitude responses recorded on mudstone and sandstone roofs; their limited thicknesses in Daw Mill could have consequences for the practical applicability of AVO.

2.4.4. Tuning effect

The objective of this section is to introduce the influence of tuning effect on the:

- variation of amplitude with offset
- inversion inaccuracy
- distortion of reflected wave-shape
- AVO curve trend

In an unpublished course note, Ostrander explained that tuning effect is the interference between two reflections. It occurs when the wavelength is longer than the layer thickness; the top and bottom reflections merge in a constructive or destructive interference.

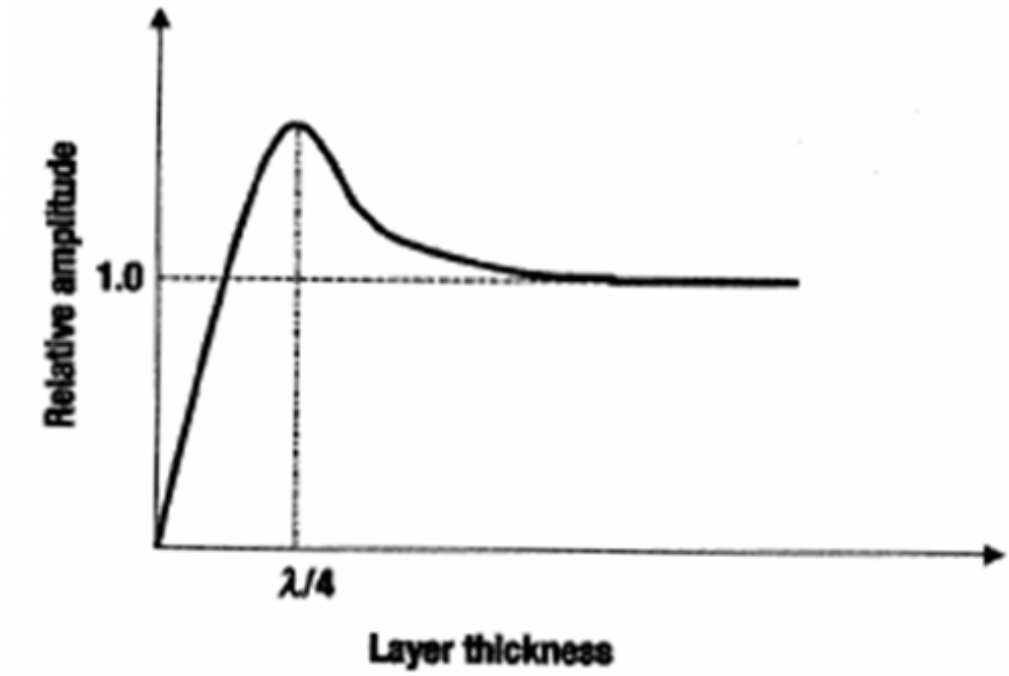

Figure 18 – Seismic amplitude as a function of layer thickness for a given wavelength (Mavko (2005)).

A layer thickness equal to $\lambda/4$ (λ: dominant wavelength) generates a maximum constructive interference (Figure 18); thinner layers cause destructive interferences. If a wavelet peak frequency is 60Hz, and the coal seam's velocity is 2400 m/s, the dominant wavelength is 2400/60 = 40 meters. In this case, the tuning thickness is 40/4 = 10 meters (the average thickness of the coal seam in Daw Mill is 6 meters).

Tuning effect has predictable effects on amplitude variation with offset, but also on the reflected waveshape.

Lin and Phair (1993) have quantified variations of tuning effect with angle of incidence, for a thin layer embedded in a homogeneous rock:

$$R_t = \omega_0 \Delta T(\theta)\cos(\theta)\dot{P}\,P(\theta) \qquad \textbf{Equation 88}$$

With: $\Delta T(\theta) = \frac{thickness_{layer} * \sqrt{1+tan(\theta)^2}}{V_{layer}}$ **Equation 89**

- ω_0 : dominant frequency of the wavelet
- $\Delta T(\theta)$: two way traveltime from the top to the base of the layer
- $\grave{P}\acute{P}(\theta)$: P-wave reflection coefficient, Equation 42 .

Equation 88 describes seismic wave reflection on a thin reflector; the amplitude of reflection varies with offset, but is also a function of:

- frequency
- a tuning amplitude varying with offset.

These two additional terms, not initially taken into account, lead to an inaccuracy of inversions made on thin-bed geology with the Shuey approximation (given by equation 87).

By introducing geometrical spreading to this basis, Bakke and Ursin (1998) have theoretically proved tuning's influence on reflected waveshapes:

$$d_0 = \frac{\grave{P}\acute{P}_1(y)}{g_1(y)} p(t - T_1(y)) + \frac{\grave{P}\acute{P}_2(y)}{g_2(y)} p(t - T_2(y)) \quad \textbf{Equation 90}$$

where

- y: offset
- t: time
- $g_i(y)$: geometrical spreading in the ith layer
- $p(t)$: seismic pulse
- $\grave{P}\acute{P}_1$: top reflection
- $\grave{P}\acute{P}_2$: bottom reflection

If:

- $\grave{P}\acute{P}_2(y) = -\grave{P}\acute{P}_1(y)$ **Equation 91**
- $g_1(y) \approx g_2(y) \approx 1$ **Equation 92**

and by assuming a small two-way traveltime:

$$d(t, y) \approx \grave{P}\acute{P}(y) \Delta T(y) p'(t) \quad \textbf{Equation 93}$$

With:

- $p'(t)$: time derivative of the seismic pulse.

The principal information coming from equation 93 is the presence of "signal distortion"; the reflected waveshape is the time derivative of the incident waveshape. This review conducted as part of this thesis led the interpreters to reconsider their initial analysis of the Daw Mill mine data. The apparent top and bottom reflections observed on seismic data are not two distinct events, but the time derivative of the same reflected seismic pulse.

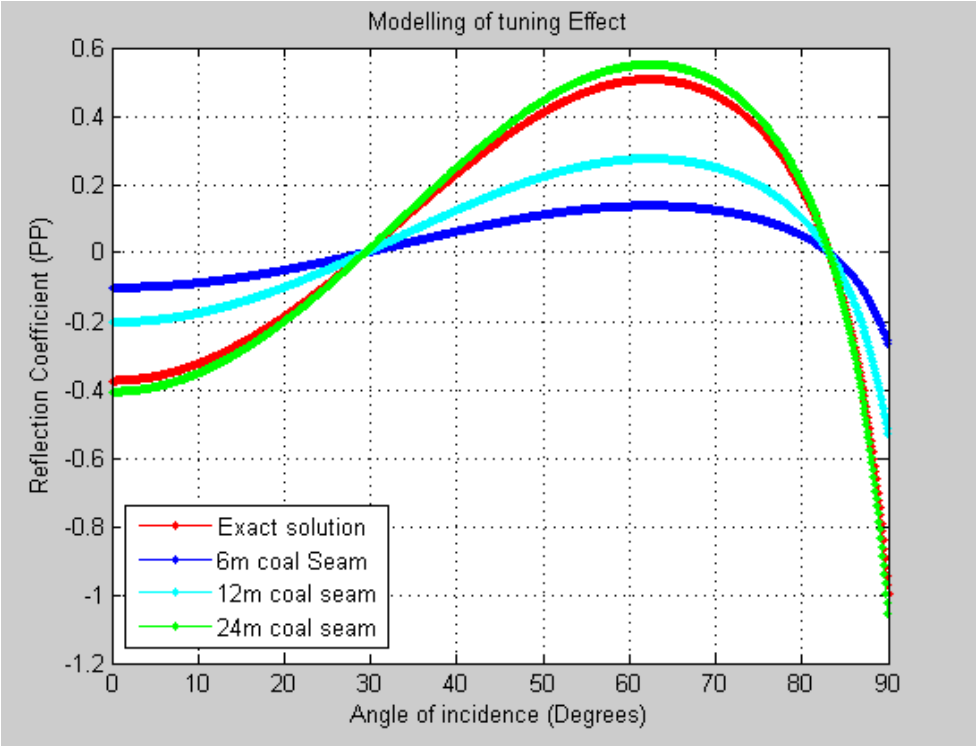

Figure 19 – Comparison between the exact Zoeppritz equations' solution and different thicknesses AVA (AVA: Amplitude Versus Angle) response. AVO response can significantly be altered by tuning effect. In this modelling, the dominant frequency is 60Hz.

The final consequence of tuning effect is its influence on AVO curve trend. Figure 19 shows a numerical application of equation 88 for different thicknesses, with an amplitude response varying from an initial decreasing trend, to conservation with offset in the tuned cases. If this trend equally affects mudstone and sandstone roofs, AVO will not have the ability to differentiate these two targets.

For assessing if tuning effect equally affects mudstone and sandstone roofs, equation 93 required an adaptation. Knowing that in Daw Mill, the coal seam floor is exclusively made of mudstone, a theory describing a tuning effect generated by a thin layer encased in a bedrock is relevant for mud-roofs. In this thesis, modifications to the Bakke and Ursin's theory have been made, and quantification of the tuning effect generated by a coal seam encased between sandstone and mudstone has been devised:

$$d(t,y)=\left\{\overset{\backslash}{P}\overset{/}{P}_1(y)+\overset{\backslash}{P}\overset{/}{P}_2(y)\right\}p(t)-\overset{\backslash}{P}\overset{/}{P}_2(y)\Delta T(y)p'(t) \qquad \textbf{Equation 94}$$

Or, under its Amplitude Variation with Angle form:

$$d(t,\theta)=\left\{\overset{\backslash}{P}\overset{/}{P}_1(\theta)+\overset{\backslash}{P}\overset{/}{P}_2(\theta)\right\}p(t)-\overset{\backslash}{P}\overset{/}{P}_2(\theta)\Delta T(\theta)p'(t) \qquad \textbf{Equation 95}$$

2.4.5. Wave propagation in finely layered media

The objective of this section is to introduce a problem linked to the issue regarding the correlation between laboratory and seismic data described in section 2.4.2. To do so, consider a velocity of 2400 m/s in coal, at two different frequencies:

- 60 Hz (seismic)
- 1 MHz (ultrasonic).

The wavelength, at ultrasonic frequencies will be comparable to a micro layering scale of 2.4 millimeters. At seismic frequency, the same micro layering will be negligible compared to the 40 meters wavelength.

Hovem (1995) made a distinction between waves propagating at these two different frequencies:

1. For low frequencies (large ratios of wavelength to layer thickness), the layered structure behaves as an effective medium; the velocity approaches the effective medium velocity, the propagation is dispersive, and no loss occurs.
2. For higher frequencies (small ratios of wavelength to layer thickness), the layered structure is described by time-average velocity; waves are evanescent, suffer scattering loss at each interface, and travel at the time averaged velocity.

It means that seismic and ultrasonic waves propagating in coal belong to two different propagation modes.

The definition of average velocity is:

$$\frac{1}{c} = \frac{h_1}{h}\frac{1}{c_1} + \frac{h_2}{h}\frac{1}{c_2} \quad \textbf{Equation 96}$$

The effective medium velocity is given by:

$$c = \sqrt{\frac{K}{\rho}} \quad \textbf{Equation 97}$$

With c_i being the sound velocity (exclusively P-wave), ρ_i the density, d_i the relative density, and:

$$K^{-1} = \frac{h_1}{h}K_1^{-1} + \frac{h_2}{h}K_2^{-1} \quad \textbf{Equation 98}$$

$$\rho = \frac{h_1}{h}\rho_1 + \frac{h_2}{h}\rho_2 \quad \textbf{Equation 99}$$

Where K_i is the bulk modulus:

$$K_i = \frac{E_i}{3(1-2\nu_i)} \quad \textbf{Equation 100}$$

Finally, the transition zone between these two propagating modes is still under debate. Hovem gave a first assessment of the limiting frequency:

$$\tan\theta_1 \tan\theta_2 = \frac{2Z_1Z_2}{Z_1^2 + Z_2^2} \quad \textbf{Equation 101}$$

With:

- $\mathbf{Z_i = \rho_i c_i}$ (**Equation 102**):impedance
- $\boldsymbol{\theta_i = 2\pi f h_i / c_i}$(**Equation 103**): phase factor

Other experimental and theoretical approaches are now giving different assessments of the cut-off frequency. For example, Stovas (2007) defined not a single, but two limiting frequencies.

2.4.6. Thermoelasticity and Attenuation

This section introduces a physical phenomenon contributing to:

- the correlation problem between laboratory and seismic data
- the theoretical non-applicability of AVO calibration from laboratory

by presenting:

1. the Neumann-Duhamel system
2. the application of potentials
3. the resolution of these equations
4. the presentation of a new set of boundary conditions

Thermal effects within an elastic solid produce heat transfer by conduction and this flow of thermal energy establishes a temperature field within the material. Most solids exhibit a volumetric change with temperature variation, and thus the presence of a temperature distribution generally induces stresses (Sadd, 2005). Sometimes, this physical phenomenon has a consequence on wave propagation and wave velocity.

In physics, the combination of heat and wave equations (called the Neumann-Duhamel system) describes thermoelasticity:

$$\nabla^2 T - \frac{1}{\chi}\frac{\partial T}{\partial t} - \eta div\left(\frac{\partial u}{\partial t}\right) = -\frac{Q}{\chi} \quad \textbf{Equation 104}$$

$$\mu\nabla^2\vec{u} + (\lambda + \mu)grad\left(div(\vec{u})\right) + \vec{X} - \gamma grad\left(\vec{T}\right) = \rho\frac{\partial^2\vec{u}}{\partial t^2} \quad \textbf{Equation 105}$$

With:

- λ and μ : Lame's parameters
- ρ : density
- $\vec{X}$: body the forces
- γ : dilatation coefficient
- λ_0 : coefficient of internal heat coefficient
- W : amount of heat per unit of volume
- C : specific heat
- $\chi = \dfrac{\lambda_0}{\rho C}$
- $Q = \dfrac{W}{\rho C}$
- $\eta = \dfrac{\gamma T_0}{\lambda_0}$

By neglecting the body forces and considering that heat is not a wave source, the system of equations is reduced to:

$$\boldsymbol{\nabla^2 T - \frac{1}{\chi}\frac{\partial T}{\partial t} - \eta div\left(\frac{\partial u}{\partial t}\right) = 0} \quad \textbf{Equation 106}$$

$$\boldsymbol{\mu\nabla^2\vec{u} + (\lambda + \mu)grad\left(div(\vec{u})\right) - \gamma grad\left(\vec{T}\right) = \rho\frac{\partial^2\vec{u}}{\partial t^2}} \quad \textbf{Equation 107}$$

In this thesis, potentials from equation 4:

$$\vec{u} = \overrightarrow{grad}(\phi) + \overrightarrow{rot}(\psi) \quad \textbf{Equation 108}$$

have been applied in equations 106 and 107.

The result is composed of three separate equations:

1. P-wave: $\Delta\boldsymbol{\phi} - \frac{\mathbf{1}}{\mathbf{V_P^2}}\frac{\boldsymbol{\partial^2\phi}}{\boldsymbol{\partial t^2}} = \frac{\boldsymbol{\gamma}}{\boldsymbol{(\lambda+2\mu)}}\mathbf{T}$ **Equation 109**

2. Temperature: $\Delta T - \frac{1}{\chi}\frac{\partial T}{\partial t} = \eta\frac{\partial \Delta\phi}{\partial t}$ **Equation 110**

3. S-wave: $\Delta\psi - \frac{1}{V_S^2}\frac{\partial^2\psi}{\partial t^2} = 0$ **Equation 111**

By using a similar approach, Boley and Weiner (1967) confirmed that thermal stresses do not affect S-waves. By using equation 110 for removing the temperature term in equation 109, the final system is:

- P-waves: $\Delta(\Delta\phi) - \frac{1}{V_P^2}\frac{\partial^2\Delta\phi}{\partial t^2} + \frac{1}{\chi}\frac{\partial(\Delta\phi)}{\partial t} - \frac{1}{\chi V_P^2}\frac{\partial^3\phi}{\partial t^3} = 0$ **Equation 112**

- S-waves: $\Delta\psi - \frac{1}{V_S^2}\frac{\partial^2\psi}{\partial t^2} = 0$ **Equation 113**

By comparing the elastic wave equation to the 1D cartesian expression of equation 112:

$$\frac{\partial^2\phi}{\partial t^2} - V_P^2\frac{\partial^2\phi}{\partial x^2} = 0$$ **Equation 114(elastic case)**

$$\frac{\partial^4\phi}{\partial x^4} - \frac{1}{V_P^2}\frac{\partial^4\phi}{\partial x^2\partial t^2} + \frac{1}{\chi}\frac{\partial^3\phi}{\partial t\partial x^2} - \frac{1}{\chi V_P^2}\frac{\partial^3\phi}{\partial t^3} = 0$$ **Equation 115 (thermoelastic case)**

And assuming $\phi(x,t) = e^{-i\omega t}\Phi(x)$ (**Equation 116**) :

$$\omega^2\Phi^2 + V_P^2\frac{\partial^2\Phi}{\partial x^2} = 0$$ **Equation 117**

$$\frac{\partial^4\Phi}{\partial x^4} + \frac{\omega^2}{V_P^2}\frac{\partial^2\Phi}{\partial x^2} - \frac{i\omega}{\chi}\frac{\partial^2\Phi}{\partial x^2} - \frac{i\omega^3}{\chi V_P^2}\Phi = 0$$ **Equation 118**

The respective solutions are, for the elastic case:

$$\phi(x,t) = A_1\exp\left(i\frac{\omega}{V_P}x - i\omega t\right) + A_2\exp\left(-i\frac{\omega}{V_P}x - i\omega t\right)$$ **Equation 119**

And for the thermoelastic case:

$$\phi(x,t) = A_1\exp\left(i\frac{\omega}{V_P}x - i\omega t\right) + A_2\exp\left(-i\frac{\omega}{V_P}x - i\omega t\right)$$
$$+ A_3\exp\left(\sqrt{\frac{\omega}{\chi}}\left(-\frac{\sqrt{2}}{2} + i\frac{\sqrt{2}}{2}\right)x - i\omega t\right)$$ **Equation 120**
$$+ A_4\exp\left(-\sqrt{\frac{\omega}{\chi}}\left(-\frac{\sqrt{2}}{2} + i\frac{\sqrt{2}}{2}\right)x - i\omega t\right)$$

The two first terms of equation 120 depicts the elastic wave "contribution", while the last two terms are related to thermoelasticity.

The sum $\left(-\frac{\sqrt{2}}{2}+i\frac{\sqrt{2}}{2}\right)$ describes the presence of attenuation, and $\sqrt{\frac{\omega}{\chi}}$ the presence of dispersivity (velocity varying with frequency).

Applications of potentials $\exp\left(i\frac{\omega}{V_P}x-i\omega t\right)$ and $\exp\left(\sqrt{\frac{\omega}{\chi}}\left(-\frac{\sqrt{2}}{2}+i\frac{\sqrt{2}}{2}\right)x-i\omega t\right)$ in equation 118 both lead to the following dispersion relation:

$$\omega\chi = iV_P \qquad \textbf{Equation 121}$$

The relation linking velocities, time, frequency and wave number is then very different from its elastic equivalent. Moreover, combination of this specific expression and presence of thermoelastic stress will lead to a set of equations different from the ones defined by Zoeppritz and Knott. Boley and Wener (1967) have shown that the boundary conditions are significantly altered with the addition of internal forces:

$$\sigma_{xx} = \lambda\Delta + 2\mu e_{xx} - (3\lambda+2\mu)\alpha T \qquad \textbf{Equation 122}$$
$$\sigma_{yy} = \lambda\Delta + 2\mu e_{yy} - (3\lambda+2\mu)\alpha T \qquad \textbf{Equation 123}$$
$$\sigma_{zz} = \lambda\Delta + 2\mu e_{zz} - (3\lambda+2\mu)\alpha T \qquad \textbf{Equation 124}$$
$$\sigma_{xy} = 2\mu\varepsilon_{xy} \qquad \textbf{Equation 125}$$
$$\sigma_{yz} = 2\mu\varepsilon_{yz} \qquad \textbf{Equation 126}$$
$$\sigma_{xz} = 2\mu\varepsilon_{xz} \qquad \textbf{Equation 127}$$

An observed AVO signal at seismic frequencies may then be fundamentally different with a measurement made with ultrasonic waves. On the other hand, these thermoelastic waves might exist by being completely negligible. This negligibility can be assessed with a dimensionless parameter defined by Boley and Weiner:

$$\delta = \frac{(3\lambda+2\mu)^2\alpha^2 T_0}{\rho^2 C_v V_P^2} \qquad \textbf{Equation 128}$$

Thermoelastic effects are negligible if $\delta << 1$.

Data supplied by Comsol multiphysics' Library sets copper properties with:

- E=110*10^9 Pa
- $\nu = 0.35$
- ρ =8700 kg/m^3
- C_v =400 W/(m.K)
- α = 17*10^(-6) K^{-1}

While Van Krevelen (1993) defined a 85% carbon content coal with:

- E=4.5*10^9 Pa
- $\nu = 0.345$
- ρ =1270 kg/m^3
- C_v =0.5 W/(m.K)
- α = *10^(-4) K^{-1}

The numerical application is $\delta = 0.0185$ for copper, and $\delta = 1375.4$ for coal; for studying coal, heat/wave coupling must be taken into account.

2.4.7. Zener

Thermoelasticity, mentioned in the preceding paragraph, is a peculiar case. In "Elasticity and Anelasticity of Metals" (1948), Zener explained that an acoustic wave propagating in a solid medium encompasses many physical phenomena, some of them being negligible at some frequencies (Figure 20). For some bandwidths, all these physical phenomena are negligible and the propagating wave is then purely elastic.

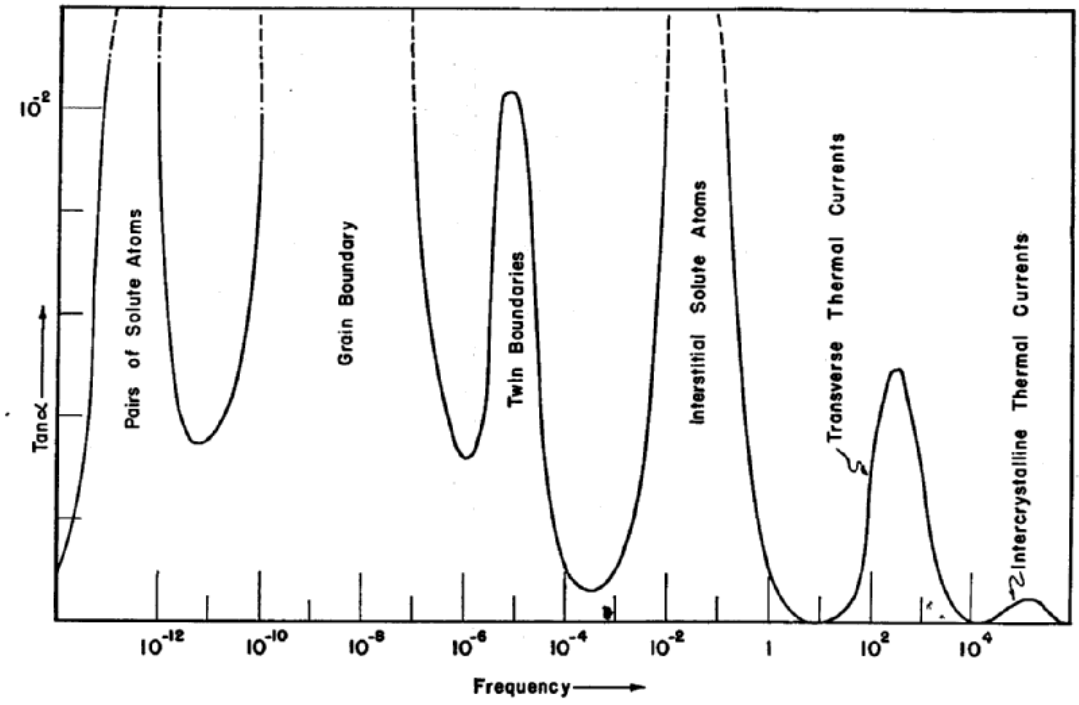

Figure 20 – A typical relaxation spectrum. The influence of each physical phenomena is non-negligible for a bandwidth. The term tan(α) is linked to the strain lag, and has a direct influence on wave velocity (Zener (1948))

The first consequence is a contribution to a phenomenon observed by Barton (2008) and Sams (1997), the static dynamic discrepancy (see Figure 21). A modulus measurement conducted with ultrasonic transducers differs from its measurement conducted statically. The second consequence is a frequency influence on velocities and moduli (Figure 22).

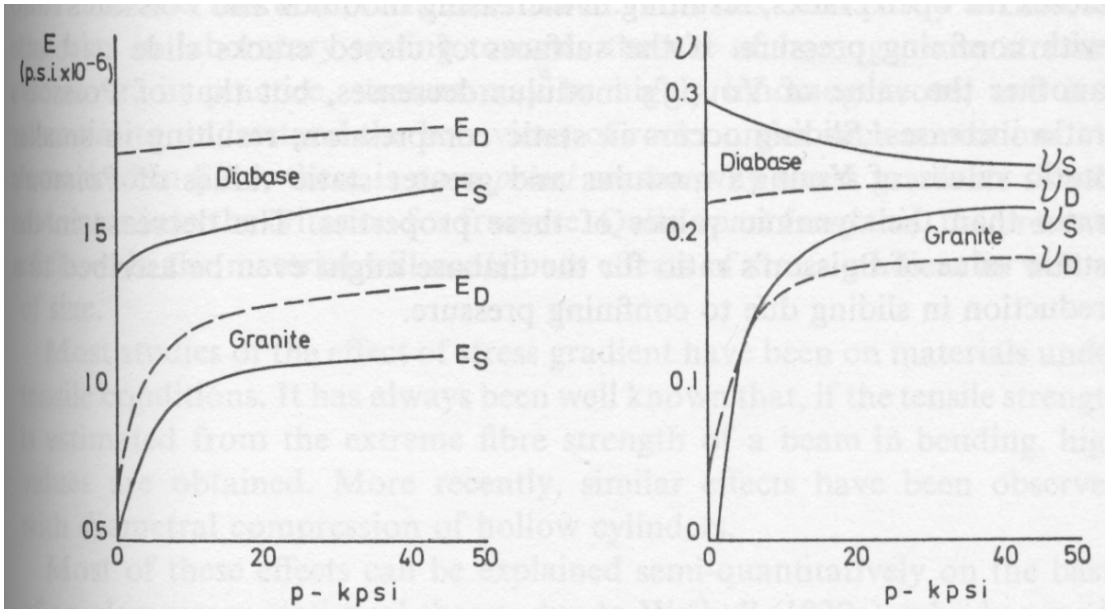

Figure 21 – Example of static/dynamic discrepancy (Jaeger and Cook (1979))

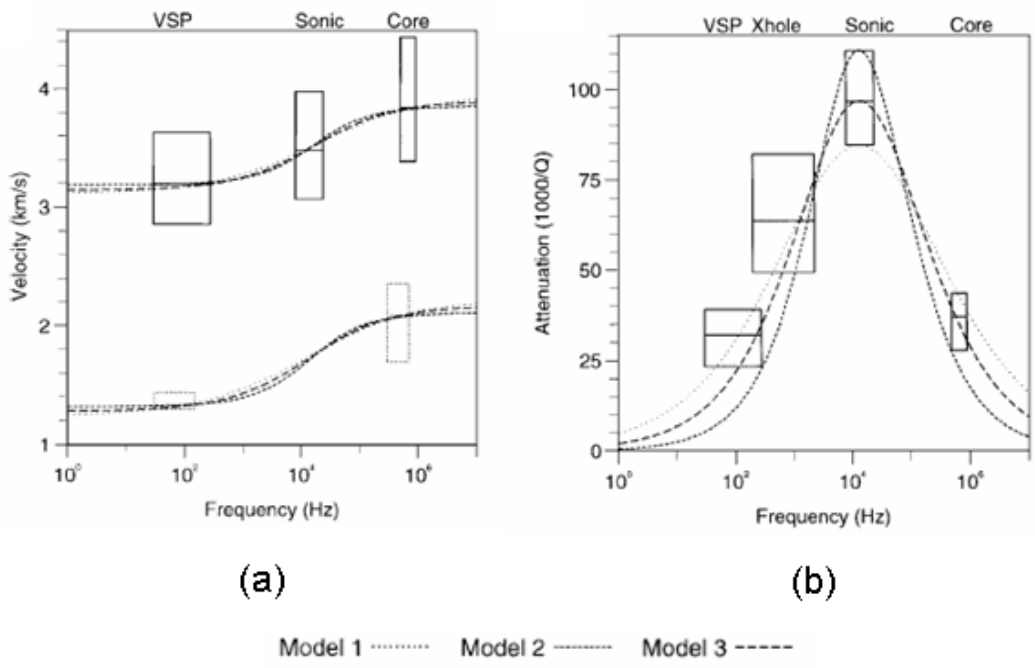

Figure 22 – Dependence of (a) V_P ,V_S (b) and P-wave attenuation on the frequency of the measurements in a finely layered sequence of limestones, sandstones, siltstones and mudstones. The curves relate the author's modelling of squirt flow losses (Sams (1997) and Barton (2007)).

The last consequence is attenuation, often referred to as internal frictions by Zener.

In the first part of his reference book, Zener explained that the two main problems of this approach are to define every existing physical phenomenon occurring during wave propagation, and numerically know all the physical properties of the propagating media. In order to bypass these difficulties, Zener proposed in the second part of his book to use "Zener models" for describing anelastic behaviours.

2.4.8. Discussion

The focus of part 2.4 was to finalize the theoretical component of the reconnaissance step by checking the applicability of AVO theory to mine planning.

At the scale of the laboratory, the presence of coal micro layering, combined with different physical phenomena occurring alongside ultrasonic wave propagation (Zener, 1948), impedes a direct correlation between seismic and laboratory data. Moreover, as physical phenomena like thermoelasticity induce new boundary conditions between two propagating media (Boley and Wener, 1967), the initial theory published by Zoeppritz may not predict the variation of amplitude with offset and a direct calibration of AVO from the laboratory may not be theoretically possible.

At seismic scale, the finite thicknesses of roofs and coal seam have two consequences:

1. the first is a problem of detectability due to seismic resolution. A roof may be invisible on a seismic section.
2. the second is the presence of a tuning effect. By interfering with the reflection on the seam floor, the reflection on top of the seam can lose its information about the roof lithology.

2.5. SUMMARY

This thesis proposes to examine:

1. the ability of AVO to differentiate mudstone from sandstone roofs overlaying a coal seam
2. the applicability of AVO calibration in the laboratory

This thesis has the following structure:

1. Introduction
2. Literature Review
3. Laboratory Testing
4. Modelling
5. Seismic interpretation
6. Conclusion

This chapter, the literature review, has provided different theoretical tools which are used in the subsequent chapters. It determined the need to collect the following set of parameters in Chapter 3:

- P- and S-wave velocities, density
- Young's Modulus, Poisson's ratio and density

and established a link between rock properties and velocities.

It has also provided for Chapter 4 the analytical expressions for exploiting the data, and numerically assessing the variation of reflected amplitude with the wave's angle of incidence. If their numerical application for mudstone roofs and sandstone roofs leads to two distinct AVO curve trends, AVO will be theoretically suitable for mine planning. The investigation into the practical applicability of this technology for mine planning, in the last chapter principally consists of checking the presence of two physical phenomena mentioned in the last part of this second chapter namely:

- tuning effect
- limitations of seismic resolution due to the principal wavelength

Finally, concerning the applicability of AVO calibration in the laboratory, the thermoelastic boundary conditions presented by Boley and Wener (1967) relate reflected amplitude variation with the wave angle of incidence to physical

phenomena not mentioned by the Zoeppritz's boundary conditions therefore an AVO calibration from the laboratory may not theoretically be possible.

Chapter 3.LABORATORY

3.1. OBJECTIVES AND ORGANIZATION OF THE CHAPTER

This experimental chapter initially focuses on AVO calibration in the laboratory, which consists of assembling a piezo-transducer array within a triaxial cell. Ultrasonic waves reflected at the interface of a bilithic structure (in Figure 3) should be recorded within a triaxial cell (shown in Figure 23), and provide AVO reflection coefficients at different incidence angles. The waves are generated by a dense array of limited size piezo components: the denser the array, the more detailed the variation of reflection coefficient with angle of incidence. Such result can be reached with limited sized piezo-components, this poses a technical challenge; the smaller the piezo-crystal, the smaller is its activation voltage and the smaller the amplitude of the ultrasonic wave propagating within a sample. This power limitation on sources, combined to attenuation, is the key parameter to compensate for the success of this modification. As the size of the piezo-components prevents the generation of higher amplitudes, this PhD thesis proposes solutions based on signal improvement with:

- reduction of attenuation by filling cracks and pores with water
- improvement of SNR (Signal to Noise Ratio) by stacking traces

These efforts have proven to be successful with coal, but the inability to fill all sandstone pores with water has prevented a total compensation of attenuation. Consequently, noise amplitude is predominant, no first arrival detection is possible, and AVO calibration is not achievable in the laboratory. This finding did not compromise the investigation into AVO's ability to discriminate mudstone from sandstone layers capping coal seams. As determined in the literature review, this assessment requires the implementation of three rock parameters in modelling:

1. Young's Modulus
2. Poisson's ratio
3. Density

The first two mechanical parameters are crucial for pillar sizing purposes; UK Coal and RMT have an extensive database of roof and floor properties. However there was sparse information on the seam investigated in this thesis, and so additional measurement of these properties in the Rock Physics laboratory was required, within the Institute of Petroleum Engineering. These measurements led to the determination of a probability distribution which is used in the next chapter in statistically proving the AVO's theoretical ability, or inability, to differentiate a Mudstone from a Sandstone roof capping a coal seam. This effort, performed independently from the AVO calibration problem, is described firstly in this chapter in a twofold structure:

1. Laboratory testing
2. AVO calibration in the laboratory

Laboratory testing: this first part presents the Young's modulus, Poisson's ratio and density of different coal samples from Daw Mill, and combines them in order to assess the probability distribution of each property. It also reviews measurement procedures and upscaling methods.

AVO Calibration in the laboratory: this second part presents the principle of the triaxial cell's modification, its implementation, and its results. It also gives technical

recommendations for any further attempt and underlines problems to tackle if in future a solution is found to the piezo-crystal limitations.

3.2. MEASUREMENT OF ROCK ELASTIC PROPERTIES IN THE LABORATORY

3.2.1. Introduction

The goal of this part is to present the rock parameters collected in the laboratory and to determine the respective probability distributions of elastic properties of mudstone, sandstone and coal samples coming from Daw Mill. The first half of this chapter reviews:

1. The description of a Hoek Cell
2. The storage of samples
3. Sample conditioning and coring
4. A measurement procedure on a sample
5. The description of an automatic picking algorithm developed by the author of this PhD
6. The attempt to upscale the measured rock properties to seismic wavelength scale
7. The origin of each sample
8. The measurements made on each sample
9. The probability distribution of Young's modulus, Poisson's ratio and density for Mudstone, sandstone and coal.

3.2.2. Description of the Hoek Cell

A Hoek Cell applies a stress regime to cylindrical samples in order to measure Poisson's ratio and Young's modulus and strength parameters. It applies a principal stress σ_1 in the axial direction, and intermediate and minor stresses σ_2 and σ_3 on the cylindrical surface. The stress-state follows the inequality $\sigma_1 > \sigma_2 = \sigma_3$.

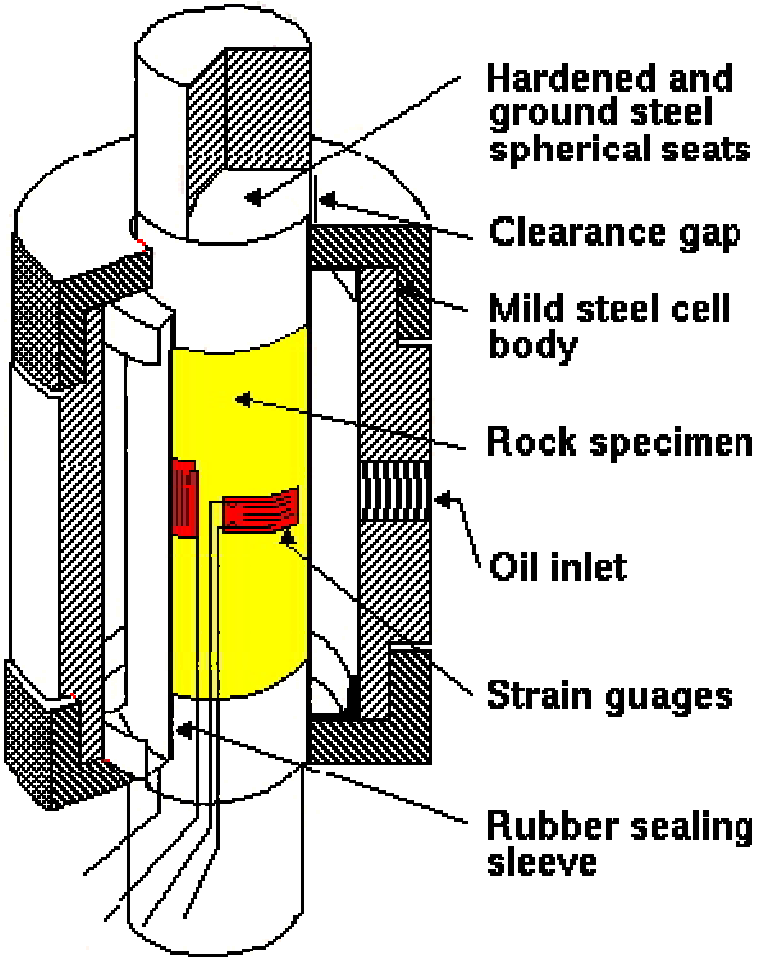

Figure 23-Schematic of a Hoek Cell (Source: Rock mechanics group from Petroleum Engineering Buildings, Heriot-Watt University)

By injecting oil in the inlet (see Figure 23), a RDP-Howden servo hydraulic compression machine applies both an annular and axial pressure on the cylindrical sample. Strain gauges (fixed to samples with epoxy resin) measure strains during the load application, and work according to the Wheatstone Bridge theory (Eldmann, Figure 24).

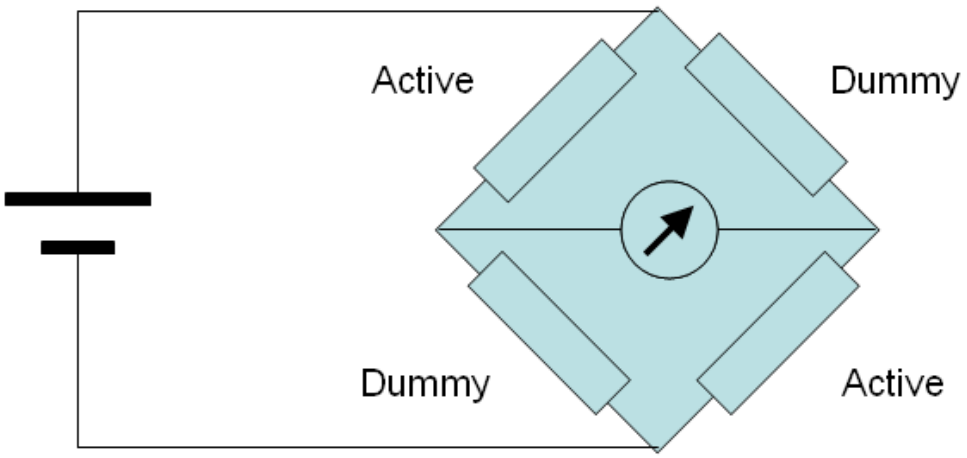

Figure 24 – Wheatstone Bridge Arrangement (Eldmann)

The hardened and ground steel spherical seats in Figure 23 have been replaced by platens incorporating transmitting and receiving piezo transducers and this allows simultaneous static and dynamic measurements. Ultrasonic acquisitions are made at 1 MHz, with a device generating and recording P- and S-waves (see Figure 25).

The transducers are calibrated to account for the platen – to – platen P and S wave travel times at the beginning of each experiment. These times do not vary unless the piezo transducer fails and needs to be replaced; this explains the different time lag reported for some samples.

The recorded trace consists of 1001 samples, with a time sampling of 0.1 microseconds. The previously-measured time lag is subtracted from the picked first-arrival's time in order to deduce each wave's travel time. Finally, travel times are divided by the sample length to compute the wave's velocity through the core.

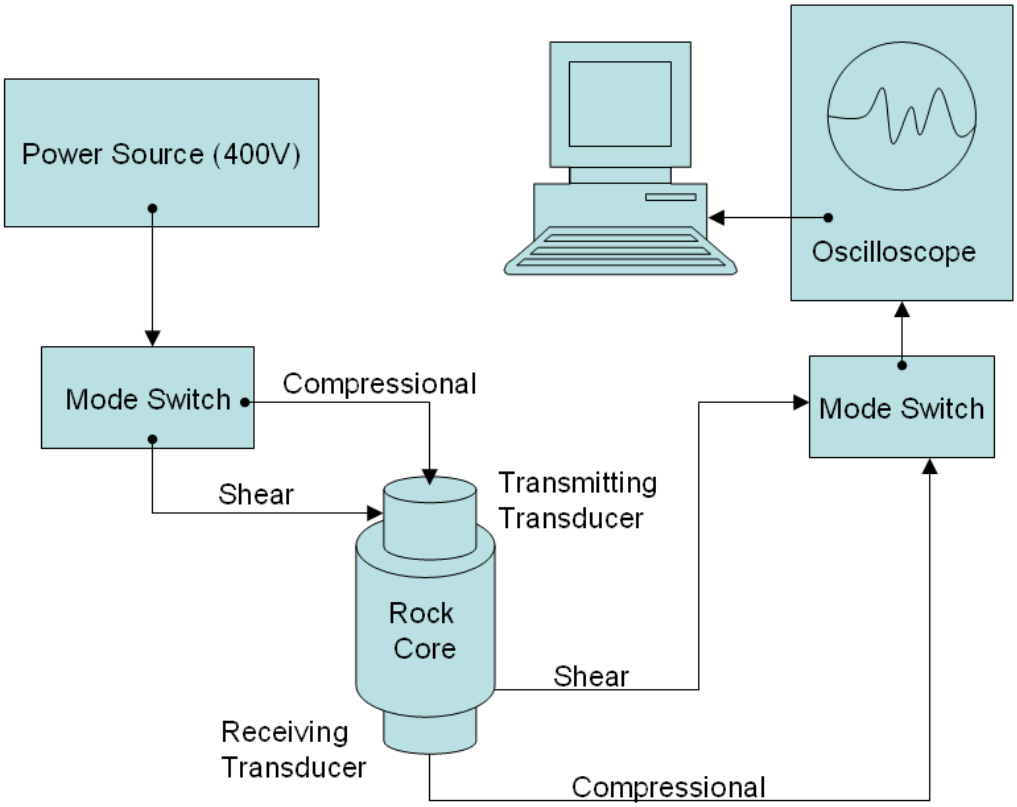

Figure 25 - Rock core compressibility apparatus for elastic wave travel time measurements (after Domenico)

The procedure was identical for all samples:

1. Calibrate the platen to platen P and S wave arrival times
2. Load application
3. Vary the axial load to determining elastic properties (Young's modulus and Poisson's ratio)
4. Record P- and S-wave travel times
5. Increase the applied stresses and go to step 3

The ideal dimensions of samples tested in the laboratory are:

1. a diameter of 36 millimetres
2. a length of 72 millimetres

Strains being plastic on cylinder's top and bottom (see the stress-strain diagram in Figure 7), an elastic deformation zone will be observed in the core's middle section (where strain gauges are placed) if its length is at least twice its diameter.

The actual state of stress in the rock core will not be homogeneous. The constraining influence of the frictional forces acting along the interface between the core and the platens hinders the lateral extension (for compression tests) . This lack of homogeneity in the stress state has implications for the determination of Poisson's ratio and Young's Modulus. Labuz and Bridell (1993) attempted to mitigate the problem by testing different lubricants between the core and the platens. Radial strains were measured near the ends and in the central portion of the core, to investigate the barreling effect. In the absence of lubrication, the radial hoop strains were as much as 50 percent higher in the central region of the core than near the ends. These authors have shown that this stress inhomogeneity can be reduced by applying a lubricant at the rock/platen interface.

3.2.3. Sample storage

Sample storage is a crucial step for preventing a “spontaneous oxidative alteration of coal upon storage" (Van Krevelen (1993) and Vandenbroucke (2007)). Oxidation of coal is a natural process observed in opencast mines, where excavated coal blocks become brittle a few minutes after their extraction; unprotected samples stored in a laboratory react in the same manner after a few days.

A trial and failure approach determined a storage method able to preserve coal samples during a year, and consisted of:

1. Placing coal samples in a sealed environment with a first layer of cling film.
2. Preserving coal samples from accidental shocks by wrapping them in a second layer of bubble wrap.
3. Improving the seal by wrapping the bubble wrap with a final layer of cling film.

However, despite the proven preservation ability of this method, the fourth recommendation on procedures made by the ISRM (International Society for Rock Mechanics Commission on Standardization of Laboratory and Field Tests), in 1979, recommends that tests shall be done 30 days after sample collection.

3.2.4. Sample conditioning and coring

The mechanical and electromagnetic (EM) properties of coal were required within the framework of the ADEMA project. Considering the brittleness of coal, the challenge was to collect sample mechanical properties without impeding the EM team, and vice versa.

Initially, sample preparation comprised:

1. collection from underground or opencast mines
2. wrapping (see "Sample Storage", paragraph 3.2.3, and Figure 26)
3. sample casing in a concrete matrix
4. hole drilling and probe insertion for EM properties measurements
5. coring (for Hoek Cell compression tests)
6. end preparation for testing
7. determination of core dimensions, weight and density
8. strain gauge application with epoxy resin
9. strain gauge electrical connections

Figure 26 – Example of coal samples stored in cling films and bubble wrap.

Steps 3 and 4 are the most damaging for samples, because;

1. moisture in drying concrete induces micro-cracks in coal.
2. probe insertion (for measuring EM properties, see Figure 29) is an invasive step requiring drilling (Figure 27) and hammering (Figure 28).

The proposed solution was to cut a coal block into two pieces:

1. one dedicated to the EM tests
2. the second dedicated to mechanical tests.

Figure 27 – The first step of probe insertion consists of drilling the holes. In this picture, the coal block is not encased in its concrete case because its dimensions exceeded the mould size.

Figure 28 – The second step of probes' introduction consists in hammering the probes within the drilled holes. Many blocks disintegrated during this process.

Figure 29 – Example of EM measurements after probes' insertion.

The coring process uses water flush, (Figure 30), and to minimise microcracking, the cores must be wrapped in absorbent paper and cling film. The absorbent paper is changed regularly to remove waste before the application of the strain gauges.

Figure 30 – Coring of a coal block

3.2.5. Measurement procedure

The procedure for measuring Poisson's Ratio and Young's modulus is in four steps:

1. application of a stress to the sample
2. record P and S waves (with the device depicted in Figure 25)
3. vary the axial stress and measure the commensurate strains (Figure 24).
4. increase stress applied to the core and repeat steps 2 to 4.

The results were recorded digitally.

3.2.6. Description of the automatic picking algorithm

Equations 67 and 68 establish a link between Poisson's ratio, Young's Modulus, P- and S-wave velocities. Therefore, the knowledge of ultrasonic velocities propagating in cores is equivalent to a dynamic assessment of the two elastic properties of interest. The first arrival of a wave propagating from the top to the bottom of a core, which carries this information, is a source of uncertainty. The author has attempted to bring some consistency by developing an automatic picking program, which consistently uses the same pattern for defining the first break. This paragraph summarizes the principles of its algorithm and the full description is in Appendix A.

The finely layered structure of coal affects the propagation of ultrasonic waves (see paragraph 2.4.5 and Figure 31). In some cases, the thickness of the microlayering also affects waveshapes, allowing small amplitude variations to precede large amplitude wave trends. In the presence of a poor signal to noise ratio, an interpreter may only be able to distinguish the presence of higher amplitudes, and indirectly attribute a velocity slower than in reality to a P-wave. In this thesis, small amplitude velocities are referred to as phase velocities, while the velocities of higher amplitude trends are referred as group velocities.

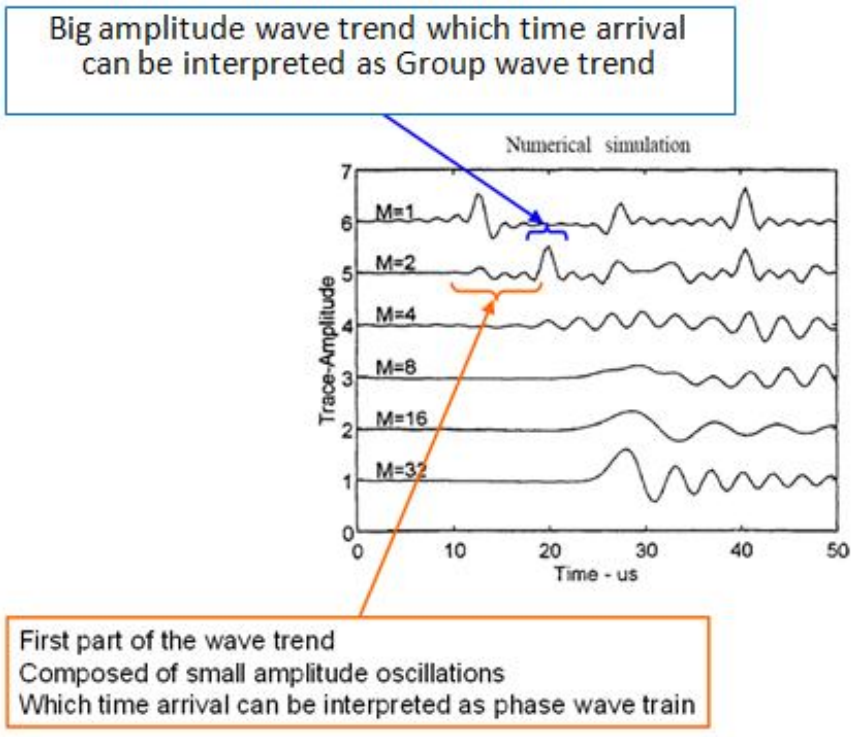

Figure 31 – Numerical simulations of the Marion/Coudin experiment. This is an acoustic model of P waves only. Some layer thickness configurations lead to have small wave trains preceding a large amplitude arrival, a pattern leading to consideration of the concepts of phase and group velocities.

The code, written in Matlab (see Appendix 7.3), performs an analysis in three steps for picking first P-wave arrivals and the group velocities determined from them:

1. Time Frequency analysis of the trace envelope (Figure 32, (a))
2. Application of a threshold for detecting the energy linked to ultrasonic wave arrivals, and approximate determination of the first arrival t(k) (Figure 32, b) .

3. The trace envelope is considered; let A(k) be the trace's envelope at t(k). If A(k-1) < A(k), then, if the precedent sample has a smaller amplitude, the first arrival is t(k-1). The implementation of this loop continues until A(k-1) > A(k); in this algorithm, the base of the first arrival envelope is the pattern considered as the first break (Figure 32, c).

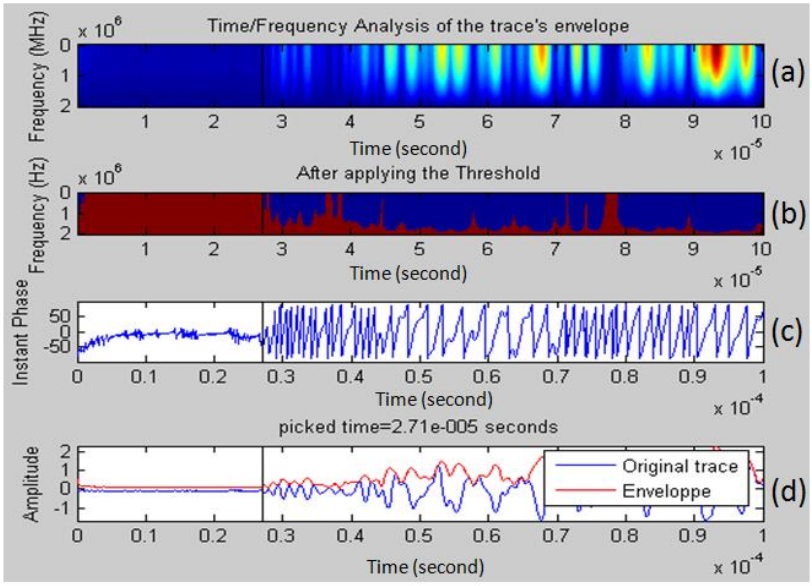

Figure 32 - Example of automatic picking. The automatic procedure is in three steps, (a) Time-Frequency analysis of the recorded trace, (b) application of a threshold for separating waves' arrivals from noise, and determination of the first arrival. (d) Refinement of the first break's determination with the base of the first arrival's envelope. (c) The instant phase helps the interpreter in assessing the quality of the first break pick.

The application of this P-wave picking algorithm to modelled traces showed a 5% difference compared to the input velocity in the model.

As other wave trends precede S-wave arrivals, S-Wave first breaks are much more uncertain, and the proposed algorithm is more empirical. It is as follows:

1. Computation of the trace envelope.
2. Computation of the logarithm of this envelope.
3. Determination of this logarithm maximum.
4. Division of this maximum by the root square of two.
5. The first amplitude equal to this number determines approximately the first S-wave arrival time.
6. A similar loop is implemented for determining the base of the envelope, which is considered to be the S-wave first break.

The implementation of this algorithm to a modelled trace has shown a 20% difference with the model's S-wave velocity (Figure 39 shows an example of S-wave picking).

3.2.7. Upscaling of rock properties from laboratory

Section 2.4.6 and 2.4.7 mention, illustrated in Figure 21 and Figure 22, the presence of a difference between static and dynamic measurements where a physical property dynamically determined has a consistently higher numerical value than when measured statically. This thesis proposes a technique based on two frequency boundaries for up scaling properties collected in the laboratory:

1. Lower frequency boundary being defined by static measurements
2. Higher frequency boundary being defined by dynamic measurements

In this thesis, upscaling has been performed with formulas proposed by Aki and Richards:

$$\boldsymbol{Q = \frac{\ln(f/0.01)}{\pi\left(\frac{V_{static}}{V_{dynamic}} - 1\right)}} \qquad \textbf{Equation 129}$$

$$\frac{V(f)}{V_{dynamic}} = 1 + \frac{1}{\pi Q} ln\left(\frac{f}{0.01}\right) \qquad \textbf{Equation 130}$$

With :

- Q: attenuation coefficient
- f: frequency at which the velocity is upscaled

The computation of V static being done with statically measured E, and equations 67 (for P-waves) and 68 (for S-waves). The result of one upscaling effort is shown in Figure 35.

The upscaling relies on sample quality, defined by the Rock Quality Designation (or RQD, Barton, 2008):

$$RQD\% = 100\left(\frac{V_{field}}{V_{lab}}\right)^2 \qquad \textbf{Equation 131}$$

From the knowledge of this parameter, the quality of each sample can be defined as poor to excellent (see figures Figure 33 and Figure 34), and then, from unreliable to reliable. Figure 36 and Figure 37 show examples of RQD computation for collected data with sample 1.1.a.

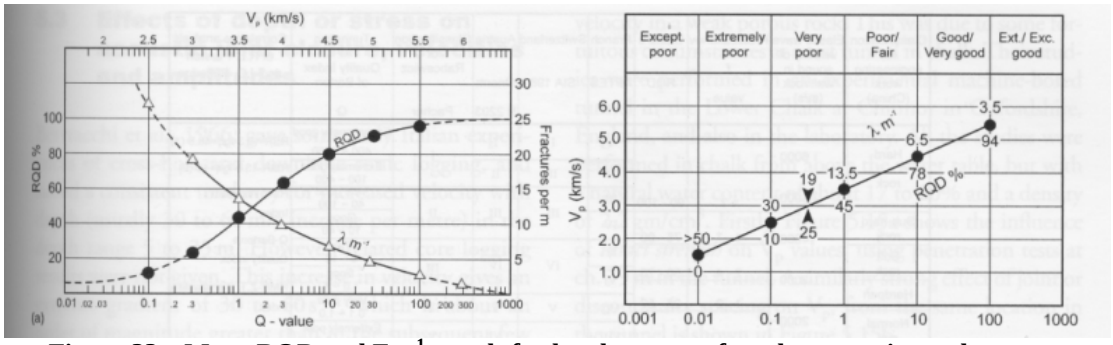

Figure 33 – Mean RQD and Fm^{-1} trends for hard, near-surface, low porosity rock masses (Barton(2007)).

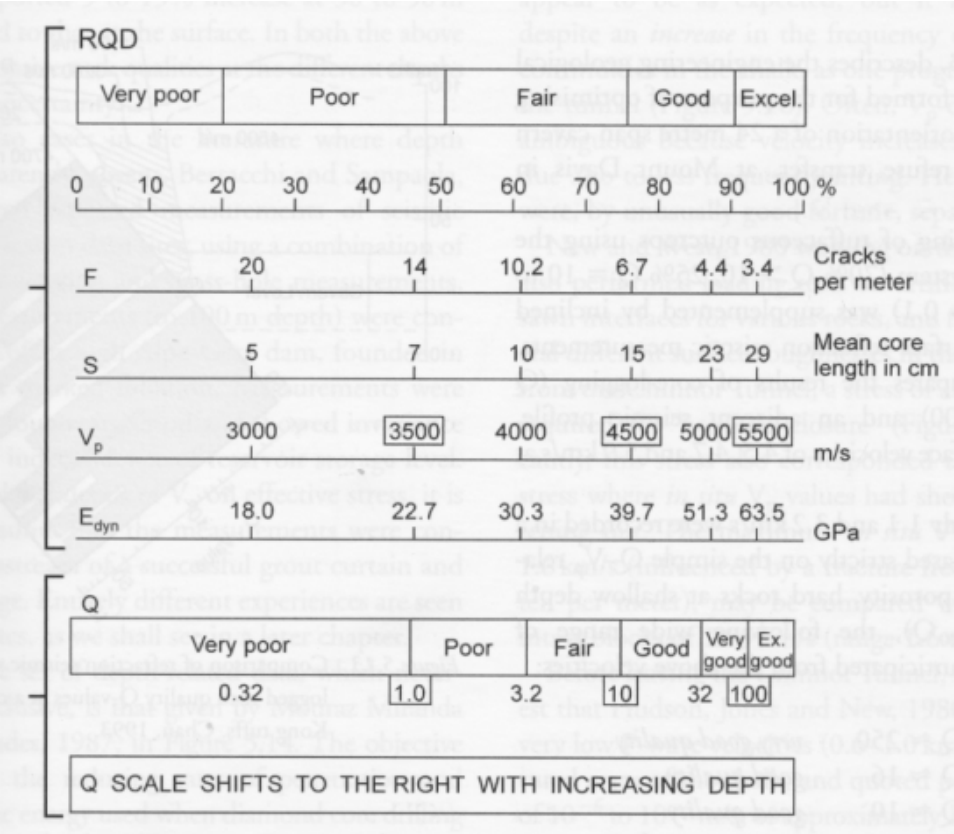

Figure 34 – Mean RQD, Fm^{-1}, V_p and E_{dyn} data for hard, near-surface, low porosity rock masses. (Barton (2007))

3.2.8. Sample Origin

Table 2 is an exhaustive list of the tested sample origin:

Sample N°	Core N°	Core's Orientation	Lithology	Location	Test Site
1	1.1a	z (orthogonal to the layering)	Coal	Daw Mill	
	1.1b				
	1.2b				
2	2.1				
9	9X	x (parallel to the layering)		Earlseat	
B	B2	X		Daw Mill	
C	C	Z			
239	239-B		Sandstone	Daw Mill	302's Coalgate
	239-C				
439	439A				
	439C				
839	839A				
1039	1039A				
2198	2198A				302's Tailgate
	2198B				

Table 2 – Sample record

3.2.9. Core 1.1a

The structure of each paragraph describing test results will remain the same, with:

- a comment on the data
- 3 tables

The three tables detail respectively:

1. Sample dimensions and weight (see Table 3)
2. Static and dynamic velocities determined at different stresses (see table Table 4)
3. Velocity upscaling of collected data with equations 129 and130.

As coal samples are a porous media their mechanical properties vary with stresses;

- initially, the presence of cracks weakens coal mechanical properties
- but measured Young's modulus increases with stress, because higher applied stresses close the same cracks

Sample number	1.1A
Pre-Test Length (mm)	76.104
Diameter (mm)	37.512
Weight (g)	101.209
Sample's density (kg/m^3)	1203.32054
P-wave calibration (µs)	18.4
S-wave calibration (µs)	28
Time shift (µs)	30

Table 3 – Sample dimensions and weight

Stress (MPa)	Static Vp (m/s)	q-P wave group velocity (m/s)	q-P wave phase velocity (m/s)	StaticVs (m/s)	Picked Vs (m/s)	qP-phase wave train RQD%	S-wave RQD%
0.710656	2431	1912	2156	1104	1576	127.17	49
1.421312	2124	1917	2528	1226	1586	70.58	60
2.771559	2208	1961	2537	1209	1579	75.79	59
5.614184	2078	1956	2562	1158	1592	65.78	53
11.1573	2321	2024	2562	1247	1609	83.48	60
16.77149	2502	2091	2597	1177	1609	92.77	53
27.92879	2420			1222			

Table 4 – Static and dynamic velocities determined at different stresses

Stress (MPa)	q-P wave group velocity upscaled to 60 Hz (m/s)	q-P wave phase velocity upscaled to 60 Hz (m/s)	S wave velocity upscaled to 60 Hz (m/s)
0.710656	2155	2293	1286
1.421312	2021	2298	1373
2.771559	2084	2352	1359
5.614184	2019	2281	1329
11.1573	2180	2441	1395
16.77149	2290	2546	1348
27.92879			

Table 5 – Laboratory velocities upscaled to 60 Hz

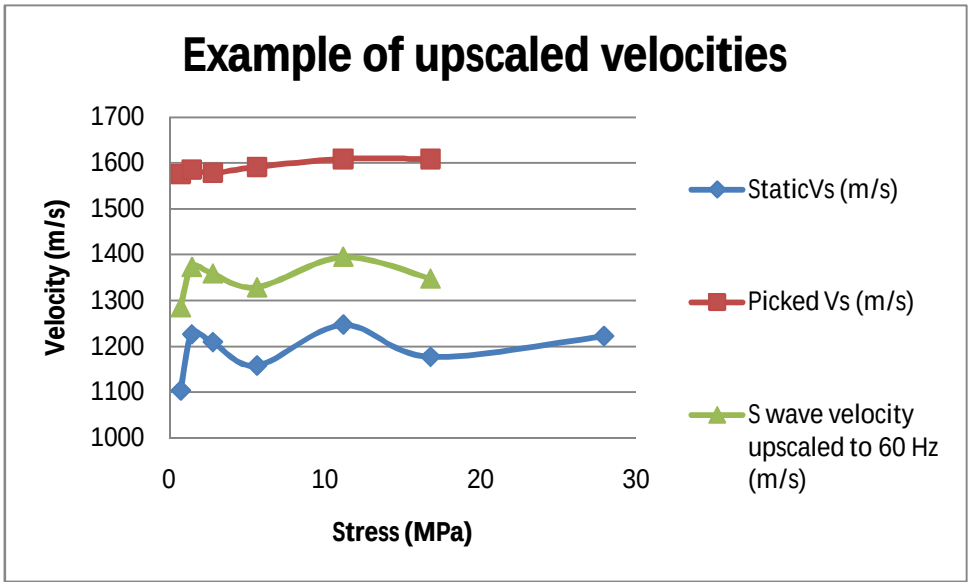

Figure 35– S-wave upscaling to 60 Hz. In the theoretical part, no static/dynamic discrepancy affecting specifically V_S has been mentioned, and this phenomenon may be studied in depth in a future project.

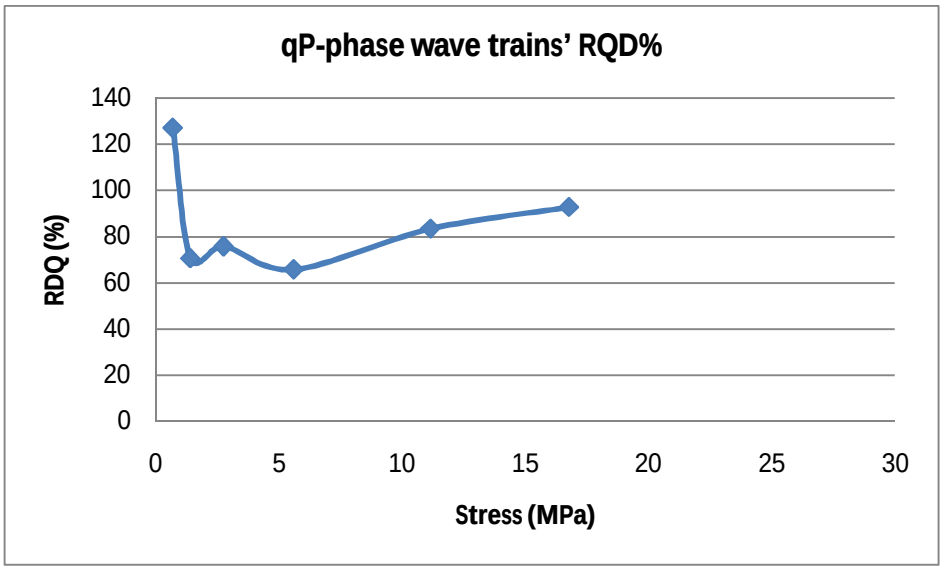

Figure 36 – P-wave RQD of sample 1.1A

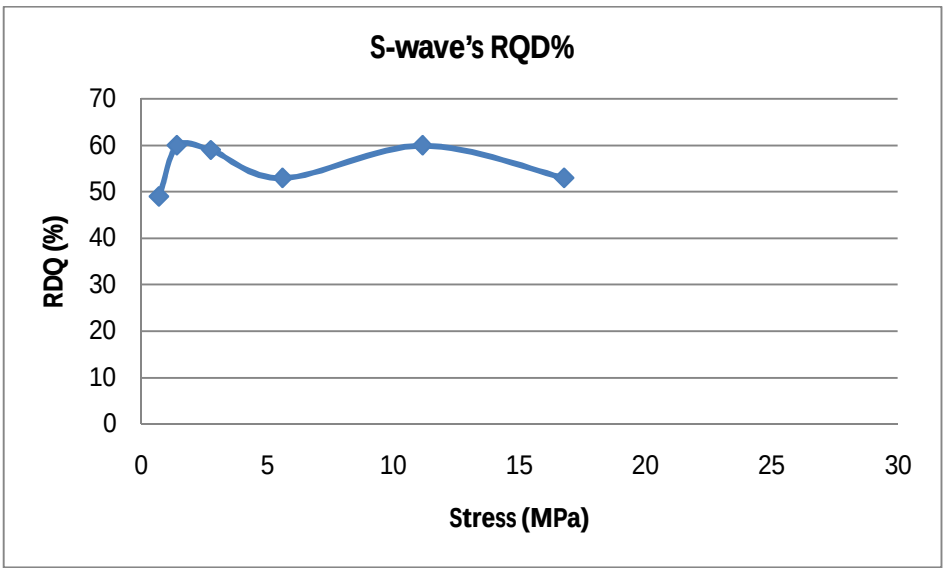

Figure 37 - P-wave RDQ of sample 1.1A

3.2.10. Core 1.1.b

1.1.b has been cored in the same coal block as 1.1.a. In both cores, two distinct wave trains are observed (Figure 38 shows the "phase" automatic picking). On the other hand, the automatic picking algorithm only picks a single feature for S-waves (as mentioned in paragraph 3.2.6. see Figure 39). Comparison of RQD% with the different percentages to Figure 33, show:

- the good quality of the measurements
- the good preservation of samples

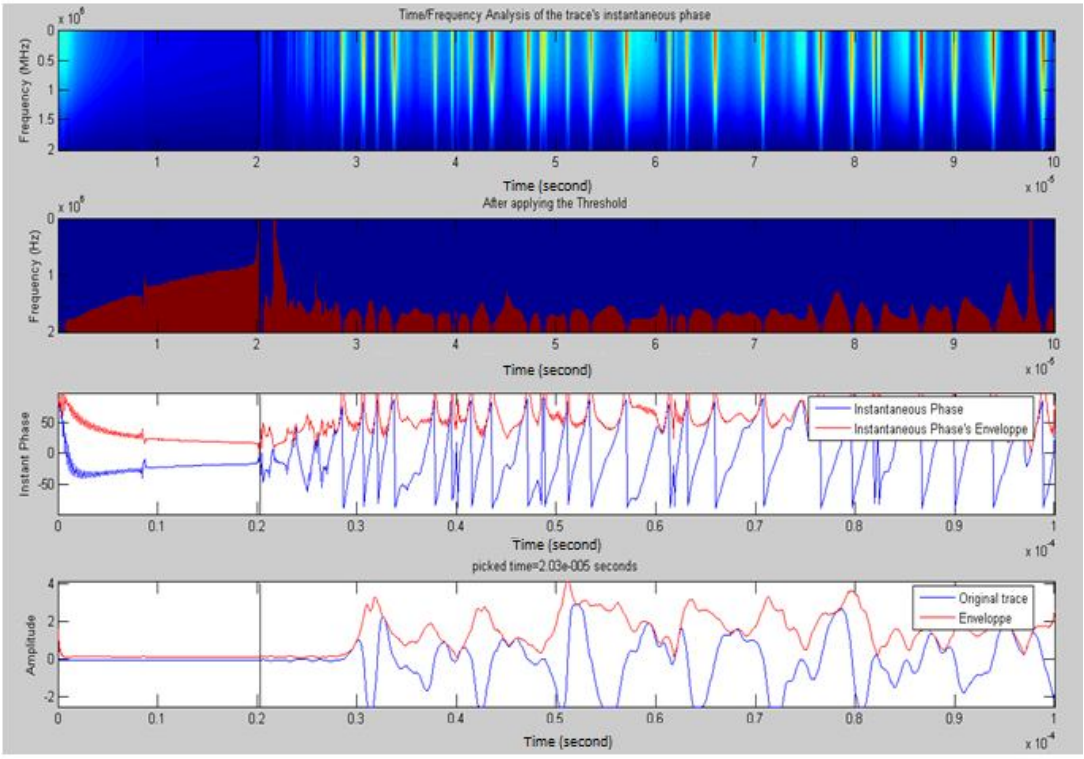

Figure 38 – Phase and group wave trains are observed as in core 1.1A. The maximum and minimum recording amplitudes have been exceeded in some traces, a fact affecting the performances of the automatic picking programs; hand picking was required.

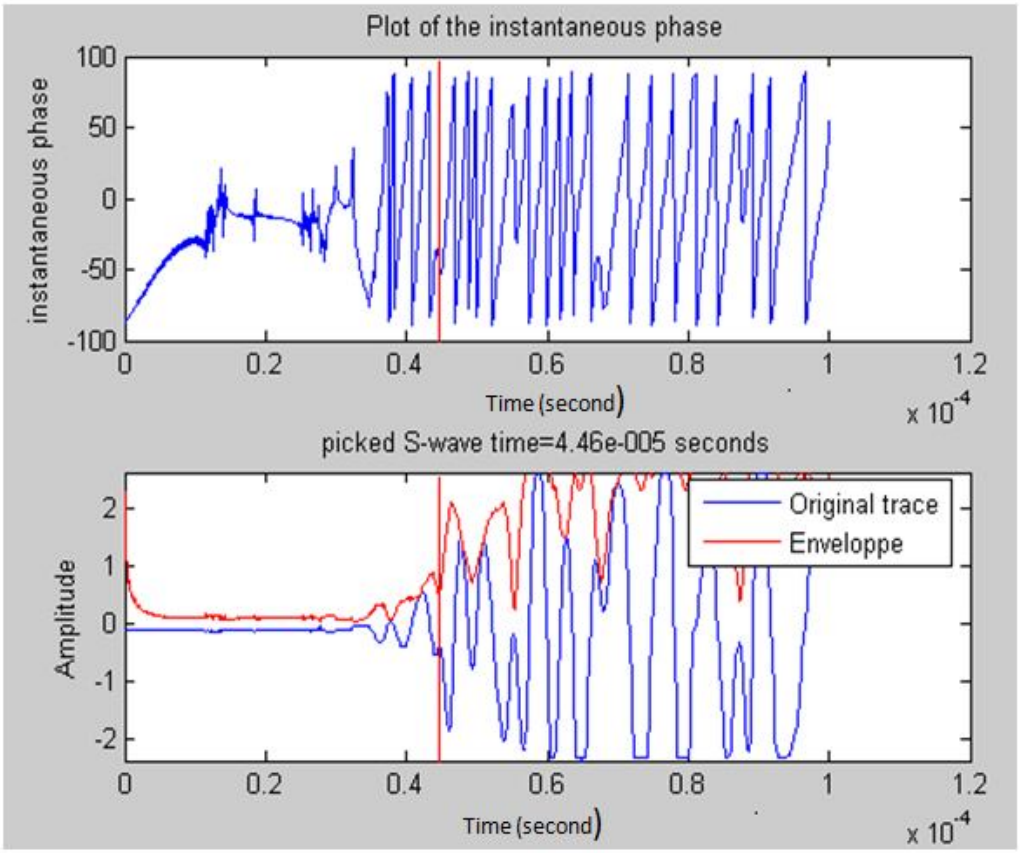

Figure 39 – The S-wave automatic picking program's performance was not affected, and precisely picked an easily recognizable S-wave pattern.

Sample number	1.1B
Pre-Test Length (mm)	76.68
Diameter (mm)	37.262
Weight (g)	101.4645
Sample's density (kg/m^3)	1213.41626
P-wave calibration (µs)	18.3
S-wave calibration (µs)	27
Time shift (µs)	30

Table 6 - Sample dimensions and weight

Stress (MPa)	Static Vp (m/s)	q-P wave group velocity (m/s)	q-P wave phase velocity (m/s)	StaticVs (m/s)	Picked Vs (m/s)	qP-phase wave trains' RQD%	S-wave's RQD%
0.720224	1965	1830	2729	1108	1543	52	52
1.440448	2234	1852	2565	1172	1540	76	58
2.808874	2321	1997	2548	1304	1565	83	69
5.689771	2313	1992	2809	1198	1575	68	58
11.30752	2460	2178	2691	1282	1591	84	65
16.99729	2622	2154	2799	1223	1611	88	58
28.30481	2608			1304			

Table 7 - Static and dynamic velocities determined at different stresses

Stress (MPa)	q-P wave group velocity upscaled to 60 Hz (m/s)	q-P wave phase velocity upscaled to 60 Hz (m/s)	S wave velocity upscaled to 60 Hz (m/s)
0.720224	1899	2264	1278
1.440448	2036	2379	1321
2.808874	2156	2423	1416
5.689771	2149	2523	1350
11.30752	2318	2564	1412
16.99729	2378	2703	1380
28.30481			

Table 8 - Laboratory velocities upscaling to 60 Hz

3.2.11. Core 1.2b

The plotter was not used to determine the strains in this test; they were determined from the digital information recorded.

Sample number	1.2B
Pre-Test Length (mm)	75.7
Diameter (mm)	37.206
Weight (g)	100.6305
Sample's density (kg/m^3)	1222.69435
P-wave calibration (µs)	18.8
S-wave calibration (µs)	27
Time shift (µs)	30

Table 9 - Sample dimensions and weight

Stress (MPa)	Static Vp (m/s)	q-P wave group velocity (m/s)	q-P wave phase velocity (m/s)	StaticVs (m/s)	Picked Vs (m/s)	qP-phase wave trains' RQD%	S-wave's RQD%
0.722394		1987	2549	1202	1499		64
1.444788	1125	1912	2665	763	1567	18	24
2.817336	1367	1921	2713	955	1567	25	37
5.706911	1964	1992	2713	1024	1567	52	43
11.34158	2443	2126	2743	1193	1571	79	58
17.04849	1906	2207	2628	1211	1824	53	44
28.39008		2301	2694	1174	1820		42

Table 10 - Static and dynamic velocities determined at different stresses

Stress (MPa)	q-P wave group velocity upscaled to 60 Hz (m/s)	q-P wave phase velocity upscaled to 60 Hz (m/s)	S wave velocity upscaled to 60 Hz (m/s)
0.722394			1326
1.444788	1396	1547	1007
2.817336	1583	1785	1171
5.706911	1977	2258	1225
11.34158	2283	2576	1346
17.04849	2037	2190	1439
28.39008			1411

Table 11 - Laboratory velocities upscaling to 60 Hz

3.2.12. Core 2.1

The RDQ% was poor (see table Table 13), therefore no data measured from this core has been used for analysis.

Sample number	2.1
Pre-Test Length (mm)	76.46
Diameter (mm)	36.366
Weight (g)	99.3305
Sample's density (kg/m^3)	1250.74097
P-wave calibration (µs)	18.8
S-wave calibration (µs)	27
Time shift (µs)	30

Table 12 - Sample's dimensions and weight

Stress (MPa)	Static Vp (m/s)	q-P wave group velocity (m/s)	q-P wave phase velocity (m/s)	StaticVs (m/s)	Picked Vs (m/s)	qP-phase wave trains' RQD%	S-wave's RQD%
0.756152		354	2160	1202	1264	3	9
1.512303	1125	672	2002	763	1298	11	10
2.948992	1367	842	2112	955	1309	16	14
5.973598	1964	1094	2066	1024	1316	28	20
11.87158	2443	1527	2118	1193	1321	52	29
17.84518	1906	1928	2044	1211	1314	89	36
29.71676		3223	2142	1174	1318	227	47

Table 13 - Static and dynamic velocities determined at different stresses

Stress (MPa)	q-P wave group velocity upscaled to 60 Hz (m/s)	q-P wave phase velocity upscaled to 60 Hz (m/s)	S wave velocity upscaled to 60 Hz (m/s)
0.756152	549	585	573
1.512303	936	979	606
2.948992	1047	1176	699
5.973598	1222	1407	796
11.87158	1493	1758	906
17.84518	1718	1981	974
29.71676	2224	2603	1062

Table 14 - Laboratory velocities upscaling to 60 Hz

3.2.13. Core 9X

This sample is one of the two successfully cored along the layering. Both S- and P-wave picking have been precise (see figure Figure 40 and Figure 41), with no distinction made between phase and group velocity. Models in the next chapter will not use these data, because the sample does not come from Daw Mill.

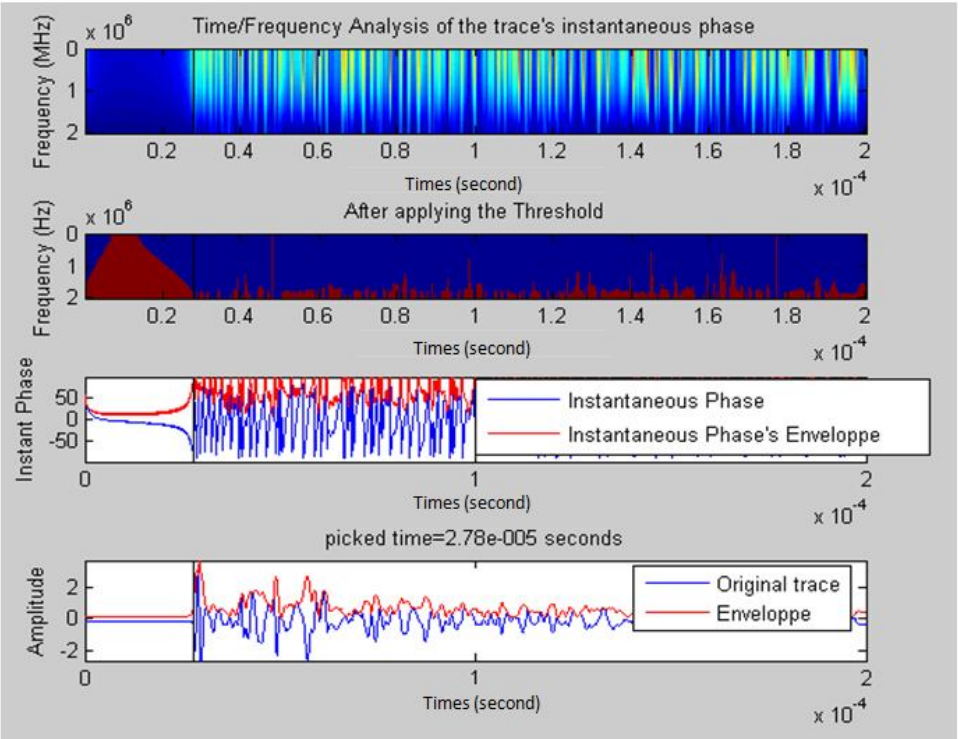

Figure 40 – Example of P-wave picking on sample 9X; no distinction can be made between phase and group velocities

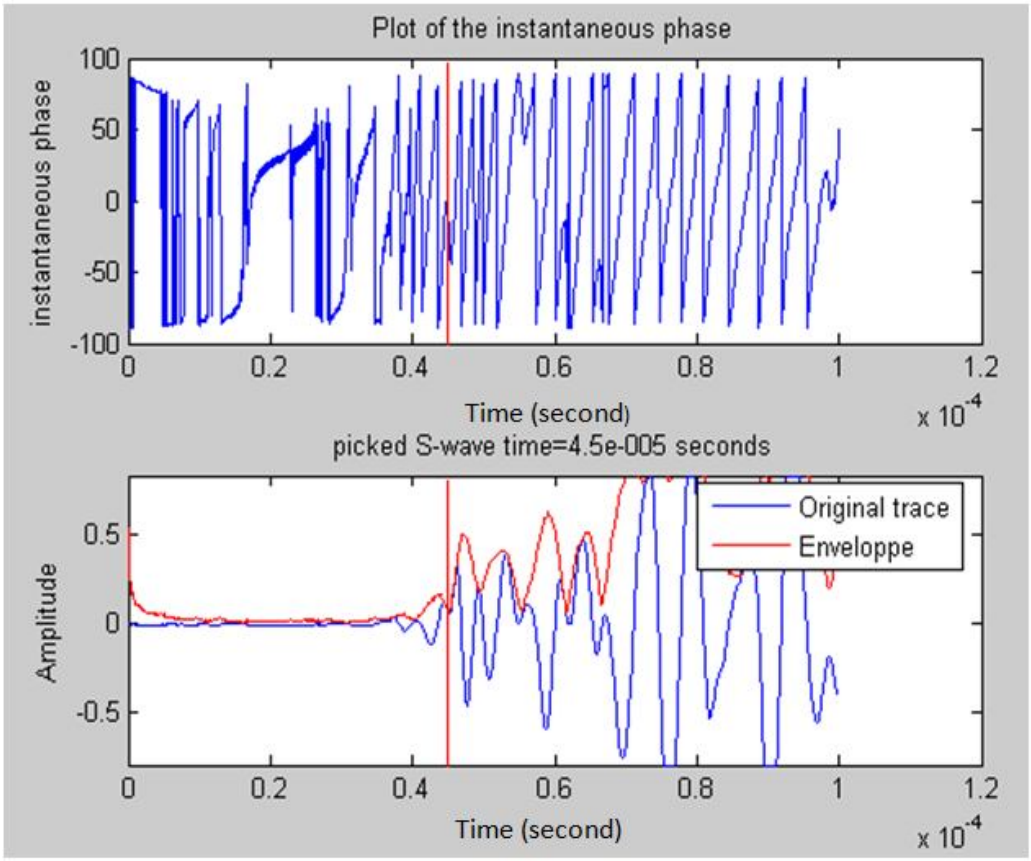

Figure 41 – Example of S-wave picking on sample 9X.

Sample number	9X
Pre-Test Length (mm)	49.106
Diameter (mm)	37.142
Weight (g)	69.494
Sample's density (kg/m^3)	1306.14772
P-wave calibration (µs)	15
S-wave calibration (µs)	37.3
Time shift (µs)	20

Table 15 - Sample dimensions and weight

Stress (MPa)	Static Vp (m/s)	Dynamic Vp (m/s)	StaticVs (m/s)	Picked Vs (m/s)	P- wave trains' RQD%	S-wave's RQD%
0.724886	1296	1342	631	612	93	106
1.449771	1301	1436	633	976	82	42
2.827054	1330	1461	636	1201	83	28
5.726596	1084	1470	503	783	54	41
11.3807	1086	1479	586	778	54	57
17.1073	1091	1488	553	980	54	32
28.488	1209	1497	575	1008	65	32

Table 16 - Static and dynamic velocities determined at different stresses

Stress (MPa)	V_P upscaled to 60 Hz (m/s)	V_S upscaled to 60 Hz (m/s)
0.724886	1317	622
1.449771	1361	759
2.827054	1389	818
5.726596	1238	605
11.3807	1242	663
17.1073	1248	696
28.488	1330	721

Table 17 - Laboratory velocities upscaling to 60 Hz

3.2.14. Core B2

B2 comes from Daw Mill, and is the second sample successfully cored along the layers. The applied stress played an important role in attenuation, it was difficult to pick the first phase wave train arrival (see Figure 42).

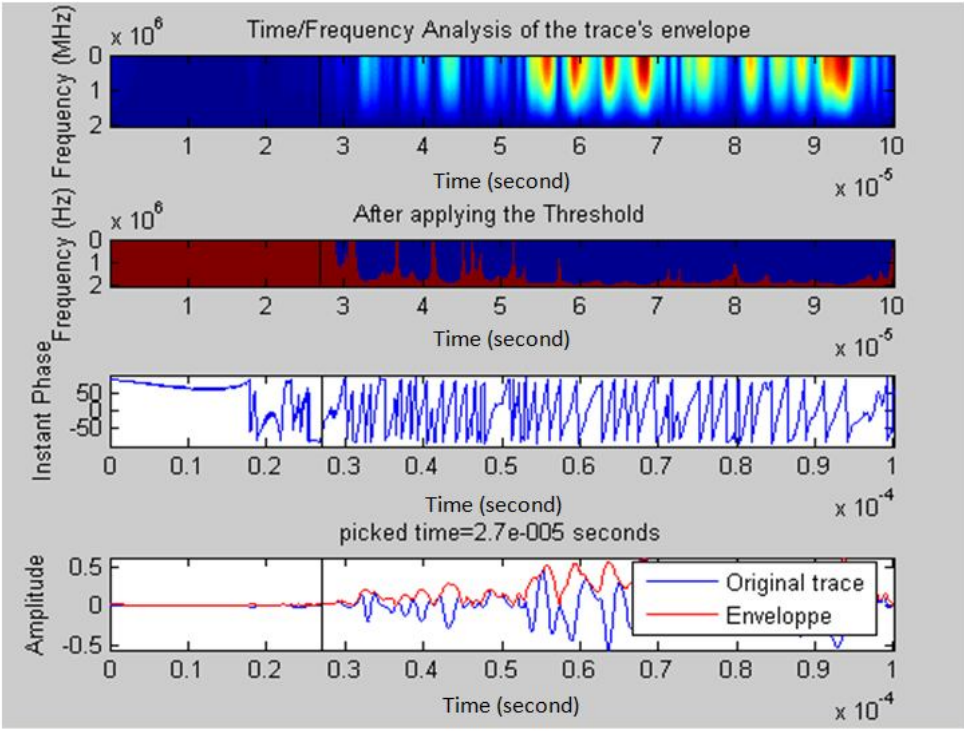

Figure 42 – Example of P-wave picking with the group wave train algorithm; this example shows the problems encountered for picking the first arrival.

Sample number	B2
Pre-Test Length (mm)	50.568
Diameter (mm)	37.232
Weight (g)	81.4177
Sample's density (kg/m^3)	1478.83745
P-wave calibration (µs)	24.95
S-wave calibration (µs)	47.7
Time shift (µs)	20

Table 18 - Sample dimensions and weight

Stress (MPa)	Static Vp (m/s)	q-P wave group velocity (m/s)	q-P wave phase velocity (m/s)	StaticVs (m/s)	Picked Vs (m/s)	qP-phase wave trains' RQD%	S-wave's RQD%
0.721385	2374	3760	3500	1187	1580	46	56
1.442771	2403	3574	3599	1230	1542	45	64
2.813403	2198	3816	2683	1187	1542	67	59
5.698944	2396	3966	3966	1312	1542	37	72
11.32575	2562	3966	3966	1350	1532	42	78
17.02469		4232	4232		1532		
28.35044		3935	3935		1556		

Table 19 - Static and dynamic velocities determined at different stresses

Stress (MPa)	q-P wave group velocity upscaled to 60 Hz (m/s)	q-P wave phase velocity upscaled to 60 Hz (m/s)	S wave velocity upscaled to 60 Hz (m/s)
0.721385	2875	2799	1345
1.442771	2843	2850	1360
2.813403	2749	2403	1332
5.698944	2947	2947	1412
11.32575	3077	3077	1431
17.02469			
28.35044			

Table 20 - Laboratory velocities upscaling to 60 Hz

3.2.15. Core C

The two wave trains observed is a feature typical of waves propagating orthogonally to the layering (see paragraph 3.2.6).

Sample number	C
Pre-Test Length (mm)	56.364
Diameter (mm)	37.262
Weight (g)	86.9303
Sample's density (kg/m^3)	1414.31832
P-wave calibration (μs)	24.95
S-wave calibration (μs)	47.7
Time shift (μs)	20

Table 21 - Sample dimensions and weight

Stress (MPa)	Static Vp (m/s)	q-P wave group velocity (m/s)	q-P wave phase velocity (m/s)	StaticVs (m/s)	Picked Vs (m/s)	qP-phase wave trains' RQD%	S-wave's RQD%
0.720224	2170	1695	2580	912	1588	71	33
1.440448	2918	2603	1563	991	1683	348	35
2.808874	1971	2155	1665	942	1713	140	30
5.689771	2079	2131	2131	1040	1634	95	40
11.30752	2213	2147	2147	1086	1606	106	46
16.99729	1903	2197	2197	900	1606	75	31
28.30481	1730	3935	3935	790	1556	68	23

Table 22 - Static and dynamic velocities determined at different stresses

Stress (MPa)	q-P wave group velocity upscaled to 60 Hz (m/s)	q-P wave phase velocity upscaled to 60 Hz (m/s)	S wave velocity upscaled to 60 Hz (m/s)
0.720224	1917	2346	1141
1.440448	2760	2071	1230
2.808874	2054	1814	1197
5.689771	2103	2103	1255
11.30752	2181	2181	1282
16.99729	2032	2032	1136
28.30481	1887	1887	1044

Table 23 - Laboratory velocities upscaling to 60 Hz

3.2.16. Core 239B

This description of sandstone's petrology is an overview of publications of Guion et al. (1995) and Rippon (1998), and of personal communications with John Rippon. These sandstones are othoquartzites brought by paleo-rivers, the flow direction being NNW-SSE. In this region, sandstones represent approximately 30% of the deposited volume, the rest of the sedimentation being mainly mudstone from marine deposition.

The granular structure of sandstone is a source of attenuation for ultrasonic waves and becomes a problem with poor coupling at smaller stresses; this manfests itself as:

- S-wave recognition becoming increasingly difficult with porosity
- no high RQD expected at the lower stress stages of the testing

Finally, an operator error on piezo sensor's delay (see paragraph 3.2.2, the first step of the acquisition, "Record of the piezo-delay") has led to a 10 microseconds uncertainty on all tests made on sandstone samples.

Sample number	239B
Pre-Test Length (mm)	58.492
Diameter (mm)	41.36
Weight (g)	207.9
Sample's density (kg/m^3)	2645.4958
P-wave calibration (μs)	28.1
S-wave calibration (μs)	64.4
Time shift (μs)	20~30

Table 24 - Sample dimensions and weight

Stress (MPa)	Static Vp (m/s)	First picked V_P (m/s)	Second picked V_P (precursors) (m/s)	StaticVs (m/s)	Picked Vs (m/s)	First picked wave train's RQD%	S-wave's RQD%
0.584573		3128	4570		2647		
1.169147	2357	3145	9914	1484	2468	6	36
2.279836	2488	3162	4178	1632	2478	35	43
4.618129	2518	3196	4999	1661	2321	25	51
9.1778	2344	3342	4957	1514	2340	22	42
13.79593	2421	3323	5176	1577	2359	22	45
22.97373	2500	3362	4570	1635	2368	30	48

Table 25 - Static and dynamic velocities determined at different stresses

Stress (MPa)	First picked V_P upscaled to 60 Hz (m/s)	Second picked V_P upscaled to 60 Hz (m/s)	S wave velocity upscaled to 60 Hz (m/s)
0.584573			
1.169147	2674	3683	1828
2.279836	2766	3075	1946
4.618129	2799	3289	1918
9.1778	2729	3121	1817
13.79593	2777	3234	1869
22.97373	2844	3180	1915

Table 26 - Laboratory velocities upscaling to 60 Hz

3.2.17. Core 239C

Sample number	239C
Pre-Test Length (mm)	74.362
Diameter (mm)	41.346
Weight (g)	207.9
Sample's density (kg/m^3)	2620.17197
P-wave calibration (μs)	28.1
S-wave calibration (μs)	64.4
Time shift (μs)	20~30

Table 27 - Sample dimensions and weight

Stress (MPa)	Static Vp (m/s)	First picked V_P (m/s)	Second picked V_P (precursors) (m/s)	StaticVs (m/s)	Picked Vs (m/s)	First picked wave train's RQD%	S-wave's RQD%
0.584969		3151	3060		1907		
1.169938	2727	3023	3276	1799	2260	81	63
2.28138	2468	3111	3320	1654	2274	63	53
4.621257	2493	3138	3151	1636	2288	63	51
9.184016	2365	3205	3305	1519	2247	54	46
13.80527	2392.	3233	3335	1551	2274	55	47
22.98929	2665	4274	5810	1681	3011	39	31

Table 28 - Static and dynamic velocities determined at different stress

Stress (MPa)	First picked V_P upscaled to 60 Hz (m/s)	Second picked V_P upscaled to 60 Hz (m/s)	S wave velocity upscaled to 60 Hz (m/s)
0.584969			
1.169938	2859	2961	1991
2.28138	2735	2809	1898
4.621257	2761	2766	1891
9.184016	2699	2732	1793
13.80527	2727	2761	1825
22.98929	3241	3580	2124

Table 29 - Laboratory velocities upscaling to 60 Hz

3.2.18. Core 439A

Sample number	439A
Pre-Test Length (mm)	78.68
Diameter (mm)	41.24
Weight (g)	277.4
Sample's density (kg/m^3)	2639.45894
P-wave calibration (μs)	28.1
S-wave calibration (μs)	64.4
Time shift (μs)	20~30

Table 30 - Sample dimensions and weight

Stress (MPa)	Static Vp (m/s)	First picked V_P (m/s)	Second picked V_P (precursors) (m/s)	StaticVs (m/s)	Picked Vs (m/s)	First picked wave train's RQD%	S-wave's RQD%
0.58798	955	3198	3626	630	1643	9	15
1.17596	2245	3085	3085	1473	1639	53	81
2.293123	2137	2969	3451	1372	1636	52	70
4.645043	2097	3098	3098	1326	1632	46	66
9.231289	2587	3098	3626	1668	1722	70	94
13.87633	2480	3251	3265	1607	1656	58	94
23.10762	2619	3334	3436	1732	1683	62	106

Table 31 - Static and dynamic velocities determined at different stresses

Stress (MPa)	First picked V_P upscaled to 60 Hz (m/s)	Second picked V_P upscaled to 60 Hz (m/s)	S wave velocity upscaled to 60 Hz (m/s)
0.58798	1429	1465	889
1.17596	2577	2577	1547
2.293123	2463	2605	1485
4.645043	2474	2474	1455
9.231289	2805	2992	1693
13.87633	2793	2797	1630
23.10762	2914	2950	1708

Table 32 - Laboratory velocities upscaling to 60 Hz

3.2.19. Core 439C

Sample number	439C
Pre-Test Length (mm)	71.276
Diameter (mm)	41.212
Weight (g)	250.5
Sample's density (kg/m^3)	2634.67559
P-wave calibration (μs)	28.1
S-wave calibration (μs)	64.4
Time shift (μs)	20~30

Table 33 - Sample dimensions and weight

Stress (MPa)	Static Vp (m/s)	First picked V_P (m/s)	Second picked V_P (precursors) (m/s)	StaticVs (m/s)	Picked Vs (m/s)	First picked wave train's RQD%	S-wave's RQD%
0.588779	2300	2795	3112	1500	1764	68	72
1.177559	2310	2806	3112	1537	1777	68	75
2.29624	2787	2828	2909	1829	2031	97	81
4.651357	2316	2828	3225	1518	2193	67	48
9.243837	2274	3112	3112	1477	2072	53	51
13.89519	2382	2945	3511	1543	2078	65	55
23.13903	2335	3020	3126	1539	2090	60	54

Table 34 - Static and dynamic velocities determined at different stresses

Stress (MPa)	First picked V_P upscaled to 60 Hz (m/s)	Second picked V_P upscaled to 60 Hz (m/s)	S wave velocity upscaled to 60 Hz (m/s)
0.588779	2510	2624	1614
1.177559	2521	2630	1642
2.29624	2806	2843	1919
4.651357	2533	2672	1776
9.243837	2605	2605	1709
13.89519	2619	2809	1757
23.13903	2615	2652	1758

Table 35 - Laboratory velocities upscaling to 60 Hz

3.2.20. Core 839A

Sample number	839A
Pre-Test Length (mm)	58.996
Diameter (mm)	41.384
Weight (g)	210.4
Sample's density (kg/m^3)	2651.3579
P-wave calibration (μs)	28.1
S-wave calibration (μs)	64.4
Time shift (μs)	20~30

Table 36 - Sample dimensions and weight

Axial Load (kN)	Static Vp (m/s)	First picked V_P (m/s)	Second picked V_P (precursors) (m/s)	StaticVs (m/s)	Picked Vs (m/s)	First picked wave train's RQD%	S-wave's RQD%
0.583895		3371	3371		2369		
1.167791	2708	3010	3430	1787	2379	81	56
2.277192	2452	3010	3430	1643	2389	66	47
4.612774	2476	3073	3710	1625	2398	65	46
9.167158	2349	3121	3371	1509	2418	57	39
13.77993	2376	3450	3450	1540	2438	47	40
22.94709	2647	3450	3933	1670	2836	59	35

Table 37 - Static and dynamic velocities determined at different loads

Axial Load (kN)	First picked V_P upscaled to 60 Hz (m/s)	Second picked V_P upscaled to 60 Hz (m/s)	S wave velocity upscaled to 60 Hz (m/s)
0.583895			
1.167791	2843	3007	2025
2.277192	2687	2833	1927
4.612774	2726	2938	1917
9.167158	2660	2742	1834
13.77993	2786	2786	1864
22.94709	2974	3130	2072

Table 38 - Laboratory velocities upscaling to 60 Hz

3.2.21. Core 1039A

Sample number	1039A
Pre-Test Length (mm)	57.152
Diameter (mm)	41.3
Weight (g)	196.1
Sample's density (kg/m^3)	2561.2748
P-wave calibration (μs)	28.1
S-wave calibration (μs)	64.4
Time shift (μs)	20~30

Table 39 - Sample dimensions and weight

Stress (MPa)	Static Vp (m/s)	First picked V_P (m/s)	Second picked V_P (precursors) (m/s)	StaticVs (m/s)	Picked Vs (m/s)	First picked wave train's RQD%	S-wave's RQD%
0.586273		2207	2342		2369		
1.172546	2761	2277	2277	1822	2379	147	140
2.286465	2499	2352	2381	1675	2389	113	125
4.631557	2525	2610	2622	1657	2398	94	181
9.204486	2395	2314	2401	1538	2418	107	45
13.83604	2423	2333	2474	1570	2438	108	46
23.04053	2698	2401	2474	1702	2836	126	53

Table 40 - Static and dynamic velocities determined at different stresses

Stress (MPa)	First picked V_P upscaled to 60 Hz (m/s)	Second picked V_P upscaled to 60 Hz (m/s)	S wave velocity upscaled to 60 Hz (m/s)
0.586273			
1.172546	2509	2509	1677
2.286465	2427	2442	1587
4.631557	2564	2569	1425
9.204486	2356	2398	1819
13.83604	2379	2447	1848
23.04053	2549	2587	1954

Table 41 - Laboratory velocities upscaling to 60 Hz

3.2.22. Core 2198B

Sample number	2198B
Pre-Test Length (mm)	61.312
Diameter (mm)	41.63
Weight (g)	275.1
Sample's density (kg/m^3)	3296.41897
P-wave calibration (μs)	28.1
S-wave calibration (μs)	64.4
Time shift (μs)	20~30

Table 42 - Sample dimensions and weight

Stress (MPa)	Static Vp (m/s)	First picked V_P (m/s)	Second picked V_P (precursors) (m/s)	StaticVs (m/s)	Picked Vs (m/s)	First picked wave train's RQD%	S-wave's RQD%
0.577015		2221	2221		1864		
1.15403	3851	3097	3097	2651	1864	147	140
2.250359	3992	3832	3832	2823	1940	113	125
4.558419	3825	3905	3905	2658	1978	94	181
9.059137	2910	4007	4007	2048	2404	107	45
13.61756	3495	3956	3956	2296	2376	108	46
22.67669	3003	3956	3956	1911	2620	126	53

Table 43 - Static and dynamic velocities determined at different stresses

Stress (MPa)	First picked V_P upscaled to 60 Hz (m/s)	Second picked V_P upscaled to 60 Hz (m/s)	S wave velocity upscaled to 60 Hz (m/s)
0.577015			
1.15403	3454	3454	2210
2.250359	3915	3915	2324
4.558419	3863	3863	2287
9.059137	3343	3343	2202
13.61756	3698	3698	2333
22.67669	3388	3388	2191

Table 44 - Laboratory velocities upscaling to 60 Hz

3.2.23. Statistical Analysis: Coal

The coal properties collected in the laboratory are statistically analysed in this section; the goal is to apply them in the next chapter which is dedicated to modelling. Data selection based on RQD% is implemented for determining the (V_P, V_S, ρ) set representative of coal properties found in the Daw Mill colliery. The outcomes of this analysis are respectively the Coal's P- and S-wave's;

- velocity distribution (tables 46, 47, 49 & 50 and figures 43, 44 & 48)
- average velocity and standard deviation (tables 53, 56, 59 & 60)

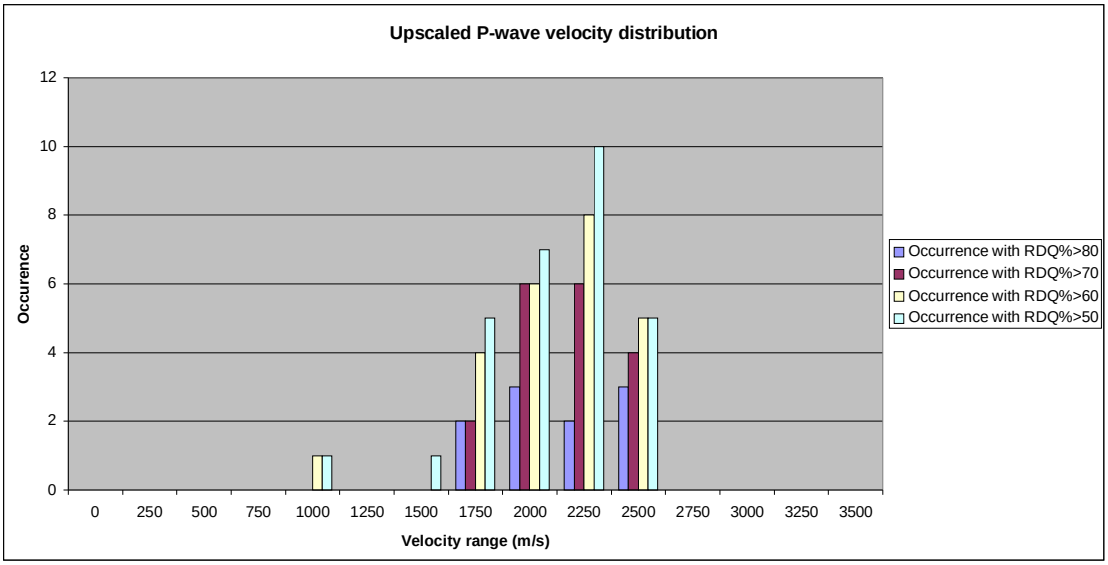

Figure 43 – Upscaled P-wave distribution of coal samples from Daw Mill

	All data included	RDQ>80%	RDQ>70%	RDQ>60%	RDQ>50%
P-wave's average velocity (m/s)	2111.028	2289.432	2274.763	2214.547	2179.403
Velocity's standard deviation (m/s)	548.8407	272.8147	237.5994	320.3639	323.8765
Maximum recorded value (m/s)	2760.42	2702.669	2702.669	2702.669	2702.669
Minimum recorded value (m/s)	549.432	1976.878	1976.878	1221.959	1221.959
Number of samples	72	10	18	24	29

Table 45 – Average and standard deviation of coal's upscaled P-wave velocity; RQD>80% means that only data displaying a Rock Quality Designation exceeding 80% are taken into account in the computation. These values stand for velocities orthogonal to the layering

Velocity Range (m/s)	Probability, all data included (%)	Probability of data with RQD%>80 (%)	Probability of data with RQD%>70 (%)	Probability of data with RQD%>60 (%)	Probability of data with RQD%>50 (%)
0	0.00	0.00	0.00	0.00	0.00
250	0.00	0.00	0.00	0.00	0.00
500	3.23	0.00	0.00	0.00	0.00
750	3.23	0.00	0.00	0.00	0.00
1000	4.84	0.00	0.00	4.35	3.57
1250	4.84	0.00	0.00	0.00	0.00
1500	4.84	0.00	0.00	0.00	3.57
1750	14.52	20.00	11.11	17.39	17.86
2000	30.65	30.00	33.33	26.09	25.00
2250	22.58	20.00	33.33	30.43	32.14
2500	9.68	30.00	22.22	21.74	17.86
2750	1.61	0.00	0.00	0.00	0.00
3000	0.00	0.00	0.00	0.00	0.00
3250	0.00	0.00	0.00	0.00	0.00
3500	0.00	0.00	0.00	0.00	0.00

Table 46 – Distribution probability of P-wave velocity in Coal; direction orthogonal to the layering

Velocity Range (m/s)	Probability, all data included (%)	Probability of data with RQD%>80 (%)	Probability of data with RQD%>70 (%)	Probability of data with RQD%>60 (%)	Probability of data with RQD%>50 (%)
0	0	0	0	0	0
250	0	0	0	0	0
500	0	0	0	0	0
750	0	0	0	0	0
1000	0	0	0	0	0
1250	0	0	0	0	0
1500	0	0	0	0	0
1750	0	0	0	0	0
2000	0	0	0	0	0
2250	10	0	0	100	100
2500	10	0	0	0	0
2750	60	0	0	0	0
3000	20	0	0	0	0
3250	0	0	0	0	0
3500	0	0	0	0	0

Table 47 – Distribution probability of P-wave velocity in Coal; direction parallel to the layering

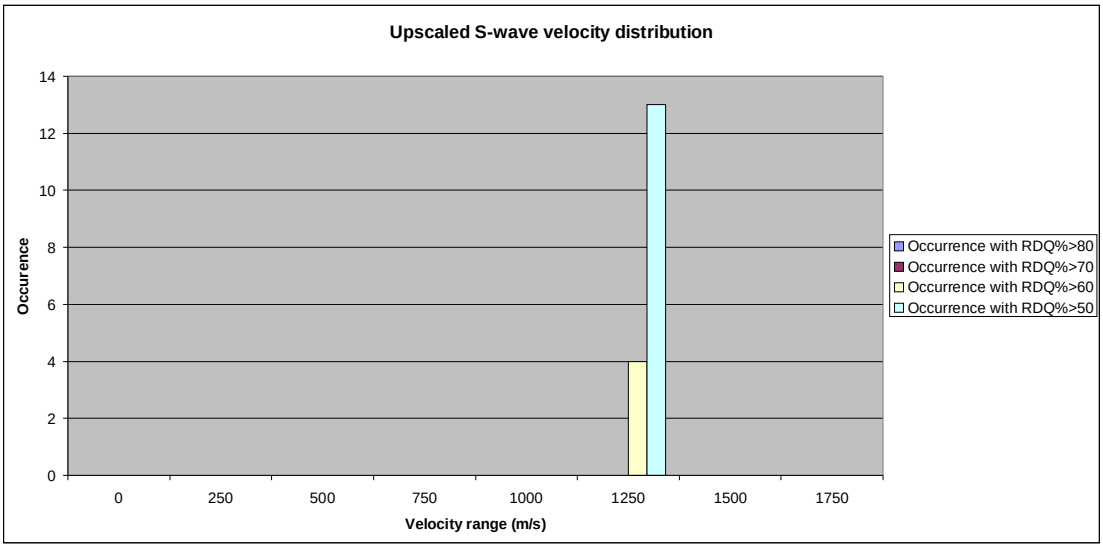

Figure 44 - Distribution probability of Coal's S-wave velocity. The insensitivity of S-wave velocity to certain physical phenomena (see paragraph 2.4.6) compensates its picking uncertainty, hence its narrower distribution compared to V_P (See Figure 46)

	All data included	RQD>80%	RQD>70%	RQD>60%	RQD>50%
S-wave's average velocity (m/s)	1209.275	0	0	1387.052	1356.37
Velocity's standard deviation (m/s)	232.5653	0	0	41.7528	38.88679
Maximum recorded value (m/s)	0	0	0	1415.637	1415.637
Minimum recorded value (m/s)	0	0	0	1325.837	1278.352
Number of samples	38	0	0	4	13

Table 48 – Average and standard deviation of coal's upscaled S-wave velocity. These values stand for velocities orthogonal to the layering

Velocity Range (m/s)	Probability, all data included (%)	Probability of data with RQD%>80 (%)	Probability of data with RQD%>70 (%)	Probability of data with RQD%>60 (%)	Probability of data with RQD%>50 (%)
0	0	0	0	0	0
250	0	0	0	0	0
500	9.0909091	0	0	0	0
750	9.0909091	0	0	0	0
1000	27.272727	0	0	0	0
1250	54.545455	0	0	100	100
1500	0	0	0	0	0
1750	0	0	0	0	0
2000	0	0	0	0	0
2250	0	0	0	0	0
2500	0	0	0	0	0
2750	0	0	0	0	0
3000	0	0	0	0	0
3250	0	0	0	0	0
3500	0	0	0	0	0

Table 49 – Probability distribution of S-wave velocity; direction orthogonal to the layering

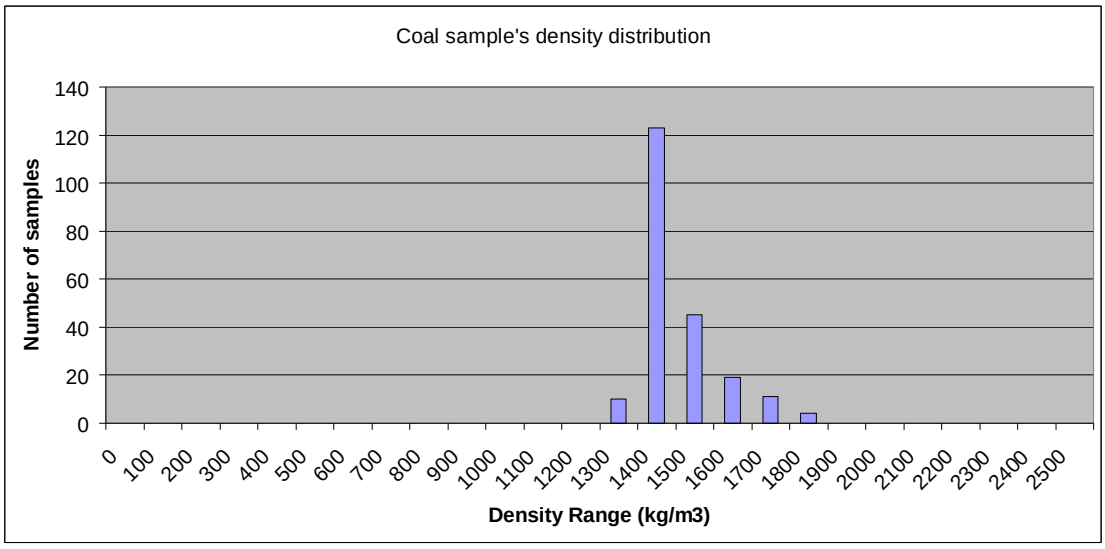

Figure 45 – Coal sample's density distribution

Density Range (kg/m^3)	Probability distribution of density(%)
0	0
100	0
200	0
300	0
400	0
500	0
600	0
700	0
800	0
900	0
1000	0
1100	0
1200	0
1300	4.716981
1400	58.01887
1500	21.22642
1600	8.962264
1700	5.188679
1800	1.886792
1900	0
2000	0
2100	0
2200	0
2300	0
2400	0
2500	0

Table 50 – Density's probability distribution

	Directions of propagation to the layering	⊥	∥
P-wave	Average velocity (m/s)	2274.763	2856.638
	Standard deviation (m/s)	237.5994	192.7401
S-wave	Average velocity (m/s)	1356.37	1375.788
	Standard deviation (m/s)	38.88679	43.08287

Table 51 – P and S-waves velocities and standard deviation of coal in different directions

Origin of the data	Laboratory	Log	Laboratory + log
Density (kg/m3)	1296.208	1418.495	1415.063
Density's standard deviation (kg/m3)	105.9903	104.0927	106.1438
Number of samples	6	206	212

Table 52 – Average density of coal in Daw Mill. The observed difference is due to measurement's procedures and sample's alteration linked to transit and coal's preparation (see paragraphs 3.2.3 and 3.2.4).

P- and S-wave velocities in the orthogonal direction of coal layering has been measured on many samples at different loads; enough data have been gathered to make a selection based on RQD, and computing for both the average velocity and its standard deviation. Selected data have an RQD% over 70%.

Concerning the data collected with the only sample cored along the layering, and coming from Daw Mill, RQD proves that the general quality of the data is poor, and shall be considered carefully. Without the challenging coring conditions (see comments on coal's britleness in paragraph 3.2.4, during coal samples' preparation) in this particular direction, it would have been possible to core coal blocks in different directions:

1. orthogonally to the layering
2. along the layering
3. 45° to the layering

and assess the anisotropy of P- and S-wave velocity in coal. As coal's fragility did not enable the measurement of the mechanical properties' variations with direction, data from the literature have completed the missing anisotropy parameters.

3.2.24. Statistical Analysis: Sandstone

Coal and sandstone's statistical analysis are similar, and based on RQD. Like in the previous paragraphs, the principal outcomes are:

- velocity distribution (tables 54, 56 & 58 and 46, 47 & 48)
- average velocity and standard deviation (tables 53, 55, 57 and 59)

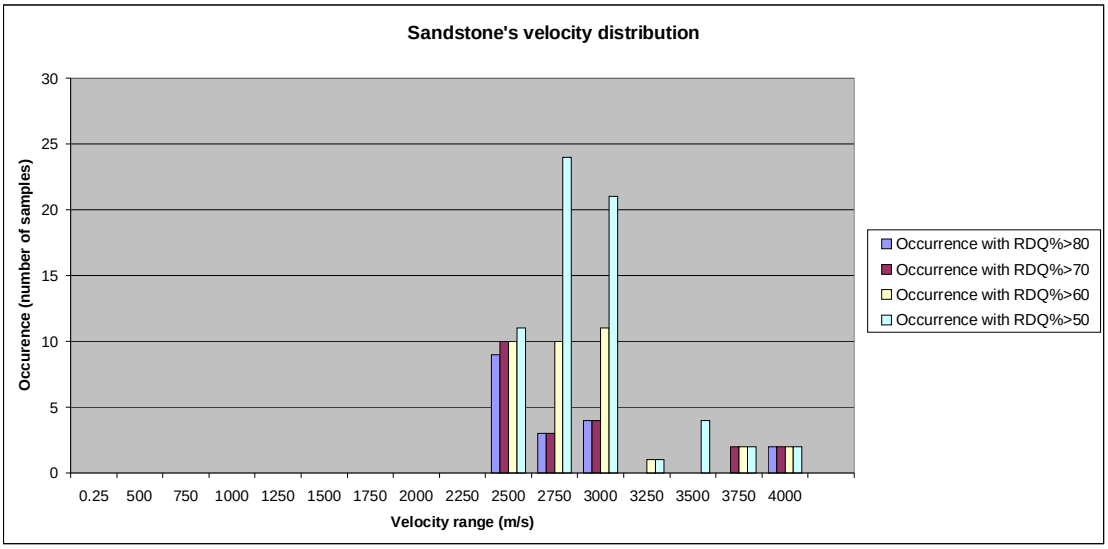

Figure 46 – Upscaled P-wave distribution of sandstone samples from Daw Mill.

	All data included	RQD>80%	RQD>70%
P-wave's average velocity (m/s)	2797.625	2694.964	2779.571
Velocity's standard deviation (m/s)	433.7859	458.0266	523.5889
Maximum recorded value (m/s)	3914.757	3862.502	3862.502
Minimum recorded value (m/s)	1428.569	2361.459	2361.459
Number of samples	100	18	21

Table 53 – Sandstone's upscaled P-wave velocity's average and standard deviation, for different RDQs.

Velocity Range (m/s)	Probability, all data included (%)	Probability of data with RQD%> 80 (%)	Probability of data with RQD%> 70 (%)	Probability of data with RQD %> 60 (%)	Probability of data with RQD %> 50 (%)
0	0	0	0	0	0
250	0	0	0	0	0
500	0	0	0	0	0
750	0	0	0	0	0
1000	0	0	0	0	0
1250	2	0	0	0	0
1500	0	0	0	0	0
1750	0	0	0	0	0
2000	0	0	0	0	0
2250	18.00	50.00	47.62	27.78	16.92
2500	33.00	16.67	14.29	27.78	36.92
2750	25.00	22.22	19.05	30.56	32.31
3000	7.00	0	0	2.78	1.54
3250	7.00	0	0	0	6.15
3500	4.00	0	9.52	5.56	3.08
3750	4.00	11.11	9.52	5.56	3.08
4000	0	0	0	0	0

Table 54 - Distribution probability of P-wave velocities in Sandstones

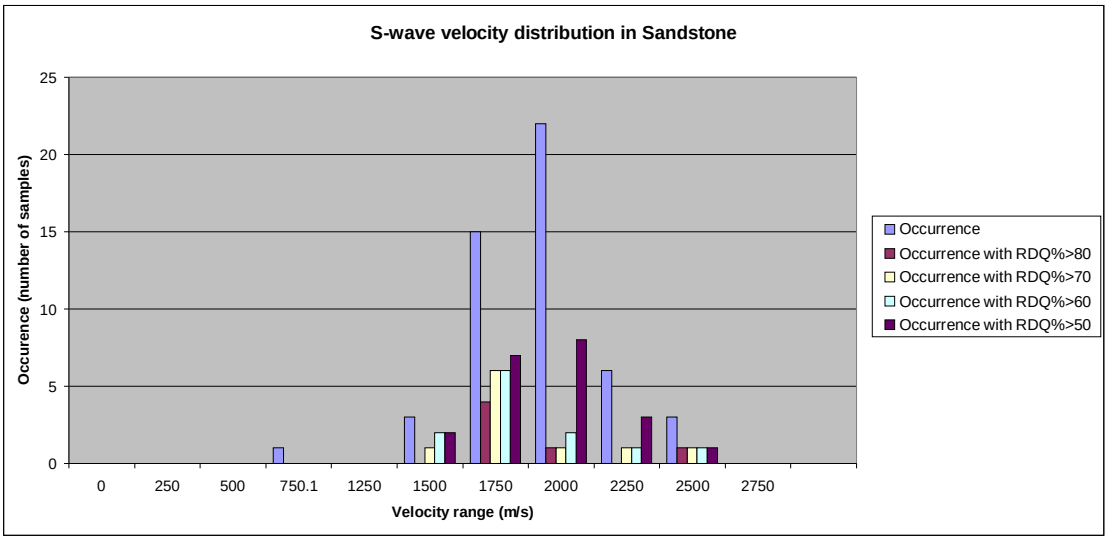

Figure 47 - Upscaled S-wave velocity distribution in sandstone samples from Daw Mill. S-wave related picking problems have much more affected the sandstone than coal.

	All data included	RQD>80%	RQD>70%	RQD>60%	RQD>50%
S-wave's average velocity (m/s)	1807.544	1775.185	1759.469	1753.409	1816.314
Velocity's standard deviation (m/s)	264.3199	307.519	294.4982	290.1849	246.7696
Maximum recorded value (m/s)	2333.228	2333.228	2333.228	2333.228	2333.228
Minimum recorded value (m/s)	889.1452	1528.255	1485.303	1455.237	1455.237
Number of samples	50	6	10	12	21

Table 55 – Sandstone's upscaled S-wave velocity's average and standard deviation, for different RDQs. These values also represent for velocities orthogonal to the layering

Velocity Range (m/s)	Probability, all data included (%)	Probability of data with RQD%>80 (%)	Probability of data with RQD%>70 (%)	Probability of data with RQD%>60 (%)	Probability of data with RQD%>50 (%)
0	0	0	0	0	0
250	0	0	0	0	0
500	0	0	0	0	0
750	2	0	0	0	0
1000	0	0	0	0	0
1250	6	0	10	16.67	9.52
1500	30	66.67	60	50	33.33
1750	44	16.67	10	16.67	38.10
2000	12	0	10	8.33	14.29
2250	6	16.67	10	8.33	4.76
2500	0	0	0	0	0
2750	0	0	0	0	0

Table 56 - Distribution probability of S-wave velocity in sandstone

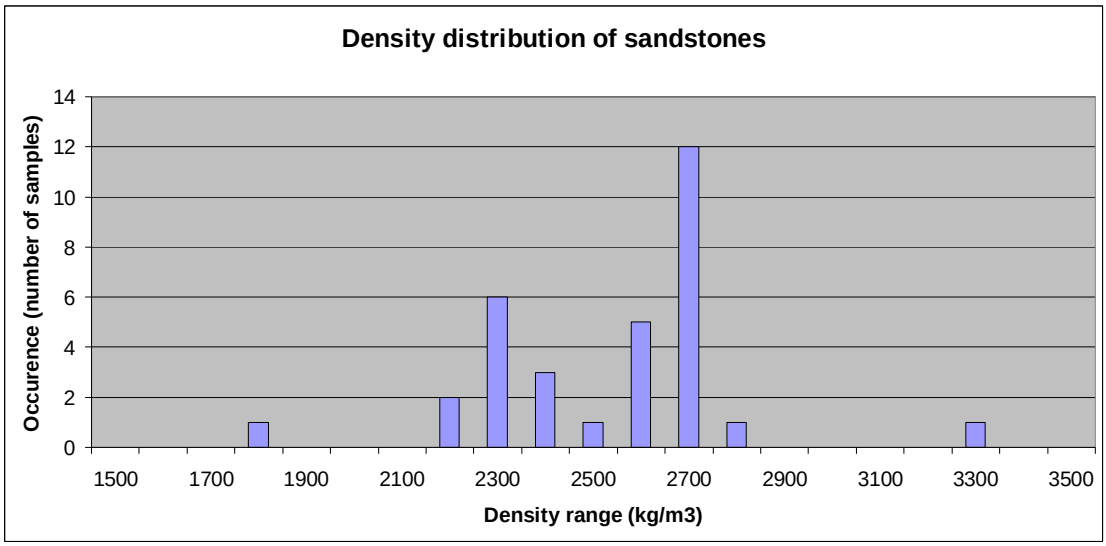

Figure 48 - Sandstone sample's density distribution

Origin of the data	Laboratory	Log	Laboratory + log
Density (kg/m3)	2711.533	2420	2492.79
Density's standard deviation (kg/m3)	238.0697	241.5	269.0052
Number of samples	8	24	32

Table 57 – Average density and standard deviation of Daw Mill's Sandstone. The observed differences are due to different measurement methods and sample's preparation.

Density Range (kg/m^3)	Probability distribution of density(%)
1500	0.00
1600	0.00
1700	0.00
1800	3.13
1900	0.00
2000	0.00
2100	0.00
2200	6.25
2300	18.75
2400	9.38
2500	3.13
2600	15.63
2700	37.50
2800	3.13
2900	0.00
3000	0.00
3100	0.00
3200	0.00
3300	3.13

Table 58 - Distribution probability of Sandstone's density

	Upscaled to 60 Hz, all data included	Upscaled to 60 Hz, RQD>80 %	Upscaled to 60 Hz, RQD>70 %	Static, all data included	Static, RQD>80 %	Static, RQD>70 %	Data collected in the Daw Mill's coal mine
Average Young's Modulus (GPa)	21.12565	19.20127	21.32767	18.08907	19.55014	21.89061	19
Young's Modulus' standard deviation (GPa)	8.057023	8.924437	10.94774	9.433093	10.5948	11.8406	10.39355
Number of samples	100	18	21	100	18	21	19

Table 59 – Comparison between static, upscaled and mine collected Young's moduli. Data with a RDQ up to 80% show an interesting correlation with the elastic property measured in the coal mine.

3.2.25. Statistical Analysis: Mudstone

The Mudstone samples were collected by external personnel, therefore the history of the sampling, storage, transportation etc. is unknown. This lead to a limited testing reprogram in the laboratory and reference was made to UK Coal's extensive database of mudstone properties, to compensate for this limited sample size. The results of both laboratory testing and the UK coal database results have produced:

- velocity distribution (Figures 49, 50 and 5)
- average velocity and standard deviation (Table 60)

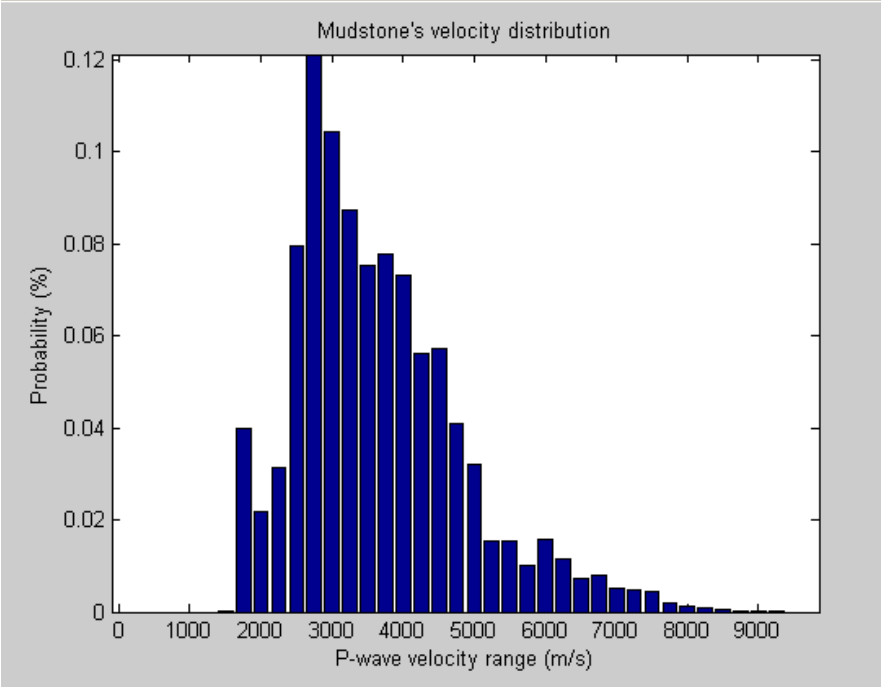

Figure 49 – P-wave velocity distribution of mudstones

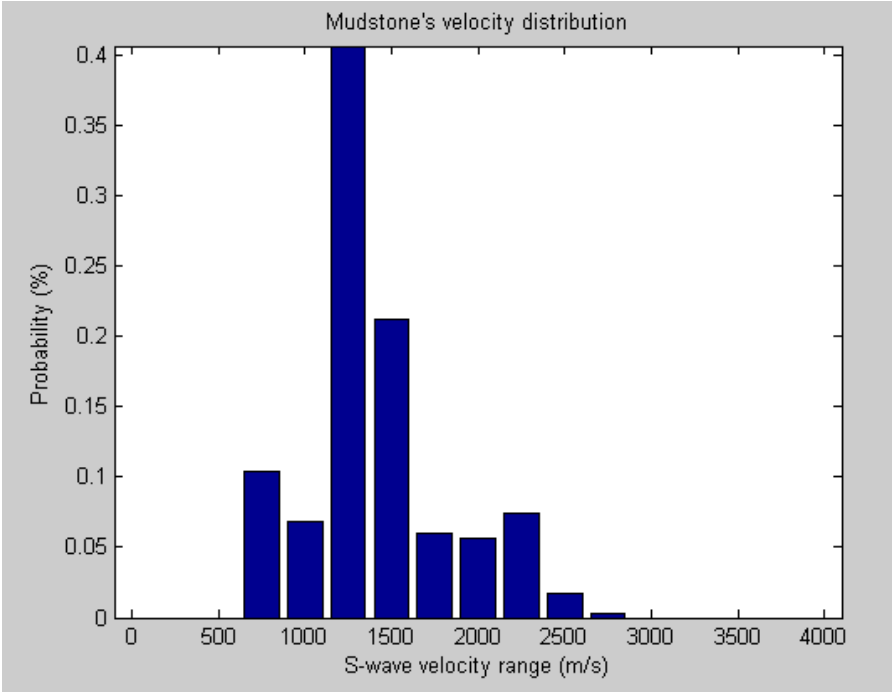

Figure 50 – S-wave velocity distribution of mudstones

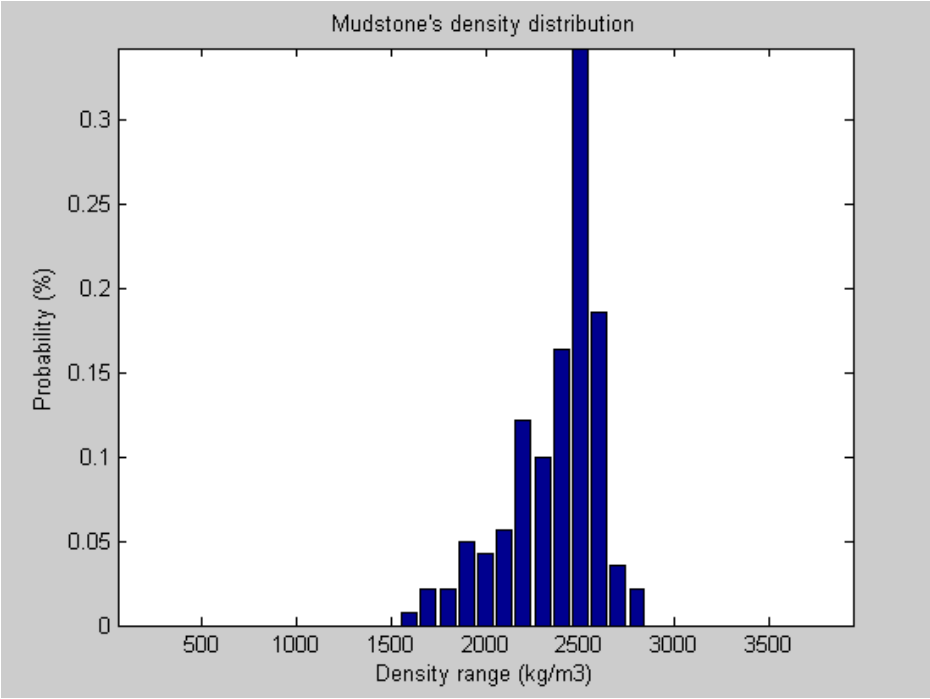

Figure 51 – Density distribution of mudstones

	Mean value	Standard deviation
P-wave velocity (m/s)	3770	402
S-wave velocity (m/s)	1532	245
Density (kg/m3)	2416	114

Table 60 - Mudstone mean properties and their standard deviation

3.2.26. Conclusion

The goal of this part, as mentioned in the introduction, is to present rock parameters collected in the laboratory and determine the respective probability distribution of the elastic properties of mudstone, sandstone and coal samples coming from Daw Mill. Data collection raised two problems:

- In finely layered media, like coal, ultrasonic waves are separated into different phases, some of them having a lower amplitude than noise. Therefore, interpreters (or automatic picking algorithms) pick later arrivals, and underestimate velocities.
- Paragraph 2.4.7 introduced causes of dispersivity and raised the concern of recalibrating a property, like velocity, from ultrasonic frequencies (1 MHz) to seismic frequencies (60 Hz).

Through automatic picking algorithm and equations 129 and 130, the author has proposed two partial solutions that indicate the potential for further improvements. The next part of this chapter introduces one of them: improving the Signal to Noise Ratio of each recorded trace

3.3. AVO CALIBRATION IN THE LABORATORY

3.3.1. Introduction

The second part of this chapter presents a triaxial cell modification, recording amplitude variations with offset, and consisting of an array of sensors placed around a sample. The chosen name for this modified device is "sensitive sleeve" because it has the ability to record wave propagation from different parts of the sample. Pragmatically, this technical modification poses two problems:

- the denser the array, the smaller the piezo-sensors shall be
- the smaller a piezo crystal becomes, the weaker the energy required for its mechanical response.

However, piezo-crystals with larger dimensions are preferred for compensating attenuation of ultrasonic waves; a part of the technical challenge will then consist of establishing a compromise between two requirements:

- array density
- power of the source.

As a dense array would provide offsets potentially useful for AVO calibration purposes, the focus was on source power compensation with techniques for limiting attenuation. The two proposed solutions are:

- filling sample pore volume with water
- applying a stack in order to improve the SNR.

The application of these two techniques enabled the recording of an ultrasonic wave through coal, but not in sandstone; in these conditions, no AVO calibration is possible from the laboratory.

The structure of this section is as follows:

1. Triaxial cell description
2. Principle of the modification
3. Dimensions of the sensitive sleeve
4. Piezo-component performances
5. Description of the NI (For National Instruments) kit
6. Sample preparation
7. Testing procedure
8. NI Kit programming
9. Coal testing
10. Sandstone testing
11. Conclusion and further recommendations

3.3.2. Triaxial Cell description

Section 3.2.2 provides a summary description of the cell; Jaeger, Cook and Zimmerman “Fundamentals of rock mechanics” (1981) has detailed reference material.

3.3.3. Principle of the modification

The principle of the modification consists of placing a sensor array in a cylinder encasing a bilithic structure (see Figure 52) consisting of:

- roof lithology (Mudstone or Sandstone)
- coal.

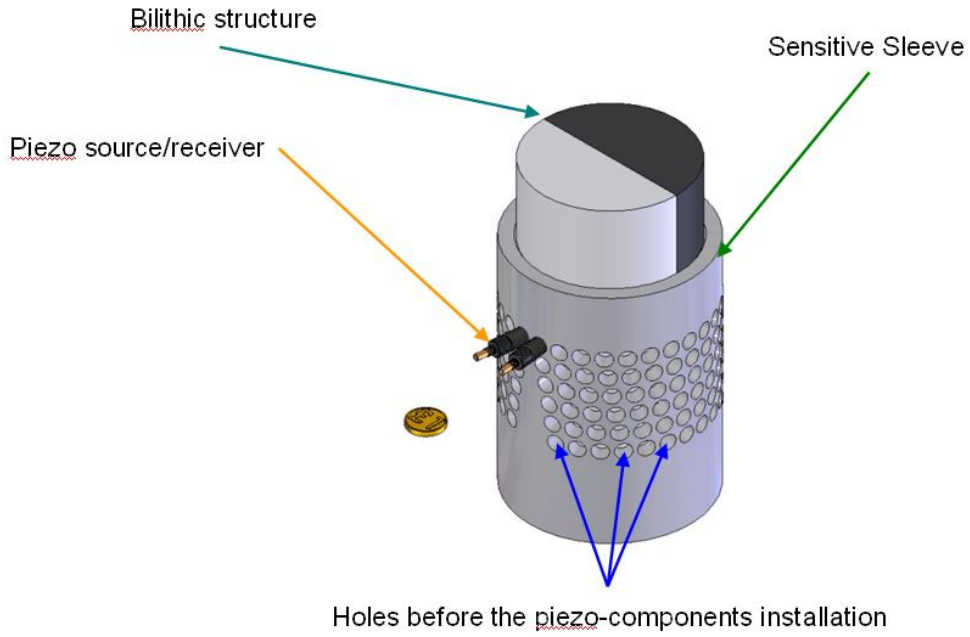

Figure 52 – Triaxial cell modification's principle. This prototype used four piezo-components. If the concept proved to be applicable, the next stage in development would require 200 receivers.

The principle, seen in Figure 3, would consist of collecting, with a bilithic sample, different reflection coefficients at different angles. A direct comparison between the data from laboratory to seismic shot gathers (as in Figure 2) would potentially improve AVO from the laboratory. This new additional step could eventually present a basis for testing inversion algorithms, and their capability to determine rock mechanical properties directly from the reflection coefficients.

3.3.4. Dimensions of the sensitive sleeve

For cylindrical core samples, the length-to-diameter ratio is between 2:1 and 3:1, and the end faces are flat and parallel surfaces. The length to diameter ratio is dictated by the existence of plastic deformation zones at the ends of the core which limit the elastic deformation zone to its mid-section. The second condition prevents specimen bending leading to stress differences within the core that produce a significant strain difference between two diametrically opposed points and, eventually, cause damage to the core.

Fulfilment of these requirements and the requirement for piezo-component (each piezo crystal having a 8 millimeters diameter, 12mm length, and powered with 4 Volts) installation results in a core sample design diameter and length of 100 millimetres diameter and 150 millimetres respectively (Figure 53).

In order to accommodate the core and the piezo crystals, the sleeve is required to be larger than the core sample. The Piezo-component diameter limits sampling to every 12 degrees, and wider coverage is obtained by shifting the first piezo component with an additional 2 degrees shift per layer (Figure 54).

The resulting sleeve is a 120 millimetres diameter by 160 millimetres length sleeve, with 6 different layers of sensors (see Figure 55). The sensor distribution among the layers is respectively:

- 30 piezo-components in section A-A (see Figure 54)

- 29 components in section E-E
- 28 components in sections B-B, C-C, D-D and F-F

171 components will be used in the final design, controlled by a a National Instrument Kit described in paragraph 3.3.6). This thesis tests the design in the bilithic structure with 4 piezo crystals.

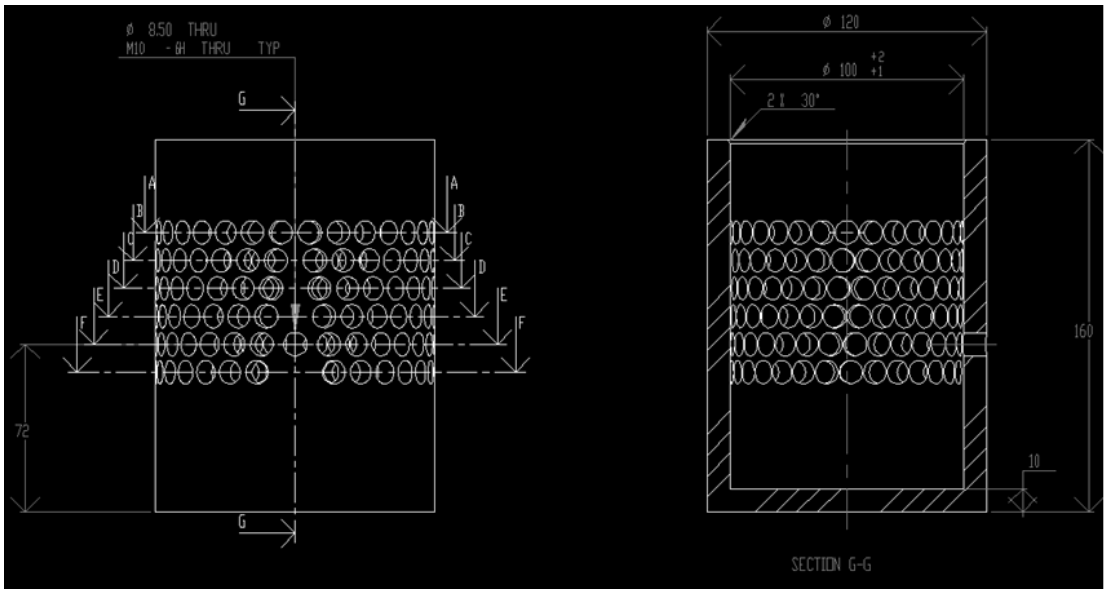

Figure 53 – Sensitive sleeve's dimensions

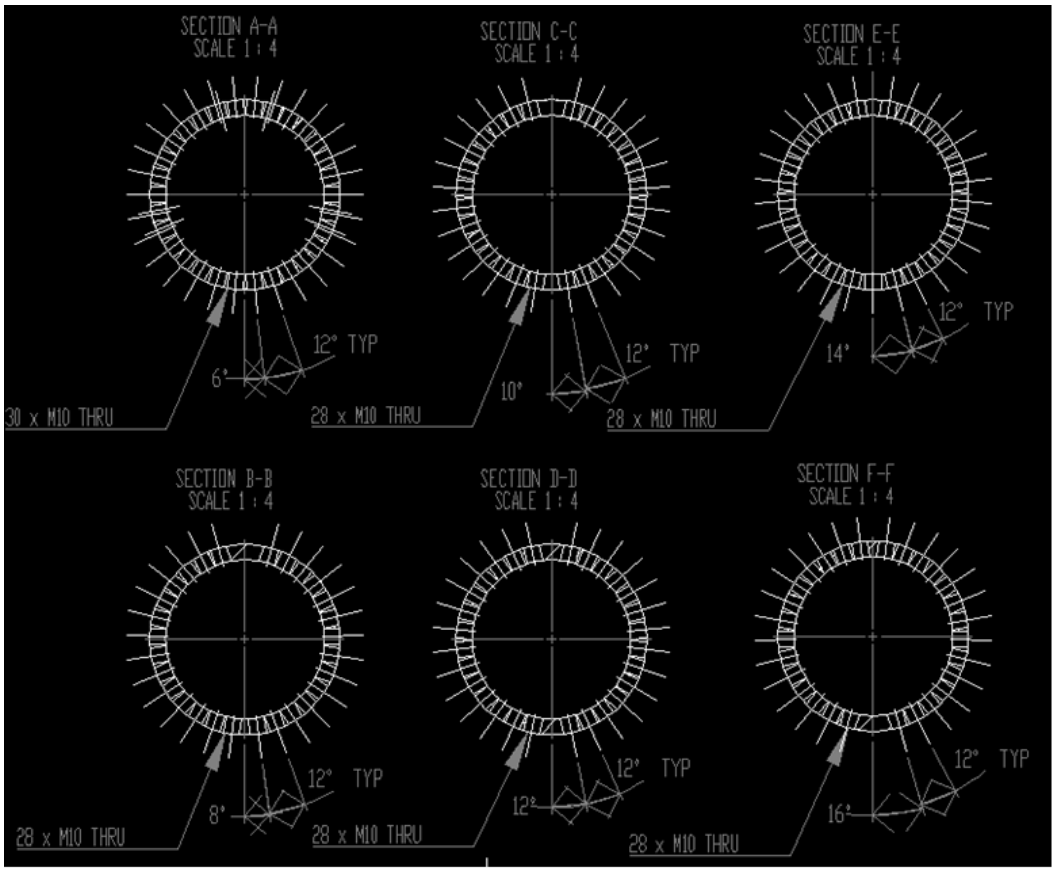

Figure 54 – Sensitive sleeve's different sections

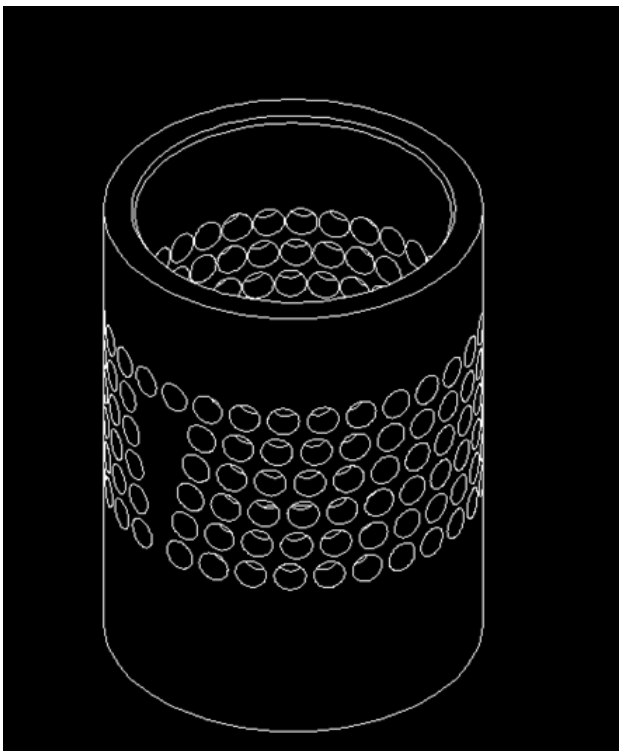

Figure 55 – Sensitive Sleeve perspective view

3.3.5. Description of piezo-component performances

References by Marton (1981), Blitz(1967) and Cady(1947) present good introductions to piezoelectricity. An aspect of applying these to a stressed system is the variation in performance of each crystal under stress. As a starting point, this thesis addresses the compatibility of transducers in the unstressed state to identify the major influences on performance of the system. The following parameters were examined in this thesis:

1. Delay between source and receiver
2. Phase
3. Amplitude difference between two sensors recording the same signal
4. Noise
5. Derivation

Piezo-crystals supplied by Envision displayed a constant level of performance over time (i.e, no derivation), and recorded the same signal for a reference impulse (i.e, the amplitude, phase and response pattern, as in Figure 57). By coupling a transducer playing the role of a source directly to a second used as a receiver, recorded traces brought to light a short delay (see Figure 56), which shall be substracted to recorded first-arrival times for properly assessing velocities, such as P- and S-wave calibration times mentioned in the first half of this chapter (example given in Table 3).

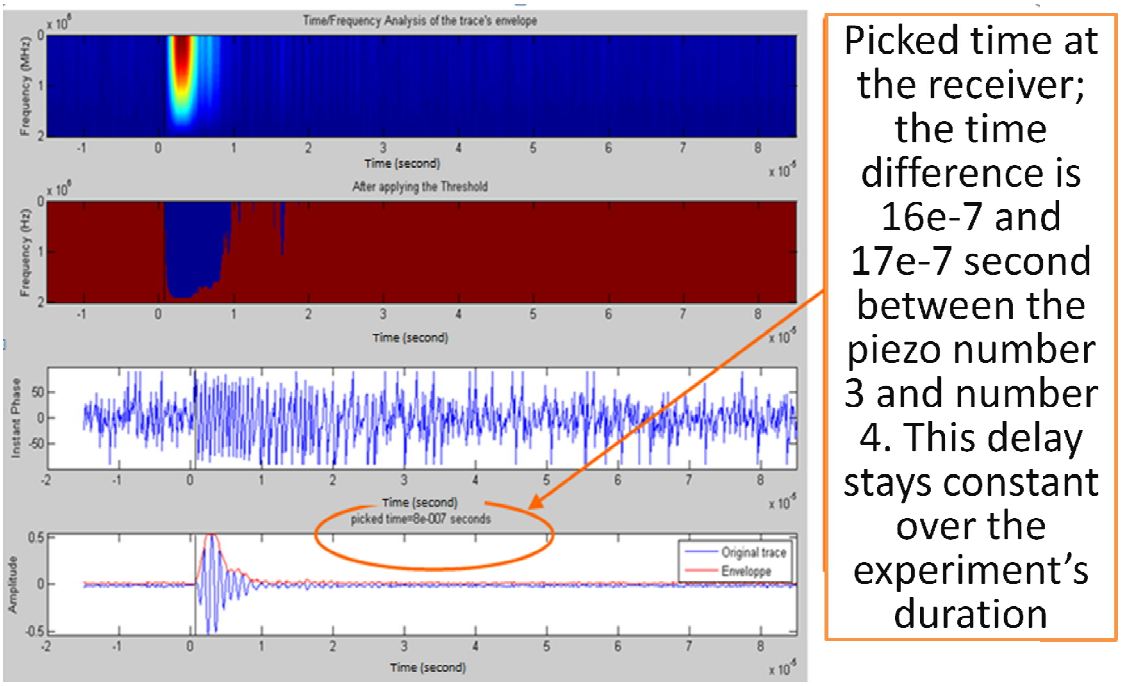

Figure 56 – When source and receiver are directly in contact with each other, piezo-components underline their own time delay.

This investigative step has underlined unexpected features of the transducers:

1. response pattern
2. polarization

Figure 57 shows in fact that transducer response to a sine electric pulse is more extended than the excitation, and that the recorded amplitude depends on wave arrival incidence (Figure 58, 59, 60)

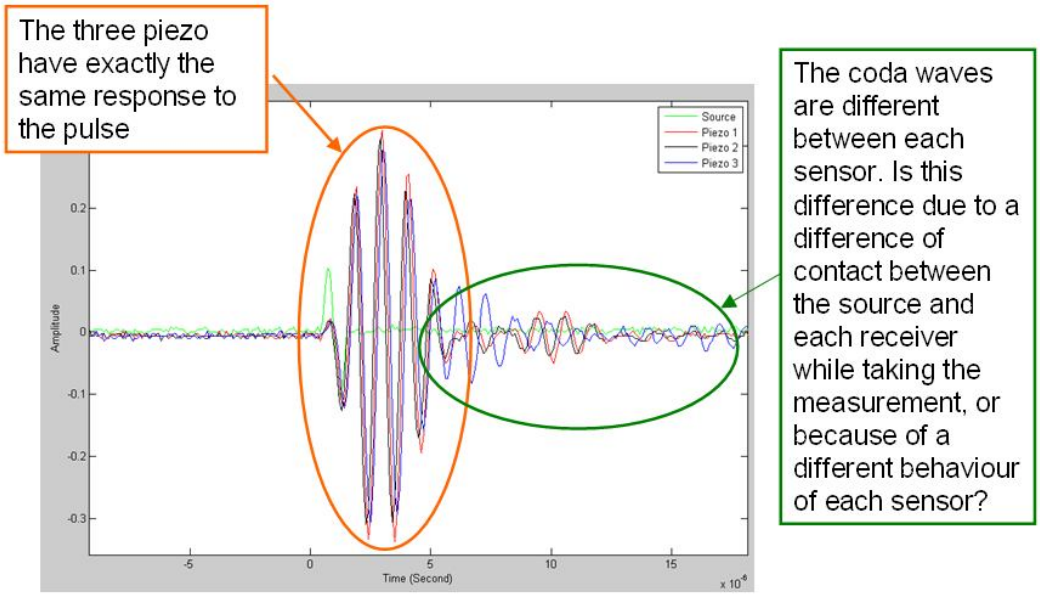

Figure 57 –In green, the electric excitation of a single sine pulse. The other curves are related to each transducer used as receiver; they all show the same characteristics for first arrival detections, but differ in their coda.

A deconvolution may be included in the processing in order to remove this non-property signature. However, this characteristic inherent to piezo-crystal polarity can also be turned into an advantage, by naturally filtering side reflected waves (i.e, waves reflected at the core/sleeve interface), and only recording reflected waves.

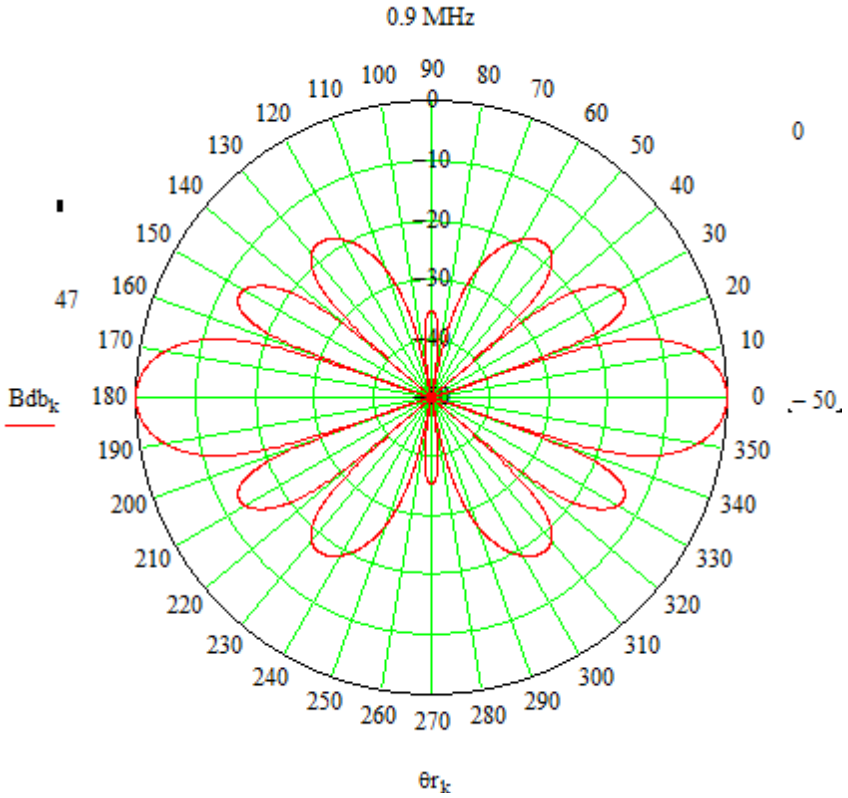

Figure 58 – Modelled Beam pattern for the PET Transducers at 0.9 MHz (Source: Envision). It represents the ability of a piezo-crystal to detect a wave coming from a direction. this grpah shows that a wave arriving at zero-incidence angle on the piezo-crystal will be recorded at its full amplitude, but will also be undetected if arriving at a 20 degrees angle of incidence.

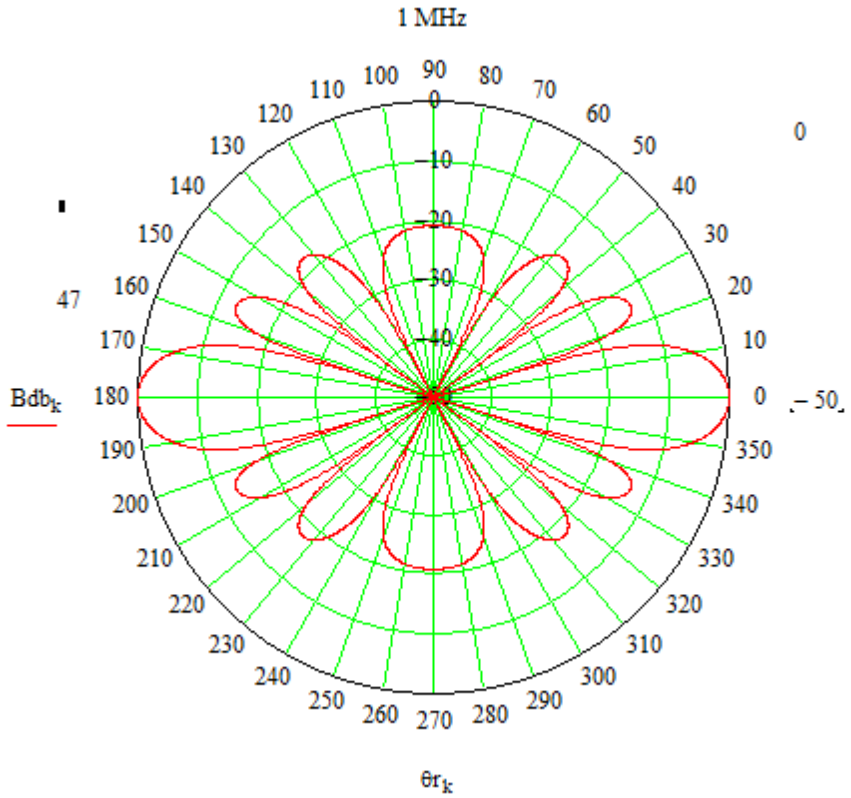

Figure 59 - Modelled Beam pattern for the PET Transducers at 1 MHz (Source: Envision)

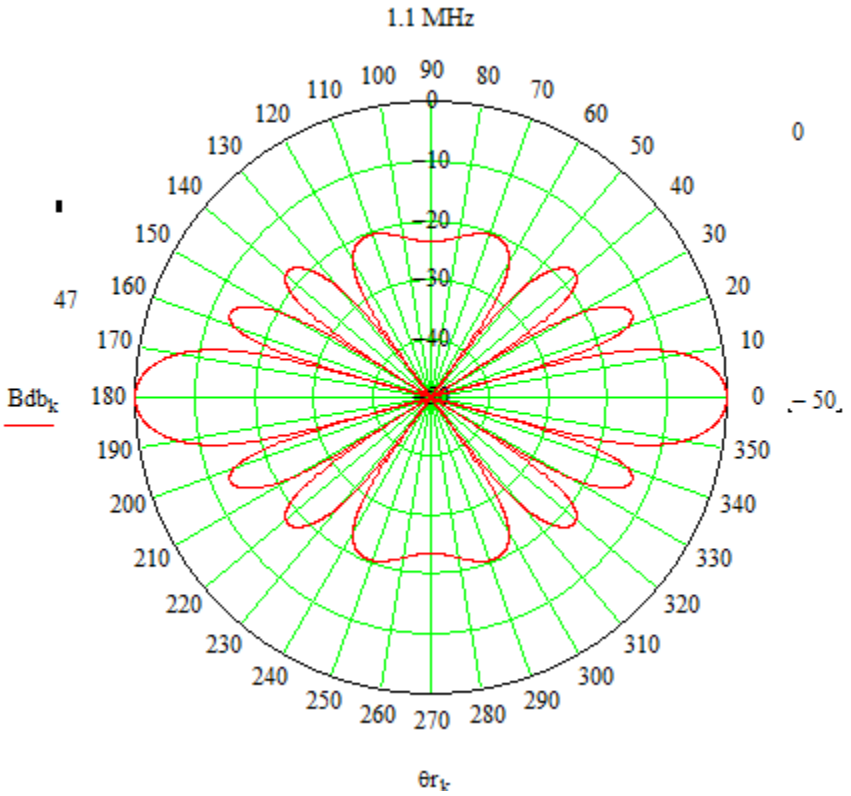

Figure 60 - Modelled Beam pattern for the PET Transducers at 1.1 MHz (Source: Envision)

3.3.6. Description of the National Instrument apparatus

Implementation of the measurements using piezo-transducers requires both source generator and recorder. After having checked the sensor performances with an oscilloscope, the next step was to assemble equipment in order to get a first automated prototype of the sensitive sleeve (see Figure 62). Block diagrams representative of the assemblage are depicted in Figure 61:

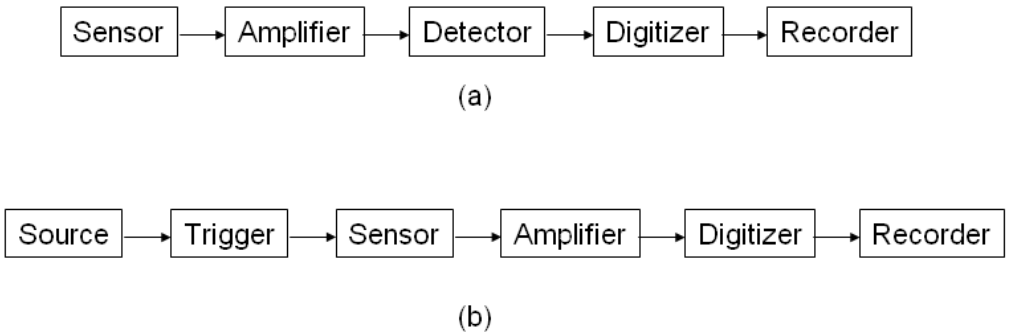

Figure 61 – Classical block diagrams of a recording chain

The complex transducers response pattern in time domain has led to decline the use any amplifier, for not adding a phase to recorded signals. The result is a weak signal lost in noise, which waveform delineation is extracted from noise with the extensive use of the stack; this technique's implementation is detailed in the paragraph dedicated to the NI (NI for National Instruments) kit programming.

The composition of this controlling equipment is:

1. 16 to 24 Bit digitizer: NI PXI 5922 card
2. 16 Bit 100 MS/s source: NI PXI-5421 card

3. 5-slot NI PXI-1033 Chassis for assembling the cards
4. NI PXI-Express Card 8360 for controlling devices from laptop

Digitizer's specifications are (Source: National Instruments):

- 24 Bit resolution to 500kS/s, ranging to 16 Bits at 15 MS/s
- 2 simultaneously samples channels
- Up to -114 dBc SFDR
- -120 dBFS rms noise
- Integrated antialias protection for all sampling rates
- Deep onboard memory -8MB/ch standard, up to 256 MB/ch

Finally, source's specifications are (Source: National Instruments):

- 12 Vpp into 50 ohms load
- Up tp 400 MS/s effective sampling rate with interpolation
- 91 dBc close-in SFQR and -62 dBc THD at 10 MHz
- 8, 32, 256 or 512 MB of onboard memory
- -148 dBm/Hz average noise density
- Optional 16-bit LVDS digital pattern output

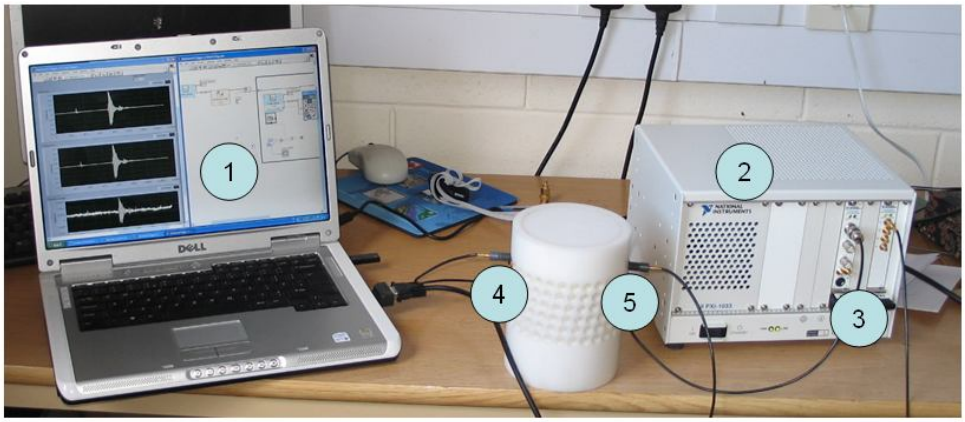

1. Controlling and recording computer
2. NI chassis
3. Source and digitizer cards inserted in the chassis
4. Piezo-transducer used as a source
5. Same piezo-transducer used as a receiver

Figure 62 – Picture of the NI kit assemblage

3.3.7. Sample preparation

Device presented in Figure 30 cored monolithic structures (Diameter: 100 millimetres, Length: 150 millimetres). Cores are cut along their length, and halves of two different lithologies are assembled (in this case, Sandstone and Coal) in order to provide a bilithic structure (like in Figure 52).

No signal was detected through sandstone and no technical solution has tackled coupling related problems between lithologies yet; this coupling is representative of the roof's coupling in Daw Mill's coalmine within this thesis.

After saturating the core with water using a vacuum pump, the sample is stored in a vessel filled with water.

3.3.8. Testing procedure

During the test, the sample, piezo-components and sensitive sleeve remain underwater.

A typical testing procedure on monolithic cores, in section A-A (see Figure 54), was:

1. to place at 0° the piezo-component used as a source
2. to place a second piezo-component used as a receiver at k^{th} X 12° (k^{th} is an integer incremented during the acquisition procedure)
3. firing source
4. recording first arrival with the receiver
5. removing the the piezo-receiver
6. incrementing to the k^{th} position
7. if k^{th} X 12° ≤ 348°, go back to step 2

The result of this type of acquisiton is shown in figure 63, with traces placed at their respective offset.

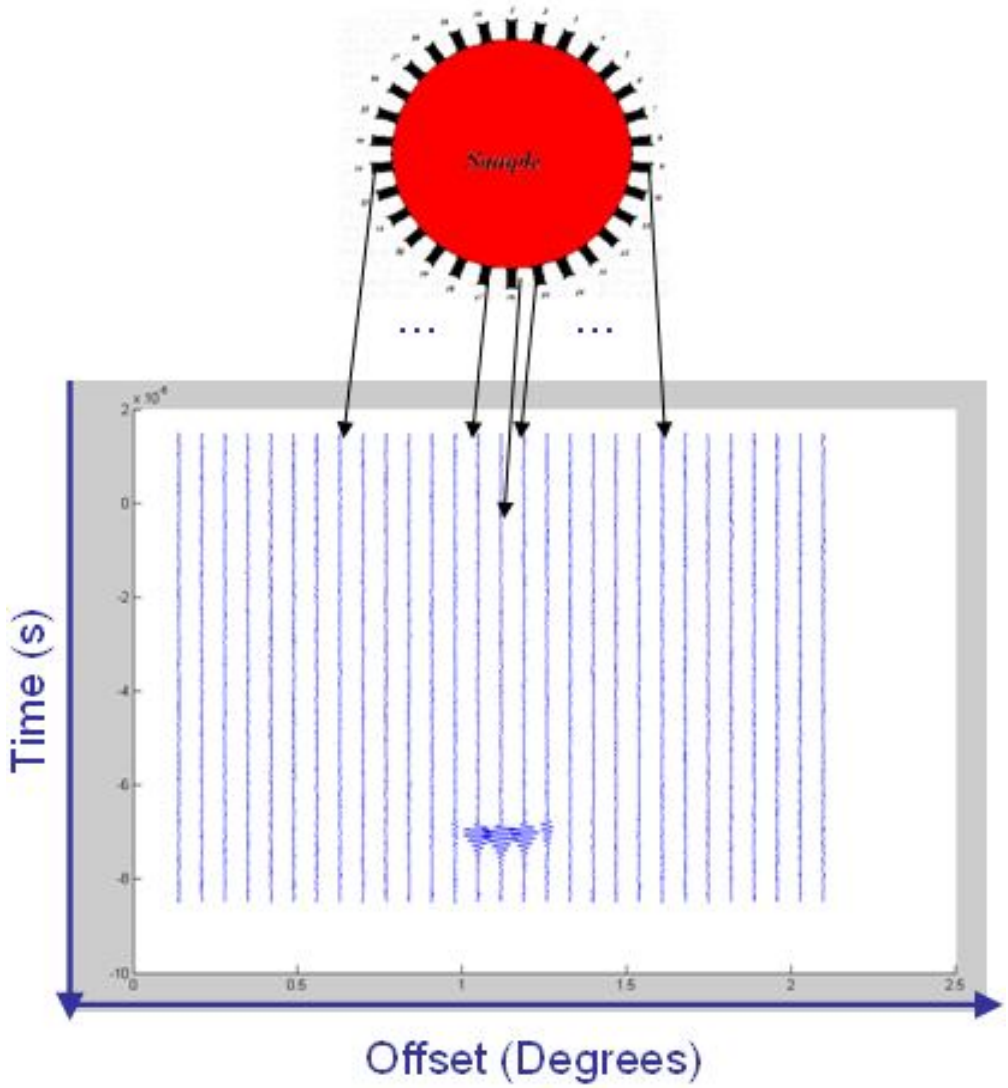

Figure 63 – Principle of a sensitive sleeve record's projection.

3.3.9. NI Kit Programming

The National Instrument kit implements the block diagram shown in Figure 65.

The presence of a preceding pulse (presumably due to bad connectors' isolation, see Figure 64) marks the exact time of the source's excitation (under the hypothesis of electricity's infinite velocity under water, compared to ultrasonic velocities). Trigger's initialization targets this feature's detection.

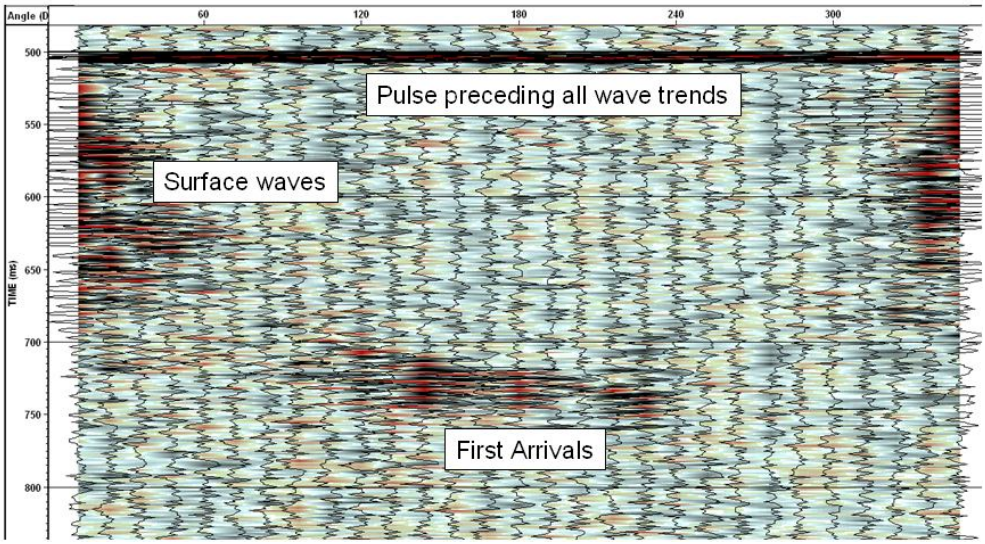

Figure 64 – Sensitive sleeve test made on coal. While all wave trends have been identified, preceding pulse nature has been more difficult to determine.

The detected signal is stored in the computer. Afterwards, the same signal is periodically sent, and every newly recorded trace is added to the initial one. This stack progressively improves the SNR (Signal to Noise Ratio).

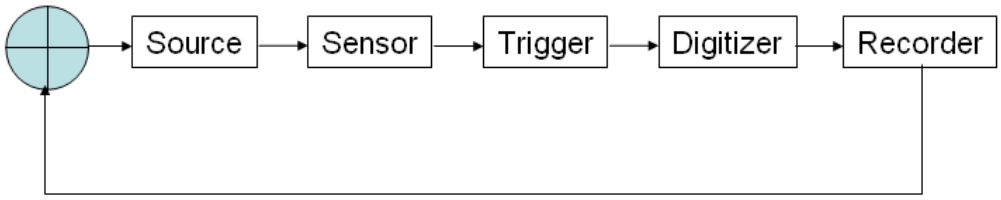

Figure 65 – Block diagram of the stacking implementation

SNR improvement is theoretically proportional to the root mean square of the stacked trace number, i.e. there is a direct link between the number of traces and SNR improvement. For practical purposes, laboratory conditions limit this improvement due to:

1. Pulse trigger precision
2. The extra time required for implementing the stacking

The limitation on the trigger precision (equal to 4e-7 second) leads to high frequency noise, by giving a toothed aspect to stacked traces.
The second limiting condition resides in the extra-time needed for recording the same trace many times; the more traces recorded, the higher the probability of

introducing random external noise; an example is given in Figure 66, where fire doors neighbour my office and are randomly slammed by passers-by. These two considerations have led to limitations in the number of stacks.

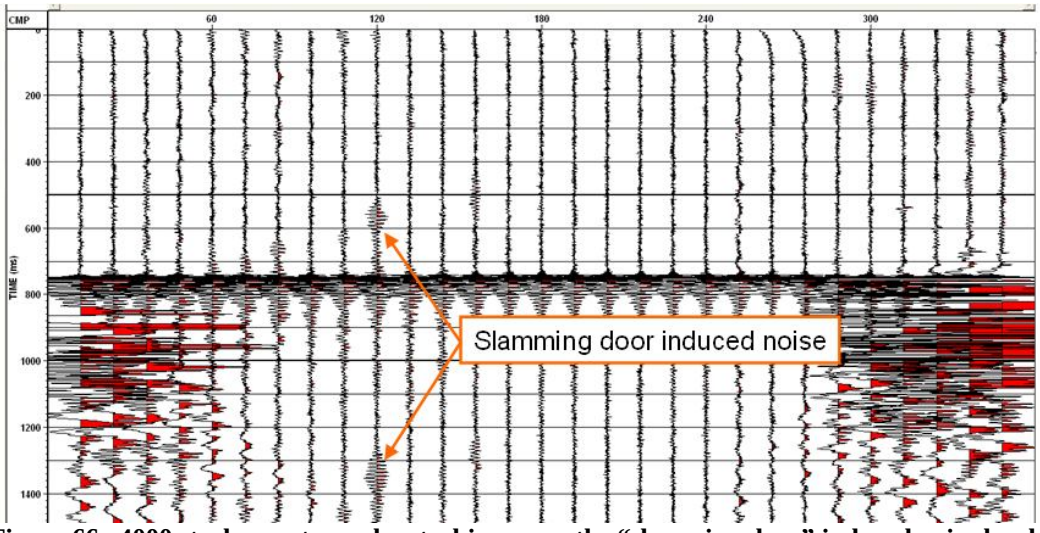

Figure 66 –4000 stacks per trace: by stacking once, the "slamming door" induced noise has left a persistent feature.

Evaluation of SNR evolution with number of stacks (see Figure 67, 68and 69) led to determine a limit of 1000 stacks per recorded trace (Figure 69), beyond which further improvement is not detected.

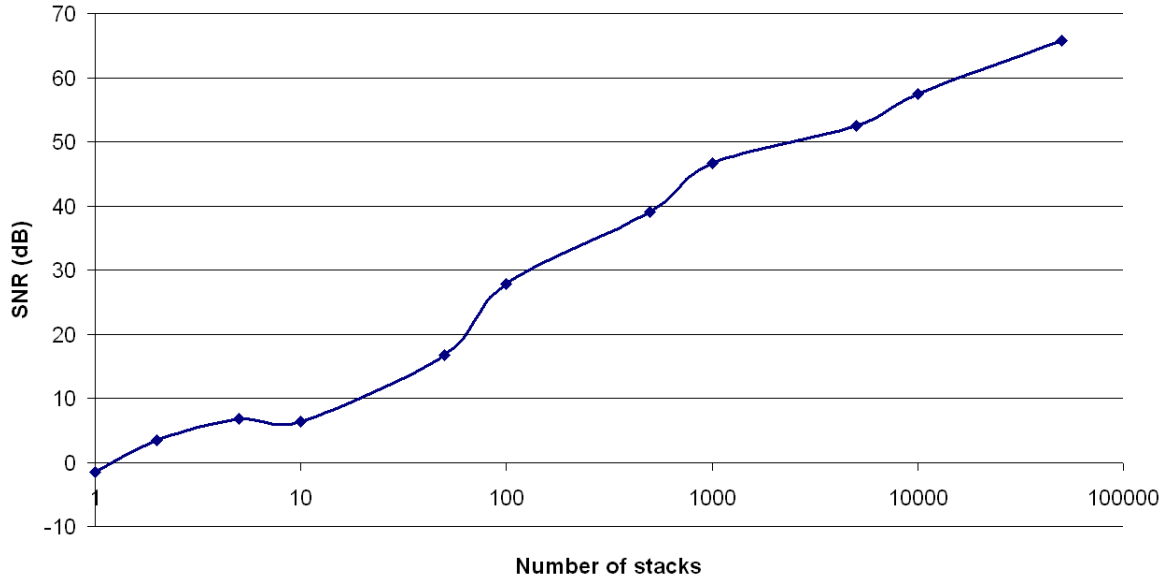

Figure 67 – SNR variation with number of stacks.

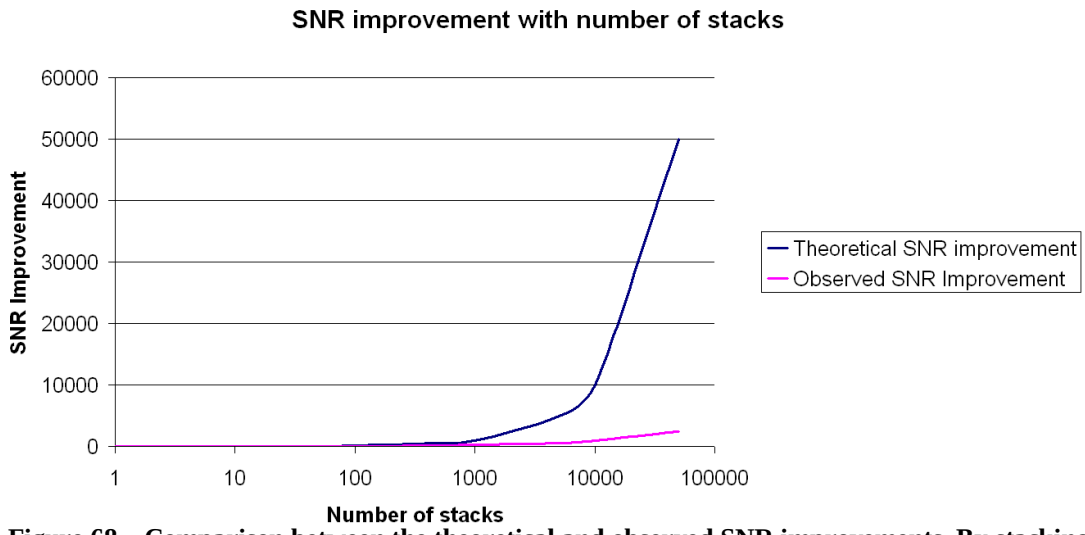

Figure 68 – Comparison between the theoretical and observed SNR improvements. By stacking N traces (N being an integer), the signal is multiplied by N. The same process doesn't stack coherently the noise, whcih amplitude only raises by the square root of N. As a consequence, the theoretical SNR improvement is equal to the ratio between signal amplitude improvement by the noise amplitude improvement; the theoretical SNR improvement is then equal to the square root of the number of stacked traces.

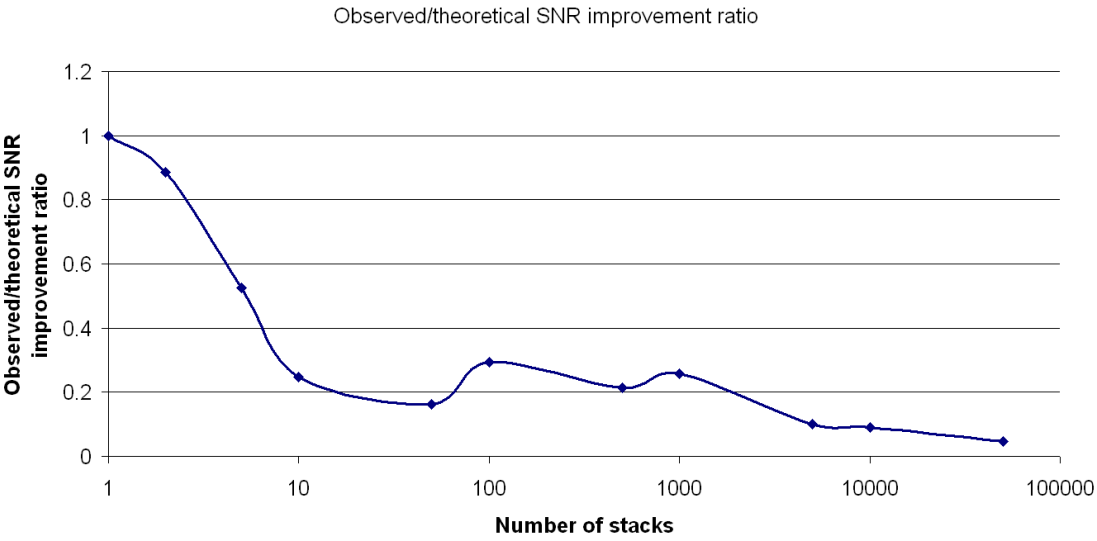

Figure 69 – When observing the ratio between the observed and theoretical respective SNR improvements, it becomes clear that the time spent beyond 1000 stacks does not improve the ratio.

3.3.10. Coal

The combination of water saturation and stacking has proven results on coal. Without these methods the recorded signal through coal was poor (see Figure 70). Water saturation of the pore space allowed the observation of propagated waves despite an unsatisfying SNR, and perfectly delineated the first arrival hyperbola when combined with stacking (see Figure 71).

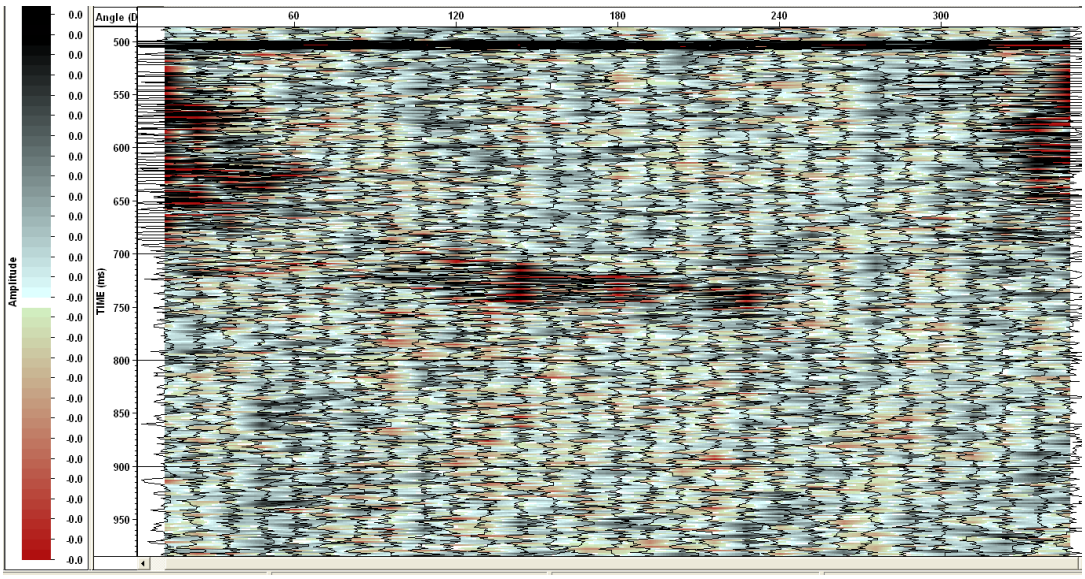

Figure 70 - Sensitive sleeve test made on coal, under water.

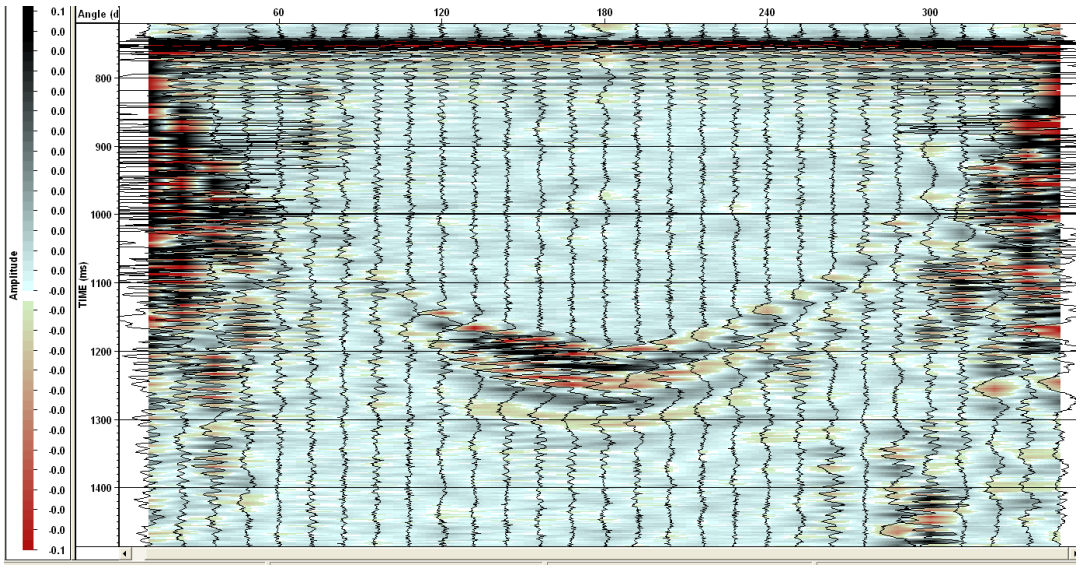

Figure 71 - Sensitive sleeve test made on the same coal sample, under water. The extensive use of stacking has improved the SNR, and helped in delineating the first arrival hyperbola.

3.3.11. Sandstone

After having successfully tested coal samples with the sensitive sleeve prototype, a good result was expected on sandstones.

Unfortunately, a combination of:

1. low power source
2. unstressed test
3. sandstone grains generating dispersion
4. attenuation generated by pores

has led to an inability to record any wave through sandstone. Figures Figure 72, 73 and 74 show preceding pulse presence (shown in Figure 64) , but no trace first arrival hyperbola (as in Figure 71).

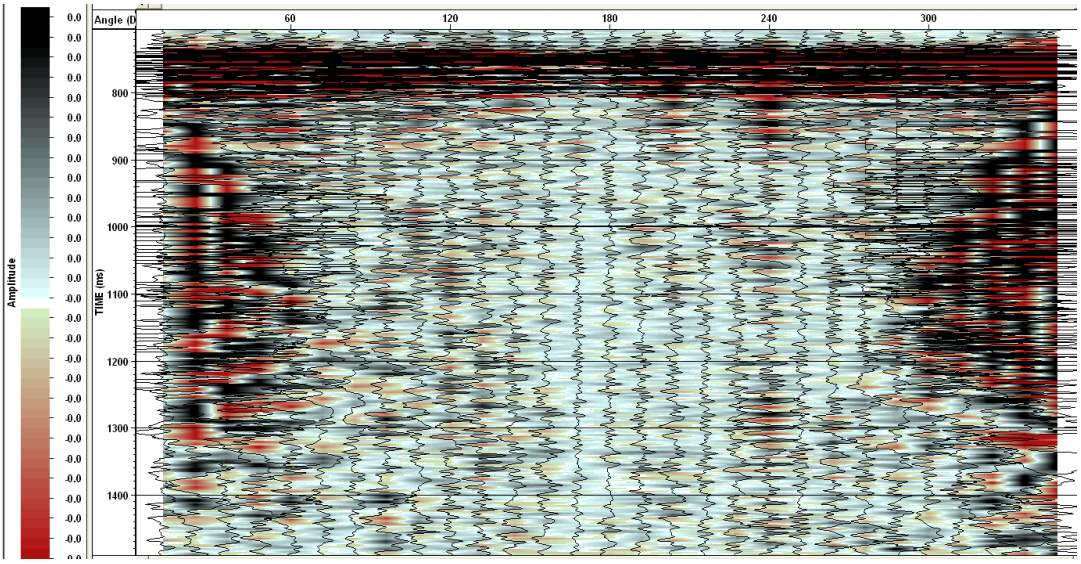

Figure 72 – Test on Sandstone, 100 stacks. The observed random noise leads to the conclusion that the SNR is insufficient; more stacks are required.

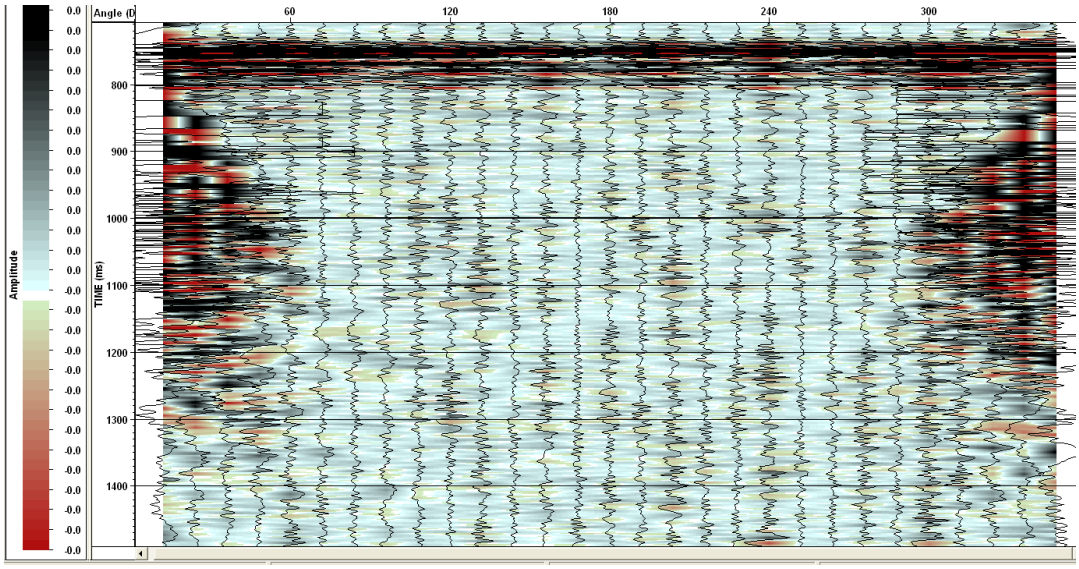

Figure 73 – Test on the same sandstone sample, 400 stacks. As no signal has been delineated, further attempts with more stacks have been implemented.

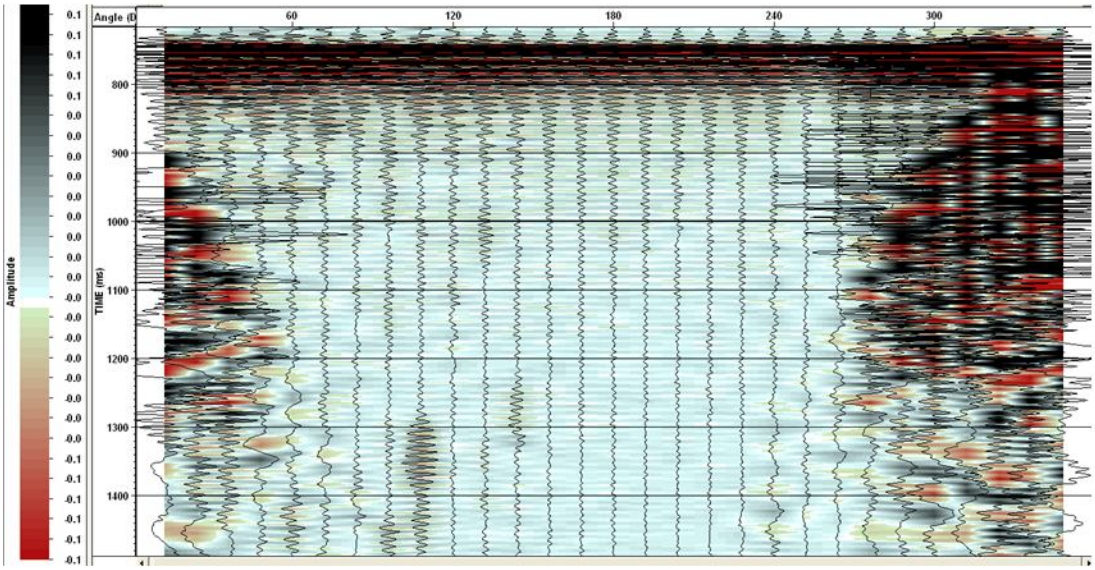

Figure 74 - Test on the same sandstone sample, 40000 stacks. The number of stacks is so high that traces have taken a toothed aspect. By seeing the apparent SNR improvement, it can be concluded that no signal has been observed through sandstone, the ultrasonic waves being dispersed by grains, and absorbed by the air encapsulated in the non-connected pores.

3.3.12. Conclusion and further recommendations

The second part of this chapter has presented a triaxial cell modification, aimed at recording amplitude variations with offset in the laboratory. It consists of an array of sensors placed around a sample. Due to the requirement for small-size piezo-crystals, the array density indirectly brought the following problem: the smaller a piezo-crystal is, the weaker the power output. Attenuation within samples may also prevent the waves being received. It was therefore important to obtain a good resolution through a respectable array density and then to compensate the small size (and power) of piezo-crystals by limiting the attenuation by:

- saturation of sample pores with water
- application of a stack in order to improve the SNR

This combination was successful with coal but showed an inability to record any wave through sandstone. The wave traces were of insufficient energy to cope with the attenuation, even if they were stacked and therefore the bilitihic experiments did not produce any meaningful results. Further development of the power of the transducers is required.

Porosity is responsible for an important attenuation at 1MHz. On top of a porosity saturation/trace staking combination, a primary solution could be a frequency reduction; a solution made at the cost of resolution and source Near Field contribution. But a 1MHz frequency is already critical. In order to prove this, consider a 2500 m/s velocity in coal; at this frequency, it would mean that the propagating wavelength would be:

$$\lambda = Velocity / f = 2500/10^6 = 0.0025 \quad m$$ **Equation 132**

The consequence for the beam angle is:

$$\theta = \lambda / d = 0.0025 / 0.008 = 0.3125 \text{ radians} = 17.9 \text{ degrees.}$$ **Equation 133**

This means that the beam is wider than the angle separating two different sensors (12 degrees, as shown in Figure 54), and therefore the piezo-components do not provide the required resolution.

Two proposed solutions for further development are:

1. the development of a piezo-crystal with sufficient power and beam-width
2. a new architecture of the sensitive sleeve, spacing piezo-crystals every 18 degrees.

The second solution would comply with beam width characteristics of the current piezo crystals (see equation 133), and use wider piezo-crystals fired with more powerful sources; a solution to attenuation must be found before considering any AVO calibration from laboratory.

The probability distribution of elastic properties of mudstone, sandstone and coal samples coming from Daw Mill were developed by:

- an automatic picking algorithm
- a recalibration of data from laboratory to seismic wavelength scale.

Chapter 4.MODELLING

4.1. INTRODUCTION

This chapter investigates the numerical modelling of the data determined from the laboratory tests. The objective is to determine if a model can discriminate sandstone from mudstone roofs over coal seams, in the region of Daw Mill. The results will be used in Chapter 5 to compare the model with the AVO results obtained from this chapter.

The modelling work is presented as follows:

1. Sensitive sleeve modelling
2. Thermoelasticity and wave propagation in finely layering media
3. Seismic interpretation, ray tracing and AVO modelling

4.2. SENSITIVE SLEEVE MODELLING

4.2.1. Introduction

The first part of this chapter presents the numerical model of the sensitive sleeve, developed with the modelling software COMSOL MULTIPHYSICS. Its implementation for different offsets laid the basis for a further comparison with real data.

The structure of this first section is:

1. Introduction to Comsol Multiphysics software
2. Development of the Graphical User Interface
3. Model sensitivity
4. Presentation of the modelled results
5. Presence of spherical waves
6. Conclusion

4.2.2. Introduction to Comsol Multiphysics Software

Comsol Multiphysics software is a Finite Element Analysis Simulator, based on codes developed by Germund Dahlquist, Royal Institute of Technology (KTH), in Stockholm. This engineering tool performs equation-based multiphysics modelling, for example, it is possible to simulate Sea Bed Logging acquisition by coupling flow in porous media with an electromagnetic field.

This software is not specialized for seismic modeling, and the author determined the most adequate toolbox for the given task to be the Structural Mechanics Module, which also provides pre-coupled physics such as thermoelasticity or piezoelectricity.

The modified triaxial cell model can furthermore benefit from the Optimization Lab (from Comsol Script) to optimise the modelling of diverse engineering designs.

4.2.3. Presentation of the Graphical User Interface (GUI)

The development of the Graphical User interface required the combination of Comsol Script and the Structural Mechanics Toolbox. This allows users to control the parameters related to source and sample mechanical properties.

Source parameters are, respectively:

1. Offset
2. Excitation Frequency
3. Excitation duration

Sample mechanical properties are:

1. Young's Modulus
2. Poisson's ratio
3. Density

It is proposed that the future development of this interface will include:

1. synthetic tests on bilithic structures
2. 3D modelling
3. variation of piezo-crystal behaviour and response under load

The different steps for developing the model with Comsol multiphysics are:

1. Design of the geometry
2. Choice of the Physics (for example, electro-magnetism or acoustic), and definition of the boundary conditions
3. Definition of the physical properties of each material
4. Computation of polygon meshes
5. Computation of the model.

Comsol Multiphysics provides computer-aided design tools for the first step, and for choosing the appropriate gridding system; if too coarse, the mesh will lead to a poor resolution, if too thin, it will generate a high frequency noise not related to the physics under study.

The chosen physics are computed with the Structural Mechanics Module of Comsol multiphysics, which includes wave propagation in elastic media and piezo-electricity. The boundary conditions between materials are the ones defined by the Zoeppritz's theory, mentioned in the second chapter.

The modelled piezo-crystal, excited by an electrical current, fires an acoustic wave at the boundary of the sleeve.

The different steps have been rationalised with Comsol Script (a module of Comsol Multiphysics), through a graphical user interface (see Figure 75). The code is given in Appendix 7.4.

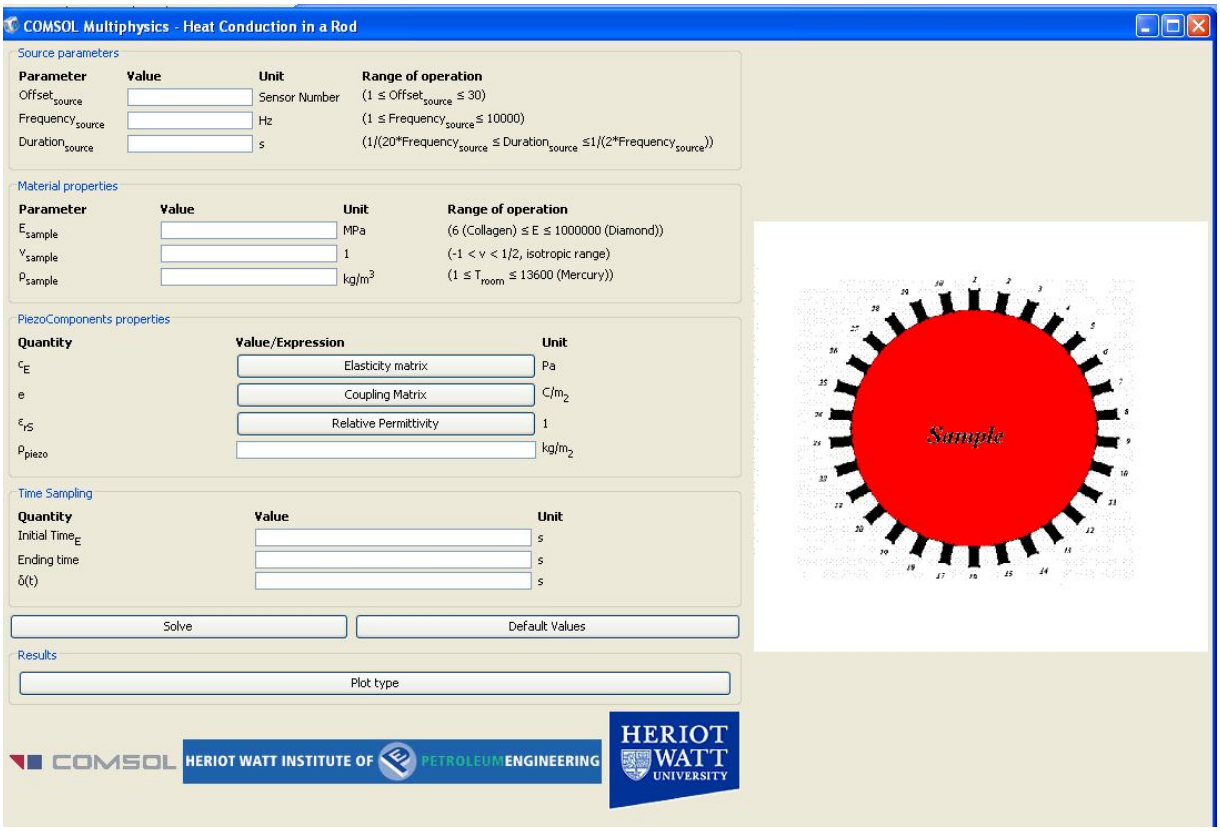

Figure 75 – Overview of the sensitive sleeve prototype

4.2.4. Modelling results

The modelling investigated:

1. shot offset
2. roof mechanical properties (i.e: Young's Modulus, Poisson's ratio and density)

The modelling was 2 dimensional and reproduced section A-A of the sleeve (figures 53 and 54). Coal, Mudstone and Sandstone properties were the mean values determined in chapter 3, in tables 52, 57 and 61. Section A-A having 30 piezo-components and modelling for two different types of roof (Sandstone and Mudstone) has led to 60 different computations.

	Vp(m/s)	Vs(m/s)	Density(kg/m^3)
Mudstone	3770	1532	2415
Sandstone	2695	1775	2493
Coal	2290	1356	1415

Table 61 –Mean rock properties determined in the laboratory

The amplitude differences observed between figures 76 and 78, and between figures77 and 79, qualitatively show the potential ability of AVO to discriminate Mud from Sand-roofs over coal seams.

Unfortunately, the absence of data collected from the sensitive sleeve does not allow a comparison between laboratory and synthetic data. The results reported in this thesis are for all offsets of section A-A and include:

1. a time-lapse sequence of figures showing wave propagation within monolithic and bilithic structures (Figure 80 is an example).
2. Seismic-like plots (figures 76, 77, 78 and 79).

Moreover, reflection/transmission amplitude differences observed between Sandstone/Mudstone over Coal raises an additional question: even if solutions to the technical issues mentioned in the conclusions of the last chapter enable the recording of signals through bilithic structures, what would the consequence of attenuation on reflection/transmission coefficients in particular be, and on AVO calibration from laboratory in general?

The inclusion of attenuation in this model could begin to answer the question.

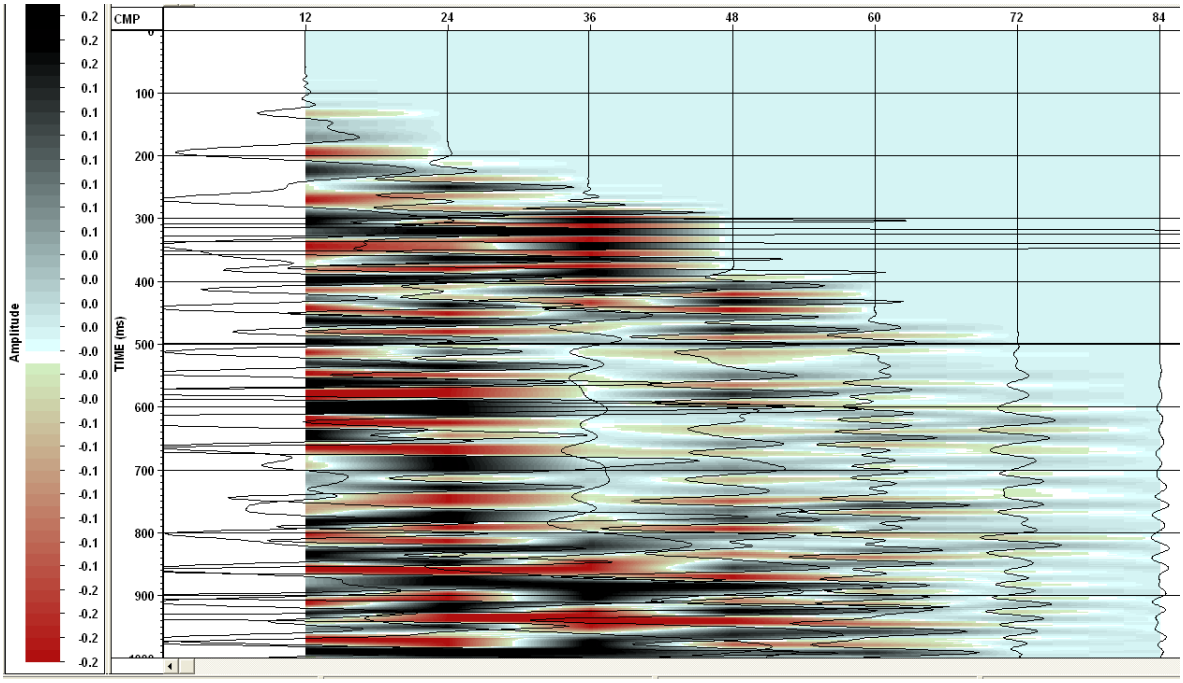

Figure 76 – Synthetic CMP (Common Mid-Point) gather from the sensitive sleeve model, mudstone roof case

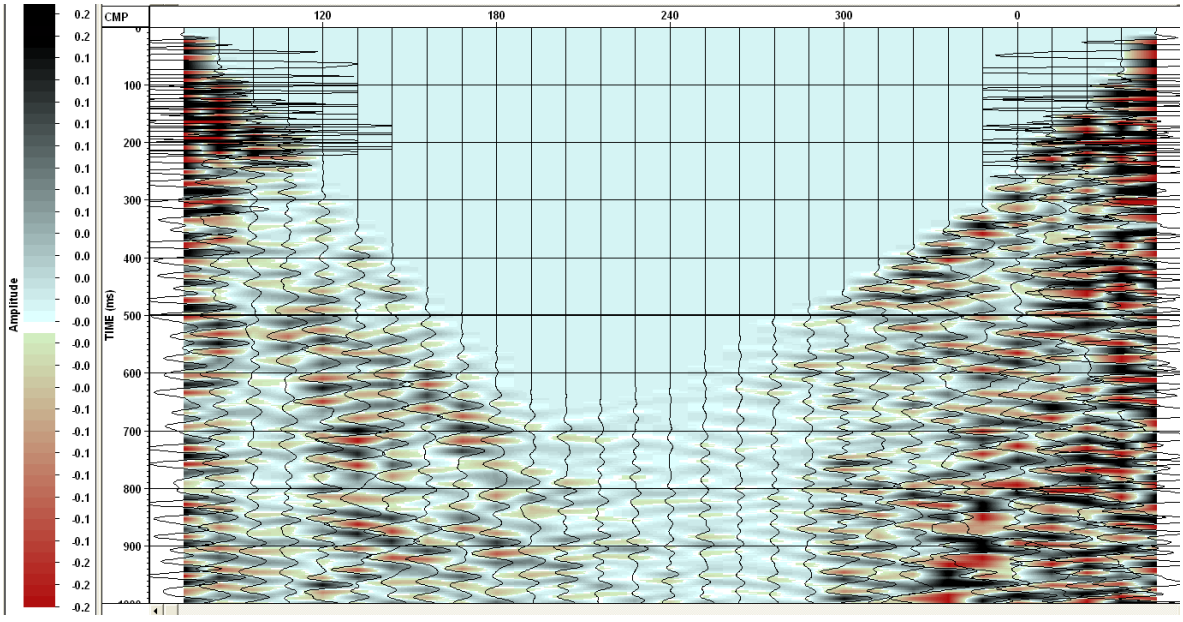

Figure 77 - Synthetic shot gathers, 60 degrees angle incidence, Mudstone Roof

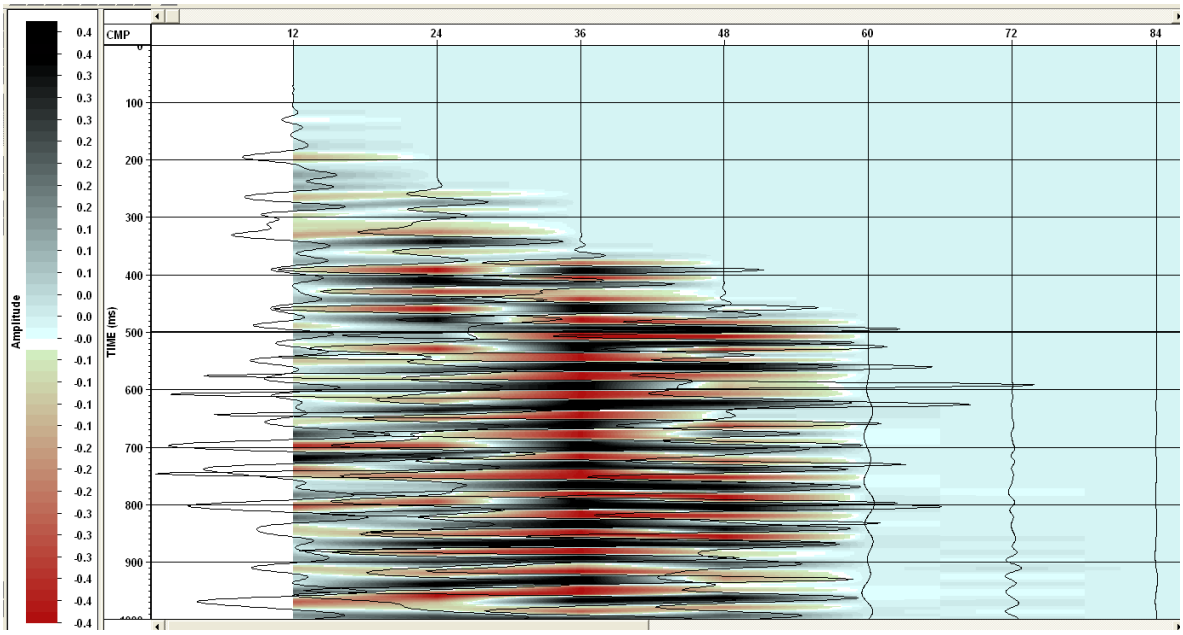

Figure 78 - Synthetic CMP gather from the sensitive sleeve model, sandstone roof case

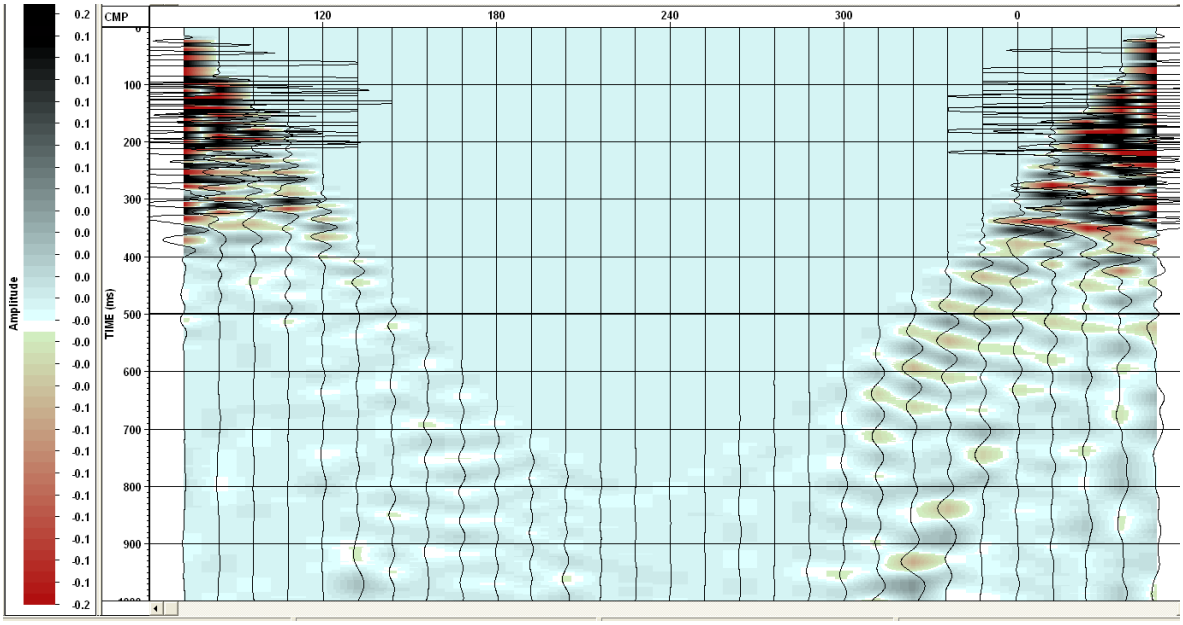

Figure 79 – Synthetic shot gathers, 60 degrees angle incidence, Sandstone Roof. While the model does not take into account any attenuation, it seems to indicate that sandstone elastic properties are troublesome for amplitude transmission and propagation. This observed feature can potentially be linked to the problems encountered in the laboratory: simply testing a sandstone sample in the modified cell under the application of a stress may not solve the problem.

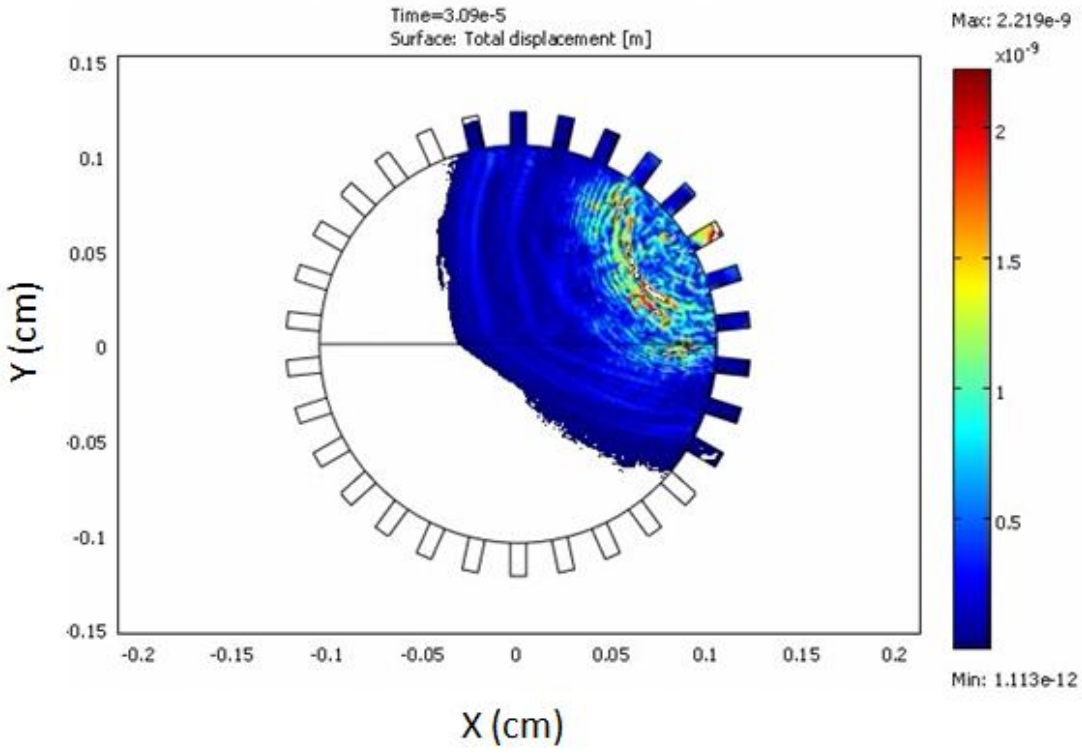

Figure 80 – Example of a wave propagation sequence in the modified sensitive sleeve. The upper half cylinder is made of mudstone and the lower half cylinder is made of coal.

4.2.5. Presence of spherical waves

Modelling with Comsol Multiphysics has also led to a reconsideration of the direct applicability of AVO theory to the sensitive sleeve. Shots observed at different times and offsets (see figures 81, 82 and 83) underline the presence of a spherical wavefront in the sample. Figure 82 depicts a reflected spherical wave, while AVO theory considers the incident and reflected waves to be plane waves; Aki and Richards (2002) have defined a second theory based on spherical wave migration. This difference between spherical wavefronts (laboratory) and plane waves (seismic) may lead to a non-straightforward calibration of AVO from laboratory.

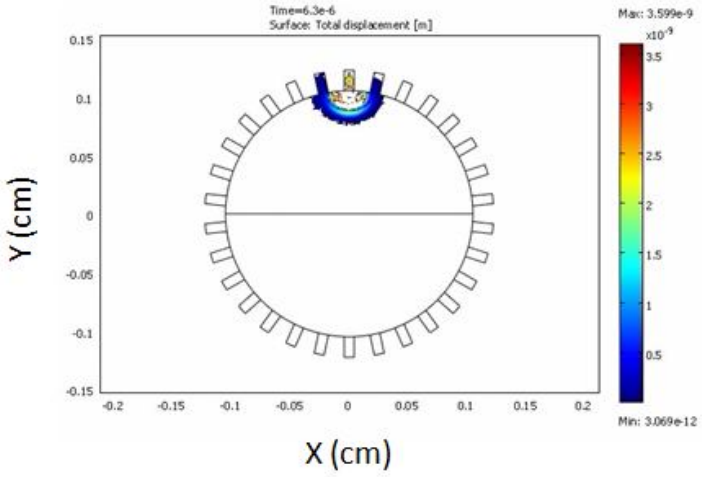

Figure 81 – Shot in the sensitive sleeve; the front wave is spherical

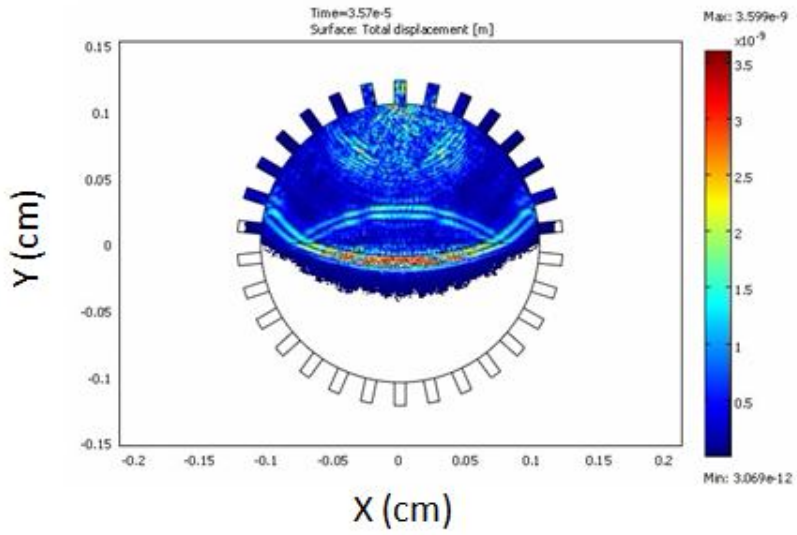

Figure 82 – The reflection clearly shows that spherical waves cannot be locally considered as plane while reaching the interface.

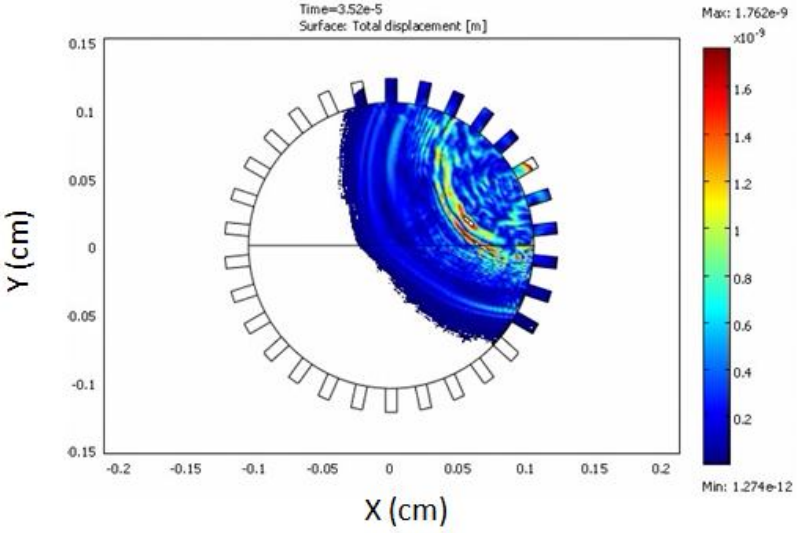

Figure 83 - Waves must also be considered as spherical with non-zero offset shots

4.2.6. Conclusion

The objective of this section was to numerically model the sensitive sleeve, and initially, make comparisons with real data coming from the modified Hoek Cell.

The extensive modelling implemented for reproducing various shot locations (more than 60) is a strong basis for any eventual development of the sensitive sleeve in future. The most significant results are the difference in reflection/transmission coefficients between Mud and Sand-roofs (see figures 76, 77, 78 and 79), a feature indicating a potential ability of AVO to discriminate these two lithologies over a coal seam. This qualitative observation will be quantitatively confirmed in the third part of this chapter.

However, this positive answer does not necessarily guarantee any AVO calibration from laboratory will be valid; attenuation coupled to spherical wavefronts may reduce differences in reflection/transmission coefficients between these two roof lithologies. Modification of the triaxial cell is required for further investigation of these effects.

4.3. THERMOELASTICITY AND WAVE PROPAGATION IN FINELY LAYERED MEDIA

4.3.1. Introduction

The second part of this chapter investigates modelling of:

- finely layered elastic media
- thermoelastic media.

These models show the non-negligible influence of these physical phenomena on dispersivity and the upscaling requirements discussed in section 3.2.7.

These models have also been used to assess the errors associated with the automatic arrival picking algorithm developed in section 3.2.6.

The structure of the second part of this chapter is as follows:

1. Introduction
2. Effect of Thermoelasticity
3. Wave propagation in finely layered media
4. Accuracy of the Wave Picking Algorithm
5. Conclusion

4.3.2. Thermoelasticity

The literature review in section 2.4.7 introduced the damping effects generated by different physical phenomena. Section 2.4.6 focuses on a physical phenomenon coupling deformation and temperature fields, thermoelasticity, as described by the Neumann-Duhamel system:

$$\nabla^2 T - \frac{1}{\chi}\frac{\partial T}{\partial t} - \eta div\left(\frac{\partial u}{\partial t}\right) = -\frac{Q}{\chi} \qquad \textbf{Equation 134}$$

$$\mu\nabla^2\vec{u} + (\lambda + \mu)grad\left(div(\vec{u})\right) + \vec{X} - \gamma grad\left(\vec{T}\right) = \rho\frac{\partial^2\vec{u}}{\partial t^2} \qquad \textbf{Equation 135}$$

Where:

- λ and μ : Lame's parameters
- ρ : density
- $\vec{X}$:body the forces
- γ :dilatation coefficient
- λ_0 :coefficient of internal heat coefficient
- W : amount of heat per unit of volume
- C : specific heat
- T_0: reference temperature
- $\chi = \dfrac{\lambda_0}{\rho C}$
- $Q = \dfrac{W}{\rho C}$
- $\eta = \dfrac{\gamma T_0}{\lambda_0}$

2D models depict the section (along the length) of an average cylindrical sample:

1. diameter: 36 millimeters
2. length: 72 millimeters

and reproduce the dynamic test depicted in section 3.2.2: a 1MHz ultrasonic wave is generated on top of a core, and recorded at its bottom. Modelling is computed for coal in two cases:

1. elastic case
2. thermoelastic case

while properties given to a 85% carbon content coal (source: Van Krevelen (1993)) are:

- E=4.5*10^9 Pa
- $\nu = 0.345$
- ρ =1270 kg/ m^3
- C_v =0.5 W/(m.K)
- α = *10^(-4) K^{-1}

Section 2.4.6 presents a dimensionless parameter defined by Boley and Weiner (1960), used for assessing the negligibility of thermo-elastic damping:

$$\delta = \frac{(3\lambda + 2\mu)^2 \alpha^2 T_0}{\rho^2 C_v V_P^2}$$ **Equation 136**

For coal, $\delta = 1375.4$. According to Boyley and Weiner, thermo-elastic damping can not be neglected for wave propagation in coal; modeling corroborates the theory by displaying important wave velocity differences between elastic and thermo-elastic cases (respectively shown in figures Figure 84 and Figure 85).

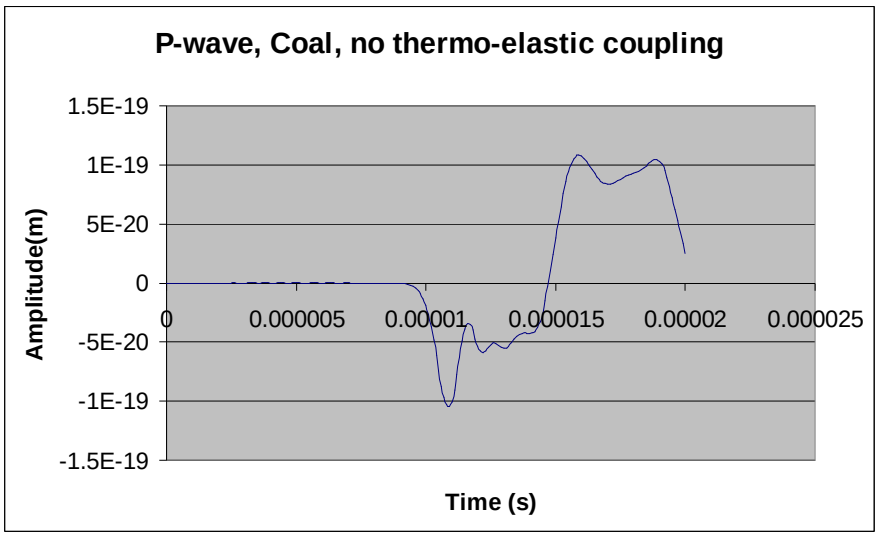

Figure 84 – Elastic P-wave propagation in coal.

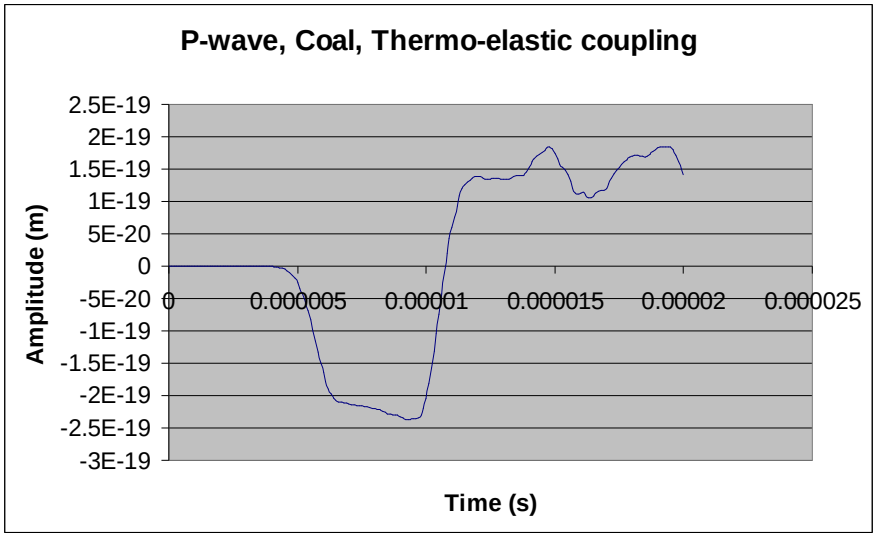

Figure 85 – Thermoelastic P-wave in coal. Comparison with Figure 84 shows a significantly faster wave

This example is just a special case of a general theory presented by Zener (section 2.4.7). Section 3.2.7 proposes solutions for handling the consequences of coupled physics on velocity, but not on reflection coefficients. Future work is required to investigate this aspect of wave transmission through rock.

4.3.3. Wave propagation in finely layered media

This section presents numerical models investigating Hovem's work, presented in section 2.4.5.

Models are 2D sections of cores along their length:

- diameter: 36 millimeters
- length: 72 and 144 millimeters

and depict coal cores as composite successions of two coal macerals (coal has been described as a layered media in paragraph 2.4.2).

The two models have the same:

- maceral mechanical properties
- periodical sucession of these two macerals
- diameter
- 1MHz propagating wave

The difference between the two models resides in the microlayer thicknesses. Let t_1 be the thickness attributed to a first maceral, and t_2 the thickness attributed to the second. In both models, the t_1/t_2 ratio is identical, but the thicknesses in one model is twice than in the other. Depending on the model, the same 1MHZ wave will propagate by a different mode. The mode, defined by Hovem (1995) for the first and second model respectively:

1. For low frequencies (large ratios of wavelength to layer thickness), the layered structure behaves as an effective medium; the velocity approaches the effective medium velocity, the propagation is dispersive, and no loss occurs.
2. For higher frequencies (small ratios of wavelength to layer thickness), the layered structure is described by time-average velocity; waves are evanescent, suffer scattering loss at each interface, and travel at the time averaged velocity.

The Comsol Multiphysics models confirm Hovem's theory by showing these two different propagating modes;

1. a wave propagating as in an effective medium (Figure 86)
2. a wave with evanescent propagation patterns (Figure 87 and Figure 88)

Theoretical confirmation of these two propagating modes raises two questions from the same observation: if seismic waves propagate at an effective velocity, and ultrasonic waves at a time-averaged velocity:

- Is an extra-calibration needed for comparing data at different scales?
- Are the laboratory data on anisotropy applicable to seismic scale?

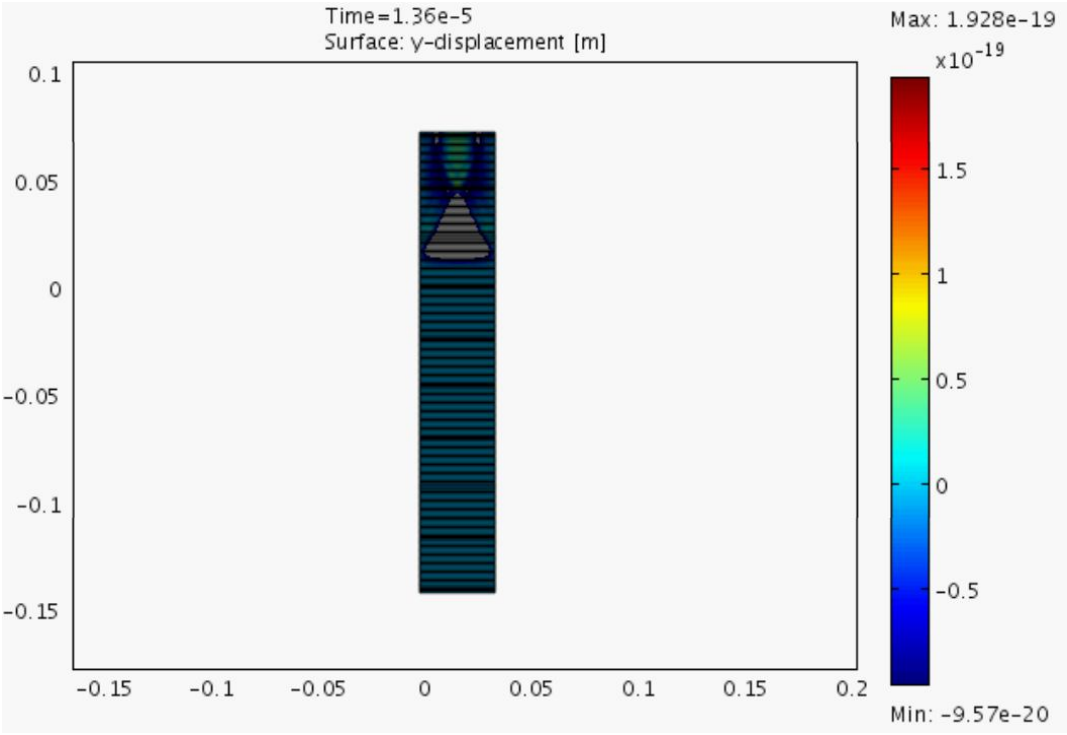

Figure 86 – First model of ultrasonic waves propagating in finely layered medium. The propagation was similar to an isotropic and homogeneous material because the wave is propagating as in an effective medium.

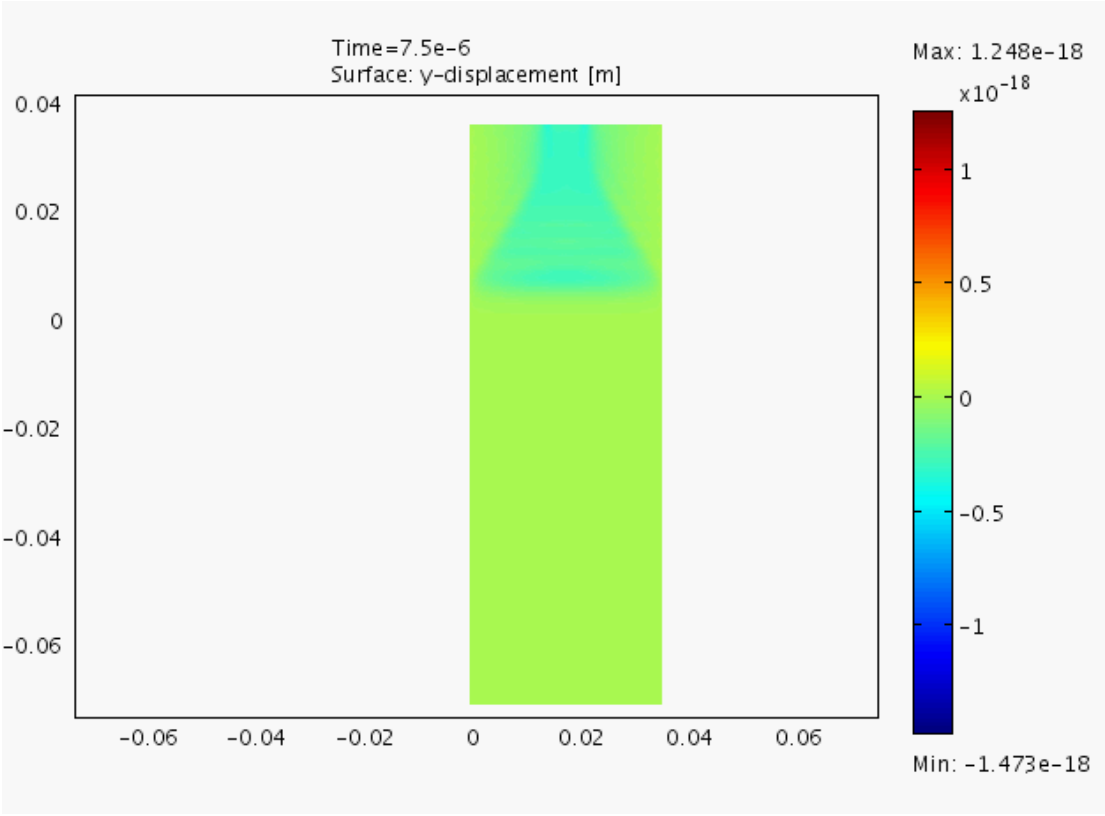

Figure 87- Early time during wave propagation – the layering is two times thinner than in figure Figure 86, and not displayed for wave propagation visibility purposes. After the shot, the wave propagates as in an homogeneous media.

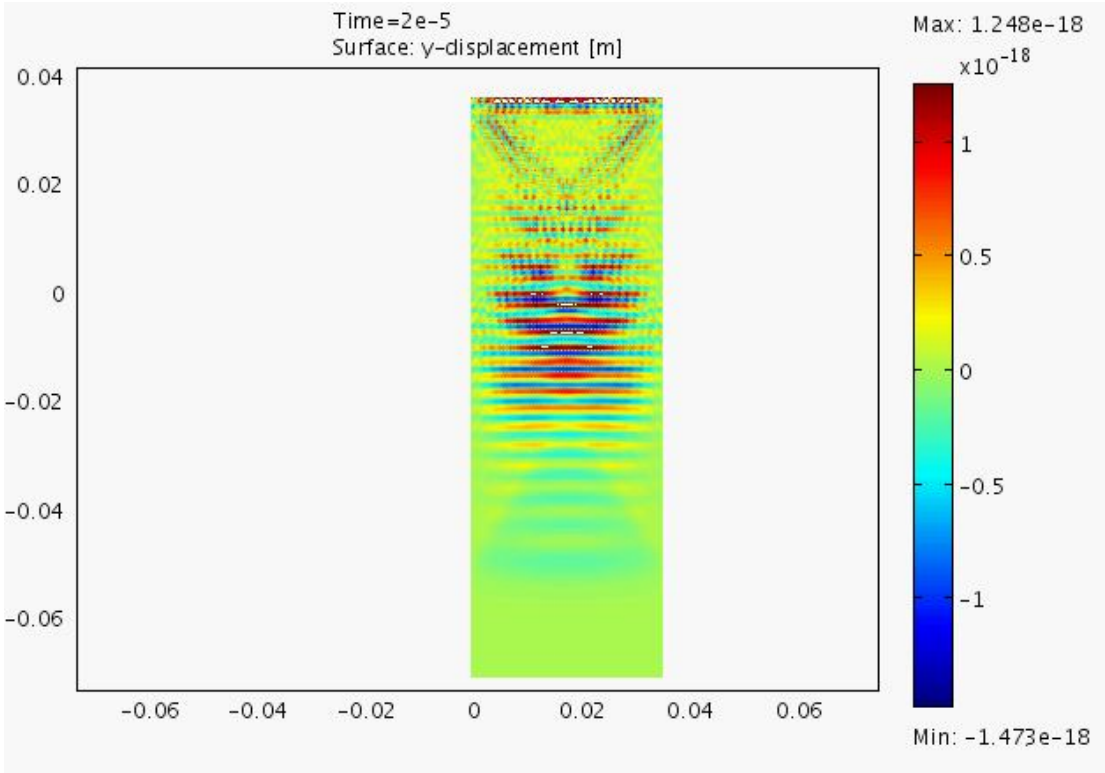

Figure 88 - Late time during wave propagation - the waves display evanescent patterns predicted by Hovem

4.3.4. Accuracy of Wave Arrival Picking

Comsol Multiphysics provided models to assess the accuracy of the picking algorithm developed as part of this thesis, and this is presented in paragraph 3.2.6. The model consisted of a 2D section along the length of a core, with the dimensions:

- diameter: 36 millimeters
- length: 72 millimeters

The model produced a 1MHz ultrasonic wave at the top of the core, and recorded its arrival at the bottom of the core. Synthetic traces were extracted for P- and S-waves. The mechanical properties of the propagating medium were known, therefore a direct comparison was possible between the actual velocity, and the velocity deduced from the automatic picking algorithm.

This comparison led to the definition of a:

- 5% absolute error for P-wave velocity
- 20% absolute error for S-wave velocity

4.3.5. Conclusion

The second part of this chapter focused on the potential causes of the static/dynamic discrepancy mentioned in Figure 21. An investigation using the Comsol Multiphysics modelling proved the non-negligible influence of two physical phenomena (thermoelasticity and fine layering) on acoustic wave velocity. This observation emphasized the need to recalibrate seismic and ultrasonic data at a reference frequency prior to their application in modelling, as mentioned in paragraph 3.2.7, but also raises the following three questions:

- Does a fine-layering propagating medium require a formula different from equations 129 and 130 for upscaling properties recorded in the laboratory?
- If seismic and ultrasonic waves propagate in coal at different modes (i.e, at effective or average velocity) are the data on anisotropy collected in the laboratory relevant to seismic scale?
- If thermoelasticity is non-negligible, what is its consequence on the reflection coefficient? Could it potentially prevent any AVO calibration from the laboratory?

4.4. SEIMIC INTERPRETATION, RAY TRACING AND AVO MODELLING

4.4.1. Introduction

The first two sections of this chapter focused on Comsol Multiphysics modelling laboratory tests, with a specific emphasis on physical phenomena affecting acoustic velocities at ultrasonic frequencies. The non-negligibility of the two cases (wave propagation in thermoelastic and in finely-layered media) underlined the need to recalibrate parameters deduced from ultrasonic data (ultrasonic wave frequency: 1MHz) to a seismic scale (average seismic frequency: 60Hz) before their application in seismic modelling.

These observations justified the recalibrations done in section 3.2, defining upscaled average parameters (Table 52, Table 57 and Table 60) of Coal, Mudstone and Sandstone. These densities, P- and S-wave velocities provided the basis of seismic modelling, and was implemented in this thesis by Matlab code (developed as part of this thesis).

Part of the code implementing these parameters provides amplitude versus offset plots, which quantitatively confirm the qualitative observation made by comparing Figure 77 and Figure 79; AVO can theoretically detect a difference between mudstone and sandstone semi-infinite roofs overlying semi-infinite coal seams. Application of each parameter distribution (From Figure 43 to Figure 51) in the same Matlab code leads to a similar conclusion.

However, lithology's finite thicknesses and their consequences (the best known being anisotropy and tuning effect) may limit this initial AVO ability to discriminate coal seams' roofs.

The last part of this chapter examines the presentation of Matlab programs,and the initial ability of AVO to differentiate Mudstone from Sandstone and the lithologies' thicknesses related problems. It follows the structure below:

1. Amplitude Vs Offset plots
2. Presentation of the ray tracing program
3. Probabilities
4. Tuning effect
5. Determination of the minimum detectable thickness
6. Cyclothem
7. Conclusion

4.4.2. Amplitude Vs Offset plots

The first Matlab code developed for this thesis implements Aki and Richards' equations 42 to 58, which compute reflection and transmission coefficients from propagating media's densities, P and S-wave velocities, and wave's incidence angle (see Appendix 7.1).

Section 2.2.2 states that these equations describe wave propagation in the following physical system:

Hypothesises on media:

- Homogeneous
- Isotropic
- Elastic
- Semi-Infinite

Hypothesises on the boundary separating the two propagating media:

- Plane
- Welded

Hypothesises on the propagating wave:

- Homogeneous
- Plane

Figure 89 is an example of the code computing variations of P-reflected waves over angle of incidence. Densities, P- and S-wave velocities are the Coal, Mudstone and Sandstone mean values determined in last chapter (see tables 52, 57 and 60). This numerical application shows a clear trend difference between semi-infinite Mud- and Sand roofs overlying semi-infinite coal layers. By introducing seismic survey's

geometry limitations (i.e, in Daw Mill, a maximum offset of 28 degrees sampled every 7 degrees), Figure 90 depicts the general trends expected in Daw Mill:

- for Mudstone roofs: conservation of reflection amplitude over incidence angle
- for Sandstone roofs: decrease of reflection amplitude over incidence angle

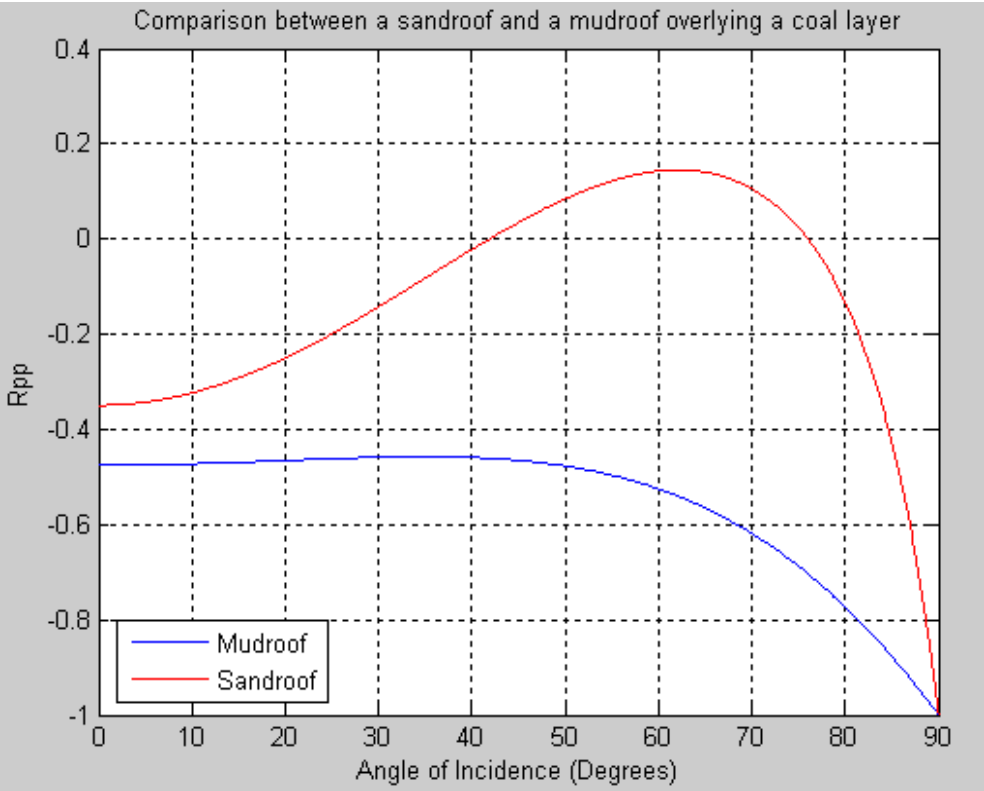

Figure 89 – Rpp coefficient variation with angle of incidence.

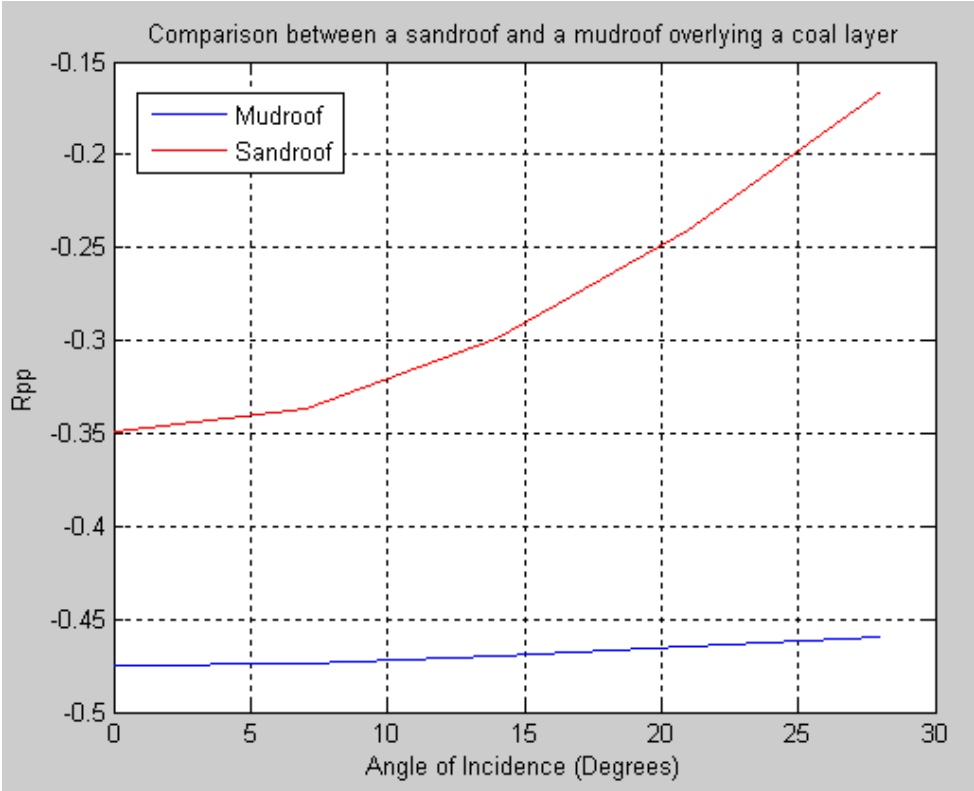

Figure 90 – This figure represents the same case depicted in figure 89, and represents a record representative of Daw Mill; i.e, a maximum offset of 28 degrees, sampled every 7 degrees.

Applications of these computed amplitudes to synthetic traces, depicted in Figure 91 and Figure 92, may be more representative of amplitude variations observed in a shot gather.

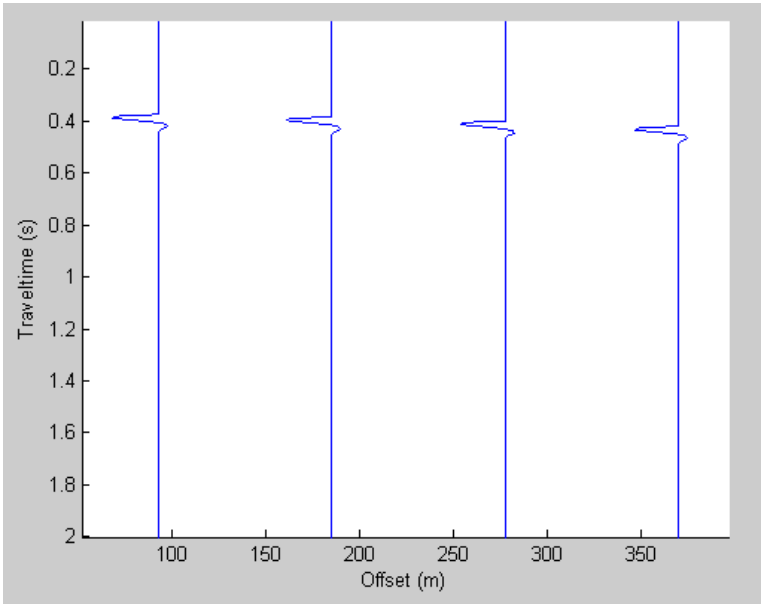

Figure 91 – Synthetic CMP gathers on a Mudstone roof

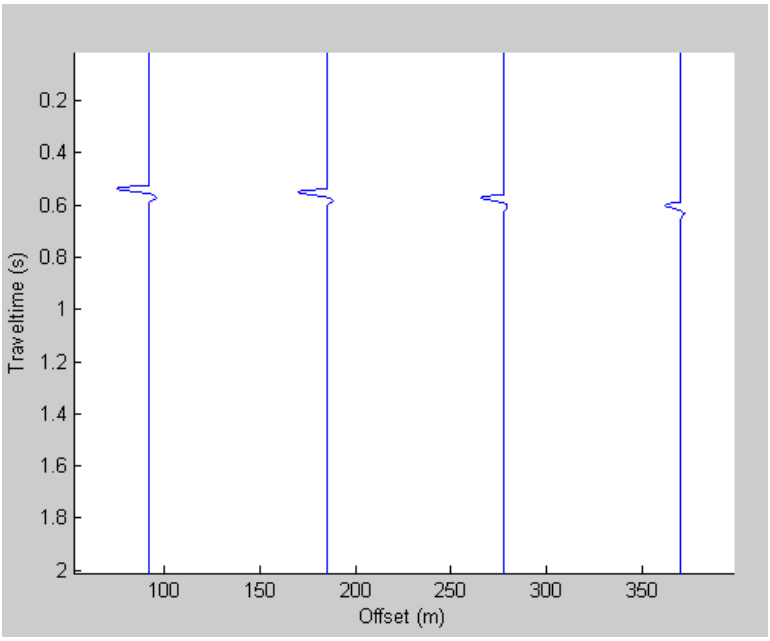

Figure 92 - Synthetic CMP gathers on a Sandstone roof

4.4.3. Presentation of the ray tracing program developed in this thesis

The ray tracing programs (presented in Appendix 7.2) successively compute the following elements:

1. Raypaths (the path taken by the travelling wave between source and receiver, and depicted in the upper part of Figure 94)
2. Traveltimes (time taken by a wave for travelling from source to receiver, and shown in the lower part of Figure 94)
3. Amplitude (Reflected amplitudes are computed by the Matlab code presented in the precedent paragraph)

4. After attributing an amplitude to each traveltime, convolution with a waveshape for modelling shot gathers (Figure 95 and Figure 96)

This program handles straight (for depicting waves propagating in layers with constant velocity) and curved (for depicting waves propagating in layers with velocity increasing or decreasing with depth) raypaths.
Curved raypath theory has been developed by authors like Galperin (1985). He summarized some of their work with the following variation of velocity with depth (depicted in Figure 93):

$$v(z) = v_0(1+\beta z)^{1/a} \quad 1 \le a \le 3$$ **Equation 137**

Galperin referred the case a=1 as a continuously varying media. Assessment of horizontal distance and traveltime from a varying velocity are, respectively:

- $$T(p) = 2\int_0^{Z(p)} \frac{dz}{\sqrt{1-p^2 v(z)^2}}$$ **Equation 138**
- $$X(p) = 2\int_0^{Z(p)} \frac{dz}{\sqrt{\frac{1}{(pv(z))^2}-1}}$$ **Equation 139**

With:

- v_0: initial velocity
- z: depth
- β: unit, [1/m]
- a: integer, no unit
- v: velocity
- T: traveltime
- X: horizontal distance, also referred as offset
- p: ray parameter
- Z: maximum depth reached by the ray
- i: incidence angle

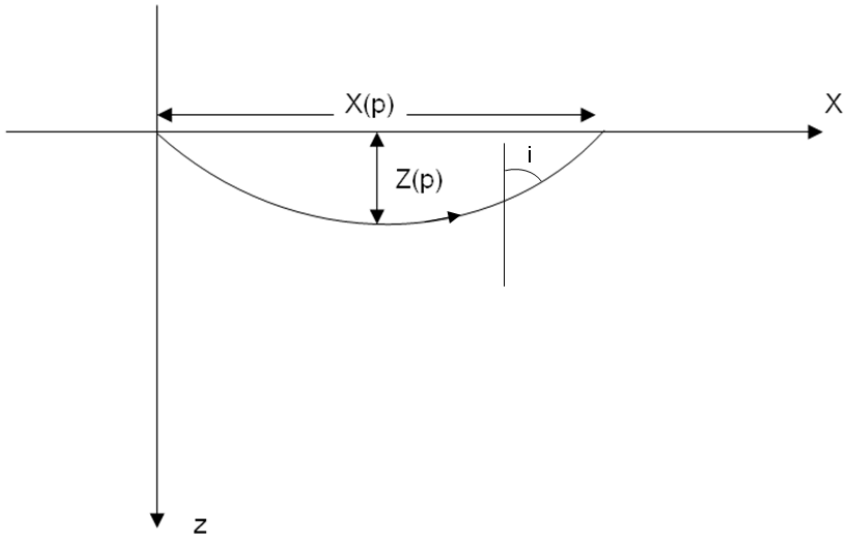

Figure 93 – Ray Path in a flat Earth Model (Aki and Richards (2002)

After computing velocities, traveltimes and raypaths with equations 137, 138 and 139, each reflection coefficient is attributed to each traveltime before convolving a wave-shape.
While both geometry and time related issues are now perfectly handled, other topics shall be developed in the future for being more representative of wave propagation in a seismic survey:

- attenuation
- anisotropy
- geometrical expansion
- reflection on dipping interfaces
- reflection on non-flat interfaces
- interfaces' dip
- reflection of spherical waves
- extension to 3D
- and so on...

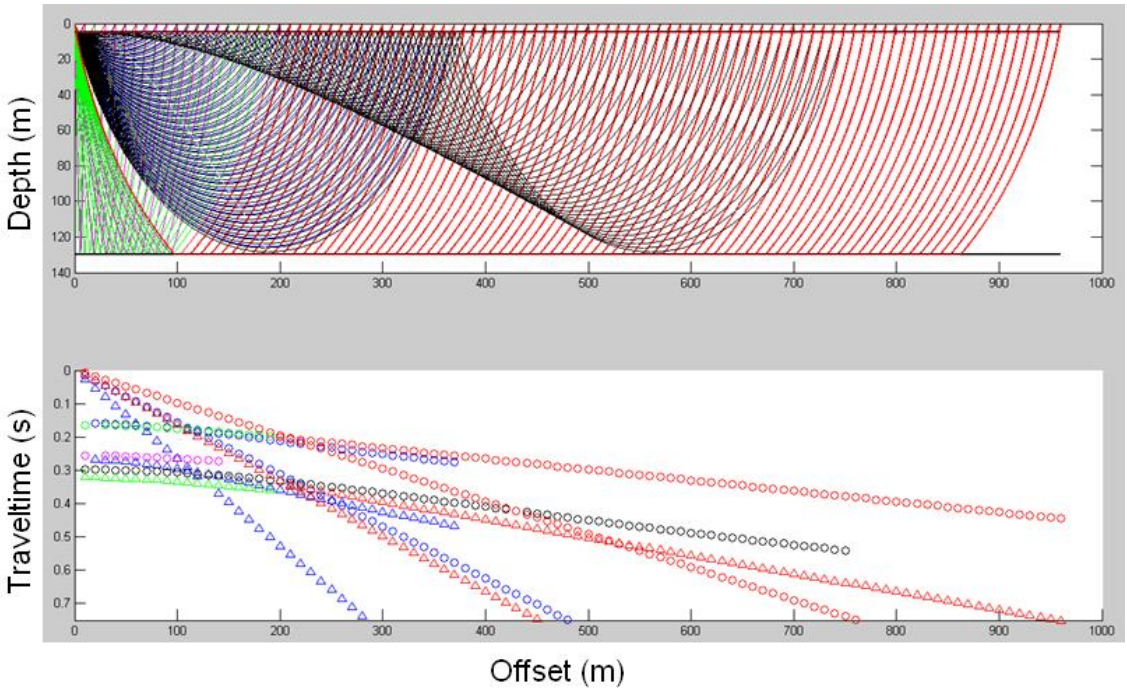

Figure 94 – Example of ray tracing program reproducing a shot in non constant velocity layers. In green are the reflected waves, the red are refracted, in the PS and SP converted waves, and finally the curved direct waves are represented in black. In the traveltimes plot, P-waves arrivals are represented by circles and S-waves by triangles. A reflection coefficient is attributed to every traveltime.

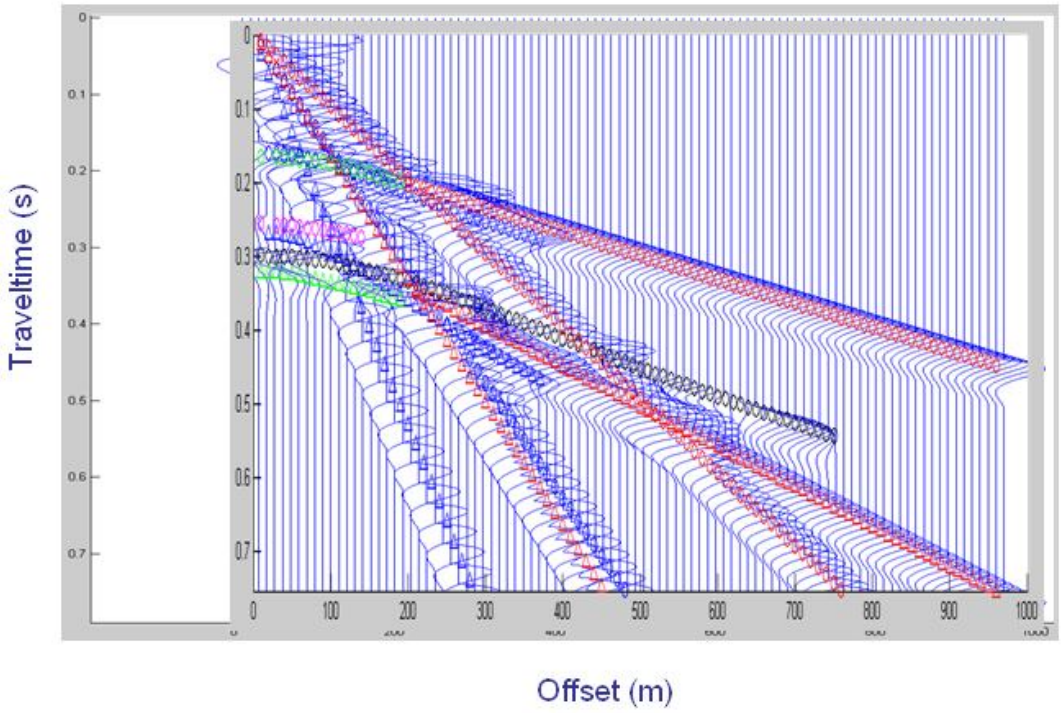

Figure 95 – Superposition of computed travel times and their associated reflection coefficients convolved to a wavelet.

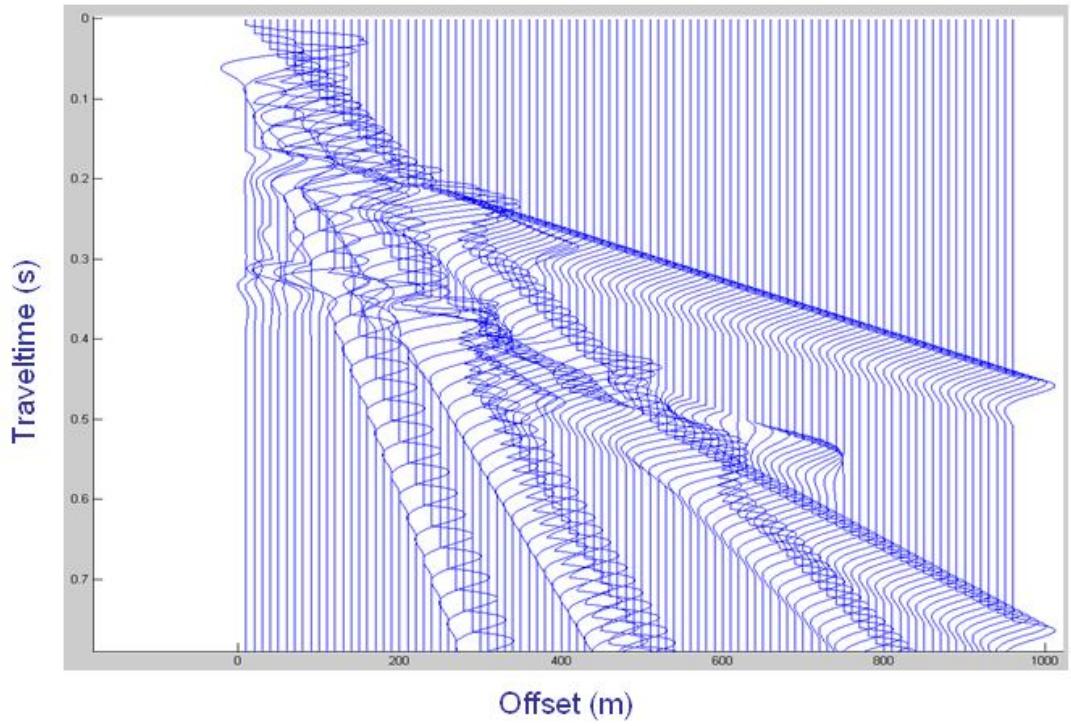

Figure 96 – A synthetic shot is obtained after convolving the travel time plot with a wavelet.

4.4.4. Probabilities

Application of different lithology average densities and P and S-wave velocities has shown, qualitatively and quantitatively in sections 4.2.4 and 4.4.2, a trend difference between Mudstone and Sandstone reflection coefficient curves over offset.

However, average parameters may not be representative of the whole variety of rock properties collected in the laboratory; respective distributions lead to a distribution

of reflection coefficients. This means that reflection responses recorded on the top of the roofs may not be unique like the ones shown in Figure 89 and Figure 90.

This multiplicity of responses for each lithology raises one question; could mudstone's range of responses overlap sandstone's range of responses?

Vp, Vs and density binomial distributions of Coal, Mudstone and Sandstone have been used for computing binomial distributions of reflection coefficients of seismic waves on Mud and Sand-roofs overlying a semi-infinite coal layer. For each roof layer, two binomial distributions have been computed:

1. with binomial distributions for each rock property (Blue curves on Figure 97)
2. with an equal probability of occurrence for each property (Red curves on Figure 97)

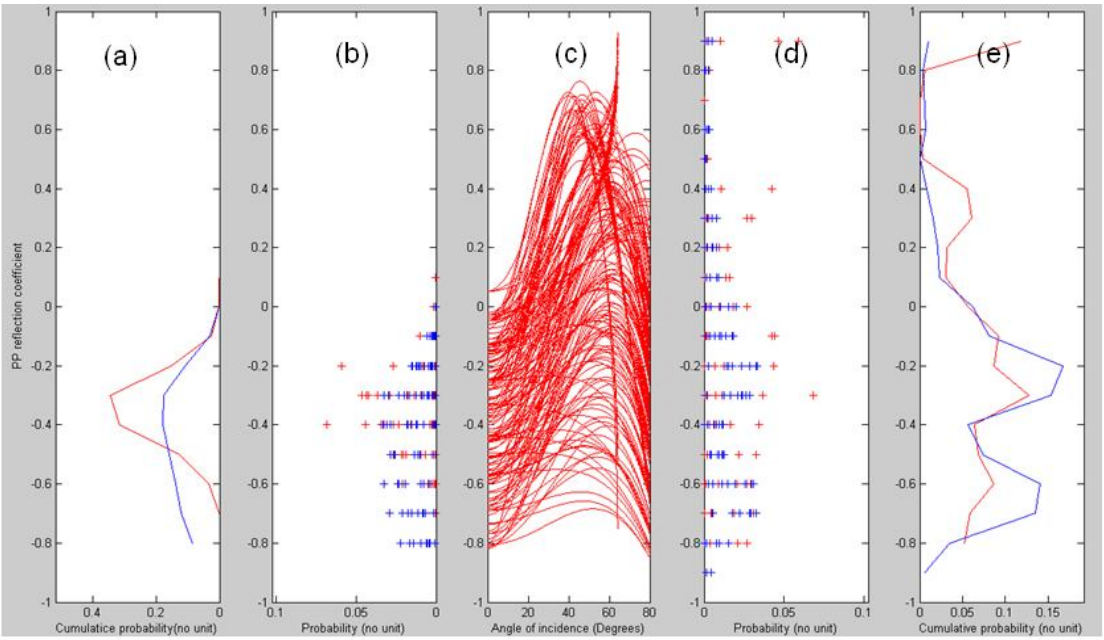

Figure 97 – Blue curves and dots are representative of the equiprobability distribution, and red ones are related to the rock properties associated to a binomial distribution. (a) Plot showing the amplitude distribution at zero offset. (e) Plot showing the amplitude distribution at maximum offset. (c) AVO curves. A simple glance a (a) and (e) shows enough differences between blue and red curves for taking into account the rock's distribution.

A brief comparison between both cases shows similar distributions, both at zero and maximum offset (28 degrees). In Figure 98, the computations implement distributions determined in laboratory. If these distributions provide the ability to compute the probability to record an amplitude for a pre-determined roof, the goal for mine planning is to determine the nature of a roof from an amplitude. This problem requires the application of Bayes' theorem. In a classical example applying this mathematical tool, the goal is to determine the provenance of a ball. Let two urns filled with balls; the first one contains 10 black balls and 30 white ones, while the second has 20 of each. The probability of having a white ball is then of 75% in the first urn, and 50% in the second; in this case, when a white ball is extracted, what is the probability of having taken it from the first urn?

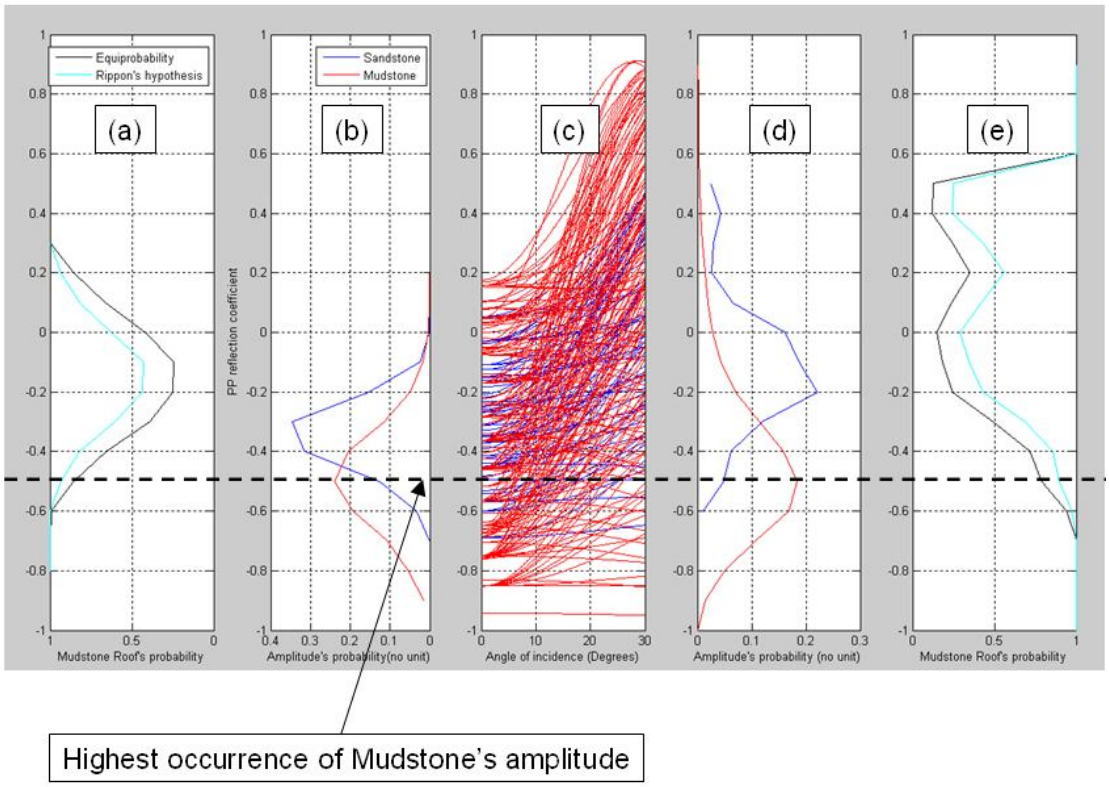

Figure 98 – Blue is representative to Sandstone, Red to Mudstone. (c) AVO curves of the different $\left(E_{Roof}, \sigma_{Roof}, \rho_{Roof}, E_{Coal}, \sigma_{Coal}, \rho_{Coal}\right)$ combinations. (b) and (d) are the amplitude distribution plots at respectively zero and maximum (30 degrees) offsets. A significant difference is observed between mud and sand-roofs.(a) and (e) are the probability plot to have a Mudroof when measuring an amplitude. The highest occurrence of Mudroof is at a 0.5 reflection coefficient value. ((b) and (d)), which also coincides with a high probability to have such a lithology ((a) and (e)).

The solutions for these two similar problems requires the:

- Probability of having an AVO amplitude on Mudroof: $P\left(A\middle|Mudroof\right)$
- Probability of having an AVO amplitude on Sandroof: $P\left(A\middle|Sandroof\right)$
- Probability of having a Mudstone roof: P(Mudroof)
- Probability of having a Sandstone roof: P(Sandroof)

Let $P\left(Mudroof\middle|A\right)$ be the probability of having a Mudroof when measuring amplitude A; according to the Bayes' theorem:

$$P\left(Mudroof\middle|A\right)=\frac{P\left(Mudroof\right)\times P\left(A\middle|Mudroof\right)}{P\left(Mudroof\right)\times P\left(A\middle|Mudroof\right)+P\left(Sandroof\right)\times P\left(A\middle|Sandroof\right)}$$

Equation 140

This formula computed curves (a) and (e) in Figure 98. Black curves are computed using the same occurrence of having Sandstone and Mudstone roofs overlying coal seams and blue curves based on the fact in the Daw Mill region sandstone represents 30% of the deposited volume. By not taking other lithologies like siltstones, a 70% probability of having Mudstone has been determined. Both cases show a similar

aptitude of AVO to discriminate Mud and Sand-roofs over coal seams, and a final analysis, shown in figure 99, confirmed this potential by observing a specific feature; a non-varying amplitude over offset is related to an 80% of chances to have a Mudstone roof overlying a coal seam.

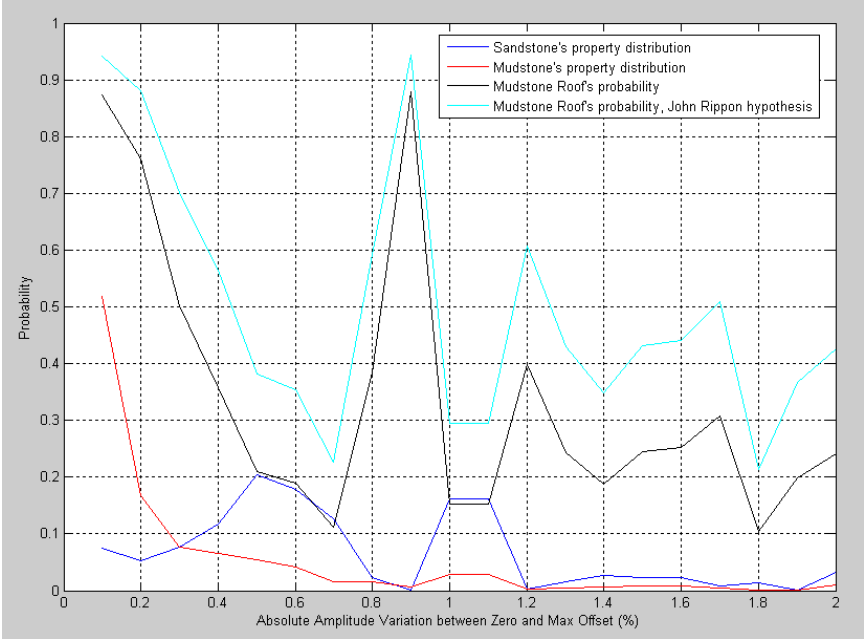

Figure 99 – The highest occurrence of amplitude preservation for mudstone roofs (less than 20% of Absolute Amplitude Variation) also guaranties a less than 20% probability of having a sandstone roof. The reciprocity is true, a 50~60% and a 100~110% absolute amplitude variation guarantying a 70~80% chance of having and sandstone roof.

4.4.5. Tuning effect

The literature review discussed the possibility of coal seam finite thickness generating a tuning effect (interference between seismic wave reflections on seam top and bottom). The consequence of this physical phenomenon on reflection coefficients has been described by equations 88 (Lin and Phair, 1993), 93 (Bakke and Ur, 1998) and 95 (computed in this thesis).

Lin and Phair's formula is an approximation for computing the tuned R_{PP} coefficient, Bakke and Ur approach is more practical for ray tracing purposes, and both formulae are applicable for a coal seam encased within the same lithology. Finally, equation 95 allows computation of AVO response of a thin reservoir encased between two lithologies; in this thesis namely a coal seam encased between a mudstone floor and a sandstone roof. Another expression of this formula is:

$$R_{tuning}(\theta) \approx \left\{R_{PP\ \ Sandstone}(\theta) - R_{PP\ \ Mudstone}(\theta)\right\} + \omega_0 \Delta T(\theta)\cos(\theta) R_{PP\ \ Mudstone}(\theta) \quad \textbf{Equation 141}$$

With:

- ω_0 : wavelet dominant frequency
- T : two way traveltime from seam top to base

Applications of equations 88 and 141 led to Figure 100:

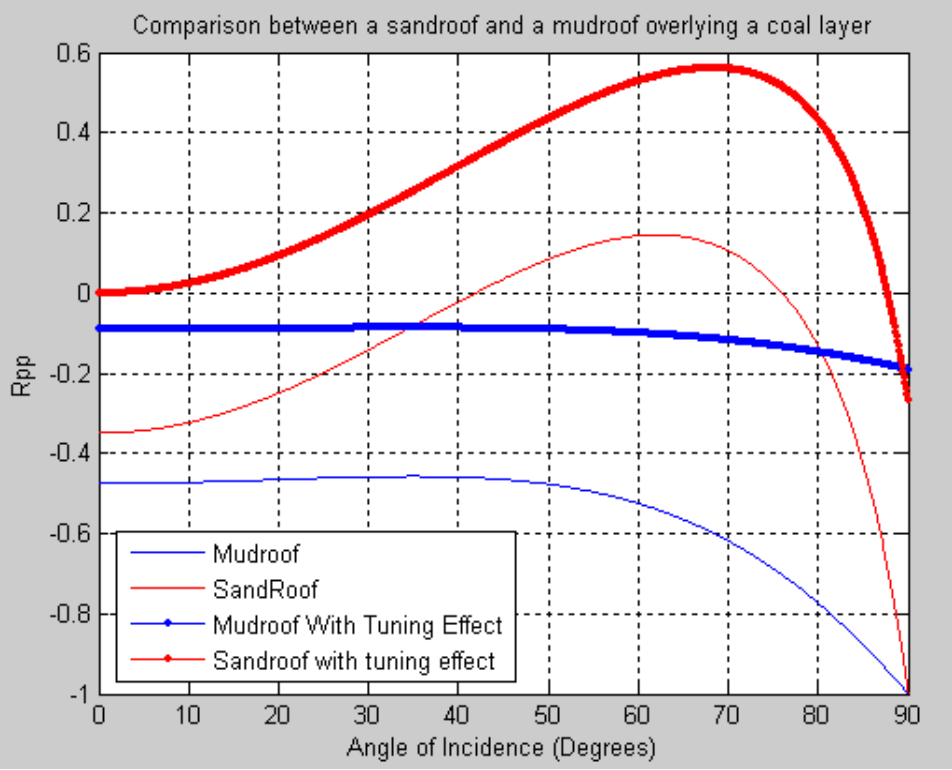

Figure 100 – Computation of tuned reflection coefficients with the original and modified Lin and Phair formula; however shall only be taken into account within 30 degrees of incidence. While this tuning effect seems to be at the origin of a significant reduction of mudstone roof's AVA response, Sandstone's answer shall see its polarity changing, with growing amplitude with offset while the half-space model initially predicted a decay.

This numerical application shows a numerical difference between tuned and non tuned reflection coefficients, but no difference in the trend of the curves. This first aspect shows that if the focus is kept on reflection coefficients' conservation over offset, tuning effect will have no effect on the conclusions deduced from Figure 99; if coal seam thickness remains constant over the Daw Mill area, tuning effect shall have no consequences for the capability of AVO to differentiate Mudstone from sandstone roofs overlying coal seams in Daw Mill. If the thickness of coal seam varies over space, it will not be possible to separate tuning from roof contributions to reflection coefficients, and AVO will not be a proper method for differentiating mud from sand-roofs.

4.4.6. Determination of the minimum detectable thickness

A factor potentially limiting AVO capability to differentiate sandstone from mudstone roofs over coal seams is roof limited thickness. Layers of thickness d will affect amplitude variations over angle if smaller than seismic wavelength λ.

Velocity in mudstones determined from average numerical values of (E, σ, ρ) led to V_P=3770 m/s. By considering a dominant frequency f = 60 Hz, the minimum observable layer's thickness is:

$$\lambda = \frac{V_P}{f} = \frac{3770}{60} \approx 62.8333\text{m} \qquad \textbf{Equation 142}$$

For sandstones, V_P=2690 m/s:

$$\lambda = \frac{V_P}{f} = \frac{2690}{60} \approx 44.8333\text{m}$$ **Equation 143**

And for coal, V_P= 2290 m/s:

$$\lambda = \frac{V_P}{f} = \frac{2290}{60} \approx 38.1667\text{m}$$ **Equation 144**

These numerical values, which all exceed the average coal's 6 meters and Sandstone/Mudstone's 3 meters average thicknesses seen in Daw Mill, indicate that all targeted layers are below the detection threshold of seismic methods. One of the potential consequences of this will be shown in the following paragraph, dedicated to cyclothems.

4.4.7. Cyclothem

Section 2.4.5 introduced Hovem's work on wave propagation in finely layered media. A part of the theory states: "When the layering period is much shorter than the wavelength, the velocity approaches the effective medium velocity". A direct application of this work could be cyclothems, a periodical succession of lithologies. Computation of an average velocity (see equation 96) of alternating 1 meter Sandstone and 2 meters Mudstone layers encasing a 6 meters coal seam shows, in Figure 101, that with AVO, no distinction can be made between mudstone and composite roofs over coal.

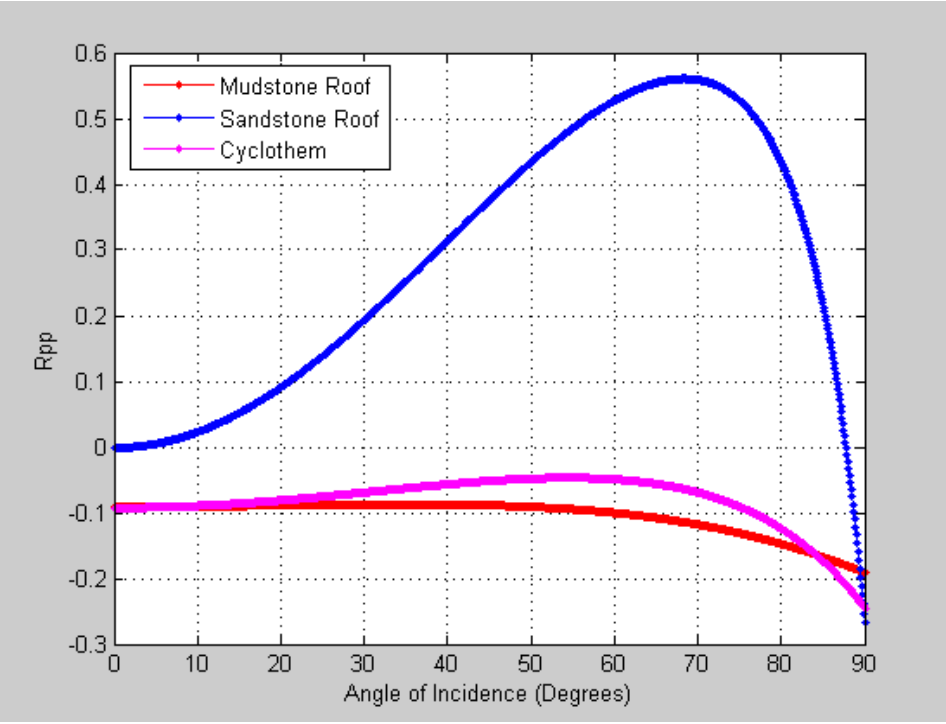

Figure 101 – Comparison of different tuned AVO signals. The coal seam is 6 meters thick, encased between either semi-infinite mudstone or cyclothems layers, except for the sandstone roof's case, which floor is made of mudstone.

The similarity of the computed amplitude variations with offset leads to the conclusion that through cyclothems, the layer's limited thickness may compromise AVO's ability to differenciate mudstone from sandstone roofs.

4.4.8. Conclusion

The last part of this chapter focuses on the computation of amplitude variations with offset. It presents different Matlab codes developed for this thesis to assess AVO's applicability to mine planning. Numerical applications of Aki and Richards' solutions (Equation 42 to equation 58) applying average values (Tables 52, 57 and 60) and binomial distributions of:

- Coal
- Mudstone
- Sandstone

led to observed amplitude conservation over offset in Mudstone's case. Consequently, AVO has the theoretical ability to differentiate semi infinite Mud and Sand- roofs over semi-infinite coal layers.
However, the limited thicknesses of the different targeted lithologies generate tuning effect (section 2.4.4), and problems of layers detection potentially leads to a potential inability to differenciate mudstone and sandstone roofs from recorded reflection coefficients.

4.5. CONCLUSIONS OF THIS CHAPTER

This chapter is the synthesis of the literature review and the chapter reporting the different laboratory experiments undertaken within the framework of this PhD thesis. It successively tackles:

Sensitive sleeve modelling: this first part presents the different models, and their implementation through a Graphical User Interface developed specifically for this project. The resulting synthetic data shall be seen as a basis for further developments, after getting some data from the sensitive sleeve (see conclusion of Chapter 3).

Thermoelasticity and wave propagation in finely layered media: this second part presents models showing that fine layering and thermoelasticity have a non-negligible role in static-dynamic discrepancy (Paragraph 2.4.7 and Figure 21)

Seismic, ray tracing and AVO: this third part presents implementation of data collected in Chapter 3, in different Matlab Codes developed specifically for this project. In this part, a direct application of probability distributions determined in chapter 3 proves statistically that AVO can discriminate a mudstone from a sandstone roof overlying a coal seam in the region of Daw Mill.

The experimental inability to record any signal through sandstone in laboratory (see last chapter's conclusion) has been a limiting factor in sensitive sleeve related modelling. This, however, shall be seen as a basis for further attempts to develop this innovation, with tools such as Graphical User Interface reproducing wave propagation within the modified Hoek Cell. Models have raised a number of issues which were unplanned at the beginning of the ADEMA project, such as the:

1. recalibration of ultrasonic data taken in finely layered media (like coal)
2. influence of thermo-elasticity and other physical phenomena on reflection coefficient
3. presence of spherical wave-fronts

Investigation of these different issues, potentially affecting reflection coefficients recorded in laboratory (and then, potentially compromising the possibility to

implement any AVO calibration from laboratory), shall precede any further investment on sensitive sleeve.

Different models with Comsol Multiphysics, for the purpose of this innovation, have forecasted (in Figure 77 and Figure 79) the ability of AVO to differentiate a mudstone from a sandstone roof overlying a coal seam. This qualitative observation has been quantitatively confirmed with the implementation of data collected in laboratory into Aki and Richards' solutions (equations 42 to 58). However, this synthesis of the litterature review and experimental data, has also emphasized a potential problem linked to the limited thickness of targeted lithologies, leading to consequences such as tuning effect (see paragraph 2.4.4). If the reflection coefficient is a function of coal layer's thickness, AVO may not be a proper method for mine planning.

Chapter 5.SEISMIC

5.1. INTRODUCTION

In the preceding chapter, the application of laboratory data in numerical applications and in modelling led to the following conclusion; AVO has the theoretical ability to differentiate a mudstone from a sandstone roof over coal seams. However, this technology may not be suitable for lithologies of limited thicknesses,which could be at the origin of a physical phenomenon known as tuning effect (constructive and destructive interferences between reflected waves). In this chapter, observation of real seismic data will show that the the phenomenon regarding the tuning effect is predominant, and leads to an inability of AVO technology to identify roof lithologies of coal seams.

This conclusion should have been deduced from a comparison between theoretical (computed in the preceding chapter) and real (recorded during the seismic survey) reflection coefficients. However, a software related problem led to the adoption of a more qualitative approach, based on the experience of Gochioco, a specialist in coal exploration using the seismic method (1990, 1991, 1998, 2002 and 2004). The resulting analysis tackles three patterns in seismic data, all of them related to the tuning effect:

- tuning effect
- presence of multiple seams
- synclines

A short description of seismic processing precedes these, in order to prove that the observed patterns are not related to signal processing artefacts.

The chapter structure is as follows:

1. Introduction
2. Processing
3. Tuning effect
4. Presence of multiple seams
5. Synclines
6. Conclusion

5.2. SEISMIC PROCESSING

Seismic processing is an important step for recovering reflection coefficients, and includes many sequences like noise removal. For example, in an AVO analysis, surface waves are considered as noise, and their removal is a mandatory step. The next figure shows how a FK filter, which appropriately removes surface waves, affects reflected waves at short offsets. The consequence of this could be the generation of a reflection coefficient increasing with offset, which could be misleading for interpreters. As a consequence, FK-filters are not suitable for AVO analyses.

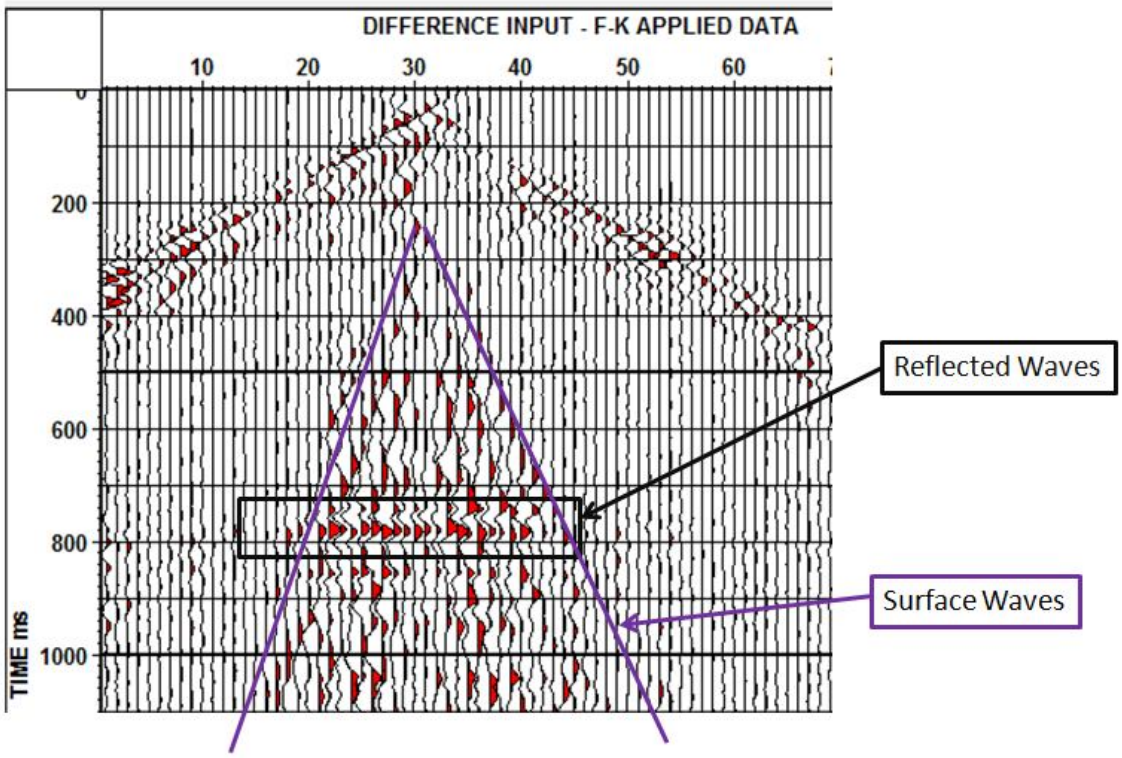

Figure 102 - Example from a training to the software VISTA. It shows the waves removed by a FK filter. The perfect removal of surface waves has a corrolary; the removal of reflected waves. As a consequence, FK-filters are not suitable for AVO analysises.

If data processed by filters non-adapted to AVO analysis are applied in inversion algorithms, some rock parameters may be inaccurately computed.

For this reason, every processing step has been carefully considered, a task devoted to Dave Paige. A private communication with him determined that with Daw Mill data, a frequency dependent tool would not provide the expected result if noise and the target's signal patterns showed a similar dominant frequency. Moreover, the poor quality of the data (inherent to every land seismic acquisition) required the following improvement efforts:

1. Additional work on refraction statics (which consist in a time shift of traces)
2. Application of a non-linear algorithm

None of these processing techniques affects amplitudes. The first processing effort listed above consists of correcting the time shifts generated by refractions generated by the shallower layers. The correction, a time shift of each trace, recovered the coherence of seismic events (reflections) at short offsets, but not at further offsets (i.e upper part of Figure 103). Dave Paige applied an averaging of the time shift between traces, a technique which led to the recovery of the coherence of the signal along the whole offset range (the perfect flat line observed in the lower part of Figure 103 attests the quality of the recovery). This processing effort recovered the reflection coefficients by increasing the coherence within the signal.

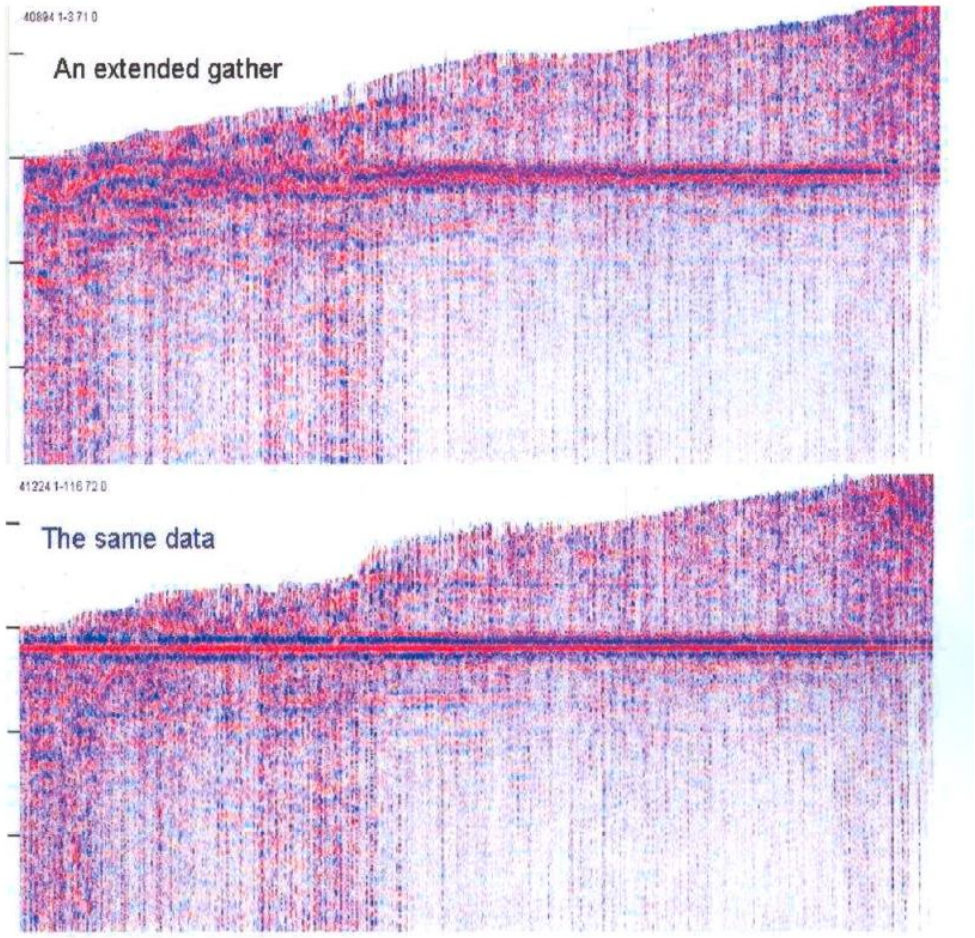

Figure 103 – Example of the improvement on the static correction done by Dave Paige; on top, the initial set of data. The only process only being a time shift of the data, the AVO analysis won't be threatened by a processing altered amplitude.

The second processing effort, the application of a non-linear algorithm, is shown in Figure 104. This tool takes advantage of the coherent nature of the noise, detectable by a pattern recognition algorithm. A targeted waveshape was removed without affecting the amplitude of other wavetrends, leaving reflection coefficients unaffected in the process.

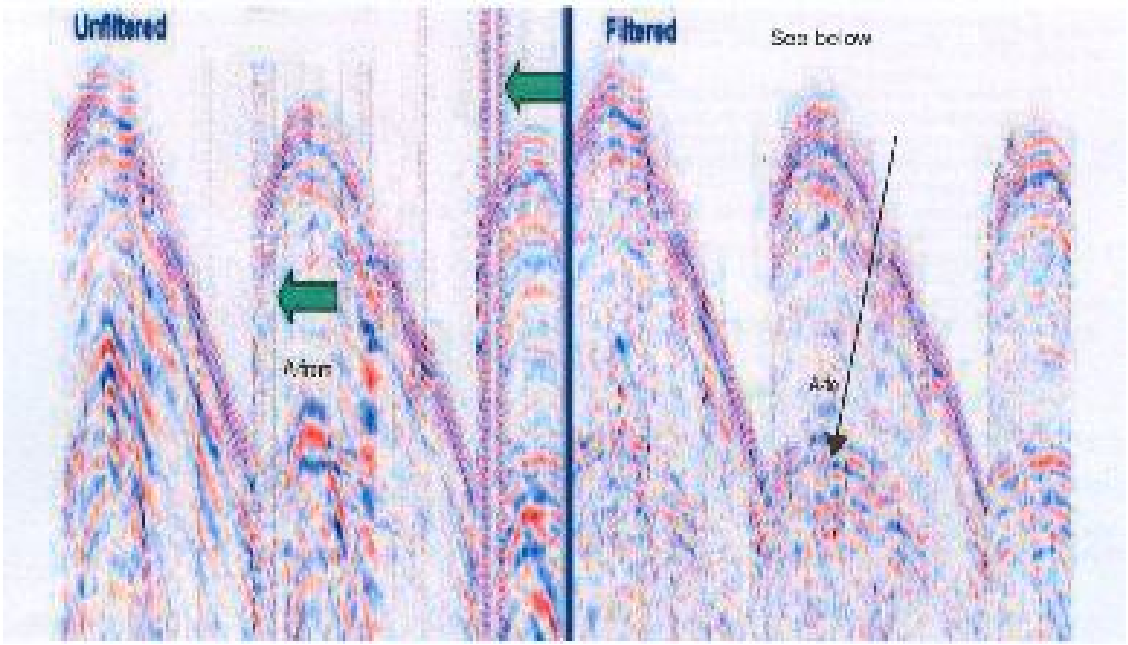

Figure 104 – Example of a result obtained by the non linear logic employed by Paige. The filtering being based on reconnaissance pattern, coherent noise is removed without affecting the target's amplitude reflection.

5.3. TUNING EFFECT

An inversion of processed data with the Shuey's equation (Equation 82) computed reflection amplitude at zero incidence (Equation 83) and the gradient (Equation 85).

Analysis of zero incidence amplitudes was considered confusing at the beginning of the ADEMA project, by showing distinct top and bottom reflections (see Figure 105). According to equation 144, seismic wavelength is supposed to be more than 38 meters; as the main coal seam is 6 meters thick, top and bottom reflection should be observed separately. I clarified the situation by proposing an explanation which neither contradicts reflection theory nor wavelength resolution; in their respective work, Lin & Phair(1993) and Bakke & Ur(1995) related that fine layers encased in bedrock affect the shape of reflected seismic waves. The shapes of the waves reflected on these reflectors are the derivative of the shape of indicent waves. This interference between top and bottom reflections has to be linked to tuning effect, a factor also affecting amplitude variations over offset (paragraph 2.4.4).

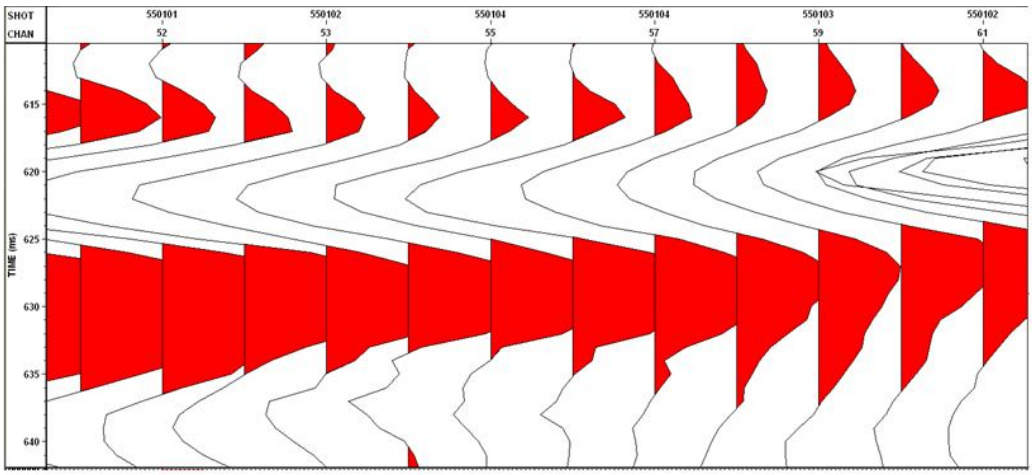

Figure 105 – Enlargement of the main coal seam reflection. The layer was known to be 6 meter thick, therefore at first sight it was surprising to observe what looked like a top and bottom reflection with a 35 metre wavelength. On such a thin layer (relative to the wavelength), a waveshape is in reality distorted into its time derivative, leading to such a pattern, and it does not contradict elementary physical rules; in Daw Mill, seismic can't possibly lead to a distinction between the main seam's roof and floor.

Variation of encased layer's thickness has consequences for amplitude variations, as shown in Figure 106. This feature is commonly taken advantage of for detecting the presence of tuning from the variations of reflection coefficients at zero offset (as in Figure 107 and Figure 108).

Confirmation of tuning effect's presence raises a question: when recording a seismic reflection coefficient, could it be possible to separate the respective contributions of roof reflection and tuning?

If not, AVO may not be a suitable method for detecting the difference between a mudstone and a sandstone roof overlying a coal seam.

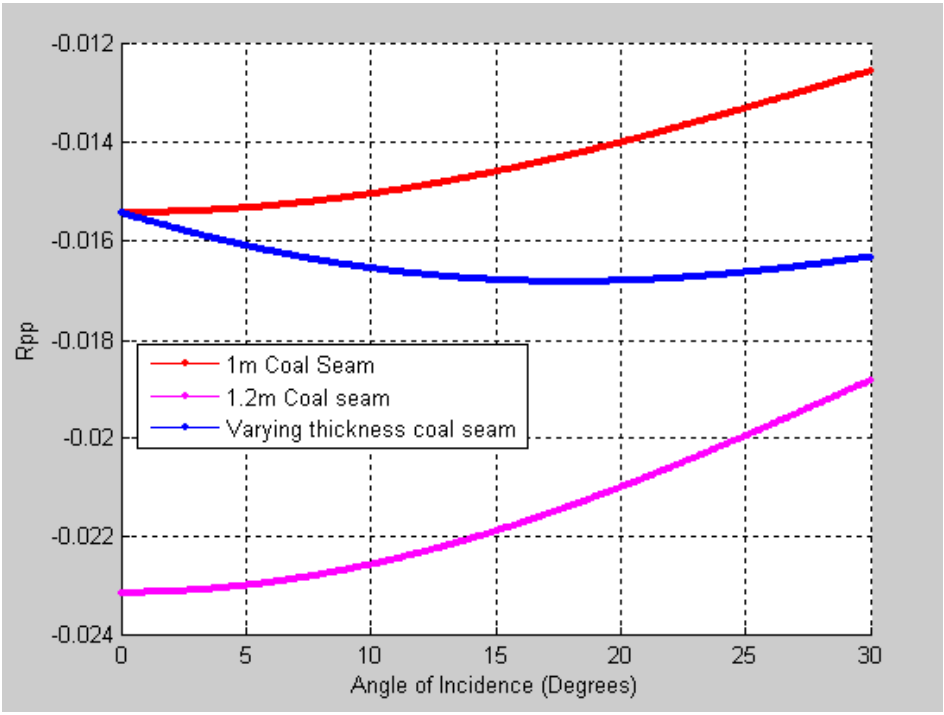

Figure 106 – Tuned reflection coefficients on a coal seam. The two first models have a constant thickness, while the third varies from 1 to 1.2 meters. This 20 centimeters change turns an initially decreasing trend into an increasing one.

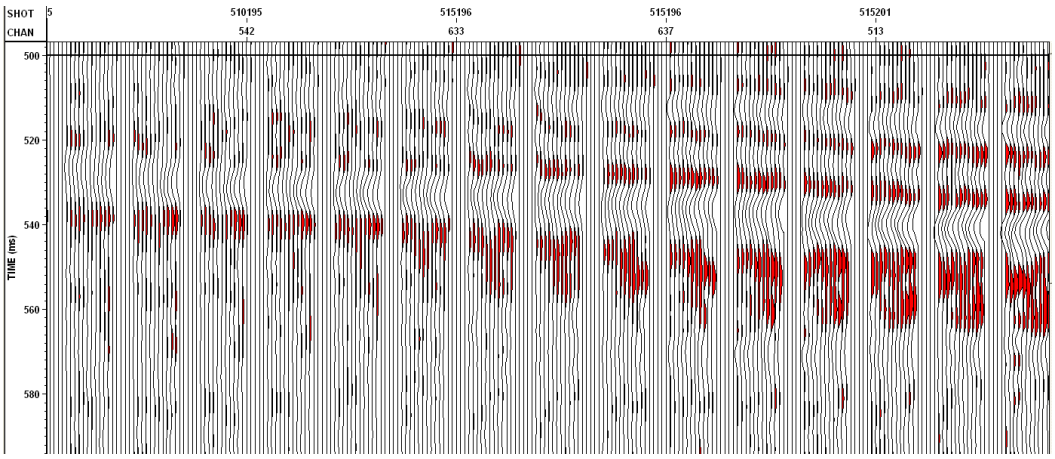

Figure 107 – Example of AVA displaying a tuning effect occurring on a thickening coal seam. The transition is gradual until reaching the maximum amplitude, generally constant over the angle of incidence.

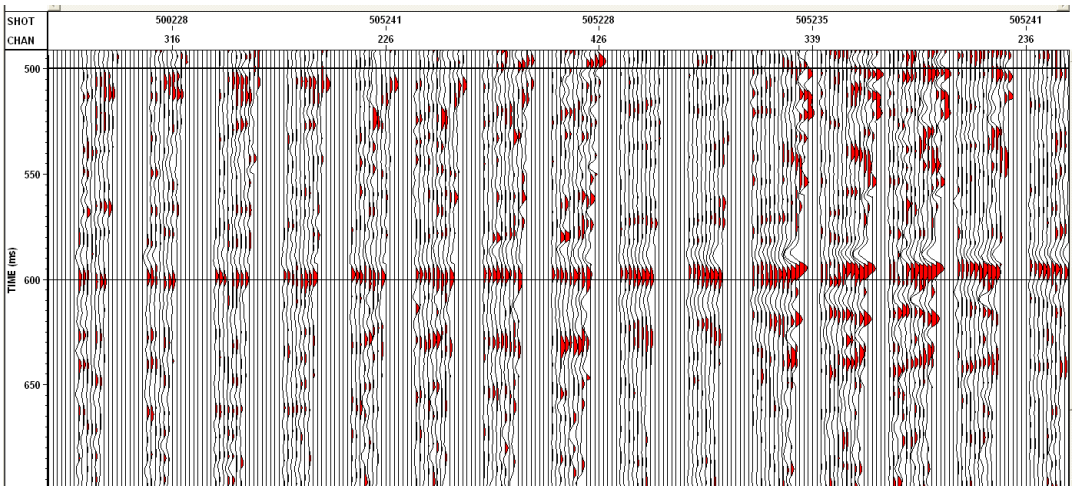

Figure 108 – Second example of AVA displaying a tuning effect occurring on a thickening coal seam.

5.4. PRESENCE OF MULTIPLE SEAMS

The presence of two coal seams, each of them having a 1 meter average thickness, also contributes to the tuning effect mentioned in the preceding paragraph. They both affect:

- bandwidth (Figure 109)
- amplitude.

Figure 109, Figure 110 and Figure 111 show the influence of the varying distance between seams on the bandwidth and reflection coefficient at zero incidences, with raising amplitudes in some cases (constructive interferences between top and bottom reflections), and decreasing in others (destructive interferences). By taking into account the implications of section 5.3, it means that variations in reflection amplitudes with offset are a function of:

- targeted lithologies
- coal seam thickness
- nearby coal seams.

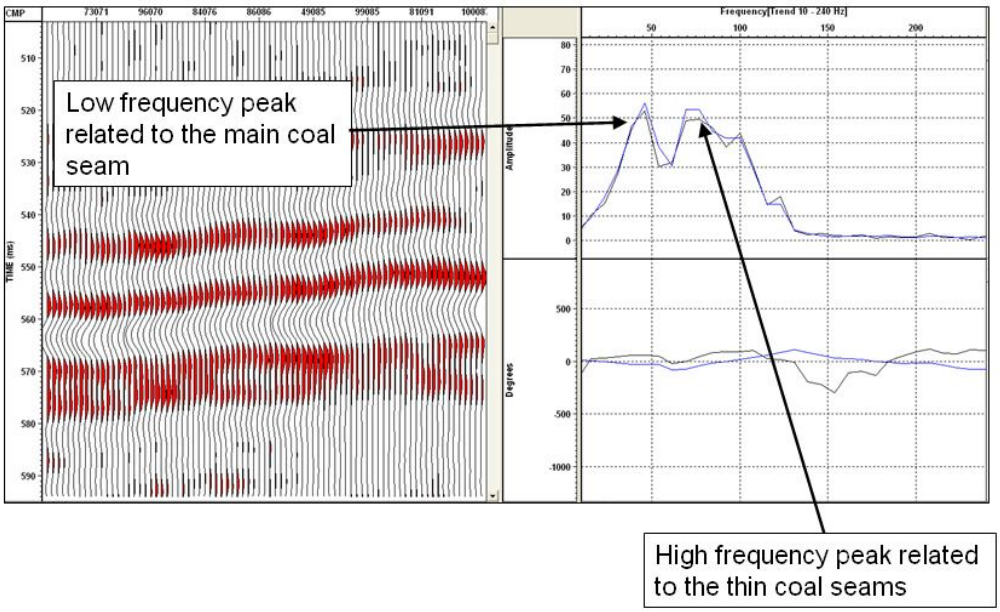

Figure 109 –Example of a seismic section and its spectrum attesting the clear presence of two different coal seams of different thicknesses.

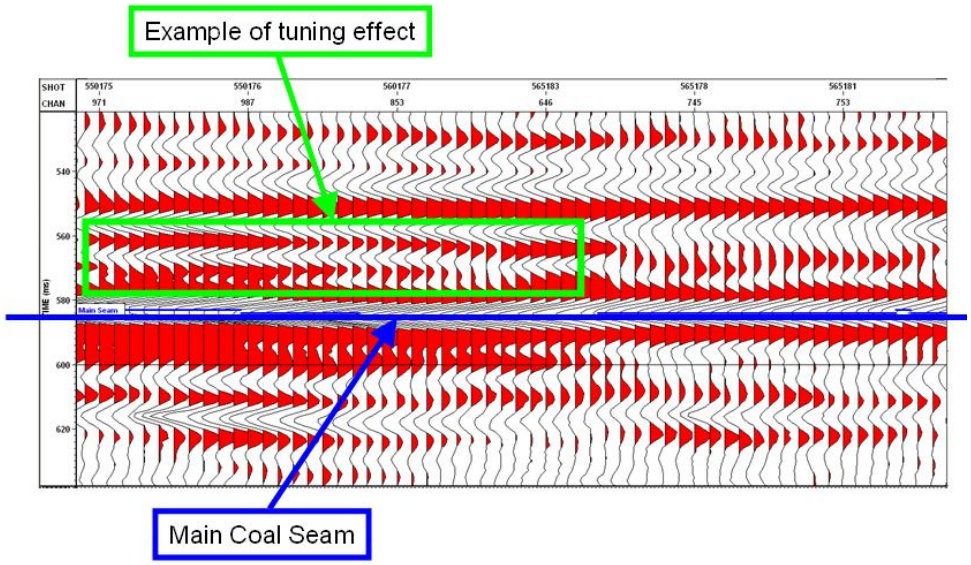

Figure 110 – Attested presence of tuning effect; a thin coal seam becomes "invisible" on the seismic section due to destructive interferences.

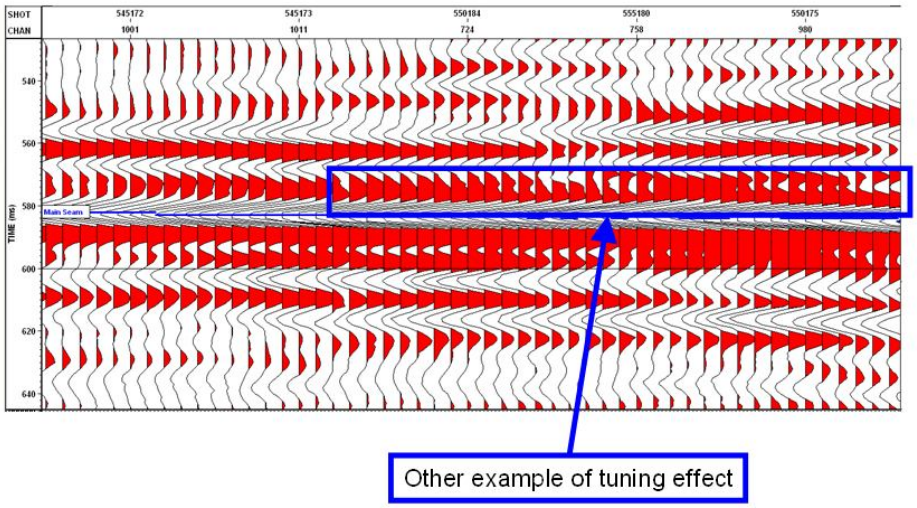

Figure 111 – Other example of tuning effect, with a coal seam progressively appearing.

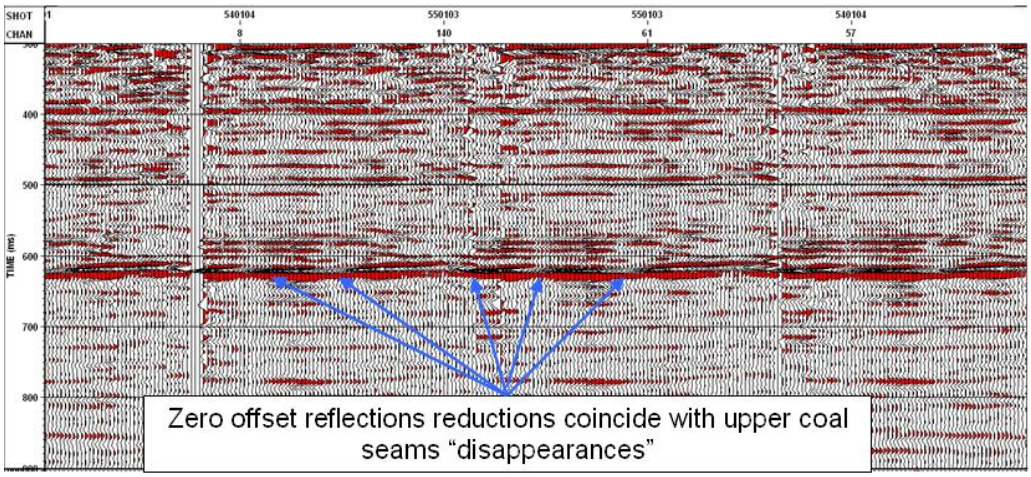

Figure 112 – Example of a zero offset section, on which the reflection coefficient diminutions coincide with appearances or/and disappearances of upper thin coal seams. These discontinuities in the 1m thin coal layers can be either of geological origin, or due to destructive interferences, the principal point is their influence on the target reflection coefficient.

5.5. SYNCLINES

The last geological feature to mention is the presence of a syncline in the data, detected in Figure 114. Figure 113 shows how such a geological feature affects the apparent reflector positioning. In AVO case, the interface's slope also affect the incidence of incident seismic waves, and then, indirectly, the variation of amplitude with offset in points a, b, c f and g. It also leads some to interferences between reflections at points d and e. As the reflection coefficients are not uniquely functions of lithologies, but also of reflector's slope and interferences with other reflections, the efficiency of AVO technology applied to synclines may be limited.

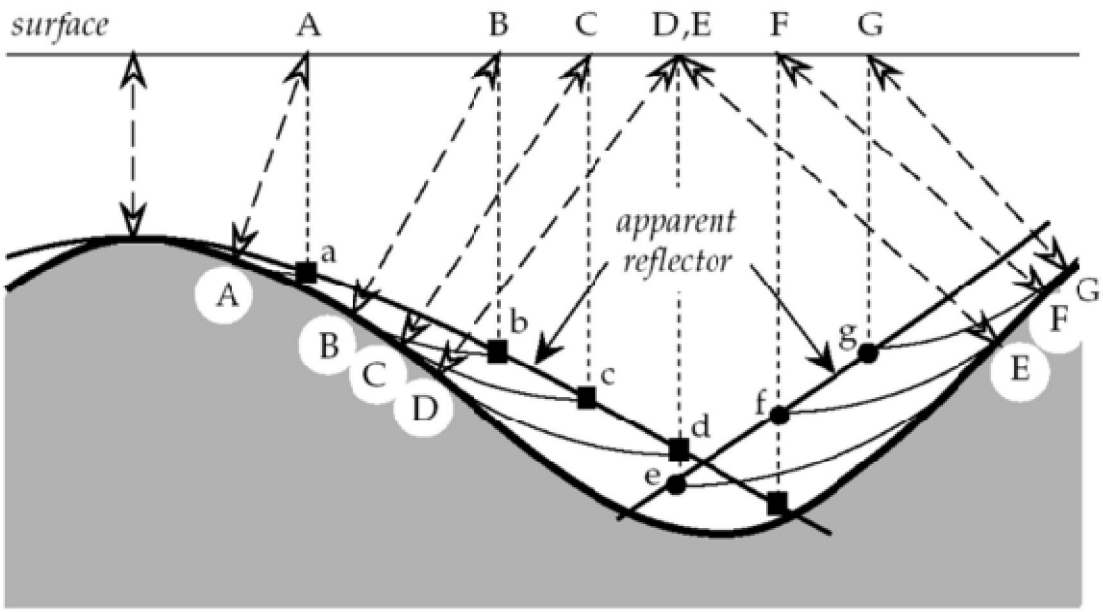

Figure 113 - Non-regular subsurface layers can create highly irregular paths (Stein and Wysession, 2003)

As it could be locally difficult to perform an AVO analysis in this specific area, a migration would naturally be advantageous. Resorting to a pre-stack depth migration would be at the expenses of price and amplitudes recovery; even if there is an obvious gain in the geometry, an extensive body of literature warns of the damage done to the reflection coefficients during the process.

By taking into account the results from sections 5.3 and 5.4, variations of reflection amplitudes with offset are a function of:

- targeted lithologies
- coal seam thickness
- coal seam's shape
- nearby coal seams.

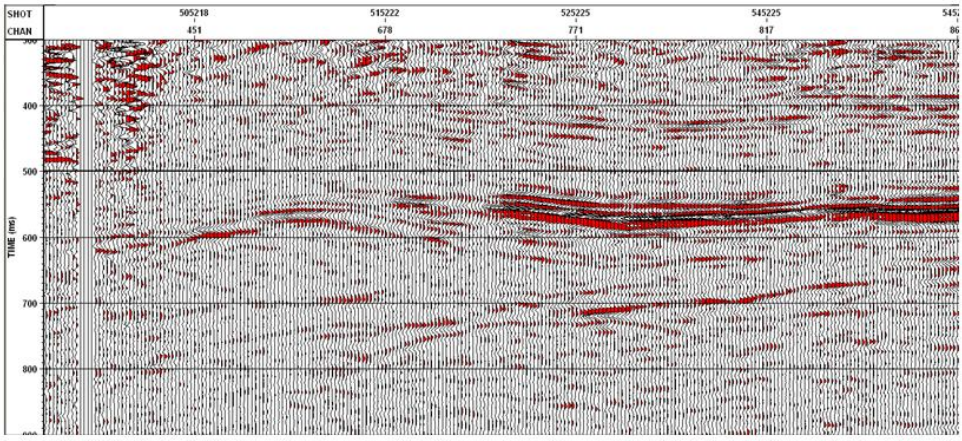

Figure 114 – Example of a syncline producing a fish tail pattern. Beyond the evident problems linked to seismic imagery and ability to clearly delineate the syncline's shape, the recorded amplitude is not resulting from a single reflection on top of a layer, but a combination of reflected waves interfering with each other.

5.6. CONCLUSIONS OF THIS CHAPTER

The purpose of this final chapter is to answer the following question: "In Daw Mill, UK, can AVO differentiate a mudstone from a sandstone roof over a coal seam?". The answer is no.

I initially wished to directly compare the recorded reflection coefficients with the numerical applications computed in the preceding chapter. If successful, a 3D distribution map of:

- reflection amplitude at zero incidence (Equation 83)
- the gradient (Equation 85)

was planned. These two parameters are the results of an inversion done with the Shuey's equation (Equation 82, defined in paragraph 2.3.7). If recorded seismic signal showed different variations of amplitude with offset between a reflection on mudstone roof and a sandstone roof, the next step was to analyse these maps for delineating Mudstone and Sandstone roofs areas.

A technical problem arising from the software Vista, developed by GEDCO, made this objective unachievable, and a led to qualitative approach, based on the bibliography written by Giochoco, a specialist of coal exploration with the seismic method.

His work oriented me to observe three patterns in reflection amplitudes at zero incidences:

- tuning effect
- presence of multiple seams
- synclines.

These examples have shown that variations of amplitude with offset are also a function of:

- coal seam thickness' variations
- coal seam shape's variations
- nearby coal seams.

By including the nature of targeted rocks, it means that the reflection coefficient is a function of at least four different parameters. As reflection coefficients are not only functions of lithologies and waves' angle of incidence, AVO is not a suitable technology for identifying the nature of roofs over coal seams. The 3D land seismic survey done in Daw Mill, UK, provided new information on the exploited coal seam's geometry. Although the use of AVO will admittedly not lead to the establishing of a distinction between mudstone and sandstone roofs over coal seams, the exploitation of this data set with technologies from petroleum engineering may provide mine planning with a new source of information.

Chapter 6.CONCLUSION

6.1. INTRODUCTION

The following chapter is the conclusion of this PhD thesis. It reiterates its background and objectives, and reviews AVO principles, their application in the methodology, and their results. Finally, outcomes and subjects requiring further work will work are discussed in the final part of the chapter.

6.2. REMINDER OF AVO PRINCIPLE

The principle of AVO technology relies on an observation described in Paragraph 1.1 which gave a description of AVO (Amplitude Versus Offset) technology. Let us consider a two layer case with their respective impedances. Two situations are possible:

- the top layer has a higher impedance
- the bottom layer has a higher impedance.

A seismic wave reflected at zero incidence will allow the determination of the presence of a boundary between these two layers, and the variation of reflected amplitudes with wave's angle of incidence will determine which layer has the highest impedance. In oil industry, analysis of the reflection coefficient enables the distinction to be made between:

1. a high impedance bottom layer(igneous intrusions, carbonates, hard streaks, lignites or wet sands)
2. a low impedance bottom layer(like gas sands on top of economically interesting reservoirs).

In the Gulf of Mexico, drilling in the location of a strong reflection coefficient at zero offset was equivalent to having a 20% probability of discovering a new oil producing reservoir. In a same area, analysis of reflection amplitude variations with offset led to an 80% drilling success (Allen & Peddy, 1993).

6.3. PhD OBJECTIVES

Paragraph 6.2 mentioned a 3D seismic survey done in Daw Mill (UK). If this improved the delineation of the coal seam geometry exploited in this region, additional efforts were required for the definition of the roof's lithologies and their extension over space. This problem is crucial as Sandstone is considered as a reliable roof, whereas Mudstone presents a risk of collapsing. AVO was thought of as a potential solution to this problem, and the specific question asked in this PhD was; "Can AVO detect a difference between a sandstone and a mudstone roof overlying a coal seam?".

Moreover, many numerical values can be attributed to the same mechanical property, depending on its method of determination. This discrepancy raised the problem of AVO calibration from the laboratory, for matching geotechnically (used by mine planners) and geophysically (provided by seismic data) determined parameters, and laid the basis of the second question; "Could an AVO calibration be done from laboratory, by adding an extra step based on a triaxial cell modification?".

The triaxial cell modification consisted of an array of piezo-components placed along the perimeter of the equipment's section (hence the name of sensitive sleeve), allowing the recording of the reflection coefficient at different angles (hence the idea of calibrating AVO from the laboratory).

The principle of its application consists of the collection, at different incidence angles, of different reflection coefficients on a bilithic structure (see Figure 3). Measured data from the laboratory should be compared to data from seismic surveys.

6.4. METHODOLOGY

The two questions of this PhD thesis:

1. Can AVO differentiate between a sandstone and a mudstone roof overlying a coal seam?
2. Could an AVO calibration be done from laboratory, by adding an extra step based on a triaxial cell modification?

are answered separately with the following chapters:

1. Introduction
2. Theoretical Review
3. Laboratory Testing : Collection of rock mechanical properties
4. Modelling : Application of these mechanical properties in modelling
5. Seismic: Comparison between modelling and real seismic data
6. Conclusion

They share Zoeppritz' equations as a common theoretical background. The resolution of this set of equations by Aki and Richards, introduced in the theoretical review, brings a set of analytical solutions (Equations 42 to 58), which computes the reflection coefficient of seismic waves at an interface with the following parameters:

- wave's angle of incidence
- layers respective P-wave velocity
- layers respective S-wave velocity
- layers respective density.

These physical properties, measured in the institute of Petroleum Engineering at the Heriot-Watt University, have been used in the solutions mentioned for assessing the expected reflection coefficient at a:

- Mudstone roof/coal interface
- Sandstone roof/coal interface.

Application of the parameters average values and distributions led to the same conclusion; AVO can theoretically differentiate between a sandroof and mudroof over a semi infinite coal layer. However, the coal seam's limited thickness may limit AVO’s ability, because it is in fact at the origin of interferences between reflections on top and bottom of the seam. Analysis of seismic data confirmed the presence of tuning effect, and led to the conclusion that AVO is ineffective in differentiating the two roof lithologies of interest.

Similarly, data collected from the modified Hoek cell should have been compared to synthetic data modelled with COMSOL MULTIPHYSICS, but piezo-components non-adapted for the circumstances have prevented this comparison due to their inability to transmit and record any signal through sandstone.

Abstracts of each chapter, as presented in the introduction of this PhD thesis, are respectively:

Chapter 1: Introduction

Chapter 2: this litterature Review discussed the basics of AVO, defined by the combination of elastic wave propagation on one hand, and the Zoeppritz's (1907) boundary conditions between two elastic layers on the other. The second part of this chapter focused on the direct link between wave propagation/reflection and rock mechanical properties and seismic processing related problems, and on the discrepancies betwen the initial hypothesises and:

1. the finely layered media observed at seismic and ultrasonic scales
2. the potentialy different boundary conditions at ultrasonic scale.

Chapter 3: Laboratory Testing. While the initial roof and floor's geotechnical database provided a useful dataset, the mechanical properties of coal seams were sparse and incomplete, hence the need to collect them in the rock laboratory facility of the Petroleum Engineering Institute (within the Heriot-Watt University). Although initially undesirable, this situation proved to have a positive outcome; the definition of a probability distribution for each mechanical property.
This effort was presented in details in the first part of the third chapter, before focusing on the tests done with the modified triaxial cell's prototype (also called Sensitive Sleeve), the first tests of which were promising while using coal samples. On the other hand, the attenuation within our sandstone samples did not allow any acquisition of any transmitted or reflected wave.

Chapter 4: Application of the laboratory data in modelling. The probability distributions (defined in Chapter 3) were used in the fourth chapter, through Aki and Richards' solutions to the Zoeppritz equations, for statistically proving the ability of AVO to discriminate Mudroof from Sandroof. Secondly, mean values were used in synthetic acquisitions within a sensitive sleeve model, in order to be compared with the real tests.

Chapter 5: AVO analysis of seismic data. In Chapter 4, as modelling showed an ability to differenciate the two different roofs mentionned, the final chapter of this PD thesis was to check the real applicabilty of AVO in mine planning.

Chapter 6: The conclusions review the data collected in the laboratory, the definition of their probability distribution, and their application in modelling. These efforts have proven that theoretically, in Daw Mill, Sandroofs can be differenciated from Mudroofs over a coal seam by using AVO. However, its practical application is compromised by the presence of cyclothems, which induce:

1. a tuning effect within (between) a (different) coal seam(s)
2. a limited roofs thickness (compared to the main seismic wavelength) leading to a potential inability to perform any characterisation.

Work on the triaxial cell's modification led to:

1. the discovery of potentially different boundary conditions at ultrasonic frequencies (theory)
2. the developement of a graphical user interface for modelling synthetic acquisitions (modelling)

3. a successful attempt in improving the signal to noise ratio (experimental effort)

6.5. RESULTS

The purpose of this PhD is to answer these two questions:

1. Can AVO differentiate between a sandstone and a mudstone roof overlying a coal seam?
2. Could an AVO calibration be done from laboratory, by adding an extra step based on a triaxial cell modification?

The theoretical answer to the first question is yes, but AVO is not applicable in Daw Mill due to the presence of tuning effect.

Concerning the second question, investigations into wave propagation coupled to other physical phenomena (see paragraph 2.4.6) has led to the modelling of the propagation of a wave in a thermo-elastic medium. This modelling showed the non-negligibility of this phenomenon coupling two different physics, and led to the conclusion that amplitudes recorded in laboratory and in seismic surveys may not be directly compared. Further development of the sensitive sleeve requires a better understanding of the theory developed by Zener (paragraph 2.4.7).

6.6. OUTCOMES

The resolution of problems unanticipated by the initial methodology for this PhD thesis has provided benefits for seismic, the laboratory and has led to the development of the sensitivie sleeve.

The benefit for seismic is the detection of tuning effect, and problems inherent to the limited thickness of roofs over coal seams.

The benefits brought to the laboratory are:

- the application of stacking to improve the signal to noise ratio of a trace recording an ultrasonic wave propagating in a core (see paragraph 3.3.9)
- an explanation for the static/dynamic discrepancy observed between ultrasonic and static measurements in laboratory (paragraph 2.4.7)
- an attempt to recalibrate laboratory measurements to the scale of seismic data (see paragraph 3.2.7)
- an automatic picking algorithm of ultrasonic first arrivals (see paragraph 3.2.6).

Finally, further efforts towards the development of the sensitive sleeve will benefit from the detection of:

- spherical waves (see paragraph 4.2.5)
- elastic wave propagation coupled to other physical phenomena

these two cases affect the reflection coefficient and potentially prevent a direct calibration of AVO from the laboratory.

6.7. FURTHER RECOMMENDED WORK

This PhD thesis has answered the two questions:

1. Can AVO differentiate between a sandstone and a mudstone roof overlying a coal seam?
2. Could an AVO calibration be done from laboratory, by adding an extra step based on a triaxial cell modification?

With the two following answers:

1. Theoretically: yes, but AVO is not applicable in Daw Mill due to tuning effect
2. Theoretically, a straightforward comparison between reflection coefficients recorded in laboratory and in a seismic survey may not be possible.

These answers including elements from seismic exploration, laboratory methods and R&D raises new questions with a similar problem;"Could the modification on the triaxial cell help a seismic data inversion algorithm in identifying a specific lithology over coal seams?"

For the detection and delineation of Sandstone roofs, an inversion algorithm unaffected by the presence of tuning effect (unlike inversions based on Shuey's approximation described in paragraph see 2.3.7) could in fact be more appropriate than AVO. The testing of this inversion algorithm will require a reconnaissance effort, and should have the ability to differentiate three different lithologies known as potential roofs over coal seams in the region of Daw Mill:

- Sandstone
- Mudstone
- Siltstone.

This reconnaissance will require, as in the third chapter of this PhD thesis, data collection in the laboratory. The mechanical properties collected may require up scaling. This recalibration could be based on the effort presented in the aforementioned chapter, and should be more elaborate and accurate.

This recalibration effort shares a common theoretical background with the triaxial cell modification; the theory of Zener(see paragraph 2.4.7), which describes elastic wave propagation coupled to other physical phenomena. If applied to AVO calibration from the laboratory, a better understanding of this phenomenon's consequences on reflection coefficients should precede any further development of the sensitive sleeve.

Sensitive sleeve development also requires technical and experimental solutions.

The technical problem to solve is the ability to record ultrasonic waves through sandstone. To do so, piezo-crystals more powerful than the ones used in this PhD thesis are required. This fact leads to two potential solutions:

- making no compromise on the resolution (and keeping a sensor every 12 degrees, like in figure 54), and waiting for further improvements from piezo-technology
- making a compromise on the resolution, and using bigger (and then, more powerful) piezo-components spaced every 18 degrees, as proposed by equation 133.

The ability to record an ultrasonic wave shall lead to the next step; records of wave propagation in a bilithic structure (see figure 52). But could it be possible to create,

between two samples in laboratory, an interface representative of the contact between two lithologies in a coal mine?

CHAPTER 7: APPENDIXES

Chapter 7.APPENDIXES

7.1. AMPLITUDE Vs OFFSET PROGRAMS

This program, coded in Matlab, is an application of the analytical solutions of the Zoeppritz's Equations, and computed by Aki and Richards.

This program has been the basis of many reflection coefficients computed in this PhD thesis, and has been modified from time to time in order to take into account some phenomena, such as anisotropy.

```
%Romaric 22th March 2006
%Sandroof or mudroof on a coal layer
%Numerical solutions of the Zoepprit's Equations.
%Computation of the reflected PP and PS coefficients in both cases, with
%the exact formulae from trhe results of the Zoeppritz's equations, from
%the book of Aki and Richards

clear all
close all

format long

%------------------------------------------------------------------------
%Computation of the exact numerical solution of the Zoeppritz's equations,
%for incident P waves

%Properties of shales
%P and S-wave respective velocities in m/s
a1=3770;
b1=1532;
%Density in kg/m3
Ro1=2415;

%Properties of coal
a2=2289.432;
b2=1356;
Ro2=1415;

%Definition of reflection angles
i1=0:0.1:90;
%Definition of ray parameter
p=sind(i1)/a1;
j1=asind(b1*p);
i2=asind(a2*p);
j2=asind(b2*p);

%Definition of the repeated used variables
```

```
a=Ro2*(1-2*b2^2*p.^2)-Ro1*(1-2*b1^2*p.^2);
b=Ro2*(1-2*b2^2*p.^2)+2*Ro1*b1^2*p.^2;
c=Ro1*(1-2*b1^2*p.^2)+2*Ro2*b2^2*p.^2;
d=2*(Ro2*b2^2-Ro1*b1^2);

%Repeated used cosine dependent terms
E=b.*cosd(i1)/a1+c.*cosd(i2)/a2;
F=b.*cosd(j1)/b1+c.*cosd(j2)/b2;
G=a-d.*cosd(i1)/a1.*cosd(j2)/b2;
H=a-d.*cosd(i2)/a2.*cosd(j1)/b1;

D=E.*F+G.*H.*p.^2;

%Computation of the Coefficients for an incident P-wave
RppShales=((b.*cosd(i1)/a1-c.*cosd(i2)/a2).*F-
(a+d.*cosd(i1)/a1.*cosd(j2)/b2).*H.*p.^2)./D;
RpsShales=-2*cosd(i1)/a1.*(a.*b+c.*d.*cosd(i2)/a2.*cosd(j2)/b2).*p*a1./(b1*D);
TppShales=2*Ro1*cosd(i1)/a1.*F*a1./(a2*D);
TpsShales=2*Ro1*cosd(i1)/a1.*H.*p*a1./(b2*D);

%Computation of the Coefficients for an incident S-wave
RspShales=-2*cosd(j1)/b1.*(a.*b+c.*d.*cosd(i2)/a2.*cosd(j2)/b2).*p*b1./(a1.*D);
RssShales=-((b.*cosd(j1)/b1-c.*cosd(j2)/b2).*E-
(a+d.*cosd(i2)/a2.*cosd(j1)/b1).*G.*p.^2)./D;
TspShales=-2*Ro1*cosd(j1)/b1.*G.*p*b1./(a2*D);
TssShales=2*Ro1*cosd(j1)/b1.*E*b1./(b2*D);

%Computation of the coefficients for an upgoing incident P-wave
RppuShales=2*Ro2*cosd(i2)/a2.*F*a2./(a1*D);
RpsuShales=-2*Ro2*cosd(i2)/a2.*G.*p*a2./(a2*D);
TppuShales=-1*((b.*cosd(i1)/a1-
c.*cosd(i2)/a2).*F+(a+d.*cosd(i2)/a2.*cosd(j1)/b1).*G.*p.^2)./D;
TpsuShales=2*cosd(i2)/a2.*(a.*c+b.*d.*cosd(i1)/a1.*cosd(j1)/b1).*p*a2./(b2*D);

%Computation of the coefficients for an upgoing incident S-wave
RspuShales=2*Ro2*cosd(j2)/b2.*H.*p*b2./(a1*D);
RssuShales=2*Ro2*cosd(j2)/b2.*E*b2./(b1*D);
TspuShales=2*cosd(j2)/b2.*(a.*c+b.*d.*cosd(i1)/a1.*cosd(j1)/b1).*p*b2./(a2*D);
TssuShales=((b.*cosd(j1)/b1-
c.*cosd(j2)/b2).*E+(a+d.*cosd(i1)/a1.*cosd(j2)/b2).*H.*p.^2)./D;

%------------------------------------------------------------------------
%Comparison with a sand roof on a coal layer

%Properties of Sandstone
a1=2695;
b1=1775;
Ro1=2493;
```

```
%Definition of the reflection angles
i1=0:0.1:90;
%Definition of the ray parameter
p=sind(i1)/a1;
j1=asind(b1*p);
i2=asind(a2*p);
j2=asind(b2*p);

%Definition of the repeated used variables
a=Ro2*(1-2*b2^2*p.^2)-Ro1*(1-2*b1^2*p.^2);
b=Ro2*(1-2*b2^2*p.^2)+2*Ro1*b1^2*p.^2;
c=Ro1*(1-2*b1^2*p.^2)+2*Ro2*b2^2*p.^2;
d=2*(Ro2*b2^2-Ro1*b1^2);

%Repeated used cosine dependent terms
E=b.*cosd(i1)/a1+c.*cosd(i2)/a2;
F=b.*cosd(j1)/b1+c.*cosd(j2)/b2;
G=a-d.*cosd(i1)/a1.*cosd(j2)/b2;
H=a-d.*cosd(i2)/a2.*cosd(j1)/b1;

D=E.*F+G.*H.*p.^2;

%Computation of the Coefficients for an incident P-wave
RppSand=((b.*cosd(i1)/a1-c.*cosd(i2)/a2).*F-
(a+d.*cosd(i1)/a1.*cosd(j2)/b2).*H.*p.^2)./D;
RpsSand=-2*cosd(i1)/a1.*(a.*b+c.*d.*cosd(i2)/a2.*cosd(j2)/b2).*p*a1./(b1*D);
TppSand=2*Ro1*cosd(i1)/a1.*F*a1./(a2*D);
TpsSand=2*Ro1*cosd(i1)/a1.*H.*p*a1./(b2*D);

%Computation of the Coefficients for an incident S-wave
RspSand=-2*cosd(j1)/b1.*(a.*b+c.*d.*cosd(i2)/a2.*cosd(j2)/b2).*p*b1./(a1.*D);
RssSand=-((b.*cosd(j1)/b1-c.*cosd(j2)/b2).*E-
(a+d.*cosd(i2)/a2.*cosd(j1)/b1).*G.*p.^2)./D;
TspSand=-2*Ro1*cosd(j1)/b1.*G.*p*b1./(a2*D);
TssSand=2*Ro1*cosd(j1)/b1.*E*b1./(b2*D);

%Computation of the coefficients for an upgoing incident P-wave
RppuSand=2*Ro2*cosd(i2)/a2.*F*a2./(a1*D);
RpsuSand=-2*Ro2*cosd(i2)/a2.*G.*p*a2./(a2*D);
TppuSand=-1*((b.*cosd(i1)/a1-
c.*cosd(i2)/a2).*F+(a+d.*cosd(i2)/a2.*cosd(j1)/b1).*G.*p.^2)./D;
TpsuSand=2*cosd(i2)/a2.*(a.*c+b.*d.*cosd(i1)/a1.*cosd(j1)/b1).*p*a2./(b2*D);

%Computation of the coefficients for an upgoing incident S-wave
RspuSand=2*Ro2*cosd(j2)/b2.*H.*p*b2./(a1*D);
RssuSand=2*Ro2*cosd(j2)/b2.*E*b2./(b1*D);
TspuSand=2*cosd(j2)/b2.*(a.*c+b.*d.*cosd(i1)/a1.*cosd(j1)/b1).*p*b2./(a2*D);
```

```
 TssuSand=((b.*cosd(j1)/b1-
c.*cosd(j2)/b2).*E+(a+d.*cosd(i1)/a1.*cosd(j2)/b2).*H.*p.^2)./D;

 %------------------------------------------------------------------------
 %Graphical part

 %Graphics for simply comparing the two Rpp coefficients
 figure,plot(i1,RppShales,'b')
 hold on, plot(i1,RppSand,'r')
 Title('Comparison between a sandroof and a mudroof overlying a coal layer');
 legend('Mudroof','Sandroof','Location','SouthWest');
 xlabel('Angle of Incidence (Degrees)')
 ylabel('Rpp')
 grid
```

7.2. RAY TRACING PROGRAMS

7.2.1. Description

The theory on which relies this program is based on the work done by Hagedoorn; whereas to consider a layer having a constant velocity, a linear velocity increase (or decrease) is considered, leading to non straight ray-pathes. It has been seen in the Theoretical chapter that such pattern may lead to a 20% incidence angle's underestimation; a problematic fact when combined to any AVO inversion.

7.2.2. Main Code

This code has also been written in Matlab

```
 clear all
 close all

 offsetmax=960;

 RC=zeros(30000,offsetmax/10);
 traveltimes=1:30628;
 traveltimes=traveltimes/10000;

 figure

 %Reflection in the first layer
 for offset = 10:10:offsetmax

    %------------------------------------------------------------------
    %The different layers
    reflecteur(offsetmax)

    %------------------------------------------------------------------
```

```
%The direct arrivals

%In the first layer
[trc,Dp]=directwave(offset);%Direct P-waves' arrival
RC(trc,offset/10)=Dp;

[trc,Ds]=directwaveS(offset);%Direct S-waves' arrival
if RC(trc,offset/10)==0
   RC(trc,offset/10)=Ds;
elseif RC(trc,offset/10)~=0
   RC(trc,offset/10)=RC(trc,offset/10)+Ds;
end

%In the second layer
[trc,Tpp]=DirectPLayer2(offset);
if isnan(trc)==0
   if RC(trc,offset/10)==0
      RC(trc,offset/10)=Tpp;
   elseif RC(trc,offset/10)~=0
      RC(trc,offset/10)=RC(trc,offset/10)+Tpp;
   end
end

[trc,Tss]=DirectSLayer2(offset);
if isnan(trc)==0
   if RC(trc,offset/10)==0
      RC(trc,offset/10)=Tss;
   elseif RC(trc,offset/10)~=0
      RC(trc,offset/10)=RC(trc,offset/10)+Tss;
   end
end

%-------------------------------------------------------------------
%The remains of the direct waves when we don't have a constant velocity
%inside a layer
[trc,Tpp]=PPLayer2(offset);
if isnan(trc)==0
   if RC(trc,offset/10)==0
      RC(trc,offset/10)=Tpp;
   elseif RC(trc,offset/10)~=0
      RC(trc,offset/10)=RC(trc,offset/10)+Tpp;
   end
end

%-------------------------------------------------------------------
%the P-waves' reflections
```

```
%First Layer
[trc,Rpp]=reflectionLayer1(offset);
if isnan(trc)==0 & isreal(Rpp)==1
   if RC(trc,offset/10)==0
      RC(trc,offset/10)=Rpp;
   elseif RC(trc,offset/10)~=0
      RC(trc,offset/10)=RC(trc,offset/10)+Rpp;
   end
end

%Second layer
clear trc Rpp
[trc,Rpp]=relectionLayer2b(offset);
if isnan(trc)==0 & isreal(Rpp)==1
   if RC(trc,offset/10)==0
      RC(trc,offset/10)=Rpp;
   elseif RC(trc,offset/10)~=0
      RC(trc,offset/10)=RC(trc,offset/10)+Rpp;
   end
end

%---------------------------------------------------------------------
%the S-wave's reflections

%First Layer
[trc,Rss]=reflectionSLayer1(offset);
if isnan(trc)==0 & isreal(Rss)==1
   if RC(trc,offset/10)==0
      RC(trc,offset/10)=Rss;
   elseif RC(trc,offset/10)~=0
      RC(trc,offset/10)=RC(trc,offset/10)+Rss;
   end
end

%Second Layer
[trc,Rss]=reflectionSLayer2b(offset);
if isnan(trc)==0 & isreal(Rss)==1
   if RC(trc,offset/10)==0
      RC(trc,offset/10)=Rss;
   elseif RC(trc,offset/10)~=0
      RC(trc,offset/10)=RC(trc,offset/10)+Rss;
   end
end

%---------------------------------------------------------------------
%The PS-waves' reflections
```

```
%Second Layer
[trc,Rps]=reflectionPSLayer2b(offset);
if isnan(trc)==0 & isreal(Rss)==1
   if RC(trc,offset/10)==0
      RC(trc,offset/10)=Rps;
   elseif RC(trc,offset/10)~=0
      RC(trc,offset/10)=RC(trc,offset/10)+Rps;
   end
end

%-------------------------------------------------------------------
%The refracted waves

%Refracted P-waves in the first layer
[trc,Rp]=refractedP(offset);
if RC(trc,offset/10)==0
   RC(trc,offset/10)=Rp;
elseif RC(trc,offset/10)~=0
   RC(trc,offset/10)=RC(trc,offset/10)+Rp;
end

%Refracted S-waves in the second layer
[trc,Rs]=refractedS(offset);
if RC(trc,offset/10)==0
   RC(trc,offset/10)=Rs;
elseif RC(trc,offset/10)~=0
   RC(trc,offset/10)=RC(trc,offset/10)+Rs;
end

%The refracted waves at the interface between the second and second
%layer
[trc,re]=refractedLayer2(offset);%P refracted waves
if isnan(trc)==0
   if RC(trc,offset/10)==0
      RC(trc,offset/10)=re;
   elseif RC(trc,offset/10)~=0
      RC(trc,offset/10)=RC(trc,offset/10)+re;
   end
end

[trc,re]=refractedSLayer2(offset);%S refracted waves
if isnan(trc)==0
   if RC(trc,offset/10)==0
      RC(trc,offset/10)=re;
   elseif RC(trc,offset/10)~=0
      RC(trc,offset/10)=RC(trc,offset/10)+re;
   end
```

```
    end

end

%-------------------------------------------------------------------------
%-------------------------------------------------------------------------
%Plot of the Synthetic Seismic
signal=0:0.01:2*pi;
signal=100*sin(signal).*exp(-signal/2);
figure,plot(signal)
figure
for offset=1:1:96

    A=conv(signal,RC(:,offset));
    hold on, plot(10*offset+A,traveltimes)

end
set(gca,'YDir','reverse')
```

7.2.3. Function reflecteur

```
function reflecteur(offsetmax)

%Dessin des relfecteurs plans dans le plan (XZ)

z1=5;
z2=130;

subplot(211)
plot([0 offsetmax],[0 0],'k','LineWidth',2)
hold on
plot([0 offsetmax],[z1 z1],'k','LineWidth',2)
hold on
plot([0 offsetmax],[z2 z2],'k','LineWidth',2)
```

7.2.4. Function directwave

```
function [trc,D]=directwave(offset)

D=1;
%-------------------------------------------------------------------------
%-------------------------------------------------------------------------
%Initialisation of the parameters
a1=3811;
b1=2263;
ratio=a1/b1;
Vp1=638;
Vs1=Vp1/ratio;
```

```
%------------------------------------------------------------------------
%------------------------------------------------------------------------
%Computation of the direct wave's traveltime
traveltime=offset/Vp1;
trc=floor(traveltime*10^4);

%------------------------------------------------------------------------
%------------------------------------------------------------------------
%We plot the result
subplot(212)
hold on
plot(offset,traveltime,'o')
```

7.2.5. Function directwaveS

```
function [trc,D]=directwaveS(offset)

D=1;
%------------------------------------------------------------------------
%------------------------------------------------------------------------
%Initialisation of the parameters
a1=3811;
b1=2263;
ratio=a1/b1;
Vp1=638;
Vs1=Vp1/ratio;

%------------------------------------------------------------------------
%------------------------------------------------------------------------
%Computation of the direct wave's traveltime
traveltime=offset/Vs1;
trc=floor(traveltime*10^4);

%------------------------------------------------------------------------
%------------------------------------------------------------------------
%We plot the result
subplot(212)
hold on
plot(offset,traveltime,'^')
```

7.2.6. Function directPlayer2

```
function [trc,Tpp]=DirectPLayer2(offset)

persistent transition

trc=NaN;
```

```
Tpp=i;
a1=3811;
b1=2263;
ratio=a1/b1;
%--------------------------------------------------------------------------
%--------------------------------------------------------------------------
%Initialzation of the parameters
p(1)=0;
Vp1=638;
Vp2=1009.6;
Vp3=3108;
%We deduce the numerical values of the other parameters from the recorded
%P-waves' velocity
Vs1=Vp1/ratio;
Vs2=Vp2/ratio;
Vs3=Vp3/ratio;
rho1=(5825+Vp1)/4.1913;
rho2=(5825+Vp2)/4.1913;
rho3=(5825+Vp3)/4.1913;
%Depth of the reflectors
z1=5;
z2=130;
%Velocity at the bottom of the second layer
k=885/70;
Vpend2=k*(z2-z1)+Vp2;
Vsend2=Vpend2/ratio;
%Sampling parameter relative to the ray path tracing
dx=0.1;

%--------------------------------------------------------------------------
%--------------------------------------------------------------------------
%We look for the ray parameter which links the source and the geophone

%Newton-Raphson method
for it=1:100

   X=p(it)*z1/sqrt(Vp1^(-2)-p(it)^2)+p(it)*(z2-z1)/sqrt(Vp2^(-2)-p(it)^2)-offset/2;
   Xprim=z1/sqrt(Vp1^(-2)-p(it)^2)+(p(it)^2)*z1/((sqrt(Vp1^(-2)-p(it)^2))^3)+...
      (z2-z1)/sqrt(Vp2^(-2)-p(it)^2)+(p(it)^2)*(z2-z1)/((sqrt(Vp2^(-2)-p(it)^2))^3);
   p(it+1)=p(it)-X/Xprim;

   if isnan(X)==1 | isreal(X)==0

      break

   end
```

```
end

%False position Method

if isnan(X)==0 & isreal(X)==1

    A2=885/70;
    transition=p(it);
    clear p
    a(1)=transition/2;
    b(1)=transition;

    for it=1:100

        fa=2*a(it)*z1/sqrt(Vp1^(-2)-a(it)^2)+2/(a(it)*A2)*sqrt(1-(a(it)*Vp2)^2)-
offset;
        fb=2*b(it)*z1/sqrt(Vp1^(-2)-b(it)^2)+2/(b(it)*A2)*sqrt(1-(b(it)*Vp2)^2)-
offset;
        c(it)=a(it)-(a(it)-b(it))*fa/(fa-fb);

        if sign(fa)==sign(fb)

            a(it+1)=c(it);
            b(it+1)=b(it);

        elseif sign(fa)~=sign(fb)

            a(it+1)=a(it);
            b(it+1)=c(it);

        end

        if isnan(c(it))==1 | isreal(c(it))==0

            break
            sprintf('toto')
            fa
            fb

        end

    end

else

    clear a b p
    A2=885/70;
```

```
    a(1)=transition/2;
    b(1)=transition;

    for it=1:100

        fa=2*a(it)*z1/sqrt(Vp1^(-2)-a(it)^2)+2/(a(it)*A2)*sqrt(1-(a(it)*Vp2)^2)-
offset;
        fb=2*b(it)*z1/sqrt(Vp1^(-2)-b(it)^2)+2/(b(it)*A2)*sqrt(1-(b(it)*Vp2)^2)-
offset;
        c(it)=a(it)-(a(it)-b(it))*fa/(fa-fb);

        if sign(fa)==sign(fb)

           a(it+1)=c(it);
           b(it+1)=b(it);

        elseif sign(fa)~=sign(fb)

           a(it+1)=a(it);
           b(it+1)=c(it);

        end

        if isnan(c(it))==1 | isreal(c(it))==0

           break
           sprintf('toto')
           fa
           fb

        end

    end

end

%---------------------------------------------------------------------------
%---------------------------------------------------------------------------
%We plot the result

%Once we get the numerical value of the ray parameter, we plot it
if exist('c')==1

    if isnan(fb)==0 & isreal(fb)==1 & offset~=10

        p=c(it-1);
```

```
%Ray path in the first layer
X=p*z1/sqrt(Vp1^(-2)-p^2);

if (X/sqrt(X^2+z1^2))<(Vp1/Vp2)

   %-------------------------------------------------------
   %Raypath

   %Raypath in the second layer which velocity vary linearly with
   %depth.
   k=885/70;
   Vz=1/p;
   R=Vz/k;
   theta0=asin(p*Vp2);
   Xz=R*cos(theta0);
   h =R*sin(theta0);
   x2=0:dx:Xz;
   theta=acos((x2-Xz)/R);
   y2=R*sin(theta)-h;
   x2=x2+X;
   y2=y2+5;
   xr2=x2(find(y2<=130));
   yr2=y2(find(y2<=130));

   if length(xr2)==length(x2) & length(x2)~=0 &
(floor(2*x2(length(x2))))==(offset-1)

      %Raypath of the reflected rays in the first layer at a
      %constant velocity.
      subplot(211)
      hold on
      plot([0 X],[0 z1],'b')
      set(gca,'YDir','reverse')
      axespace=axis;

%        whos x2
%        x2(length(x2))

      plot(x2,y2,'b')
      plot(2*x2(length(x2))-x2,y2,'b')
      plot([2*x2(length(x2))-X 2*x2(length(x2))],[z1 0],'b')

      %-------------------------------------------------------
      %Traveltime

      A2=k;
      B2=Vp2;
```

```
        traveltime=2*sqrt(X^2+z1^2)/Vp1;
        traveltime2=2/k*asinh(1/(p*Vp2));
        traveltime=traveltime+traveltime2;
        trc=floor(traveltime*10^4);
        subplot(212)
        hold on
        plot(offset,traveltime,'o')
        set(gca,'YDir','reverse')
        axetime=axis;

        %-------------------------------------------------------------
        %Reflection and transmission coefficients on the first
        %interface
        i1=asind(p*Vp1);%Angle of incidence
        j1=asind(Vs1*p);
        i2=asind(Vp2*p);
        j2=asind(Vs2*p);

        if isreal(i1)==1 & isreal(j1)==1 & isreal(i2)==1 & isreal(j2)==1

            %Definition of the repeated used variables
            a=rho2*(1-2*Vs2^2*p^2)-rho1*(1-2*Vs1^2*p^2);
            b=rho2*(1-2*Vs2^2*p^2)+2*rho1*Vs1^2*p^2;
            c=rho1*(1-2*Vs1^2*p^2)+2*rho2*Vs2^2*p^2;
            d=2*(rho2*Vs2^2-rho1*Vs1^2);

            %Repeated used cosine dependent terms
            E=b*cosd(i1)/Vp1+c*cosd(i2)/Vp2;
            F=b*cosd(j1)/Vs1+c*cosd(j2)/Vs2;
            G=a-d*cosd(i1)/Vp1*cosd(j2)/Vs2;
            H=a-d*cosd(i2)/Vp2*cosd(j1)/Vs1;

            D=E*F+G*H*p^2;

            %Transmission coefficient at the first interface
            Tpp12=2*rho1*cosd(i1)/Vp1*F*Vp1/(Vp2*D);
            %Transmission coefficient from the layer 2 to the layer 1,
            %for the way back from the reflection
            Tpp21=2*rho2*cosd(i2)/Vp2*F*Vp2/(Vp1*D);

            Tpp=Tpp12*Tpp21;

        end

    end

end
```

```
    end

end
```

7.2.7. Function DirectSlayer2

```
function [trc,Tpp]=DirectSLayer2(offset)

persistent transition

trc=NaN;
Tpp=i;
a1=3811;
b1=2263;
ratio=a1/b1;
%--------------------------------------------------------------------------
%--------------------------------------------------------------------------
%Initialzation of the parameters
p(1)=0;
Vp1=638;
Vp2=1009.6;
Vp3=3108;
%We deduce the numerical values of the other parameters from the recorded
%P-waves' velocity
Vs1=Vp1/ratio;
Vs2=Vp2/ratio;
Vs3=Vp3/ratio;
rho1=(5825+Vp1)/4.1913;
rho2=(5825+Vp2)/4.1913;
rho3=(5825+Vp3)/4.1913;
%Depth of the reflectors
z1=5;
z2=130;
%Velocity at the bottom of the second layer
k=885/70;
Vpend2=k*(z2-z1)+Vp2;
Vsend2=Vpend2/ratio;
%Sampling parameter relative to the ray path tracing
dx=0.1;

%--------------------------------------------------------------------------
%--------------------------------------------------------------------------
%We look for the ray parameter which links the source and the geophone

%Newton-Raphson method
for it=1:100
```

```
    X=p(it)*z1/sqrt(Vs1^(-2)-p(it)^2)+p(it)*(z2-z1)/sqrt(Vs2^(-2)-p(it)^2)-offset/2;
    Xprim=z1/sqrt(Vs1^(-2)-p(it)^2)+(p(it)^2)*z1/((sqrt(Vs1^(-2)-p(it)^2))^3)+...
       (z2-z1)/sqrt(Vs2^(-2)-p(it)^2)+(p(it)^2)*(z2-z1)/((sqrt(Vs2^(-2)-p(it)^2))^3);
    p(it+1)=p(it)-X/Xprim;

    if isnan(X)==1 | isreal(X)==0

       break

    end

 end

 %False position Method

 if isnan(X)==0 & isreal(X)==1

    A2=885/(70*ratio);
    transition=p(it);
    clear p
    a(1)=transition/2;
    b(1)=transition;

    for it=1:100

       fa=2*a(it)*z1/sqrt(Vs1^(-2)-a(it)^2)+2/(a(it)*A2)*sqrt(1-(a(it)*Vs2)^2)-offset;
       fb=2*b(it)*z1/sqrt(Vs1^(-2)-b(it)^2)+2/(b(it)*A2)*sqrt(1-(b(it)*Vs2)^2)-
offset;
       c(it)=a(it)-(a(it)-b(it))*fa/(fa-fb);

       if sign(fa)==sign(fb)

          a(it+1)=c(it);
          b(it+1)=b(it);

       elseif sign(fa)~=sign(fb)

          a(it+1)=a(it);
          b(it+1)=c(it);

       end

       if isnan(c(it))==1 | isreal(c(it))==0

          break
          sprintf('toto')
          fa
```

```
            fb

        end

    end

else

    clear a b p
    A2=885/(70*ratio);
    a(1)=transition/2;
    b(1)=transition;

    for it=1:100

        fa=2*a(it)*z1/sqrt(Vs1^(-2)-a(it)^2)+2/(a(it)*A2)*sqrt(1-(a(it)*Vs2)^2)-offset;
        fb=2*b(it)*z1/sqrt(Vs1^(-2)-b(it)^2)+2/(b(it)*A2)*sqrt(1-(b(it)*Vs2)^2)-
offset;
        c(it)=a(it)-(a(it)-b(it))*fa/(fa-fb);

        if sign(fa)==sign(fb)

            a(it+1)=c(it);
            b(it+1)=b(it);

        elseif sign(fa)~=sign(fb)

            a(it+1)=a(it);
            b(it+1)=c(it);

        end

        if isnan(c(it))==1 | isreal(c(it))==0

            break
            sprintf('toto')
            fa
            fb

        end

    end

end

%-----------------------------------------------------------------------
%-----------------------------------------------------------------------
```

```
%We plot the result

%Once we get the numerical value of the ray parameter, we plot it
if exist('c')==1

   if isnan(fb)==0 & isreal(fb)==1 & offset~=10

      p=c(it-1);

      %Ray path in the first layer
      X=p*z1/sqrt(Vs1^(-2)-p^2);

      if (X/sqrt(X^2+z1^2))<(Vs1/Vs2)

         %-------------------------------------------------------------
         %Raypath

         %Raypath in the second layer which velocity vary linearly with
         %depth.
         k=885/(70*ratio);
         Vz=1/p;
         R=Vz/k;
         theta0=asin(p*Vs2);
         Xz=R*cos(theta0);
         h =R*sin(theta0);
         x2=0:dx:Xz;
         theta=acos((x2-Xz)/R);
         y2=R*sin(theta)-h;
         x2=x2+X;
         y2=y2+5;
         xr2=x2(find(y2<=130));
         yr2=y2(find(y2<=130));

         if length(xr2)==length(x2) & length(x2)~=0 &
(floor(2*x2(length(x2))))==(offset-1)

            %Raypath of the reflected rays in the first layer at a
            %constant velocity.
            subplot(211)
            hold on
            plot([0 X],[0 z1],'b')
            set(gca,'YDir','reverse')
            axespace=axis;

%              whos x2
%              x2(length(x2))
```

```
plot(x2,y2,'b')
plot(2*x2(length(x2))-x2,y2,'b')
plot([2*x2(length(x2))-X 2*x2(length(x2))],[z1 0],'b')

%-------------------------------------------------------------
%Traveltime

A2=k;
B2=Vs2;
traveltime=2*sqrt(X^2+z1^2)/Vs1;
traveltime2=2/k*asinh(1/(p*Vs2));
traveltime=traveltime+traveltime2;
trc=floor(traveltime*10^4);
subplot(212)
hold on
plot(offset,traveltime,'^')
set(gca,'YDir','reverse')
axetime=axis;

%-------------------------------------------------------------
%Reflection and transmission coefficients on the first
%interface
i1=asind(p*Vp1);%Angle of incidence
j1=asind(Vs1*p);
i2=asind(Vp2*p);
j2=asind(Vs2*p);

if isreal(i1)==1 & isreal(j1)==1 & isreal(i2)==1 & isreal(j2)==1

   %Definition of the repeated used variables
   a=rho2*(1-2*Vs2^2*p^2)-rho1*(1-2*Vs1^2*p^2);
   b=rho2*(1-2*Vs2^2*p^2)+2*rho1*Vs1^2*p^2;
   c=rho1*(1-2*Vs1^2*p^2)+2*rho2*Vs2^2*p^2;
   d=2*(rho2*Vs2^2-rho1*Vs1^2);

   %Repeated used cosine dependent terms
   E=b*cosd(i1)/Vp1+c*cosd(i2)/Vp2;
   F=b*cosd(j1)/Vs1+c*cosd(j2)/Vs2;
   G=a-d*cosd(i1)/Vp1*cosd(j2)/Vs2;
   H=a-d*cosd(i2)/Vp2*cosd(j1)/Vs1;

   D=E*F+G*H*p^2;

   %Transmission coefficient at the first interface
   Tpp12=2*rho1*cosd(i1)/Vp1*F*Vp1/(Vp2*D);
   %Transmission coefficient from the layer 2 to the layer 1,
   %for the way back from the reflection
```

```
                Tpp21=2*rho2*cosd(i2)/Vp2*F*Vp2/(Vp1*D);

                Tpp=Tpp12*Tpp21;

            end

        end

    end

end
```

7.2.8. Function PPlayer2

```
function [trc,Tpp]=PPLayer2(offset)

persistent transition

trc=NaN;
Tpp=i;
a1=3811;
b1=2263;
ratio=a1/b1;
%---------------------------------------------------------------------------
%---------------------------------------------------------------------------
%Initialzation of the parameters
p(1)=0;
Vp1=638;
Vp2=1009.6;
Vp3=3108;
%We deduce the numerical values of the other parameters from the recorded
%P-waves' velocity
Vs1=Vp1/ratio;
Vs2=Vp2/ratio;
Vs3=Vp3/ratio;
rho1=(5825+Vp1)/4.1913;
rho2=(5825+Vp2)/4.1913;
rho3=(5825+Vp3)/4.1913;
%Depth of the reflectors
z1=5;
z2=130;
%Velocity at the bottom of the second layer
k=885/70;
Vpend2=k*(z2-z1)+Vp2;
Vsend2=Vpend2/ratio;
```

```
%Sampling parameter relative to the ray path tracing
dx=0.1;

%-------------------------------------------------------------------------
%-------------------------------------------------------------------------
%We look for the ray parameter which links the source and the geophone

%Methode de la secante
a(1)=1/Vp3;
a(2)=1/Vp2;

A2=885/70;

for it=2:100

    fa1=2*a(it-1)*z1/sqrt(Vp1^(-2)-a(it-1)^2)+4/(a(it-1)*A2)*sqrt(1-(a(it-
1)*Vp2)^2)-offset;
    fa2=2*a(it)*z1/sqrt(Vp1^(-2)-a(it)^2)+4/(a(it)*A2)*sqrt(1-(a(it)*Vp2)^2)-offset;
    a(it+1)=a(it)-(a(it)-a(it-1))/(fa2-fa1)*fa2;

    if isnan(a(it+1))==1

        a=a(1:it);
        break

    end

end

%-------------------------------------------------------------------------
%-------------------------------------------------------------------------
%We plot the result

%Once we get the numerical value of the ray parameter, we plot it
p=a(length(a));

% if p<=(1/Vp3) & isreal(p)==1

    fa2=p*z1/sqrt(Vp1^(-2)-p^2)+...
    (sqrt(1-(p*Vp2)^2)-sqrt(1-(p*(A2*(z2-z1)+Vp2))^2))/(A2*p);
    offset;

    %Ray path in the first layer
    X=p*z1/sqrt(Vp1^(-2)-p^2);

%     if (X/sqrt(X^2+z1^2))<(Vp1/Vp2)
```

```
%-----------------------------------------------------------
%Raypath

%Raypath in the second layer which velocity vary linearly with
%depth.
k=885/70;
Vz=1/p;
R=Vz/k;
theta0=asin(p*Vp2);
Xz=R*cos(theta0);
h =R*sin(theta0);
x2=0:dx:Xz;
theta=acos((x2-Xz)/R);
y2=R*sin(theta)-h;
x2=x2+X;
y2=y2+5;
xr2=x2(find(y2<=130));
yr2=y2(find(y2<=130));

if length(xr2)==length(x2) & length(x2)~=0

   %Raypath of the reflected rays in the first layer at a
   %constant velocity.
   subplot(211)
   hold on
   plot([0 X],[0 z1],'k')
   set(gca,'YDir','reverse')
   axespace=axis;

   plot(x2,y2,'k')
   plot(2*x2(length(x2))-x2,y2,'k')
   plot(2*x2(length(x2))+x2-2*X,y2,'k')
   plot(4*x2(length(x2))-x2-2*X,y2,'k')
   plot([(4*x2(length(x2))-3*X) (4*x2(length(x2))-2*X)],[z1 0],'k')

   %-----------------------------------------------------------
   %Traveltime

   A2=k;
   B2=Vp2;
   traveltime=2*sqrt(X^2+z1^2)/Vp1;
   traveltime2=4/k*asinh(1/(p*Vp2));
   traveltime=traveltime+traveltime2;
   trc=floor(traveltime*10^4);
   subplot(212)
   hold on
   plot(offset,traveltime,'ko')
```

```
            set(gca,'YDir','reverse')
            axetime=axis;

            %-----------------------------------------------------------
            %Reflection and transmission coefficients on the first
            %interface
            i1=asind(p*Vp1);%Angle of incidence
            j1=asind(Vs1*p);
            i2=asind(Vp2*p);
            j2=asind(Vs2*p);

            if isreal(i1)==1 & isreal(j1)==1 & isreal(i2)==1 & isreal(j2)==1

                %Definition of the repeated used variables
                a=rho2*(1-2*Vs2^2*p^2)-rho1*(1-2*Vs1^2*p^2);
                b=rho2*(1-2*Vs2^2*p^2)+2*rho1*Vs1^2*p^2;
                c=rho1*(1-2*Vs1^2*p^2)+2*rho2*Vs2^2*p^2;
                d=2*(rho2*Vs2^2-rho1*Vs1^2);

                %Repeated used cosine dependent terms
                E=b*cosd(i1)/Vp1+c*cosd(i2)/Vp2;
                F=b*cosd(j1)/Vs1+c*cosd(j2)/Vs2;
                G=a-d*cosd(i1)/Vp1*cosd(j2)/Vs2;
                H=a-d*cosd(i2)/Vp2*cosd(j1)/Vs1;

                D=E*F+G*H*p^2;

                %Reflection between the second layer and the first one for
                %an upcoming layer
                Rpp21=-1*((b*cos(i1)/Vp1-
c*cos(i2)/Vp2)*F+(a+d*cos(i2)/Vp2*cos(j1)/Vs1)*G*p^2)/D;

                %Transmission coefficient at the first interface
                Tpp12=2*rho1*cosd(i1)/Vp1*F*Vp1/(Vp2*D);
                %Transmission coefficient from the layer 2 to the layer 1,
                %for the way back from the reflection
                Tpp21=2*rho2*cosd(i2)/Vp2*F*Vp2/(Vp1*D);

                Tpp=Rpp21*Tpp12*Tpp21;

            end

        end

    end
```

7.2.9. Function reflectionLayer1

```
function [trc,Rpp]=reflectionLayer1(offset)

trc=NaN;
Rpp=i;
a1=3811;
b1=2263;
ratio=a1/b1;
%--------------------------------------------------------------------------
%--------------------------------------------------------------------------
%Initialization of the parameters
p(1)=0;
Vp1=638;
Vp2=1009.6;
%We deduce the numerical values of the other parameters from the recorded
%P-waves' velocity
Vs1=Vp1/ratio;
Vs2=Vp2/ratio;
rho1=(5825+Vp1)/4.1913;
rho2=(5825+Vp2)/4.1913;
%Depth of the reflectors
z=5;
%--------------------------------------------------------------------------
%--------------------------------------------------------------------------
%Research of the ray parameter which links the source and the geophone

X=p*z/sqrt(Vp1^(-2)-p^2)-offset/2;
Xprim=z/sqrt(Vp1^(-2)-p^2)+(p^2)*z/((sqrt(Vp1^(-2)-p^2))^3);

for it=1:100

   X=p(it)*z/sqrt(Vp1^(-2)-p(it)^2)-offset/2;
   Xprim=z/sqrt(Vp1^(-2)-p(it)^2)+(p(it)^2)*z/((sqrt(Vp1^(-2)-p(it)^2))^3);
   p(it+1)=p(it)-X/Xprim;

   if isnan(X)==1 | isreal(X)==0

      break

   end

end
%--------------------------------------------------------------------------
%--------------------------------------------------------------------------
%We plot the result

if isnan(X)==0 & isreal(X)==1
```

```
X=p(it)*z/sqrt(Vp1^(-2)-p(it)^2);

if (X/sqrt(X^2+z^2))<(Vp1/Vp2)

   %Raypath of the reflected rays in the first layer
   subplot(211)
   hold on
   plot([0 X],[0 z])
   plot([X 2*X],[z 0])
   set(gca,'YDir','reverse')
   axespace=axis;

   %Computation of the traveltimes
   subplot(212)
   traveltime=2*sqrt(X^2+z^2)/Vp1;
   trc=floor(traveltime*10^4);
   hold on
   plot(offset,traveltime,'o')
   set(gca,'YDir','reverse')
   axetime=axis;
   axis([axespace(1) axespace(2) 0 axetime(4)])

   %Computation of the Reflection Coefficient of the reflected P-Wave
   i1=asind(p(it)*Vp1);%Angle of incidence
   j1=asind(Vs1*p(it));
   i2=asind(Vp2*p(it));
   j2=asind(Vs2*p(it));

   if isreal(i1)==1 & isreal(j1)==1 & isreal(i2)==1 & isreal(j2)==1

      %Definition of the repeated used variables
      a=rho2*(1-2*Vs2^2*p(it)^2)-rho1*(1-2*Vs1^2*p(it)^2);
      b=rho2*(1-2*Vs2^2*p(it)^2)+2*rho1*Vs1^2*p(it)^2;
      c=rho1*(1-2*Vs1^2*p(it)^2)+2*rho2*Vs2^2*p(it)^2;
      d=2*(rho2*Vs2^2-rho1*Vs1^2);

      %Repeated used cosine dependent terms
      E=b*cosd(i1)/Vp1+c*cosd(i2)/Vp2;
      F=b*cosd(j1)/Vs1+c*cosd(j2)/Vs2;
      G=a-d*cosd(i1)/Vp1*cosd(j2)/Vs2;
      H=a-d*cosd(i2)/Vp2*cosd(j1)/Vs1;

      D=E*F+G*H*p(it)^2;

      %Computation of the Reflection Coefficient
```

```
            Rpp=((b*cosd(i1)/Vp1-c*cosd(i2)/Vp2)*F-
(a+d*cosd(i1)/Vp1*cosd(j2)/Vs2)*H*p(it)^2)/D;

        end
    end
end
```

7.2.10. Function reflectionLayer2b

```
function [trc,Rpp23]=relectionLayer2b(offset)

trc=NaN;
Rpp12=i;
Rpp23=i;
a1=3811;
b1=2263;
ratio=a1/b1;
%--------------------------------------------------------------------------
%--------------------------------------------------------------------------
%Initialzation of the parameters
p(1)=0;
Vp1=638;
Vp2=1009.6;
Vp3=3108;
%We deduce the numerical values of the other parameters from the recorded
%P-waves' velocity
Vs1=Vp1/ratio;
Vs2=Vp2/ratio;
Vs3=Vp3/ratio;
rho1=(5825+Vp1)/4.1913;
rho2=(5825+Vp2)/4.1913;
rho3=(5825+Vp3)/4.1913;
%Depth of the reflectors
z1=5;
z2=130;
%Velocity at the bottom of the second layer
k=885/70;
Vpend2=k*(z2-z1)+Vp2;
Vsend2=Vpend2/ratio;
%Sampling parameter relative to the ray path tracing
dx=0.1;

%--------------------------------------------------------------------------
%--------------------------------------------------------------------------
%We look for the ray parameter which links the source and the geophone

%Methode de la secante
```

```
a(1)=10^-5;
a(2)=1/Vp3;

A2=885/70;

for it=2:100

    fa1=a(it-1)*z1/sqrt(Vp1^(-2)-a(it-1)^2)+...
       (sqrt(1-(a(it-1)*Vp2)^2)-sqrt(1-(a(it-1)*(A2*(z2-z1)+Vp2))^2))/(A2*a(it-1))-
offset/2;
    fa2=a(it)*z1/sqrt(Vp1^(-2)-a(it)^2)+...
       (sqrt(1-(a(it)*Vp2)^2)-sqrt(1-(a(it)*(A2*(z2-z1)+Vp2))^2))/(A2*a(it))-
offset/2;
    a(it+1)=a(it)-(a(it)-a(it-1))/(fa2-fa1)*fa2;

    if isnan(a(it+1))==1

       a=a(1:it);
       break

    end

end

%--------------------------------------------------------------------------
%--------------------------------------------------------------------------
%We plot the result

%Once we get the numerical value of the ray parameter, we plot it
p=a(length(a));

if p<=(1/Vp3) & isreal(p)==1

    fa2=p*z1/sqrt(Vp1^(-2)-p^2)+...
    (sqrt(1-(p*Vp2)^2)-sqrt(1-(p*(A2*(z2-z1)+Vp2))^2))/(A2*p);
    offset;

    %Ray path in the first layer
    X=p*z1/sqrt(Vp1^(-2)-p^2);

    if (X/sqrt(X^2+z1^2))<(Vp1/Vp2)

    %-------------------------------------------------------------
    %Raypath

    %Raypath of the reflected rays in the first layer at a
    %constant velocity.
```

```
subplot(211)
hold on
plot([0 X],[0 z1],'g')
set(gca,'YDir','reverse')
axespace=axis;

%Raypath in the second layer which velocity vary linearly with
%depth.
k=885/70;
Vz=1/p;
R=Vz/k;
theta0=asin(p*1009.6);
Xz=R*cos(theta0);
h =R*sin(theta0);
x2=0:dx:Xz;
theta=acos((x2-Xz)/R);
y2=R*sin(theta)-h;
x2=x2+X;
y2=y2+5;
xr2=x2(find(y2<=130));
yr2=y2(find(y2<=130));
plot(xr2,yr2,'g')
plot(2*xr2(length(xr2))-xr2,yr2,'g')
plot([2*xr2(length(xr2))-X 2*xr2(length(xr2))],[z1 0],'g')

 %-------------------------------------------------------------
 %Traveltime

 A2=k;
 B2=Vp2;
 traveltime=2*sqrt(X^2+z1^2)/Vp1;
 traveltime2=-2/A2*(atanh(1/sqrt(1-(p*(A2*(z2-z1)+B2))^2))-atanh(1/sqrt(1-
(p*B2)^2)));
 traveltime=traveltime+traveltime2;
 trc=floor(traveltime*10^4);
 subplot(212)
 hold on
 plot(offset,traveltime,'go')
 set(gca,'YDir','reverse')
 axetime=axis;
 axis([axespace(1) axespace(2) 0 axetime(4)])

 %-------------------------------------------------------------
 %Reflection and transmission coefficients on the first
 %interface
 i1=asind(p*Vp1);%Angle of incidence
 j1=asind(Vs1*p);
```

```
i2=asind(Vp2*p);
j2=asind(Vs2*p);

if isreal(i1)==1 & isreal(j1)==1 & isreal(i2)==1 & isreal(j2)==1

    %Definition of the repeated used variables
    a=rho2*(1-2*Vs2^2*p^2)-rho1*(1-2*Vs1^2*p^2);
    b=rho2*(1-2*Vs2^2*p^2)+2*rho1*Vs1^2*p^2;
    c=rho1*(1-2*Vs1^2*p^2)+2*rho2*Vs2^2*p^2;
    d=2*(rho2*Vs2^2-rho1*Vs1^2);

    %Repeated used cosine dependent terms
    E=b*cosd(i1)/Vp1+c*cosd(i2)/Vp2;
    F=b*cosd(j1)/Vs1+c*cosd(j2)/Vs2;
    G=a-d*cosd(i1)/Vp1*cosd(j2)/Vs2;
    H=a-d*cosd(i2)/Vp2*cosd(j1)/Vs1;

    D=E*F+G*H*p^2;

    %Computation of the Reflection Coefficient at the first
    %interface between the layer 1 and 2.
    Rpp12=((b*cosd(i1)/Vp1-c*cosd(i2)/Vp2)*F-
(a+d*cosd(i1)/Vp1*cosd(j2)/Vs2)*H*p^2)/D;
    %Transmission coefficient at the first interface
    Tpp12=2*rho1*cosd(i1)/Vp1*F*Vp1/(Vp2*D);
    %Transmission coefficient from the layer 2 to the layer 1,
    %for the way back from the reflection
    Tpp21=2*rho2*cosd(i2)/Vp2*F*Vp2/(Vp1*D);

    %-------------------------------------------------------
    %Now, we need to compute the coefficient reflection between
    %the layers 2 and 3
    i2=asind(p*Vpend2);%Angle of incidence
    j2=asind(Vsend2*p);
    i3=asind(Vp3*p);
    j3=asind(Vs3*p);

    if isreal(i2)==1 & isreal(j2)==1 & isreal(i3)==1 & isreal(j3)==1

    %Definition of the repeated used variables
    a=rho3*(1-2*Vs3^2*p^2)-rho2*(1-2*Vsend2^2*p^2);
    b=rho3*(1-2*Vs3^2*p^2)+2*rho2*Vsend2^2*p^2;
    c=rho2*(1-2*Vsend2^2*p^2)+2*rho3*Vs3^2*p^2;
    d=2*(rho3*Vs3^2-rho2*Vsend2^2);

    %Repeated used cosine dependent terms
    E=b*cosd(i2)/Vpend2+c*cosd(i3)/Vp3;
```

```
        F=b*cosd(j2)/Vsend2+c*cosd(j3)/Vs3;
        G=a-d*cosd(i2)/Vpend2*cosd(j3)/Vs3;
        H=a-d*cosd(i3)/Vp3*cosd(j2)/Vsend2;

        D=E*F+G*H*p^2;

        %Computation of the Reflection Coefficient at the first
        %interface between the layer 1 and 2.
        Rpp23=((b*cosd(i2)/Vpend2-c*cosd(i3)/Vp3)*F-
(a+d*cosd(i2)/Vpend2*cosd(j3)/Vs3)*H*p^2)/D;
        %Transmission coefficient at the first interface
        Tpp23=2*rho2*cosd(i2)/Vpend2*F*Vpend2/(Vp3*D);

        Rpp23=Rpp23*Tpp12*Tpp21;

        %-----------------------------------------------------
        %And now we need to cumpute the transmission
        %reflection for the way back between the laers 2 and 1

        end
     end
    end
 end
```

7.2.11. Function reflectionSLayer1

```
 function [trc,Rss]=reflectionSLayer1(offset)

 trc=NaN;
 Rss=i;
 a1=3811;
 b1=2263;
 ratio=a1/b1;
 %-------------------------------------------------------------------------
 %-------------------------------------------------------------------------
 %Initialization of the parameters
 p(1)=0;
 Vp1=638;
 Vp2=1009.6;
 %We deduce the numerical values of the other parameters from the recorded
 %P-waves' velocity
 Vs1=Vp1/ratio;
 Vs2=Vp2/ratio;
 rho1=(5825+Vp1)/4.1913;
 rho2=(5825+Vp2)/4.1913;
 %Depth of the reflectors
 z=5;
```

```
%-------------------------------------------------------------------------
%-------------------------------------------------------------------------
%Research of the ray parameter which links the source and the geophone

X=p*z/sqrt(Vs1^(-2)-p^2)-offset/2;
Xprim=z/sqrt(Vs1^(-2)-p^2)+(p^2)*z/((sqrt(Vs1^(-2)-p^2))^3);

for it=1:100

   X=p(it)*z/sqrt(Vs1^(-2)-p(it)^2)-offset/2;
   Xprim=z/sqrt(Vs1^(-2)-p(it)^2)+(p(it)^2)*z/((sqrt(Vs1^(-2)-p(it)^2))^3);
   p(it+1)=p(it)-X/Xprim;

   if isnan(X)==1 | isreal(X)==0

      break

   end

end

%-------------------------------------------------------------------------
%-------------------------------------------------------------------------
%We plot the result

if isnan(X)==0 & isreal(X)==1

   X=p(it)*z/sqrt(Vp1^(-2)-p(it)^2);

   if (X/sqrt(X^2+z^2))<(Vp1/Vp2)

      %Raypath of the reflected rays in the first layer
      subplot(211)
      hold on
      plot([0 X],[0 z])
      plot([X 2*X],[z 0])
      set(gca,'YDir','reverse')
      axespace=axis;

      %Computation of the traveltimes
      subplot(212)
      traveltime=2*sqrt(X^2+z^2)/Vp1;
      trc=floor(traveltime*10^4);
      hold on
      plot(offset,traveltime,'^')
      set(gca,'YDir','reverse')
      axetime=axis;
```

```
        axis([axespace(1) axespace(2) 0 axetime(4)])

        %Computation of the Reflection Coefficient of the reflected P-Wave
        i1=asind(p(it)*Vp1);%Angle of incidence
        j1=asind(Vs1*p(it));
        i2=asind(Vp2*p(it));
        j2=asind(Vs2*p(it));

        if isreal(i1)==1 & isreal(j1)==1 & isreal(i2)==1 & isreal(j2)==1

            %Definition of the repeated used variables
            a=rho2*(1-2*Vs2^2*p(it)^2)-rho1*(1-2*Vs1^2*p(it)^2);
            b=rho2*(1-2*Vs2^2*p(it)^2)+2*rho1*Vs1^2*p(it)^2;
            c=rho1*(1-2*Vs1^2*p(it)^2)+2*rho2*Vs2^2*p(it)^2;
            d=2*(rho2*Vs2^2-rho1*Vs1^2);

            %Repeated used cosine dependent terms
            E=b*cosd(i1)/Vp1+c*cosd(i2)/Vp2;
            F=b*cosd(j1)/Vs1+c*cosd(j2)/Vs2;
            G=a-d*cosd(i1)/Vp1*cosd(j2)/Vs2;
            H=a-d*cosd(i2)/Vp2*cosd(j1)/Vs1;

            D=E*F+G*H*p(it)^2;

            %Computation of the Reflection Coefficient
            Rss=-((b*cosd(j1)/Vs1-c*cosd(j2)/Vs2)*E-
(a+d*cosd(i2)/Vp2*cosd(j1)/Vs1)*G*p^2)/D;

        end

    end

end
```

7.2.12. Function reflectionSLayer2b

```
function [trc,Rss23]=reflectionSLayer2b(offset)

trc=NaN;
Rpp12=i;
Rss23=i;
a1=3811;
b1=2263;
ratio=a1/b1;
%---------------------------------------------------------------------
%---------------------------------------------------------------------
%Initialzation of the parameters
```

```
p(1)=0;
Vp1=638;
Vp2=1009.6;
Vp3=3108;
%We deduce the numerical values of the other parameters from the recorded
%P-waves' velocity
Vs1=Vp1/ratio;
Vs2=Vp2/ratio;
Vs3=Vp3/ratio;
rho1=(5825+Vp1)/4.1913;
rho2=(5825+Vp2)/4.1913;
rho3=(5825+Vp3)/4.1913;
%Depth of the reflectors
z1=5;
z2=130;
%Velocity at the bottom of the second layer
k=885/70;
Vpend2=k*(z2-z1)+Vp2;
Vsend2=Vpend2/ratio;
%Sampling parameter relative to the ray path tracing
dx=0.1;

%------------------------------------------------------------------------
%------------------------------------------------------------------------
%We look for the ray parameter which links the source and the geophone

%Methode de la secante
a(1)=10^-5;
a(2)=1/Vp3;

A2=885/(70*ratio);

for it=2:100

    fa1=a(it-1)*z1/sqrt(Vs1^(-2)-a(it-1)^2)+...
       (sqrt(1-(a(it-1)*Vs2)^2)-sqrt(1-(a(it-1)*(A2*(z2-z1)+Vs2))^2))/(A2*a(it-1))-
offset/2;
    fa2=a(it)*z1/sqrt(Vs1^(-2)-a(it)^2)+...
       (sqrt(1-(a(it)*Vs2)^2)-sqrt(1-(a(it)*(A2*(z2-z1)+Vs2))^2))/(A2*a(it))-offset/2;
    a(it+1)=a(it)-(a(it)-a(it-1))/(fa2-fa1)*fa2;

    if isnan(a(it+1))==1

       a=a(1:it);
       break

    end
```

```
end

%-------------------------------------------------------------------------
%-------------------------------------------------------------------------
%We plot the result

%Once we get the numerical value of the ray parameter, we plot it
p=a(length(a));

if p<=(1/Vs3) & isreal(p)==1

   fa2=p*z1/sqrt(Vs1^(-2)-p^2)+...
   (sqrt(1-(p*Vs2)^2)-sqrt(1-(p*(A2*(z2-z1)+Vs2))^2))/(A2*p);
   offset;

   %Ray path in the first layer
   X=p*z1/sqrt(Vs1^(-2)-p^2);

   if (X/sqrt(X^2+z1^2))<(Vs1/Vs2)

      %-------------------------------------------------------------
      %Raypath

      %Raypath of the reflected rays in the first layer at a
      %constant velocity.
      subplot(211)
      hold on
      plot([0 X],[0 z1],'g')
      set(gca,'YDir','reverse')
      axespace=axis;

      %Raypath in the second layer which velocity vary linearly with
      %depth.
      k=885/(70*ratio);
      Vz=1/p;
      R=Vz/k;
      theta0=asin(p*Vs2);
      Xz=R*cos(theta0);
      h =R*sin(theta0);
      x2=0:dx:Xz;
      theta=acos((x2-Xz)/R);
      y2=R*sin(theta)-h;
      x2=x2+X;
      y2=y2+5;
      xr2=x2(find(y2<=130));
      yr2=y2(find(y2<=130));
```

```
plot(xr2,yr2,'g')
plot(2*xr2(length(xr2))-xr2,yr2,'g')
plot([2*xr2(length(xr2))-X 2*xr2(length(xr2))],[z1 0],'g')

%-------------------------------------------------------------
%Traveltime

A2=k/ratio;
B2=Vs2;
traveltime=2*sqrt(X^2+z1^2)/Vs1;
traveltime2=-2/A2*(atanh(1/sqrt(1-(p*(A2*(z2-z1)+B2))^2))-atanh(1/sqrt(1-
(p*B2)^2)));
traveltime=traveltime+traveltime2;
trc=floor(traveltime*10^4);
subplot(212)
hold on
plot(offset,traveltime,'g^')
set(gca,'YDir','reverse')
axetime=axis;
axis([axespace(1) axespace(2) 0 traveltime])

%-------------------------------------------------------------
%Reflection and transmission coefficients on the first
%interface
i1=asind(p*Vp1);%Angle of incidence
j1=asind(Vs1*p);
i2=asind(Vp2*p);
j2=asind(Vs2*p);

if isreal(i1)==1 & isreal(j1)==1 & isreal(i2)==1 & isreal(j2)==1

   %Definition of the repeated used variables
   a=rho2*(1-2*Vs2^2*p^2)-rho1*(1-2*Vs1^2*p^2);
   b=rho2*(1-2*Vs2^2*p^2)+2*rho1*Vs1^2*p^2;
   c=rho1*(1-2*Vs1^2*p^2)+2*rho2*Vs2^2*p^2;
   d=2*(rho2*Vs2^2-rho1*Vs1^2);

   %Repeated used cosine dependent terms
   E=b*cosd(i1)/Vp1+c*cosd(i2)/Vp2;
   F=b*cosd(j1)/Vs1+c*cosd(j2)/Vs2;
   G=a-d*cosd(i1)/Vp1*cosd(j2)/Vs2;
   H=a-d*cosd(i2)/Vp2*cosd(j1)/Vs1;

   D=E*F+G*H*p^2;

   %Computation of the Reflection Coefficient at the first
   %interface between the layer 1 and 2.
```

```
        Rss12=-((b*cosd(j1)/Vs1-c*cosd(j2)/Vs2)*E-
(a+d*cosd(i2)/Vp2*cosd(j1)/Vs1)*G*p^2)/D;
        %Transmission coefficient at the first interface
        Tss12=2*rho1*cosd(j1)/Vs1*E*Vs1/(Vs2*D);
        %Transmission coefficient from the layer 2 to the layer 1,
        %for the way back from the reflection
        Tss21=2*rho2*cosd(j2)/Vs2*E*Vs2/(Vs1*D);

        %-------------------------------------------------------
        %Now, we need to compute the coefficient reflection between
        %the layers 2 and 3
        i2=asind(p*Vpend2);%Angle of incidence
        j2=asind(Vsend2*p);
        i3=asind(Vp3*p);
        j3=asind(Vs3*p);

        if isreal(i2)==1 & isreal(j2)==1 & isreal(i3)==1 & isreal(j3)==1

            %Definition of the repeated used variables
            a=rho3*(1-2*Vs3^2*p^2)-rho2*(1-2*Vsend2^2*p^2);
            b=rho3*(1-2*Vs3^2*p^2)+2*rho2*Vsend2^2*p^2;
            c=rho2*(1-2*Vsend2^2*p^2)+2*rho3*Vs3^2*p^2;
            d=2*(rho3*Vs3^2-rho2*Vsend2^2);

            %Repeated used cosine dependent terms
            E=b*cosd(i2)/Vpend2+c*cosd(i3)/Vp3;
            F=b*cosd(j2)/Vsend2+c*cosd(j3)/Vs3;
            G=a-d*cosd(i2)/Vpend2*cosd(j3)/Vs3;
            H=a-d*cosd(i3)/Vp3*cosd(j2)/Vsend2;

            D=E*F+G*H*p^2;

            %Computation of the Reflection Coefficient at the first
            %interface between the layer 1 and 2.
            Rss23=-((b*cosd(j2)/Vsend2-c*cosd(j3)/Vs3)*E-
(a+d*cosd(i3)/Vp3*cosd(j2)/Vsend2)*G*p^2)/D;
            %Transmission coefficient at the first interface
            Tss23=2*rho2*cosd(j2)/Vsend2*E*Vsend2/(Vs3*D);

            Rss23=Rss23*Tss12*Tss21;

        end

    end

end
```

```
end
```

7.2.13. Function refractedP

```
function [trc,Rp]=refractedP(offset)

Rp=1;
%--------------------------------------------------------------------------
%--------------------------------------------------------------------------
%Initialization of the parameters
a1=3811;
b1=2263;
ratio=a1/b1;
Vp1=638;
Vp2=1009.6;
Vs1=Vp1/ratio;
z1=5;


%--------------------------------------------------------------------------
%--------------------------------------------------------------------------
%P-refracted waves' pathway

%P-incident wave's critical angle
ipc=asind(Vp1/Vp2);

if (offset/sqrt(offset^2+z1^2))>(Vp1/Vp2)

   subplot(211)
   hold on,plot([0 z1*tand(ipc)],[0 z1],'r')
   hold on,plot([(offset-z1*tand(ipc)) offset],[z1 0],'r')
   hold on,plot([z1*tand(ipc) (offset-z1*tand(ipc))],[z1 z1],'r')

end

%--------------------------------------------------------------------------
%--------------------------------------------------------------------------
%Computation of the refracted wave's traveltime

if (offset/sqrt(offset^2+z1^2))>(Vp1/Vp2)

   traveltime1=2*sqrt(z1*tand(ipc))/Vp1;
   traveltime2=(offset-2*z1*tand(ipc))/Vp2;
   traveltime=traveltime1+traveltime2;
   trc=floor(traveltime*10^4);

   subplot(212)
```

```
    hold on
    plot(offset,traveltime,'ro')

end
```

7.2.14. Function refractedS

```
function [trc,Rs]=refractedS(offset)

Rs=1;
%--------------------------------------------------------------------------
%--------------------------------------------------------------------------
%Initialization of the parameters
a1=3811;
b1=2263;
ratio=a1/b1;
Vp1=638;
Vp2=1009.6;
Vs1=Vp1/ratio;
Vs2=Vp2/ratio;
z1=5;


%--------------------------------------------------------------------------
%--------------------------------------------------------------------------
%P-refracted waves' pathway

%P-incident wave's critical angle
ipc=asind(Vs1/Vs2);

if (offset/sqrt(offset^2+z1^2))>(Vs1/Vs2)

    subplot(211)
    hold on,plot([0 z1*tand(ipc)],[0 z1],'r')
    hold on,plot([(offset-z1*tand(ipc)) offset],[z1 0],'r')
    hold on,plot([z1*tand(ipc) (offset-z1*tand(ipc))],[z1 z1],'r')

end

%--------------------------------------------------------------------------
%--------------------------------------------------------------------------
%Computation of the refracted wave's traveltime

if (offset/sqrt(offset^2+z1^2))>(Vs1/Vs2)

    traveltime1=2*sqrt(z1*tand(ipc))/Vs1;
    traveltime2=(offset-2*z1*tand(ipc))/Vs2;
```

```
    traveltime=traveltime1+traveltime2;
    trc=floor(traveltime*10^4);

    subplot(212)
    hold on
    plot(offset,traveltime,'r^')

end
```

7.2.15. Function refractedLayer2

```
function [trc,re]=refractedLayer2(offset)

trc=NaN;
re=1;
a1=3811;
b1=2263;
ratio=a1/b1;
%--------------------------------------------------------------------------
%--------------------------------------------------------------------------
%Initialzation of the parameters
p(1)=0;
Vp1=638;
Vp2=1009.6;
Vp3=3108;
%We deduce the numerical values of the other parameters from the recorded
%P-waves' velocity
Vs1=Vp1/ratio;
Vs2=Vp2/ratio;
Vs3=Vp3/ratio;
rho1=(5825+Vp1)/4.1913;
rho2=(5825+Vp2)/4.1913;
rho3=(5825+Vp3)/4.1913;
%Depth of the reflectors
z1=5;
z2=130;
%Velocity at the bottom of the second layer
k=885/70;
Vpend2=k*(z2-z1)+Vp2;
Vsend2=Vpend2/ratio;
%Sampling parameter relative to the ray path tracing
dx=0.1;

%--------------------------------------------------------------------------
%--------------------------------------------------------------------------
%Assessment of the refracted ray's parameter on the second interface
%between the second and third interface
```

```
%critical ray parameter
p=1/Vp3;

%--------------------------------------------------------------------------
%--------------------------------------------------------------------------
%Raypath

%Ray path in the first layer
X=p*z1/sqrt(Vp1^(-2)-p^2);

%Raypath in the second layer which velocity vary linearly with
%depth.
k=885/70;
Vz=1/p;
R=Vz/k;
theta0=asin(p*1009.6);
Xz=R*cos(theta0);
h =R*sin(theta0);
x2=0:dx:Xz;
theta=acos((x2-Xz)/R);
y2=R*sin(theta)-h;
x2=x2+X;
y2=y2+5;
xr2=x2(find(y2<=130));
yr2=y2(find(y2<=130));

if offset>=2*(xr2(length(xr2))+X)

   %Raypath of the reflected rays in the first layer at a
   %constant velocity.
   subplot(211)
   hold on
   plot([0 X],[0 z1],'r')
   plot([(offset-X) offset],[z1 0],'r')
   set(gca,'YDir','reverse')
   axespace=axis;

   %Raypath of the reflected rays in the second layer which velocity vary
   %linearly with the depth
   plot(xr2,yr2,'r')
   plot(offset-xr2,yr2,'r')
   plot([xr2(length(xr2)) (offset-xr2(length(xr2)))],[z2 z2],'r')

   %Computation of the traveltime
   A2=k;
   B2=Vp2;
```

```
    traveltime=2*sqrt(X^2+z1^2)/Vp1;
    traveltime2=-2/A2*(atanh(1/sqrt(1-(p*(A2*(z2-z1)+B2))^2))-atanh(1/sqrt(1-
(p*B2)^2)));
    traveltime3=(offset-2*xr2(length(xr2)))/Vp3;
    traveltime=traveltime+traveltime2+traveltime3;
    trc=floor(traveltime*10^4);
    subplot(212)
    hold on
    plot(offset,traveltime,'ro')
    set(gca,'YDir','reverse')
    axetime=axis;
 %     axis([axespace(1) axespace(2) 0 axetime(4)])

 end
```

7.2.16. Function refractedSlayer2

```
 function [trc,re]=refractedSLayer2(offset)

 trc=NaN;
 re=1;
 a1=3811;
 b1=2263;
 ratio=a1/b1;
 %--------------------------------------------------------------------------
 %--------------------------------------------------------------------------
 %Initialzation of the parameters
 p(1)=0;
 Vp1=638;
 Vp2=1009.6;
 Vp3=3108;
 %We deduce the numerical values of the other parameters from the recorded
 %P-waves' velocity
 Vs1=Vp1/ratio;
 Vs2=Vp2/ratio;
 Vs3=Vp3/ratio;
 rho1=(5825+Vp1)/4.1913;
 rho2=(5825+Vp2)/4.1913;
 rho3=(5825+Vp3)/4.1913;
 %Depth of the reflectors
 z1=5;
 z2=130;
 %Velocity at the bottom of the second layer
 k=885/70;
 Vpend2=k*(z2-z1)+Vp2;
 Vsend2=Vpend2/ratio;
 %Sampling parameter relative to the ray path tracing
```

```
dx=0.1;

%------------------------------------------------------------------------
%------------------------------------------------------------------------
%Assessment of the refracted ray's parameter on the second interface
%between the second and third interface

%critical ray parameter
p=1/Vs3;

%------------------------------------------------------------------------
%------------------------------------------------------------------------
%Raypath

%Ray path in the first layer
X=p*z1/sqrt(Vp1^(-2)-p^2);

%Raypath in the second layer which velocity vary linearly with
%depth.
k=885/(70*ratio);
Vz=1/p;
R=Vz/k;
theta0=asin(p*Vs2);
Xz=R*cos(theta0);
h =R*sin(theta0);
x2=0:dx:Xz;
theta=acos((x2-Xz)/R);
y2=R*sin(theta)-h;
x2=x2+X;
y2=y2+5;
xr2=x2(find(y2<=130));
yr2=y2(find(y2<=130));

if offset>=2*(xr2(length(xr2))+X)

   %Raypath of the reflected rays in the first layer at a
   %constant velocity.
   subplot(211)
   hold on
   plot([0 X],[0 z1],'r')
   plot([(offset-X) offset],[z1 0],'r')
   set(gca,'YDir','reverse')
   axespace=axis;

   %Raypath of the reflected rays in the second layer which velocity vary
   %linearly with the depth
   plot(xr2,yr2,'r')
```

```
    plot(offset-xr2,yr2,'r')
    plot([xr2(length(xr2)) (offset-xr2(length(xr2)))],[z2 z2],'r')

    %Computation of the traveltime
    A2=k;
    B2=Vs2;
    traveltime=2*sqrt(X^2+z1^2)/Vs1;
    traveltime2=-2/A2*(atanh(1/sqrt(1-(p*(A2*(z2-z1)+B2))^2))-atanh(1/sqrt(1-
(p*B2)^2)));
    traveltime3=(offset-2*xr2(length(xr2)))/Vs3;
    traveltime=traveltime+traveltime2+traveltime3;
    trc=floor(traveltime*10^4);
    subplot(212)
    hold on
    plot(offset,traveltime,'r^')
    set(gca,'YDir','reverse')
    axetime=axis;
    axis([axespace(1) axespace(2) 0 traveltime])

 end
```

7.3. AUTOMATIC PICKING PROGRAMS

7.3.1. Principles

These programs have broadly been inspired by different matlab codes found in the following reference: “QUINQUIS (2000). Le traitement du signal sous Matlab.”

7.3.2. P-wave picking algorithm

```
close all
clear all

%--------------------------------------------------------------------
%--------------------------------------------------------------------
%Excel file reading part

%We start by looking for the Excel-File that we want to read

%We began by looking for the file
startpathname='H:\';

[filename,pathname]=uigetfile('.xls','Open the excel file',startpathname);

%in order to finally buid the whole pathname
if isequal(filename,0)|isequal(pathname,0)
   filename = 0;
   pathname = 0;
```

```
   openingfilename=0;
else
   startpathname=pathname;
   openingfilename=[pathname,filename];
end

if openingfilename~=0

   %We read the Excel-File
   [excelmatrix,headertext]=xlsread(openingfilename);

end

excelmatrix(:,2) = 1.1*excelmatrix(:,2);

%--------------------------------------------------------------------------
%--------------------------------------------------------------------------
%Hilbert Transform Part

enveloppe =
sqrt(real(hilbert(excelmatrix(:,2))).^2+imag(hilbert(excelmatrix(:,2))).^2);
instantphase = atand(imag(hilbert(excelmatrix(:,2)))./real(hilbert(excelmatrix(:,2))));
instantfreq = diff(instantphase)./diff(excelmatrix(:,2));
timefreq=excelmatrix(:,1);
timefreq=diff(timefreq)+timefreq(1:(size(timefreq,1)-1));
denveloppe=diff(enveloppe)./diff(excelmatrix(:,2));

%--------------------------------------------------------------------------
%--------------------------------------------------------------------------
%Representation temps frequence
Wsize=2; %size of the Analysis window
Fe=4000000;%Sampling Frequency
[Cspec,F,T]=specgram(instantphase,128,Fe,Wsize);
[CspecTrace,F,T]=specgram(excelmatrix(:,2),128,Fe,Wsize);
% Cspec=(Cspec>10);

%--------------------------------------------------------------------------
%--------------------------------------------------------------------------
%Automatic picking part

%--------------------------------------------------------------------------
%Application du seuil

%On recherche le seuil le plus adapte afin de mieux detecter, au milieu du
%bruit, la premiere arrivee dans l'espace temps frequence.

pickSeuil = find(min(instantphase)==instantphase);
```

```
%Pour gagner du temps, on utilise les inconvenients des pixels, qui du
%coup, deviennent un avantage!:)
minSeuil = min(min(abs(Cspec)));
maxSeuil = max(max(abs(Cspec)));
pasPixel = (maxSeuil - minSeuil)/64;

attempt = abs(Cspec(15,:));

%On verifie que le minimum pointe ne se situe pas trop en aval de la trace
verification = find(attempt >= (minSeuil + 5*pasPixel));

if verification(1) < pickSeuil

   instantphase1 = instantphase(1:verification(1));
   pickSeuil = find(min(instantphase1)==instantphase1);

end

%On recherche le seuil le plus adapte
seuil = minSeuil;
Cseuil = (abs(Cspec)<seuil);

if max(abs(Cspec(:,1)))/max(max(abs(Cspec))) >= 1/15

   seuil = max(max(abs(Cspec)))/15;
   Cseuil=(abs(Cspec)<seuil);

else

   while isempty(find(Cseuil(:,1:pickSeuil)==0))==0;

      seuil = seuil + pasPixel;
      Cseuil=(abs(Cspec)<seuil);

   end
end

%--------------------------------------------------------------------------
%une fois que le seuil est applique, on pointe automatiquement
%Automatic picking of the first arrival (P- or S-Wave!)
[ligne,colonne]=find(Cseuil==0);
pick = colonne(1);

if pick == 1

   while Cseuil(1,pick) == 0
```

```
        pick = pick + 1;

    end

    while Cseuil(1,pick) == 1

        pick = pick + 1;

    end

end

%Once the first arrival is detected, we will look for the pick
while instantphase(pick-1)<=instantphase(pick)
    pick=pick-1;
end

while abs(excelmatrix(pick,2))==abs(excelmatrix(pick-1,2))
    pick=pick+1;
end

%And then, the picked time is
pickedtime=excelmatrix(pick,1);


%------------------------------------------------------------------------
%------------------------------------------------------------------------
%Graphic Part

figure(2);clf;
subplot(411)
timefreq=excelmatrix(:,1);
timefreq=diff(timefreq)+timefreq(1:(size(timefreq,1)-1));
imagesc(timefreq,F,abs(Cspec));
shading interp;
xlabel('Time (microsecs)');
ylabel('Frequency (MHz)');
title('Time/Frequency Analysis of the trace''s envelope');
%Here we show where we have picked the trace
hold on,vect=0:100;
xpick=pickedtime*ones(101,1);
V=axis;
ypick= V(3)+(V(4)-V(3))/101*vect;
plot(xpick,ypick,'k');

subplot(412)
```

```
imagesc(timefreq,F,Cseuil);
xlabel('Time (microsecs)');
ylabel('Frequency (Hz)');
title('After applying the Threshold');
%Here we show where we have picked the trace
hold on,vect=0:100;
xpick=pickedtime*ones(101,1);
V=axis;
ypick= V(3)+(V(4)-V(3))/101*vect;
plot(xpick,ypick,'k');

subplot(413)
plot(excelmatrix(:,1),instantphase)
V=axis;
axis([V(1) max(excelmatrix(:,1)) 1.1*min(instantphase) 1.1*max(instantphase)])
xlabel('Time (microsecs)')
ylabel('Instant Phase')
%Here we show where we have picked the trace
hold on,vect=0:100;
xpick=pickedtime*ones(101,1);
V=axis;
ypick= V(3)+(V(4)-V(3))/101*vect;
plot(xpick,ypick,'k');

subplot(414)
plot(excelmatrix(:,1),excelmatrix(:,2));
hold on, plot(excelmatrix(:,1),enveloppe,'r');
V=axis;
axis([V(1) max(excelmatrix(:,1)) min(excelmatrix(:,2)) max(enveloppe)])
xlabel('Time (microsecs)');
ylabel('Amplitude');
title(['picked time=',num2str(pickedtime),' seconds'])
legend('Original trace','Enveloppe')
%Here we show where we have picked the trace
hold on,vect=0:100;
xpick=pickedtime*ones(101,1);
V=axis;
ypick= V(3)+(V(4)-V(3))/101*vect;
plot(xpick,ypick,'k');
```

7.3.3. S-wave picking algorithm

This algorithm has proven to be efficient with different types of rocks. The selection criteria has been made on an empirical observation; it is then thought that this criteria is only applicable to this laboratory material.

```
close all
clear all
```

```
%------------------------------------------------------------------------
%------------------------------------------------------------------------
%Excel file reading part

%We start by looking for the Excel-File that we want to read

%We began by looking for the file
startpathname='H:\';

[filename,pathname]=uigetfile('.xls','Open the excel file',startpathname);

%in order to finally buid the whole pathname
if isequal(filename,0)|isequal(pathname,0)
   filename = 0;
   pathname = 0;
   openingfilename=0;
else
   startpathname=pathname;
   openingfilename=[pathname,filename];
end

if openingfilename~=0

   %We read the Excel-File
   [excelmatrix,headertext]=xlsread(openingfilename);

end

%------------------------------------------------------------------------
%------------------------------------------------------------------------
%Hilbert Transform Part

enveloppe =
sqrt(real(hilbert(excelmatrix(:,2))).^2+imag(hilbert(excelmatrix(:,2))).^2);
instantphase =
atand(imag(hilbert(excelmatrix(:,2)))./real(hilbert(excelmatrix(:,2))));
instantfreq = diff(instantphase)./diff(excelmatrix(:,2));
timefreq=excelmatrix(:,1);
timefreq=diff(timefreq)+timefreq(1:(size(timefreq,1)-1));
denveloppe=diff(enveloppe)./diff(excelmatrix(:,2));

%------------------------------------------------------------------------
%------------------------------------------------------------------------
%Representation temps frequence
Wsize=2; %size of the Analysis window
Fe=4000000;%Sampling Frequency
```

```
[Cspec,F,T]=specgram(enveloppe,128,Fe,Wsize);
[CspecTrace,F,T]=specgram(excelmatrix(:,2),128,Fe,Wsize);
% Cspec=(Cspec>10);

%-------------------------------------------------------------------------
%-------------------------------------------------------------------------
%Automatic picking for S-waves

%Automatic picking of the first arrival (P- or S-Wave!)
clear pick
pick = find(log(enveloppe/max(enveloppe))+1>=0);
pick = pick(find(pick>100));
pick = pick(1);

%Once the first arrival is detected, we will look for the local minimum
while enveloppe(pick-1)<=enveloppe(pick) | enveloppe(pick-2)<=enveloppe(pick)
      pick=pick-1;
end

%And then, the picked time is
pickedtime=excelmatrix(pick,1);

%On le represente graphiquement
figure,

subplot(411),imagesc(timefreq,F,abs(CspecTrace))
V=axis;
xlabel('Time (microsecs)');
ylabel('Frequency (Hz)');
title('Time Frequency Analysis');
%Here we show where we have picked the trace
hold on,vect=0:100;
xpick=pickedtime*ones(101,1);
V=axis;
ypick= V(3)+(V(4)-V(3))/101*vect;
plot(xpick,ypick,'k');

subplot(412)
timefreq=excelmatrix(:,1);
timefreq=diff(timefreq)+timefreq(1:(size(timefreq,1)-1));
imagesc(timefreq,F,abs(Cspec));
shading interp;
xlabel('Time (microsecs)');
ylabel('Frequency (MHz)');
title('Time/Frequency Analysis of the trace''s envelope');
%Here we show where we have picked the trace
hold on,vect=0:100;
```

```
xpick=pickedtime*ones(101,1);
V=axis;
ypick= V(3)+(V(4)-V(3))/101*vect;
plot(xpick,ypick,'k');

subplot(413),plot(excelmatrix(:,1),instantphase);
%Here we show where we have picked the trace
hold on,vect=0:100;
xpick=pickedtime*ones(101,1);
V=axis;
axis([V(1) max(excelmatrix(:,1)) 1.1*min(instantphase) 1.1*max(instantphase)]);
ypick= V(3)+(V(4)-V(3))/101*vect;
plot(xpick,ypick,'k');
xlabel('Time (microsecs)');
ylabel('instantaneous phase');
title('Plot of the instantaneous phase');

%And we do the same thing by showing the trace and its enveloppe
subplot(414),plot(excelmatrix(:,1),excelmatrix(:,2))
hold on, plot(excelmatrix(:,1),enveloppe,'r')
V=axis;
axis([V(1) max(excelmatrix(:,1)) min(excelmatrix(:,2)) max(enveloppe)])
xlabel('Time (microsecs)');
ylabel('Amplitude');
title(['picked S-wave time=',num2str(pickedtime),' seconds'])
%Here we show where we have picked the trace
hold on,vect=0:100;
xpick=pickedtime*ones(101,1);
V=axis
ypick= V(3)+(V(4)-V(3))/101*vect;
plot(xpick,ypick,'k');
```

7.4. COMSOL MULTIPHYSICS PROGRAM

7.4.1. Principle

This program has been inspired by an exercice seen during a Comsol conference, help in October 2007 in Grenoble, France.

The required toolbox is the structural mechanics one, which grants an access to the piezo-electric related physics.

7.4.2. Main program

```
function BilithicModel_gui_v2(event)

% COMSOL Multiphysics Model M-file
% Generated by COMSOL 3.3 (COMSOL 3.3.0.405, $Date: 2006/08/31 18:03:47
$)
```

```
flclear fem

global offset amplitudeSource frequencySource durationSource...
                    YoungModulusSample PoissonSample densitySample...
                    YoungModulusSample2 PoissonSample2 densitySample2...
                    InitialTime EndingTime TimeSampling

% COMSOL version
clear vrsn
vrsn.name = 'COMSOL 3.3';
vrsn.ext = '';
vrsn.major = 0;
vrsn.build = 405;
vrsn.rcs = '$Name:  $';
vrsn.date = '$Date: 2006/08/31 18:03:47 $';
fem.version = vrsn;

% Geometry
g1=rect2(1,0.2,'base','corner','pos',[0,0]);
g1=move(g1,[0.10000000000000009,-0.1]);
g2=rect2('100','40','base','corner','pos',{'0','0'},'rot','0');
g3=rect2(100,20,'base','corner','pos',[0,40]);
g4=rect2(100,20,'base','corner','pos',[0,60]);
parr={point2(20,80)};
g5=geomcoerce('point',parr);
parr={point2(40,80)};
g6=geomcoerce('point',parr);
g2=scale(g2,2,1,0,0);
g3=scale(g3,2,1,0,0);
g4=scale(g4,2,1,0,0);

% Analyzed geometry
clear p s
p.objs={g5,g6};
p.name={'PT1','PT2'};
p.tags={'g5','g6'};

s.objs={g2,g3,g4};
s.name={'R1','R2','R3'};
s.tags={'g2','g3','g4'};

fem.draw=struct('p',p,'s',s);
fem.geom=geomcsg(fem);
g7=rect2(200,80,'base','corner','pos',[0,0]);

% Analyzed geometry
```

```
clear p s
p.objs={g5,g6};
p.name={'PT1','PT2'};
p.tags={'g5','g6'};

s.objs={g7};
s.name={'R3'};
s.tags={'g7'};

fem.draw=struct('p',p,'s',s);
fem.geom=geomcsg(fem);

% Constants
fem.const = {'ramp','10', ...
  'magnitude','-5'};

% Constants
fem.const = {'ramp','10', ...
  'magnitude','-5'};

% Constants
fem.const = {'ramp','10', ...
  'magnitude','-5e5'};

% Constants
fem.const = {'ramp','10', ...
  'magnitude','-5e10'};

% Constants
fem.const = {'ramp','10', ...
  'magnitude','-5e8'};

% Constants
fem.const = {'ramp','10', ...
  'magnitude','-5e5'};

% Constants
fem.const = {'ramp','1e-5', ...
  'magnitude','-5e5'};
% COMSOL Multiphysics Model M-file
% Generated by COMSOL 3.3a (COMSOL 3.3.0.511, $Date: 2007/02/02 19:05:58
$)

% COMSOL version
clear vrsn
vrsn.name = 'COMSOL 3.3';
vrsn.ext = 'a';
```

```
vrsn.major = 0;
vrsn.build = 511;
vrsn.rcs = '$Name:  $';
vrsn.date = '$Date: 2007/02/02 19:05:58 $';
fem.version = vrsn;

% Constants
fem.const = {'ramp','1e-5', ...
  'magnitude','-5e5'};

% Constants
fem.const = {'ramp','1e-5', ...
  'magnitude','-5e5'};
% COMSOL Multiphysics Model M-file
% Generated by COMSOL 3.3a (COMSOL 3.3.0.511, $Date: 2007/02/02 19:05:58
$)

% COMSOL version
clear vrsn
vrsn.name = 'COMSOL 3.3';
vrsn.ext = 'a';
vrsn.major = 0;
vrsn.build = 511;
vrsn.rcs = '$Name:  $';
vrsn.date = '$Date: 2007/02/02 19:05:58 $';
fem.version = vrsn;

% Constants
fem.const = {'ramp','1e-7', ...
  'magnitude','-5e5'};

% Constants
fem.const = {'ramp','1e-7', ...
  'magnitude','-5e5'};
% COMSOL Multiphysics Model M-file
% Generated by COMSOL 3.3a (COMSOL 3.3.0.511, $Date: 2007/02/02 19:05:58
$)

% COMSOL version
clear vrsn
vrsn.name = 'COMSOL 3.3';
vrsn.ext = 'a';
vrsn.major = 0;
vrsn.build = 511;
vrsn.rcs = '$Name:  $';
vrsn.date = '$Date: 2007/02/02 19:05:58 $';
fem.version = vrsn;
```

```
% Constants
fem.const = {'ramp','1e-7', ...
  'magnitude','-5e5'};
% COMSOL Multiphysics Model M-file
% Generated by COMSOL 3.3a (COMSOL 3.3.0.511, $Date: 2007/02/02 19:05:58
$)

% COMSOL version
clear vrsn
vrsn.name = 'COMSOL 3.3';
vrsn.ext = 'a';
vrsn.major = 0;
vrsn.build = 511;
vrsn.rcs = '$Name:  $';
vrsn.date = '$Date: 2007/02/02 19:05:58 $';
fem.version = vrsn;

% Geometry
g1=rect2(40,80,'base','corner','pos',[0,0]);
g2=rect2(20,40,'base','corner','pos',[0,0]);
g3=rect2('35','70','base','corner','pos',{'0','0'},'rot','0');
g4=rect2('3.5','7','base','corner','pos',{'0','0'},'rot','0');
g8=rect2('5','10','base','corner','pos',{'0','0'},'rot','0');
gg=geomedit(g5);
gg{1}=point2(0.1,10);
g9=geomedit(g5,gg);
gg=geomedit(g6);
gg{1}=point2(4.9,10);
g10=geomedit(g6,gg);

% Analyzed geometry
clear p s
p.objs={g9,g10};
p.name={'PT1','PT2'};
p.tags={'g9','g10'};

s.objs={g8};
s.name={'R3'};
s.tags={'g8'};

fem.draw=struct('p',p,'s',s);
fem.geom=geomcsg(fem);
% COMSOL Multiphysics Model M-file
% Generated by COMSOL 3.3a (COMSOL 3.3.0.511, $Date: 2007/02/02 19:05:58
$)
```

```
% COMSOL version
clear vrsn
vrsn.name = 'COMSOL 3.3';
vrsn.ext = 'a';
vrsn.major = 0;
vrsn.build = 511;
vrsn.rcs = '$Name:  $';
vrsn.date = '$Date: 2007/02/02 19:05:58 $';
fem.version = vrsn;

% Geometry
g1=rect2('36*10^-3','72*10^-3','base','corner','pos',{'0','0'},'rot','0');
gg=geomedit(g9);
gg{1}=point2(1.0E-4,0.072);
g2=geomedit(g9,gg);
gg=geomedit(g10);
gg{1}=point2(0.0359,0.072);
g3=geomedit(g10,gg);

% Analyzed geometry
clear p s
p.objs={g2,g3};
p.name={'PT1','PT2'};
p.tags={'g2','g3'};

s.objs={g1};
s.name={'R3'};
s.tags={'g1'};

fem.draw=struct('p',p,'s',s);
fem.geom=geomcsg(fem);
% COMSOL Multiphysics Model M-file
% Generated by COMSOL 3.3a (COMSOL 3.3.0.511, $Date: 2007/02/02 19:05:58
$)

% COMSOL version
clear vrsn
vrsn.name = 'COMSOL 3.3';
vrsn.ext = 'a';
vrsn.major = 0;
vrsn.build = 511;
vrsn.rcs = '$Name:  $';
vrsn.date = '$Date: 2007/02/02 19:05:58 $';
fem.version = vrsn;

% Constants
fem.const = {'ramp','1e-8', ...
```

```
  'magnitude','-5e5'};

% Constants
fem.const = {'ramp','1e-8', ...
  'magnitude','-5e5'};

% Constants
fem.const = {'ramp','1e-9', ...
  'magnitude','-5e5'};

% Constants
fem.const = {'ramp','1e-9', ...
  'magnitude','-5e5'};

% Constants
fem.const = {'ramp','1e-8', ...
  'magnitude','-5e5'};

% Constants
fem.const = {'ramp','1e-8', ...
  'magnitude','-5e5'};

% Geometry
g4=rect2('0.036','0.144','base','corner','pos',{'0','-72*10^-3'},'rot','0');

% Analyzed geometry
clear p s
p.objs={g3,g2};
p.name={'PT2','PT1'};
p.tags={'g3','g2'};

s.objs={g4};
s.name={'R3'};
s.tags={'g4'};

fem.draw=struct('p',p,'s',s);
fem.geom=geomcsg(fem);
% COMSOL Multiphysics Model M-file
% Generated by COMSOL 3.3a (COMSOL 3.3.0.511, $Date: 2007/02/02 19:05:58
$)

% COMSOL version
clear vrsn
vrsn.name = 'COMSOL 3.3';
vrsn.ext = 'a';
vrsn.major = 0;
vrsn.build = 511;
```

```
vrsn.rcs = '$Name:  $';
vrsn.date = '$Date: 2007/02/02 19:05:58 $';
fem.version = vrsn;

% Geometry
g1=rect2('0.036','0.215','base','corner','pos',{'0','-0.144'},'rot','0');
g5=rect2('0.036','0.216','base','corner','pos',{'0','-0.144'},'rot','0');

% Analyzed geometry
clear p s
p.objs={g3,g2};
p.name={'PT2','PT1'};
p.tags={'g3','g2'};

s.objs={g5};
s.name={'R3'};
s.tags={'g5'};

fem.draw=struct('p',p,'s',s);
fem.geom=geomcsg(fem);
% COMSOL Multiphysics Model M-file
% Generated by COMSOL 3.3a (COMSOL 3.3.0.511, $Date: 2007/02/02 19:05:58
$)

% COMSOL version
clear vrsn
vrsn.name = 'COMSOL 3.3';
vrsn.ext = 'a';
vrsn.major = 0;
vrsn.build = 511;
vrsn.rcs = '$Name:  $';
vrsn.date = '$Date: 2007/02/02 19:05:58 $';
fem.version = vrsn;

% Constants
fem.const = {'ramp','2e-7', ...
  'magnitude','-5e5'};

% Constants
fem.const = {'ramp','2e-7', ...
  'magnitude','-5e5'};

% Constants
fem.const = {'ramp','4e-7', ...
  'magnitude','-5e5'};

% Constants
```

```
 fem.const = {'ramp','4e-7', ...
  'magnitude','-5e5'};

 % Constants
 fem.const = {'ramp','1e-6', ...
  'magnitude','-5e5'};

 % Constants
 fem.const = {'ramp','1e-6', ...
  'magnitude','-5e5'};
 % COMSOL Multiphysics Model M-file
 % Generated by COMSOL 3.3a (COMSOL 3.3.0.511, $Date: 2007/02/02 19:05:58
$)

 % COMSOL version
 clear vrsn
 vrsn.name = 'COMSOL 3.3';
 vrsn.ext = 'a';
 vrsn.major = 0;
 vrsn.build = 511;
 vrsn.rcs = '$Name:  $';
 vrsn.date = '$Date: 2007/02/02 19:05:58 $';
 fem.version = vrsn;

 % Geometry
 g1=circ2('0.12','base','center','pos',{'0','0'},'rot','0');
 g4=circ2('0.1','base','center','pos',{'0','0'},'rot','0');
 g6=geomcomp({g1,g4},'ns',{'g1','g4'},'sf','g1-g4','edge','none');
 g7=rect2('10','112','base','corner','pos',{'0','0'},'rot','0');
 g8=rect2('0.10','0.12','base','corner','pos',{'0','0'},'rot','0');
 g9=rect2('0.010','0.012','base','corner','pos',{'0','0'},'rot','0');
 g10=rect2('0.010','0.012','base','center','pos',{'0','0'},'rot','0');
 g11=rect2('0.010','0.012','base','center','pos',{'0','0.1'},'rot','0');
 g12=rect2('0.010','0.022','base','center','pos',{'0','0.1'},'rot','0');
 g13=rect2('0.010','0.022','base','center','pos',{'0','0.11'},'rot','0');
 g14=rect2('0.010','0.025','base','center','pos',{'0','0.11'},'rot','0');
 g15=rect2('0.0085','0.025','base','center','pos',{'0','0.11'},'rot','0');
 [g16]=geomcopy({g15});
 g19=rect2('0.0085','0.025','base','center','pos',{'0','-0.11'},'rot','0');
 g20=rect2('0.0085','0.025','base','center','pos',{'0.11*cos(90)','-
0.11*sin(90)'},'rot','0');
 g21=rect2('0.0085','0.025','base','center','pos',{'0.11*cos(90*pi/180)','-
0.11*sin(90*pi/180)'},'rot','0');
 g22=rect2('0.0085','0.025','base','center','pos',{'0.11*cos(6*pi/180)','-
0.11*sin(6*pi/180)'},'rot','0');
 g23=rect2('0.0085','0.025','base','center','pos',{'0.11*cos(84*pi/180)','-
0.11*sin(84*pi/180)'},'rot','0');
```

```
 g24=rect2('0.0085','0.025','base','center','pos',{'0.11*cos(84*pi/180)','-
0.11*sin(84*pi/180)'},'rot','6');
 [g25]=geomcopy({g24});
 g71=rect2('0.0085','0.025','base','center','pos',{'0.11*cos(12*pi/180)','0.11*sin(12*p
i/180)'},'rot','12');
 g72=rect2('0.0085','0.025','base','center','pos',{'0.11*cos(12*pi/180)','0.11*sin(12*p
i/180)'},'rot','102');
 g73=rect2('0.0085','0.025','base','center','pos',{'0.11*cos(24*pi/180)','0.11*sin(24*p
i/180)'},'rot','114');
 g74=rect2('0.0085','0.025','base','center','pos',{'0.11*cos(6*pi/180)','0.11*sin(6*pi/1
80)'},'rot','6');
 g75=rect2('0.0085','0.025','base','center','pos',{'0.11*cos(6*pi/180)','0.11*sin(6*pi/1
80)'},'rot','96');
 [g76]=geomcopy({g75});
 [g77]=geomcopy({g76});
 g77=move(g77,[0,0]);
 g78=rect2('0.0085','0.025','base','center','pos',{'0.11*cos(18*pi/180)','0.11*sin(18*p
i/180)'},'rot','108');
 [g79]=geomcopy({g76});
 g79=move(g79,[0,0]);
 g80=rect2('0.0085','0.025','base','center','pos',{'0.11*cos(30*pi/180)','0.11*sin(30*p
i/180)'},'rot','96');
 g81=rect2('0.0085','0.025','base','center','pos',{'0.11*cos(30*pi/180)','0.11*sin(30*p
i/180)'},'rot','120');
 [g82]=geomcopy({g76});
 g82=move(g82,[0,0]);
 g83=rect2('0.0085','0.025','base','center','pos',{'0.11*cos(42*pi/180)','0.11*sin(42*p
i/180)'},'rot','132');
 [g84]=geomcopy({g76});
 g84=move(g84,[0,0]);
 g85=rect2('0.0085','0.025','base','center','pos',{'0.11*cos(54*pi/180)','0.11*sin(54*p
i/180)'},'rot','144');
 [g86]=geomcopy({g76});
 g86=move(g86,[0,0]);
 g87=rect2('0.0085','0.025','base','center','pos',{'0.11*cos(66*pi/180)','0.11*sin(66*p
i/180)'},'rot','156');
 [g88]=geomcopy({g76});
 g88=move(g88,[0,0]);
 g89=rect2('0.0085','0.025','base','center','pos',{'0.11*cos(78*pi/180)','0.11*sin(78*p
i/180)'},'rot','168');
 [g90]=geomcopy({g76});
 g90=move(g90,[0,0]);
 g91=rect2('0.0085','0.025','base','center','pos',{'0.11*cos(90*pi/180)','0.11*sin(90*p
i/180)'},'rot','180');
 [g92]=geomcopy({g76});
 g92=move(g92,[0,0]);
 g93=rect2('0.0085','0.025','base','center','pos',{'0.11*cos(102*pi/180)','0.11*sin(102
*pi/180)'},'rot','192');
 [g94]=geomcopy({g76});
```

```
 g94=move(g94,[0,0]);
 g95=rect2('0.0085','0.025','base','center','pos',{'0.11*cos(114*pi/180)','0.11*sin(114
*pi/180)'},'rot','204');
 [g96]=geomcopy({g76});
 g96=move(g96,[0,0]);
 g97=rect2('0.0085','0.025','base','center','pos',{'0.11*cos(126*pi/180)','0.11*sin(126
*pi/180)'},'rot','216');
 [g98]=geomcopy({g76});
 g98=move(g98,[0,0]);
 g99=rect2('0.0085','0.025','base','center','pos',{'0.11*cos(126*pi/180)','0.11*sin(126
*pi/180)'},'rot','216');
 g100=rect2('0.0085','0.025','base','center','pos',{'0.11*cos(138*pi/180)','0.11*sin(13
8*pi/180)'},'rot','228');
 [g101]=geomcopy({g76});
 g101=move(g101,[0,0]);
 g102=rect2('0.0085','0.025','base','center','pos',{'0.11*cos(150*pi/180)','0.11*sin(15
0*pi/180)'},'rot','240');
 [g103]=geomcopy({g76});
 g103=move(g103,[0,0]);
 g104=rect2('0.0085','0.025','base','center','pos',{'0.11*cos(162*pi/180)','0.11*sin(16
2*pi/180)'},'rot','252');
 [g105]=geomcopy({g76});
 g105=move(g105,[0,0]);
 g106=rect2('0.0085','0.025','base','center','pos',{'0.11*cos(174*pi/180)','0.11*sin(17
4*pi/180)'},'rot','264');
 g107=rect2('0.0085','0.025','base','center','pos',{'0.11*cos(186*pi/180)','0.11*sin(18
6*pi/180)'},'rot','276');
 [g108]=geomcopy({g76});
 g108=move(g108,[0,0]);
 g109=rect2('0.0085','0.025','base','center','pos',{'0.11*cos(174*pi/180)','0.11*sin(17
4*pi/180)'},'rot','264');
 g110=rect2('0.0085','0.025','base','center','pos',{'0.11*cos(198*pi/180)','0.11*sin(19
8*pi/180)'},'rot','288');
 g111=rect2('0.0085','0.025','base','center','pos',{'0.11*cos(174*pi/180)','0.11*sin(17
4*pi/180)'},'rot','174');
 g112=rect2('0.0085','0.025','base','center','pos',{'0.11*cos(174*pi/180)','0.11*sin(17
4*pi/180)'},'rot','264');
 [g113]=geomcopy({g76});
 g113=move(g113,[0,0]);
 g114=rect2('0.0085','0.025','base','center','pos',{'0.11*cos(198*pi/180)','0.11*sin(19
8*pi/180)'},'rot','288');
 [g115]=geomcopy({g76});
 g115=move(g115,[0,0]);
 g116=rect2('0.0085','0.025','base','center','pos',{'0.11*cos(210*pi/180)','0.11*sin(21
0*pi/180)'},'rot','300');
 [g117]=geomcopy({g76});
 g117=move(g117,[0,0]);
 g118=rect2('0.0085','0.025','base','center','pos',{'0.11*cos(222*pi/180)','0.11*sin(22
2*pi/180)'},'rot','312');
```

```
[g119]=geomcopy({g76});
g119=move(g119,[0,0]);
g120=rect2('0.0085','0.025','base','center','pos',{'0.11*cos(234*pi/180)','0.11*sin(234*pi/180)'},'rot','324');
[g121]=geomcopy({g76});
g121=move(g121,[0,0]);
g122=rect2('0.0085','0.025','base','center','pos',{'0.11*cos(246*pi/180)','0.11*sin(246*pi/180)'},'rot','336');
[g123]=geomcopy({g76});
g123=move(g123,[0,0]);
g124=rect2('0.0085','0.025','base','center','pos',{'0.11*cos(258*pi/180)','0.11*sin(258*pi/180)'},'rot','348');
[g125]=geomcopy({g76});
g125=move(g125,[0,0]);
g126=rect2('0.0085','0.025','base','center','pos',{'0.11*cos(270*pi/180)','0.11*sin(270*pi/180)'},'rot','360');
[g127]=geomcopy({g76});
g127=move(g127,[0,0]);
g128=rect2('0.0085','0.025','base','center','pos',{'0.11*cos(282*pi/180)','0.11*sin(282*pi/180)'},'rot','96');
g129=rect2('0.0085','0.025','base','center','pos',{'0.11*cos(282*pi/180)','0.11*sin(282*pi/180)'},'rot','372');
[g130]=geomcopy({g76});
g130=move(g130,[0,0]);
g131=rect2('0.0085','0.025','base','center','pos',{'0.11*cos(294*pi/180)','0.11*sin(294*pi/180)'},'rot','96');
g132=rect2('0.0085','0.025','base','center','pos',{'0.11*cos(294*pi/180)','0.11*sin(294*pi/180)'},'rot','384');
[g133]=geomcopy({g76});
g133=move(g133,[0,0]);
g134=rect2('0.0085','0.025','base','center','pos',{'0.11*cos(306*pi/180)','0.11*sin(306*pi/180)'},'rot','396');
g135=rect2('0.0085','0.025','base','center','pos',{'0.11*cos(318*pi/180)','0.11*sin(318*pi/180)'},'rot','408');
[g136]=geomcopy({g76});
g136=move(g136,[0,0]);
g137=rect2('0.0085','0.025','base','center','pos',{'0.11*cos(306*pi/180)','0.11*sin(306*pi/180)'},'rot','396');
[g138]=geomcopy({g76});
g138=move(g138,[0,0]);
g139=rect2('0.0085','0.025','base','center','pos',{'0.11*cos(330*pi/180)','0.11*sin(330*pi/180)'},'rot','420');
[g140]=geomcopy({g76});
g140=move(g140,[0,0]);
g141=rect2('0.0085','0.025','base','center','pos',{'0.11*cos(342*pi/180)','0.11*sin(342*pi/180)'},'rot','432');
[g142]=geomcopy({g76});
g142=move(g142,[0,0]);
```

```
g143=rect2('0.0085','0.025','base','center','pos',{'0.11*cos(354*pi/180)','0.11*sin(354*pi/180)'},'rot','444');
[g158,g159,g160,g161,g162,g163,g164,g165,g166,g167,g168,g169,g170,g171,g172,g173,g174,g175,g176,g177,g178,g179,g180,g181,g182,g183,g184,g185,g186,g187]=geomcopy({g78,g81,g83,g84,g85,g87,g89,g91,g93,g95,g97,g100,g102,g104,g107,g112,g114,g116,g118,g120,g122,g124,g126,g129,g132,g135,g137,g139,g141,g143});
g188=geomcomp({g6,g78,g81,g83,g84,g85,g87,g89,g91,g93,g95,g97,g100,g102,g104,g107,g112,g114,g116,g118,g120,g122,g124,g126,g129,g132,g135,g137,g139,g141,g143},'ns',{'g6','g78','g81','g83','g84','g85','g87','g89','g91','g93','g95','g97','g100','g102','g104','g107','g112','g114','g116','g118','g120','g122','g124','g126','g129','g132','g135','g137','g139','g141','g143'},'sf','g6-g78-g81-g83-g84-g85-g87-g89-g91-g93-g95-g97-g100-g102-g104-g107-g112-g114-g116-g118-g120-g122-g124-g126-g129-g132-g135-g137-g139-g141-g143','edge','none');
g219=circ2('0.1','base','center','pos',{'0','0'},'rot','0');
[g220,g221,g222,g223,g224,g225,g226,g227,g228,g229,g230,g231,g232,g233,g234,g235,g236,g237,g238,g239,g240,g241,g242,g243,g244,g245,g246,g247,g248,g249]=geomcopy({g158,g159,g160,g161,g162,g163,g164,g165,g166,g167,g168,g169,g170,g171,g172,g173,g174,g175,g176,g177,g178,g179,g180,g181,g182,g183,g184,g185,g186,g187});
g220=move(g220,[0,0]);
g221=move(g221,[0,0]);
g222=move(g222,[0,0]);
g223=move(g223,[0,0]);
g224=move(g224,[0,0]);
g225=move(g225,[0,0]);
g226=move(g226,[0,0]);
g227=move(g227,[0,0]);
g228=move(g228,[0,0]);
g229=move(g229,[0,0]);
g230=move(g230,[0,0]);
g231=move(g231,[0,0]);
g232=move(g232,[0,0]);
g233=move(g233,[0,0]);
g234=move(g234,[0,0]);
g235=move(g235,[0,0]);
g236=move(g236,[0,0]);
g237=move(g237,[0,0]);
g238=move(g238,[0,0]);
g239=move(g239,[0,0]);
g240=move(g240,[0,0]);
g241=move(g241,[0,0]);
g242=move(g242,[0,0]);
g243=move(g243,[0,0]);
g244=move(g244,[0,0]);
g245=move(g245,[0,0]);
g246=move(g246,[0,0]);
g247=move(g247,[0,0]);
g248=move(g248,[0,0]);
```

```
g249=move(g249,[0,0]);
g251=geomcomp({g219,g220,g221,g222,g223,g224,g225,g226,g227,g228,g229,g
230,g231,g232,g233,g234,g235,g236,g237,g238,g239,g240,g241,g242,g243,g244,g
245,g246,g247,g248,g249},'ns',{'C1','R1','R2','R3','R4','R5','R6','R7','R8','R9','R10','
R11','R12','R13','R14','R15','R16','R17','R18','R19','R20','R21','R22','R23','R24','R25',
'R26','R27','R28','R29','R30'},'sf','R1+R2+R3+R4+R5+R6+R7+R8+R9+R10+R11+
R12+R13+R14+R15+R16+R17+R18+R19+R20+R21+R22+R23+R24+R25+R26+
R27+R28+R29+R30-C1','edge','none');
g252=geomcomp({g251},'ns',{'CO1'},'sf','CO1','edge','none');
g253=circ2('0.1','base','center','pos',{'0','0'},'rot','0');

% Analyzed geometry
clear s
s.objs={g188,g252,g253};
s.name={'CO2','CO3','C1'};
s.tags={'g188','g252','g253'};

fem.draw=struct('s',s);
fem.geom=geomcsg(fem);
[g254,g255,g256]=geomcopy({g188,g252,g253});
g257=circ2('0.15','base','center','pos',{'0','0'},'rot','0');
g258=circ2('0.12','base','center','pos',{'0','0'},'rot','0');
g259=circ2('0.14','base','center','pos',{'0','0'},'rot','0');
g260=circ2('0.13','base','center','pos',{'0','0'},'rot','0');
g261=circ2('0.125','base','center','pos',{'0','0'},'rot','0');
g262=geomcomp({g188,g252,g253,g261},'ns',{'CO2','CO3','C1','C2'},'sf','C2-C1-
CO2-CO3','edge','none');
g263=geomcomp({g262},'ns',{'CO1'},'sf','CO1','edge','none');
[g264,g265,g266]=geomcopy({g254,g255,g256});
g264=move(g264,[0,0]);
g265=move(g265,[0,0]);
g266=move(g266,[0,0]);
[g267,g268,g269,g270]=geomcopy({g263,g264,g265,g266});
g271=square2('0.5','base','corner','pos',{'0','0'},'rot','0');
g272=square2('0.5','base','center','pos',{'0','0'},'rot','0');
g274=geomcomp({g263,g264,g265,g266,g272},'ns',{'CO2','CO1','CO3','C1','SQ1'}
,'sf','SQ1-CO2-CO1-CO3-C1','edge','none');
g275=geomcomp({g274},'ns',{'CO4'},'sf','CO4','edge','none');
[g276,g277,g278,g279]=geomcopy({g267,g268,g269,g270});
g276=move(g276,[0,0]);
g277=move(g277,[0,0]);
g278=move(g278,[0,0]);
g279=move(g279,[0,0]);

% Analyzed geometry
clear s
s.objs={g275,g276,g277,g278,g279};
s.name={'CO1','CO2','CO3','CO4','C1'};
```

```
 s.tags={'g275','g276','g277','g278','g279'};

 fem.draw=struct('s',s);
 fem.geom=geomcsg(fem);
 % COMSOL Multiphysics Model M-file
 % Generated by COMSOL 3.3a (COMSOL 3.3.0.511, $Date: 2007/02/02 19:05:58
$)

 % COMSOL version
 clear vrsn
 vrsn.name = 'COMSOL 3.3';
 vrsn.ext = 'a';
 vrsn.major = 0;
 vrsn.build = 511;
 vrsn.rcs = '$Name:  $';
 vrsn.date = '$Date: 2007/02/02 19:05:58 $';
 fem.version = vrsn;

 % Constants
 fem.const = {'ramp','1e-6', ...
  'magnitude','-5e5', ...
  'VpSand','3811', ...
  'VsSand','2302', ...
  'VpCoal','2652', ...
  'VsCoal','1280', ...
  'rho_sand','2250', ...
  'rho_coal','1270', ...
  'gamma_sand','VsSand/VpSand', ...
  'gamma_coal','VsCoal/VpCoal', ...
  'sigma_sand','(2*gamma_sand^2-1)/(2*(gamma_sand^2-1))', ...
  'sigma_coal','(2*gamma_coal^2-1)/(2*(gamma_coal^2-1))', ...
  'nu_sand','rho_sand*VsSand^2', ...
  'nu_coal','rho_coal*VsCoal^2', ...
  'E_sand','2*(1+sigma_sand)*nu_sand', ...
  'E_coal','2*(1+sigma_coal)*nu_coal'};

 % Constants
 fem.const = {'ramp','1e-6', ...
  'magnitude','-5e5', ...
  'VpSand','3811', ...
  'VsSand','2302', ...
  'VpCoal','2652', ...
  'VsCoal','1280', ...
  'rho_sand','2250', ...
  'rho_coal','1270', ...
  'gamma_sand','VsSand/VpSand', ...
  'gamma_coal','VsCoal/VpCoal', ...
```

```
  'sigma_sand','(2*gamma_sand^2-1)/(2*(gamma_sand^2-1))', ...
  'sigma_coal','(2*gamma_coal^2-1)/(2*(gamma_coal^2-1))', ...
  'nu_sand','rho_sand*VsSand^2', ...
  'nu_coal','rho_coal*VsCoal^2', ...
  'E_sand','2*(1+sigma_sand)*nu_sand', ...
  'E_coal','2*(1+sigma_coal)*nu_coal'};

% Constants
fem.const = {'ramp','1e-6', ...
  'magnitude','-5e5', ...
  'VpSand','3811', ...
  'VsSand','2302', ...
  'VpCoal','2652', ...
  'VsCoal','1280', ...
  'rho_sand','2250', ...
  'rho_coal','1270', ...
  'gamma_sand','VsSand/VpSand', ...
  'gamma_coal','VsCoal/VpCoal', ...
  'sigma_sand','(2*gamma_sand^2-1)/(2*(gamma_sand^2-1))', ...
  'sigma_coal','(2*gamma_coal^2-1)/(2*(gamma_coal^2-1))', ...
  'nu_sand','rho_sand*VsSand^2', ...
  'nu_coal','rho_coal*VsCoal^2', ...
  'E_sand','2*(1+sigma_sand)*nu_sand', ...
  'E_coal','2*(1+sigma_coal)*nu_coal'};

% Geometry
carr={curve2([-0.1,0.1],[0,0],[1,1])};
g1=geomcoerce('curve',carr);

% Analyzed geometry
clear c s
c.objs={g1};
c.name={'B1'};
c.tags={'g1'};

s.objs={g275,g277,g278,g276};
s.name={'CO1','CO3','CO4','CO2'};
s.tags={'g275','g277','g278','g276'};

fem.draw=struct('c',c,'s',s);
fem.geom=geomcsg(fem);
carr={curve2([-2,-2,-1.5],[1,1.5,1.5],[1,0.7071067811865475,1]), ...
  curve2([-1.5,-1,-1],[1.5,1.5,1],[1,0.7071067811865475,1]), ...
  curve2([-1,-2],[1,1],[1,1])};
g2=geomcoerce('solid',carr);
carr={curve2([-0.1,-0.1,0],[0,0.1,0.1],[1,0.7071067811865475,1]), ...
  curve2([0,0.1,0.1],[0.1,0.1,0],[1,0.7071067811865475,1]), ...
```

```
  curve2([0.1,-0.1],[0,0],[1,1])};
 g3=geomcoerce('solid',carr);
 carr={curve2([0.1,0.1,0],[0,-0.1,-0.1],[1,0.7071067811865475,1]), ...
  curve2([0,-0.1,-0.1],[-0.1,-0.1,0],[1,0.7071067811865475,1]), ...
  curve2([-0.1,0.1],[0,0],[1,1])};
 g4=geomcoerce('solid',carr);

 % Analyzed geometry
 clear s
 s.objs={g275,g277,g278,g276,g3,g4};
 s.name={'CO1','CO3','CO4','CO2','CO5','CO6'};
 s.tags={'g275','g277','g278','g276','g3','g4'};

 fem.draw=struct('s',s);
 fem.geom=geomcsg(fem);

 % Constants
 fem.const = {'ramp','1e-6', ...
  'magnitude','-5e5', ...
  'VpSand','3811', ...
  'VsSand','2302', ...
  'VpCoal','2652', ...
  'VsCoal','1280', ...
  'rho_sand','2250', ...
  'rho_coal','1270', ...
  'gamma_sand','VsSand/VpSand', ...
  'gamma_coal','VsCoal/VpCoal', ...
  'sigma_sand','(2*gamma_sand^2-1)/(2*(gamma_sand^2-1))', ...
  'sigma_coal','(2*gamma_coal^2-1)/(2*(gamma_coal^2-1))', ...
  'nu_sand','rho_sand*VsSand^2', ...
  'nu_coal','rho_coal*VsCoal^2', ...
  'E_sand','2*(1+sigma_sand)*nu_sand', ...
  'E_coal','2*(1+sigma_coal)*nu_coal'};
 % COMSOL Multiphysics Model M-file
 % Generated by COMSOL 3.3a (COMSOL 3.3.0.511, $Date: 2007/02/02 19:05:58
$)

 % COMSOL version
 clear vrsn
 vrsn.name = 'COMSOL 3.3';
 vrsn.ext = 'a';
 vrsn.major = 0;
 vrsn.build = 511;
 vrsn.rcs = '$Name:  $';
 vrsn.date = '$Date: 2007/02/02 19:05:58 $';
 fem.version = vrsn;
```

```
% Geometry
g1=circ2('0.1','base','center','pos',{'0','0'},'rot','0');

% Analyzed geometry
clear s
s.objs={g278,g275,g277,g276,g1};
s.name={'CO4','CO1','CO3','CO2','C1'};
s.tags={'g278','g275','g277','g276','g1'};

fem.draw=struct('s',s);
fem.geom=geomcsg(fem);

% Constants
fem.const = {'ramp','1e-6', ...
  'magnitude','-5e5'};

% Constants
fem.const = {'ramp','1e-6', ...
  'magnitude','-5e5'};

% Geometry

% Analyzed geometry
clear s
s.objs={g278,g277,g276,g1};
s.name={'CO4','CO3','CO2','C1'};
s.tags={'g278','g277','g276','g1'};

fem.draw=struct('s',s);
fem.geom=geomcsg(fem);
g2=circ2('0.1','base','center','pos',{'0','0'},'rot','0');

% Analyzed geometry
clear s
s.objs={g278,g277,g276,g275,g2};
s.name={'CO4','CO3','CO2','CO1','C1'};
s.tags={'g278','g277','g276','g275','g2'};

fem.draw=struct('s',s);
fem.geom=geomcsg(fem);
% COMSOL Multiphysics Model M-file
% Generated by COMSOL 3.3a (COMSOL 3.3.0.511, $Date: 2007/02/02 19:05:58
$)

% COMSOL version
clear vrsn
vrsn.name = 'COMSOL 3.3';
```

```
vrsn.ext = 'a';
vrsn.major = 0;
vrsn.build = 511;
vrsn.rcs = '$Name:  $';
vrsn.date = '$Date: 2007/02/02 19:05:58 $';
fem.version = vrsn;

% Constants
fem.const = {'ramp','1e-6', ...
  'magnitude','-5e5'};

% Constants
fem.const = {'ramp','1e-7', ...
  'magnitude','-5e5'};

% Constants
fem.const = {'ramp','1e-5', ...
  'magnitude','-5e5'};

% Constants
fem.const = {'ramp','1e-5', ...
  'magnitude','-5e5'};

% Constants
fem.const = {'ramp','2e-6', ...
  'magnitude','-5e5'};

% Constants
fem.const = {'ramp','2e-6', ...
  'magnitude','-5e5'};

% Constants
fem.const = {'ramp','2e-6', ...
  'magnitude','-5e5'};

% Constants
fem.const = {'ramp','2e-6', ...
  'magnitude','-5e5'};

% Geometry
carr={curve2([-0.1,-0.1,0],[0,0.1,0.1],[1,0.7071067811865475,1]), ...
  curve2([0,0.1,0.1],[0.1,0.1,0],[1,0.7071067811865475,1]), ...
  curve2([0.1,-0.1],[0,0],[1,1])};
g1=geomcoerce('solid',carr);
carr={curve2([-0.1,-0.1,0],[0,-0.1,-0.1],[1,0.7071067811865475,1]), ...
  curve2([0,0.1,0.1],[-0.1,-0.1,0],[1,0.7071067811865475,1]), ...
  curve2([0.1,-0.1],[0,0],[1,1])};
```

```
g3=geomcoerce('solid',carr);

% Analyzed geometry
clear s
s.objs={g278,g275,g277,g276,g1,g3};
s.name={'CO4','CO1','CO3','CO2','Sandstone','coal'};
s.tags={'g278','g275','g277','g276','g1','g3'};

fem.draw=struct('s',s);
fem.geom=geomcsg(fem);

% Constants
fem.const = {'ramp','2e-6', ...
  'magnitude','-5e5'};

% Constants
fem.const = {'ramp','2e-6', ...
  'magnitude','-5e5'};
% COMSOL Multiphysics Model M-file
% Generated by COMSOL 3.3a (COMSOL 3.3.0.511, $Date: 2007/02/02 19:05:58
$)

% COMSOL version
clear vrsn
vrsn.name = 'COMSOL 3.3';
vrsn.ext = 'a';
vrsn.major = 0;
vrsn.build = 511;
vrsn.rcs = '$Name:  $';
vrsn.date = '$Date: 2007/02/02 19:05:58 $';
fem.version = vrsn;

% Geometry
g2=circ2('0.1','base','center','pos',{'0','0'},'rot','0');

% Analyzed geometry
clear s
s.objs={g278,g275,g277,g276,g2};
s.name={'CO4','CO1','CO3','CO2','C1'};
s.tags={'g278','g275','g277','g276','g2'};

fem.draw=struct('s',s);
fem.geom=geomcsg(fem);
% COMSOL Multiphysics Model M-file
% Generated by COMSOL 3.3a (COMSOL 3.3.0.511, $Date: 2007/02/02 19:05:58
$)
```

```
% COMSOL version
clear vrsn
vrsn.name = 'COMSOL 3.3';
vrsn.ext = 'a';
vrsn.major = 0;
vrsn.build = 511;
vrsn.rcs = '$Name:  $';
vrsn.date = '$Date: 2007/02/02 19:05:58 $';
fem.version = vrsn;

% Constants
fem.const = {'ramp','2e-6', ...
  'magnitude','-5e5', ...
  'SourceFrequency','1e6'};

% Constants
fem.const = {'ramp','1e-7', ...
  'magnitude','-5e5', ...
  'SourceFrequency','1e6'};

% Constants
fem.const = {'ramp','1e-7', ...
  'magnitude','-5e5', ...
  'SourceFrequency','1e6'};

% Constants
fem.const = {'ramp','1e-6', ...
  'magnitude','-5e5', ...
  'SourceFrequency','1e6'};

% Constants
fem.const = {'ramp','1e-6', ...
  'magnitude','-5e5', ...
  'SourceFrequency','1e6'};

% Constants
fem.const = {'ramp','1e-6', ...
  'magnitude','-5e5', ...
  'SourceFrequency','1e6'};
% COMSOL Multiphysics Model M-file
% Generated by COMSOL 3.4 (COMSOL 3.4.0.248, $Date: 2007/10/10 16:07:51
$)

% COMSOL version
clear vrsn
vrsn.name = 'COMSOL 3.4';
vrsn.ext = '';
```

```
vrsn.major = 0;
vrsn.build = 248;
vrsn.rcs = '$Name:  $';
vrsn.date = '$Date: 2007/10/10 16:07:51 $';
fem.version = vrsn;

% Geometry
[g1,g3,g4,g5,g6]=geomcopy({g2,g278,g275,g276,g277});

% Analyzed geometry
clear s
s.objs={g2,g278};
s.name={'C1','CO4'};
s.tags={'g2','g278'};

fem.draw=struct('s',s);
fem.geom=geomcsg(fem);
g7=circ2('0.11','base','center','pos',{'0','0'},'rot','0');
g8=circ2('0.102','base','center','pos',{'0','0'},'rot','0');

% Analyzed geometry
clear s
s.objs={g278,g8};
s.name={'CO4','C1'};
s.tags={'g278','g8'};

fem.draw=struct('s',s);
fem.geom=geomcsg(fem);
g9=circ2('0.105','base','center','pos',{'0','0'},'rot','0');

% Analyzed geometry
clear s
s.objs={g278,g9};
s.name={'CO4','C1'};
s.tags={'g278','g9'};

fem.draw=struct('s',s);
fem.geom=geomcsg(fem);
[g10]=geomcopy({g9});
g12=geomcomp({g9},'ns',{'C1'},'sf','C1','edge','none');
[g16,g17]=geomcopy({g278,g12});
g18=geomcomp({g278,g12},'ns',{'g278','g12'},'sf','g278*g12','edge','none');
[g19,g20]=geomcopy({g16,g17});
g19=move(g19,[0,0]);
g20=move(g20,[0,0]);
g21=geomcomp({g19,g18},'ns',{'g19','g18'},'sf','g19-g18','edge','none');
```

```
% Analyzed geometry
clear s
s.objs={g20,g21};
s.name={'CO3','CO4'};
s.tags={'g20','g21'};

fem.draw=struct('s',s);
fem.geom=geomcsg(fem);
% COMSOL Multiphysics Model M-file
% Generated by COMSOL 3.4 (COMSOL 3.4.0.248, $Date: 2007/10/10 16:07:51
$)

% COMSOL version
clear vrsn
vrsn.name = 'COMSOL 3.4';
vrsn.ext = '';
vrsn.major = 0;
vrsn.build = 248;
vrsn.rcs = '$Name:  $';
vrsn.date = '$Date: 2007/10/10 16:07:51 $';
fem.version = vrsn;

% Geometry
g1=rect2(0.05,0.05,'base','corner','pos',[-0.25,0.05]);
g1=move(g1,[-0.024999999999999994,0.024999999999999994]);
g1=move(g1,[0.04999999999999999,-0.05]);

% Analyzed geometry
clear s
s.objs={g21,g20};
s.name={'CO4','CO3'};
s.tags={'g21','g20'};

fem.draw=struct('s',s);
fem.geom=geomcsg(fem);
% COMSOL Multiphysics Model M-file
% Generated by COMSOL 3.4 (COMSOL 3.4.0.248, $Date: 2007/10/10 16:07:51
$)

% COMSOL version
clear vrsn
vrsn.name = 'COMSOL 3.4';
vrsn.ext = '';
vrsn.major = 0;
vrsn.build = 248;
vrsn.rcs = '$Name:  $';
vrsn.date = '$Date: 2007/10/10 16:07:51 $';
```

```
fem.version = vrsn;

% Constants
fem.const = {'ramp',durationSource, ...
  'magnitude',amplitudeSource, ...
  'SourceFrequency',frequencySource};
% COMSOL Multiphysics Model M-file
% Generated by COMSOL 3.4 (COMSOL 3.4.0.248, $Date: 2007/10/10 16:07:51
$)

% COMSOL version
clear vrsn
vrsn.name = 'COMSOL 3.4';
vrsn.ext = '';
vrsn.major = 0;
vrsn.build = 248;
vrsn.rcs = '$Name:  $';
vrsn.date = '$Date: 2007/10/10 16:07:51 $';
fem.version = vrsn;

% Geometry
carr={curve2([-0.105,0.105],[0,0],[1,1])};
g2=geomcoerce('curve',carr);

% Analyzed geometry
clear c s
c.objs={g2};
c.name={'B1'};
c.tags={'g2'};

s.objs={g21,g20};
s.name={'CO4','CO3'};
s.tags={'g21','g20'};

fem.draw=struct('c',c,'s',s);
fem.geom=geomcsg(fem);

% COMSOL Multiphysics Model M-file
% Generated by COMSOL 3.4 (COMSOL 3.4.0.248, $Date: 2007/10/10 16:07:51
$)

% COMSOL version
clear vrsn
vrsn.name = 'COMSOL 3.4';
vrsn.ext = '';
vrsn.major = 0;
vrsn.build = 248;
```

```
vrsn.rcs = '$Name:  $';
vrsn.date = '$Date: 2007/10/10 16:07:51 $';
fem.version = vrsn;

% Initialize mesh
fem.mesh=meshinit(fem, ...
                  'hauto',2, ...
                  'xscale',0.5, ...
                  'yscale',0.5);

% (Default values are not included)

% Application mode 1
clear appl
appl.mode.class = 'PiezoPlaneStrain';
appl.module = 'SME';
appl.gporder = 4;
appl.cporder = 2;
appl.assignsuffix = '_smppn';
clear prop
prop.analysis='time';
appl.prop = prop;
clear bnd
bnd.electrictype = {'cont','V0','V0'};
bnd.Fy = {0,0,'force'};
bnd.ind = [2,2,2,2,2,2,2,2,2,2,2,2,2,2,2,2,1,2,2,2,2,2,2,2,2,2,2,2,2, ...
  2,2,2,2,2,2,2,2,2,2,2,2,2,2,2,2,3,2,2,2,2,2,2,2,2,2,2,2,2,2,2,2,2, ...
  2,2,2,2,2,2,2,2,2,2,2,2,2,2,2,2,2,2,2,2,2,2,2,2,2,2,1,1,2,2,1,1,2, ...
  2,1,1,2,2,1,1,2,2,1,1,2,2,1,1,2,2,1,1,2,2,1,1,1,1,2,2,1,1,2,2,1,1,2,2, ...
  1,1,2,2,1,1,2,2,1,1,2,2,1,1,2,2,1,1,2,2];
appl.bnd = bnd;
clear equ
equ.materialmodel = {'piezoelectric','piezoelectric','piezoelectric','piezoelectric', ...
  'piezoelectric','piezoelectric','iso','iso','piezoelectric','piezoelectric', ...
  'piezoelectric','piezoelectric','piezoelectric','piezoelectric','piezoelectric', ...
  'piezoelectric','piezoelectric','piezoelectric','piezoelectric','piezoelectric', ...
  'piezoelectric','piezoelectric','piezoelectric','piezoelectric','piezoelectric', ...
  'piezoelectric','piezoelectric','piezoelectric','piezoelectric','piezoelectric', ...
  'piezoelectric','piezoelectric'};
equ.nu = {0.33,0.33,0.33,0.33,0.33,0.33,0.4374,0.3768,0.33, ...
  0.33,0.33,0.33,0.33,0.33,0.33,0.33,0.33,0.33,0.33,0.33,0.33, ...
  0.33,0.33,0.33,0.33,0.33,0.33,0.33,0.33,0.33,0.33,0.33, ...
  0.33};
equ.epsilonrT = {{4.52,0,0;0,4.52,0;0,0,4.68}};
equ.epsilonrS = {{4.68,0,0;0,4.68,0;0,0,4.68},{4.68,0,0; ...
  0,4.68,0;0,0,4.68},{4.68,0,0;0,4.68,0;0,0,4.68}, ...
  {4.68,0,0;0,4.68,0;0,0,4.68},{4.68,0,0;0,4.68, ...
```

```
   0;0,0,4.68},{4.68,0,0;0,4.68,0;0,0,4.68},{4.4093, ...
   0,0;0,4.4092,0;0,0,4.68},{4.4093,0,0;0,4.4092, ...
   0;0,0,4.68},{4.68,0,0;0,4.68,0;0,0,4.68},{4.68, ...
   0,0;0,4.68,0;0,0,4.68},{4.68,0,0;0,4.68,0;0, ...
   0,4.68},{4.68,0,0;0,4.68,0;0,0,4.68},{4.68,0, ...
   0;0,4.68,0;0,0,4.68},{4.68,0,0;0,4.68,0;0,0, ...
   4.68},{4.68,0,0;0,4.68,0;0,0,4.68},{4.68,0,0; ...
   0,4.68,0;0,0,4.68},{4.68,0,0;0,4.68,0;0,0,4.68}, ...
   {4.68,0,0;0,4.68,0;0,0,4.68},{4.68,0,0;0,4.68, ...
   0;0,0,4.68},{4.68,0,0;0,4.68,0;0,0,4.68},{4.68, ...
   0,0;0,4.68,0;0,0,4.68},{4.68,0,0;0,4.68,0;0, ...
   0,4.68},{4.68,0,0;0,4.68,0;0,0,4.68},{4.68,0, ...
   0;0,4.68,0;0,0,4.68},{4.68,0,0;0,4.68,0;0,0, ...
   4.68},{4.68,0,0;0,4.68,0;0,0,4.68},{4.68,0,0; ...
   0,4.68,0;0,0,4.68},{4.68,0,0;0,4.68,0;0,0,4.68}, ...
   {4.68,0,0;0,4.68,0;0,0,4.68},{4.68,0,0;0,4.68, ...
   0;0,0,4.68},{4.68,0,0;0,4.68,0;0,0,4.68},{4.68, ...
   0,0;0,4.68,0;0,0,4.68}};
 equ.rho =
{'2651[kg/m^3]','2651[kg/m^3]','2651[kg/m^3]','2651[kg/m^3]','2651[kg/m^3]', ...
   '2651[kg/m^3]','2600[kg/m^3]','1400[kg/m^3]','2651[kg/m^3]','2651[kg/m^3]', ...
   '2651[kg/m^3]','2651[kg/m^3]','2651[kg/m^3]','2651[kg/m^3]','2651[kg/m^3]', ...
   '2651[kg/m^3]','2651[kg/m^3]','2651[kg/m^3]','2651[kg/m^3]','2651[kg/m^3]', ...
   '2651[kg/m^3]','2651[kg/m^3]','2651[kg/m^3]','2651[kg/m^3]','2651[kg/m^3]', ...
   '2651[kg/m^3]','2651[kg/m^3]','2651[kg/m^3]','2651[kg/m^3]','2651[kg/m^3]', ...
   '2651[kg/m^3]','2651[kg/m^3]'};
 equ.cE =
{{'8.67362e+010[Pa]','6.98527e+009[Pa]','1.19104e+010[Pa]','1.79081e+010[Pa]',  ...
   '0[Pa]','0[Pa]';'6.98527e+009[Pa]','8.67362e+010[Pa]','1.19104e+010[Pa]', ...
   '-1.79081e+010[Pa]','0[Pa]','0[Pa]';'1.19104e+010[Pa]','1.19104e+010[Pa]', ...
   '1.07194e+011[Pa]','0[Pa]','0[Pa]','0[Pa]';'1.79081e+010[Pa]','-
1.79081e+010[Pa]', ...
   '0[Pa]','5.79428e+010[Pa]','0[Pa]','0[Pa]';'0[Pa]','0[Pa]','0[Pa]','0[Pa]', ...

'5.79492e+010[Pa]','1.79224e+010[Pa]';'0[Pa]','0[Pa]','0[Pa]','0[Pa]','1.79224e+010[
Pa]', ...
   '3.99073e+010[Pa]'}};
 equ.E = {2.0e11,2.0e11,2.0e11,2.0e11,2.0e11,2.0e11,'13.5e9[Pa]', ...
   '4.5e9[Pa]',2.0e11,2.0e11,2.0e11,2.0e11,2.0e11,2.0e11,2.0e11, ...
   2.0e11,2.0e11,2.0e11,2.0e11,2.0e11,2.0e11,2.0e11,2.0e11, ...
   2.0e11,2.0e11,2.0e11,2.0e11,2.0e11,2.0e11,2.0e11,2.0e11, ...
   2.0e11};
 equ.sE = {{'1.277e-011[1/Pa]','-1.79e-012[1/Pa]','-1.22e-012[1/Pa]','-4.5e-
012[1/Pa]', ...
   '0[1/Pa]','0[1/Pa]';'-1.79e-012[1/Pa]','1.277e-011[1/Pa]','-1.22e-012[1/Pa]', ...
   '4.5e-012[1/Pa]','0[1/Pa]','0[1/Pa]';'-1.22e-012[1/Pa]','-1.22e-012[1/Pa]', ...
   '9.6e-012[1/Pa]','0[1/Pa]','0[1/Pa]','0[1/Pa]';'-4.5e-012[1/Pa]','4.5e-012[1/Pa]', ...
   '0[1/Pa]','2.004e-011[1/Pa]','0[1/Pa]','0[1/Pa]';'0[1/Pa]','0[1/Pa]','0[1/Pa]', ...
```

```
    '0[1/Pa]','2.004e-011[1/Pa]','-9e-012[1/Pa]';'0[1/Pa]','0[1/Pa]','0[1/Pa]', ...
    '0[1/Pa]','-9e-012[1/Pa]','2.91e-011[1/Pa]'}};
  equ.rhov = {'force23','force24','force22','force25','force21','force26',0, ...
    0,'force20','force27','force19','force28','force18','force29','force17', ...
    'force30','force16','force1','force15','force2','force14','force3','force13', ...
    'force4','force12','force5','force11','force6','force10','force7','force9', ...
    'force8'};
  equ.d = {{'-2.3e-012[C/N]','2.3e-012[C/N]','0[C/N]','-6.7e-013[C/N]','0[C/N]', ...
    '0[C/N]';'0[C/N]','0[C/N]','0[C/N]','0[C/N]','0[C/N]','6.7e-013[C/N]','4.6e-012[C/N]'; ...
    '0[C/N]','0[C/N]','0[C/N]','0[C/N]','0[C/N]','0[C/N]'}};
  equ.e = {{'0[C/m^2]','0[C/m^2]','0[C/m^2]','0[C/m^2]','0[C/m^2]','0[C/m^2]'; ...
    '0[C/m^2]','0[C/m^2]','0[C/m^2]','0[C/m^2]','0[C/m^2]','0[C/m^2]';'0[C/m^2]', ...
    '0[C/m^2]','0.19543[C/m^2]','0[C/m^2]','0[C/m^2]','0[C/m^2]'},{'0[C/m^2]', ...
    '0[C/m^2]','0[C/m^2]','0[C/m^2]','0[C/m^2]','0[C/m^2]';'0[C/m^2]','0[C/m^2]', ...

'0[C/m^2]','0[C/m^2]','0[C/m^2]','0[C/m^2]';'0[C/m^2]','0[C/m^2]','0.19543[C/m^2]'
, ...
    '0[C/m^2]','0[C/m^2]','0[C/m^2]'},{'0[C/m^2]','0[C/m^2]','0[C/m^2]','0[C/m^2]', ...
    '0[C/m^2]','0[C/m^2]';'0[C/m^2]','0[C/m^2]','0[C/m^2]','0[C/m^2]','0[C/m^2]', ...
    '0[C/m^2]';'0[C/m^2]','0[C/m^2]','0.19543[C/m^2]','0[C/m^2]','0[C/m^2]', ...
    '0[C/m^2]'},{'0[C/m^2]','0[C/m^2]','0[C/m^2]','0[C/m^2]','0[C/m^2]','0[C/m^2]'; ...
    '0[C/m^2]','0[C/m^2]','0[C/m^2]','0[C/m^2]','0[C/m^2]','0[C/m^2]';'0[C/m^2]', ...
    '0[C/m^2]','0.19543[C/m^2]','0[C/m^2]','0[C/m^2]','0[C/m^2]'},{'0[C/m^2]', ...
    '0[C/m^2]','0[C/m^2]','0[C/m^2]','0[C/m^2]','0[C/m^2]';'0[C/m^2]','0[C/m^2]', ...

'0[C/m^2]','0[C/m^2]','0[C/m^2]','0[C/m^2]';'0[C/m^2]','0[C/m^2]','0.19543[C/m^2]'
, ...
    '0[C/m^2]','0[C/m^2]','0[C/m^2]'},{'0[C/m^2]','0[C/m^2]','0[C/m^2]','0[C/m^2]', ...
    '0[C/m^2]','0[C/m^2]';'0[C/m^2]','0[C/m^2]','0[C/m^2]','0[C/m^2]','0[C/m^2]', ...
    '0[C/m^2]';'0[C/m^2]','0[C/m^2]','0.19543[C/m^2]','0[C/m^2]','0[C/m^2]', ...
    '0[C/m^2]'},{'-0.19543[C/m^2]','0.19543[C/m^2]','0[C/m^2]','-0.12120[C/m^2]', ...

'0[C/m^2]','0[C/m^2]';'0[C/m^2]','0[C/m^2]','0[C/m^2]','0[C/m^2]','0.12127[C/m^2]'
, ...
    '0.19558[C/m^2]';'0[C/m^2]','0[C/m^2]','0[C/m^2]','0[C/m^2]','0[C/m^2]', ...
    '0[C/m^2]'},{'-0.19543[C/m^2]','0.19543[C/m^2]','0[C/m^2]','-0.12120[C/m^2]', ...

'0[C/m^2]','0[C/m^2]';'0[C/m^2]','0[C/m^2]','0[C/m^2]','0[C/m^2]','0.12127[C/m^2]'
, ...
    '0.19558[C/m^2]';'0[C/m^2]','0[C/m^2]','0[C/m^2]','0[C/m^2]','0[C/m^2]', ...
    '0[C/m^2]'},{'0[C/m^2]','0[C/m^2]','0[C/m^2]','0[C/m^2]','0[C/m^2]','0[C/m^2]'; ...
    '0[C/m^2]','0[C/m^2]','0[C/m^2]','0[C/m^2]','0[C/m^2]','0[C/m^2]';'0[C/m^2]', ...
    '0[C/m^2]','0.19543[C/m^2]','0[C/m^2]','0[C/m^2]','0[C/m^2]'},{'0[C/m^2]', ...
    '0[C/m^2]','0[C/m^2]','0[C/m^2]','0[C/m^2]','0[C/m^2]';'0[C/m^2]','0[C/m^2]', ...

'0[C/m^2]','0[C/m^2]','0[C/m^2]','0[C/m^2]';'0[C/m^2]','0[C/m^2]','0.19543[C/m^2]'
, ...
    '0[C/m^2]','0[C/m^2]','0[C/m^2]'},{'0[C/m^2]','0[C/m^2]','0[C/m^2]','0[C/m^2]', ...
```

'0[C/m^2]','0[C/m^2]';0[C/m^2]','0[C/m^2]','0[C/m^2]','0[C/m^2]','0[C/m^2]', ...
'0[C/m^2]';0[C/m^2]','0[C/m^2]','0.19543[C/m^2]','0[C/m^2]','0[C/m^2]', ...
'0[C/m^2]'},{'0[C/m^2]','0[C/m^2]','0[C/m^2]','0[C/m^2]','0[C/m^2]','0[C/m^2]'; ...
'0[C/m^2]','0[C/m^2]','0[C/m^2]','0[C/m^2]','0[C/m^2]','0[C/m^2]';0[C/m^2]', ...
'0[C/m^2]','0.19543[C/m^2]','0[C/m^2]','0[C/m^2]','0[C/m^2]'},{'0[C/m^2]', ...
'0[C/m^2]','0[C/m^2]','0[C/m^2]','0[C/m^2]','0[C/m^2]';0[C/m^2]','0[C/m^2]', ...

'0[C/m^2]','0[C/m^2]','0[C/m^2]','0[C/m^2]';0[C/m^2]','0[C/m^2]','0.19543[C/m^2]'
, ...
'0[C/m^2]','0[C/m^2]','0[C/m^2]'},{'0[C/m^2]','0[C/m^2]','0[C/m^2]','0[C/m^2]', ...
'0[C/m^2]','0[C/m^2]';0[C/m^2]','0[C/m^2]','0[C/m^2]','0[C/m^2]','0[C/m^2]', ...
'0[C/m^2]';0[C/m^2]','0[C/m^2]','0.19543[C/m^2]','0[C/m^2]','0[C/m^2]', ...
'0[C/m^2]'},{'0[C/m^2]','0[C/m^2]','0[C/m^2]','0[C/m^2]','0[C/m^2]','0[C/m^2]'; ...
'0[C/m^2]','0[C/m^2]','0[C/m^2]','0[C/m^2]','0[C/m^2]','0[C/m^2]';0[C/m^2]', ...
'0[C/m^2]','0.19543[C/m^2]','0[C/m^2]','0[C/m^2]','0[C/m^2]'},{'0[C/m^2]', ...
'0[C/m^2]','0[C/m^2]','0[C/m^2]','0[C/m^2]','0[C/m^2]';0[C/m^2]','0[C/m^2]', ...

'0[C/m^2]','0[C/m^2]','0[C/m^2]','0[C/m^2]';0[C/m^2]','0[C/m^2]','0.19543[C/m^2]'
, ...
'0[C/m^2]','0[C/m^2]','0[C/m^2]'},{'0[C/m^2]','0[C/m^2]','0[C/m^2]','0[C/m^2]', ...
'0[C/m^2]','0[C/m^2]';0[C/m^2]','0[C/m^2]','0[C/m^2]','0[C/m^2]','0[C/m^2]', ...
'0[C/m^2]';0[C/m^2]','0[C/m^2]','0.19543[C/m^2]','0[C/m^2]','0[C/m^2]', ...
'0[C/m^2]'},{'0[C/m^2]','0[C/m^2]','0[C/m^2]','0[C/m^2]','0[C/m^2]','0[C/m^2]'; ...
'0[C/m^2]','0[C/m^2]','0[C/m^2]','0[C/m^2]','0[C/m^2]','0[C/m^2]';0[C/m^2]', ...
'0[C/m^2]','0.19543[C/m^2]','0[C/m^2]','0[C/m^2]','0[C/m^2]'},{'0[C/m^2]', ...
'0[C/m^2]','0[C/m^2]','0[C/m^2]','0[C/m^2]','0[C/m^2]';0[C/m^2]','0[C/m^2]', ...

'0[C/m^2]','0[C/m^2]','0[C/m^2]','0[C/m^2]';0[C/m^2]','0[C/m^2]','0.19543[C/m^2]'
, ...
'0[C/m^2]','0[C/m^2]','0[C/m^2]'},{'0[C/m^2]','0[C/m^2]','0[C/m^2]','0[C/m^2]', ...
'0[C/m^2]','0[C/m^2]';0[C/m^2]','0[C/m^2]','0[C/m^2]','0[C/m^2]','0[C/m^2]', ...
'0[C/m^2]';0[C/m^2]','0[C/m^2]','0.19543[C/m^2]','0[C/m^2]','0[C/m^2]', ...
'0[C/m^2]'},{'0[C/m^2]','0[C/m^2]','0[C/m^2]','0[C/m^2]','0[C/m^2]','0[C/m^2]'; ...
'0[C/m^2]','0[C/m^2]','0[C/m^2]','0[C/m^2]','0[C/m^2]','0[C/m^2]';0[C/m^2]', ...
'0[C/m^2]','0.19543[C/m^2]','0[C/m^2]','0[C/m^2]','0[C/m^2]'},{'0[C/m^2]', ...
'0[C/m^2]','0[C/m^2]','0[C/m^2]','0[C/m^2]','0[C/m^2]';0[C/m^2]','0[C/m^2]', ...

'0[C/m^2]','0[C/m^2]','0[C/m^2]','0[C/m^2]';0[C/m^2]','0[C/m^2]','0.19543[C/m^2]'
, ...
'0[C/m^2]','0[C/m^2]','0[C/m^2]'},{'0[C/m^2]','0[C/m^2]','0[C/m^2]','0[C/m^2]', ...
'0[C/m^2]','0[C/m^2]';0[C/m^2]','0[C/m^2]','0[C/m^2]','0[C/m^2]','0[C/m^2]', ...
'0[C/m^2]';0[C/m^2]','0[C/m^2]','0.19543[C/m^2]','0[C/m^2]','0[C/m^2]', ...
'0[C/m^2]'},{'0[C/m^2]','0[C/m^2]','0[C/m^2]','0[C/m^2]','0[C/m^2]','0[C/m^2]'; ...
'0[C/m^2]','0[C/m^2]','0[C/m^2]','0[C/m^2]','0[C/m^2]','0[C/m^2]';0[C/m^2]', ...
'0[C/m^2]','0.19543[C/m^2]','0[C/m^2]','0[C/m^2]','0[C/m^2]'},{'0[C/m^2]', ...
'0[C/m^2]','0[C/m^2]','0[C/m^2]','0[C/m^2]','0[C/m^2]';0[C/m^2]','0[C/m^2]', ...

```
'0[C/m^2]','0[C/m^2]','0[C/m^2]','0[C/m^2]';'0[C/m^2]','0[C/m^2]','0.19543[C/m^2]'
, ...
    '0[C/m^2]','0[C/m^2]','0[C/m^2]'},{'0[C/m^2]','0[C/m^2]','0[C/m^2]','0[C/m^2]', ...
    '0[C/m^2]','0[C/m^2]';'0[C/m^2]','0[C/m^2]','0[C/m^2]','0[C/m^2]','0[C/m^2]', ...
    '0[C/m^2]';'0[C/m^2]','0[C/m^2]','0.19543[C/m^2]','0[C/m^2]','0[C/m^2]', ...
    '0[C/m^2]'},{'0[C/m^2]','0[C/m^2]','0[C/m^2]','0[C/m^2]','0[C/m^2]','0[C/m^2]'; ...
    '0[C/m^2]','0[C/m^2]','0[C/m^2]','0[C/m^2]','0[C/m^2]','0[C/m^2]';'0[C/m^2]', ...
    '0[C/m^2]','0.19543[C/m^2]','0[C/m^2]','0[C/m^2]','0[C/m^2]'},{'0[C/m^2]', ...
    '0[C/m^2]','0[C/m^2]','0[C/m^2]','0[C/m^2]','0[C/m^2]';'0[C/m^2]','0[C/m^2]', ...

'0[C/m^2]','0[C/m^2]','0[C/m^2]','0[C/m^2]';'0[C/m^2]','0[C/m^2]','0.19543[C/m^2]'
, ...
    '0[C/m^2]','0[C/m^2]','0[C/m^2]'},{'0[C/m^2]','0[C/m^2]','0[C/m^2]','0[C/m^2]', ...
    '0[C/m^2]','0[C/m^2]';'0[C/m^2]','0[C/m^2]','0[C/m^2]','0[C/m^2]','0[C/m^2]', ...
    '0[C/m^2]';'0[C/m^2]','0[C/m^2]','0.19543[C/m^2]','0[C/m^2]','0[C/m^2]', ...
    '0[C/m^2]'},{'0[C/m^2]','0[C/m^2]','0[C/m^2]','0[C/m^2]','0[C/m^2]','0[C/m^2]'; ...
    '0[C/m^2]','0[C/m^2]','0[C/m^2]','0[C/m^2]','0[C/m^2]','0[C/m^2]';'0[C/m^2]', ...
    '0[C/m^2]','0.19543[C/m^2]','0[C/m^2]','0[C/m^2]','0[C/m^2]'},{'0[C/m^2]', ...
    '0[C/m^2]','0[C/m^2]','0[C/m^2]','0[C/m^2]','0[C/m^2]';'0[C/m^2]','0[C/m^2]', ...

'0[C/m^2]','0[C/m^2]','0[C/m^2]','0[C/m^2]';'0[C/m^2]','0[C/m^2]','0.19543[C/m^2]'
, ...
    '0[C/m^2]','0[C/m^2]','0[C/m^2]'},{'0[C/m^2]','0[C/m^2]','0[C/m^2]','0[C/m^2]', ...
    '0[C/m^2]','0[C/m^2]';'0[C/m^2]','0[C/m^2]','0[C/m^2]','0[C/m^2]','0[C/m^2]', ...
    '0[C/m^2]';'0[C/m^2]','0[C/m^2]','0.19543[C/m^2]','0[C/m^2]','0[C/m^2]', ...
    '0[C/m^2]'}};
  equ.ind = [1,2,3,4,5,6,7,8,9,10,11,12,13,14,15,16,17,18,19,20,21,22,23, ...
    24,25,26,27,28,29,30,31,32];
  appl.equ = equ;
  fem.appl{1} = appl;
  fem.frame = {'ref'};
  fem.border = 1;
  clear units;
  units.basesystem = 'SI';
  fem.units = units;

  % Global expressions
  fem.globalexpr = {'force','(t<ramp)*sin(2*pi*SourceFrequency*t)', ...
    'force1',['(',num2str(offset),'==1)*force'], ...
    'force2',['(',num2str(offset),'==2)*force'], ...
    'force3',['(',num2str(offset),'==3)*force'], ...
    'force4',['(',num2str(offset),'==4)*force'], ...
    'force5',['(',num2str(offset),'==5)*force'], ...
    'force6',['(',num2str(offset),'==6)*force'], ...
    'force7',['(',num2str(offset),'==7)*force'], ...
    'force8',['(',num2str(offset),'==8)*force'], ...
    'force9',['(',num2str(offset),'==9)*force'], ...
```

```
  'force10',['(',num2str(offset),'==10)*force'], ...
  'force11',['(',num2str(offset),'==11)*force'], ...
  'force12',['(',num2str(offset),'==12)*force'], ...
  'force13',['(',num2str(offset),'==13)*force'], ...
  'force14',['(',num2str(offset),'==14)*force'], ...
  'force15',['(',num2str(offset),'==15)*force'], ...
  'force16',['(',num2str(offset),'==16)*force'], ...
  'force17',['(',num2str(offset),'==17)*force'], ...
  'force18',['(',num2str(offset),'==18)*force'], ...
  'force19',['(',num2str(offset),'==19)*force'], ...
  'force20',['(',num2str(offset),'==20)*force'], ...
  'force21',['(',num2str(offset),'==21)*force'], ...
  'force22',['(',num2str(offset),'==22)*force'], ...
  'force23',['(',num2str(offset),'==23)*force'], ...
  'force25',['(',num2str(offset),'==25)*force'], ...
  'force26',['(',num2str(offset),'==26)*force'], ...
  'force27',['(',num2str(offset),'==27)*force'], ...
  'force28',['(',num2str(offset),'==28)*force'], ...
  'force29',['(',num2str(offset),'==29)*force'], ...
  'force30',['(',num2str(offset),'==30)*force'], ...
  'force31',['(',num2str(offset),'==31)*force'], ...
  'force32',['(',num2str(offset),'==32)*force'], ...
  'force24',['(',num2str(offset),'==24)*force']};

% Library materials
clear lib
lib.mat{1}.name='Copper';
lib.mat{1}.varname='mat1';
lib.mat{1}.variables.nu='0.35';
lib.mat{1}.variables.E='110e9[Pa]';
lib.mat{1}.variables.mur='1';
lib.mat{1}.variables.sigma='5.998e7[S/m]';
lib.mat{1}.variables.epsilonr='1';
lib.mat{1}.variables.alpha='17e-6[1/K]';
lib.mat{1}.variables.C='385[J/(kg*K)]';
lib.mat{1}.variables.rho='8700[kg/m^3]';
lib.mat{1}.variables.k='400[W/(m*K)]';
lib.mat{2}.name='Granite';
lib.mat{2}.varname='mat2';
lib.mat{2}.variables.nu='0.25';
lib.mat{2}.variables.E='60e9[Pa]';
lib.mat{2}.variables.alpha='7e-6[1/K]';
lib.mat{2}.variables.C='850[J/(kg*K)]';
lib.mat{2}.variables.rho='2600[kg/m^3]';
lib.mat{3}.name='Iron';
lib.mat{3}.varname='mat3';
lib.mat{3}.variables.nu='0.29';
```

```
 lib.mat{3}.variables.E='200e9[Pa]';
 lib.mat{3}.variables.mur='4000';
 lib.mat{3}.variables.sigma='1.12e7[S/m]';
 lib.mat{3}.variables.epsilonr='1';
 lib.mat{3}.variables.alpha='12.2e-6[1/K]';
 lib.mat{3}.variables.C='440[J/(kg*K)]';
 lib.mat{3}.variables.rho='7870[kg/m^3]';
 lib.mat{3}.variables.k='76.2[W/(m*K)]';
 lib.mat{4}.name='Quartz';
 lib.mat{4}.varname='mat4';
 lib.mat{4}.variables.epsilonrT={{'4.52',['(',num2str(offset),'==1)*force'],'0'},{'4.52'
,'0'},{'4.68'}};
 lib.mat{4}.variables.d={{'-2.3e-012[C/N]','2.3e-012[C/N]','0[C/N]','-6.7e-
013[C/N]','0[C/N]','0[C/N]'},{'0[C/N]','0[C/N]','0[C/N]','0[C/N]','6.7e-
013[C/N]','4.6e-012[C/N]'},{'0[C/N]','0[C/N]','0[C/N]','0[C/N]','0[C/N]','0[C/N]'}};
 lib.mat{4}.variables.e={{'-0.19543[C/m^2]','0.19543[C/m^2]','0[C/m^2]','-
0.12120[C/m^2]','0[C/m^2]','0[C/m^2]'},{'0[C/m^2]','0[C/m^2]','0[C/m^2]','0[C/m^
2]','0.12127[C/m^2]','0.19558[C/m^2]'},{'0[C/m^2]','0[C/m^2]','0[C/m^2]','0[C/m^2
]','0[C/m^2]','0[C/m^2]'}};
 lib.mat{4}.variables.epsilonrS={{'4.4093','0','0'},{'4.4092','0'},{'4.68'}};
 lib.mat{4}.variables.sE={{'1.277e-011[1/Pa]','-1.79e-012[1/Pa]','-1.22e-
012[1/Pa]','-4.5e-012[1/Pa]','0[1/Pa]','0[1/Pa]'},{'1.277e-011[1/Pa]','-1.22e-
012[1/Pa]','4.5e-012[1/Pa]','0[1/Pa]','0[1/Pa]'},{'9.6e-
012[1/Pa]','0[1/Pa]','0[1/Pa]','0[1/Pa]'},{'2.004e-
011[1/Pa]','0[1/Pa]','0[1/Pa]'},{'2.004e-011[1/Pa]','-9e-012[1/Pa]'},{'2.91e-
011[1/Pa]'}};
 lib.mat{4}.variables.rho='2651[kg/m^3]';
 lib.mat{4}.variables.cE={{'8.67362e+010[Pa]','6.98527e+009[Pa]','1.19104e+010[
Pa]','1.79081e+010[Pa]','0[Pa]','0[Pa]'},{'8.67362e+010[Pa]','1.19104e+010[Pa]','-
1.79081e+010[Pa]','0[Pa]','0[Pa]'},{'1.07194e+011[Pa]','0[Pa]','0[Pa]','0[Pa]'},{'5.79
428e+010[Pa]','0[Pa]','0[Pa]'},{'5.79492e+010[Pa]','1.79224e+010[Pa]'},{'3.99073e
+010[Pa]'}};

 fem.lib = lib;

 % Multiphysics
 fem=multiphysics(fem);

 % Extend mesh
 fem.xmesh=meshextend(fem, ...
                'linshape',[]);

 % Solve problem
 fem.sol=femtime(fem, ...
            'solcomp',{'v','u','V'}, ...
            'outcomp',{'v','u','V'}, ...

'tlist',[str2num(InitialTime):str2num(TimeSampling):str2num(EndingTime)], ...
            'atol',{'0.010'}, ...
```

```
            'rtol',0.1, ...
            'tout','tlist', ...
            'tsteps','strict');

 % Save current fem structure for restart purposes
 fem0=fem;

 % Plot solution
 postplot(fem, ...
        'tridata',{'disp_smppn','cont','internal','unit','m'}, ...
        'tridlim',[4.612646777171712E-12 3.505565220769333E-9], ...
        'trimap','jet(1024)', ...
        'solnum','end', ...
        'title','Time=1e-4    Surface: Total displacement [m]', ...
        'axisvisible','off', ...
        'axis',[-0.28013932643239997,0.2479272256918416,-
0.15271611089307338,0.15271611089307338]);

 % Plot in cross-section or along domain
 postcrossplot(fem,0,[1.1*[0.1*cos((90-12)*pi/180),0.1*cos((90-
24)*pi/180),0.1*cos((90-36)*pi/180),0.1*cos((90-48)*pi/180),0.1*cos((90-
60)*pi/180),0.1*cos((90-72)*pi/180),0.1*cos((90-84)*pi/180),0.1*cos((90-
96)*pi/180),0.1*cos((90-108)*pi/180),0.1*cos((90-120)*pi/180),0.1*cos((90-
132)*pi/180),0.1*cos((90-144)*pi/180),0.1*cos((90-156)*pi/180),0.1*cos((90-
168)*pi/180),0.1*cos((90-180)*pi/180),0.1*cos((90-192)*pi/180),0.1*cos((90-
204)*pi/180),0.1*cos((90-216)*pi/180),0.1*cos((90-228)*pi/180),0.1*cos((90-
240)*pi/180),0.1*cos((90-252)*pi/180),0.1*cos((90-264)*pi/180),0.1*cos((90-
276)*pi/180),0.1*cos((90-288)*pi/180),0.1*cos((90-300)*pi/180),0.1*cos((90-
312)*pi/180),0.1*cos((90-324)*pi/180),0.1*cos((90-336)*pi/180),0.1*cos((90-
348)*pi/180)];1.1*[0.1*sin((90-12)*pi/180),0.1*sin((90-24)*pi/180),0.1*sin((90-
36)*pi/180),0.1*sin((90-48)*pi/180),0.1*sin((90-60)*pi/180),0.1*sin((90-
72)*pi/180),0.1*sin((90-84)*pi/180),0.1*sin((90-96)*pi/180),0.1*sin((90-
108)*pi/180),0.1*sin((90-120)*pi/180),0.1*sin((90-132)*pi/180),0.1*sin((90-
144)*pi/180),0.1*sin((90-156)*pi/180),0.1*sin((90-168)*pi/180),0.1*sin((90-
180)*pi/180),0.1*sin((90-192)*pi/180),0.1*sin((90-204)*pi/180),0.1*sin((90-
216)*pi/180),0.1*sin((90-228)*pi/180),0.1*sin((90-240)*pi/180),0.1*sin((90-
252)*pi/180),0.1*sin((90-264)*pi/180),0.1*sin((90-276)*pi/180),0.1*sin((90-
288)*pi/180),0.1*sin((90-300)*pi/180),0.1*sin((90-312)*pi/180),0.1*sin((90-
324)*pi/180),0.1*sin((90-336)*pi/180),0.1*sin((90-348)*pi/180)]], ...
            'pointdata','We_smppn+ 1e-5*sign(y)*acos(x/0.11)', ...
            'title','V + 10*sign(y)*acos(x/0.11)', ...
            'axislabel',{'Time','We_smppn+ 1e-5*sign(y)*acos(x/0.11)'});

 % Plot in cross-section or along domain
 figure
 postcrossplot(fem,0,[1.1*[0.1*cos((90-12*str2num(offset))*pi/180),0.1*cos((90-
12*(str2num(offset)+1))*pi/180),0.1*cos((90-
12*(str2num(offset)+2))*pi/180),0.1*cos((90-
12*(str2num(offset)+3))*pi/180),0.1*cos((90-
12*(str2num(offset)+4))*pi/180),0.1*cos((90-
```

```
12*(str2num(offset)+5))*pi/180),0.1*cos((90-
12*(str2num(offset)+6))*pi/180),0.1*cos((90-
12*(str2num(offset)+7))*pi/180),0.1*cos((90-
12*(str2num(offset)+8))*pi/180),0.1*cos((90-
12*(str2num(offset)+9))*pi/180),0.1*cos((90-
12*(str2num(offset)+10))*pi/180),0.1*cos((90-
12*(str2num(offset)+11))*pi/180),0.1*cos((90-
12*(str2num(offset)+12))*pi/180),0.1*cos((90-
12*(str2num(offset)+13))*pi/180),0.1*cos((90-
12*(str2num(offset)+14))*pi/180),0.1*cos((90-
12*(str2num(offset)+15))*pi/180),0.1*cos((90-
12*(str2num(offset)+16))*pi/180),0.1*cos((90-
12*(str2num(offset)+17))*pi/180),0.1*cos((90-
12*(str2num(offset)+18))*pi/180),0.1*cos((90-
12*(str2num(offset)+19))*pi/180),0.1*cos((90-
12*(str2num(offset)+20))*pi/180),0.1*cos((90-
12*(str2num(offset)+21))*pi/180),0.1*cos((90-
12*(str2num(offset)+22))*pi/180),0.1*cos((90-
12*(str2num(offset)+23))*pi/180),0.1*cos((90-
12*(str2num(offset)+24))*pi/180),0.1*cos((90-
12*(str2num(offset)+25))*pi/180),0.1*cos((90-
12*(str2num(offset)+26))*pi/180),0.1*cos((90-
12*(str2num(offset)+27))*pi/180),0.1*cos((90-
12*(str2num(offset)+28))*pi/180)];1.1*[0.1*sin((90-
12*str2num(offset))*pi/180),0.1*sin((90-
12*(str2num(offset)+1))*pi/180),0.1*sin((90-
12*(str2num(offset)+2))*pi/180),0.1*sin((90-
12*(str2num(offset)+3))*pi/180),0.1*sin((90-
12*(str2num(offset)+4))*pi/180),0.1*sin((90-
12*(str2num(offset)+5))*pi/180),0.1*sin((90-
12*(str2num(offset)+6))*pi/180),0.1*sin((90-
12*(str2num(offset)+7))*pi/180),0.1*sin((90-
12*(str2num(offset)+8))*pi/180),0.1*sin((90-
12*(str2num(offset)+9))*pi/180),0.1*sin((90-
12*(str2num(offset)+10))*pi/180),0.1*sin((90-
12*(str2num(offset)+11))*pi/180),0.1*sin((90-
12*(str2num(offset)+12))*pi/180),0.1*sin((90-
12*(str2num(offset)+13))*pi/180),0.1*sin((90-
12*(str2num(offset)+14))*pi/180),0.1*sin((90-
12*(str2num(offset)+15))*pi/180),0.1*sin((90-
12*(str2num(offset)+16))*pi/180),0.1*sin((90-
12*(str2num(offset)+17))*pi/180),0.1*sin((90-
12*(str2num(offset)+18))*pi/180),0.1*sin((90-
12*(str2num(offset)+19))*pi/180),0.1*sin((90-
12*(str2num(offset)+20))*pi/180),0.1*sin((90-
12*(str2num(offset)+21))*pi/180),0.1*sin((90-
12*(str2num(offset)+22))*pi/180),0.1*sin((90-
12*(str2num(offset)+23))*pi/180),0.1*sin((90-
12*(str2num(offset)+24))*pi/180),0.1*sin((90-
12*(str2num(offset)+25))*pi/180),0.1*sin((90-
12*(str2num(offset)+26))*pi/180),0.1*sin((90-
```

```
12*(str2num(offset)+27))*pi/180),0.1*sin((90-
12*(str2num(offset)+28))*pi/180)]], ...
            'pointdata','We_smppn+ 1e-5*sign(y)*acos(x/0.11)', ...
            'title','V + 10*sign(y)*acos(x/0.11)', ...
            'axislabel',{'Time','We_smppn+ 1e-5*sign(y)*acos(x/0.11)'});

 % Plot solution
 figure
 postplot(fem, ...
        'tridata',{'disp_smppn','cont','internal','unit','m'}, ...
        'trimap','jet(1024)', ...
        'solnum','end', ...
        'title','Time=1e-4    Surface: Total displacement [m]', ...
        'axisvisible','off', ...
        'axis',[-0.2797817932947254,0.24756969255416705,-
0.15271611089307338,0.15271611089307338]);

 % Plot solution
 postplot(fem, ...
        'tridata',{'disp_smppn','cont','internal','unit','m'}, ...
        'tridlim',[1.7200882143231783E-12 3.5382710273111157E-9], ...
        'trimap','jet(1024)', ...
        'solnum','end', ...
        'title','Time=1e-4    Surface: Total displacement [m]', ...
        'axisvisible','off', ...
        'axis',[-0.2802509672145198,0.24803886647396145,-
0.15271611089307338,0.15271611089307338]);

 % Animate solution
 postmovie(fem, ...
         'tridata',{'disp_smppn','cont','internal','unit','m'}, ...
         'tridlim',[1.7200882143231783E-12 3.5382710273111157E-9], ...
         'trimap','jet(1024)', ...
         'axisvisible','off', ...
         'axis',[-0.2802509672145198,0.24803886647396145,-
0.15271611089307338,0.15271611089307338], ...
         'fps',10);
```

7.4.3. Function sleeve_al2

```
 function sleeve_al(event)

 % sleeve_al listen to the sleeve_gui actions, and call the related actions.

 f1=event.parent;
 if isequal(event.source,f1.get('solvebutton'))
   sleeve_GUI_OK2(event)
   BilithicModel_gui_v2(event)
```

```
elseif isequal(event.source,f1.get('defbutton'))
  setdefaults2(f1);
else
  img=f1.get('image');
  img.setVisible(true);
  ax=f1.get('axis');
  ax.setVisible(false);
end
```

7.4.4. Function sleeve_GUI_OK2

```
function sleeve_GUI_OK2(event)

dialog=event.parent;

global offset amplitudeSource frequencySource durationSource...
                    YoungModulusSample PoissonSample densitySample...
                    YoungModulusSample2 PoissonSample2 densitySample2...
                    InitialTime EndingTime TimeSampling

%Source properties
offset = dialog.get('Offset').getValue;
frequencySource = dialog.get('FrequencySource').getValue;
durationSource = dialog.get('DurationSource').getValue;
amplitudeSource = dialog.get('AmplitudeSource').getValue;

%First Layer's Sample elastic mechanical properties
YoungModulusSample = dialog.get('Esample').getValue;
PoissonSample = dialog.get('nusample').getValue;
densitySample = dialog.get('rhosample').getValue;

%Second Layer's Sample elastic mechanical properties
YoungModulusSample2 = dialog.get('Esample2').getValue;
PoissonSample2 = dialog.get('nusample2').getValue;
densitySample2 = dialog.get('rhosample2').getValue;

%And finally, the time sampling required for solving the problem
InitialTime = dialog.get('InitialTime').getValue;
EndingTime = dialog.get('EndingTime').getValue;
TimeSampling = dialog.get('TimeSampling').getValue;
```

7.4.5. Function setdefaults2

```
function setdefaults2(f1)

f1.get('Offset').setValue('1');
f1.get('FrequencySource').setValue('1e6');
f1.get('DurationSource').setValue('1e-6');
```

```
f1.get('Esample').setValue('13.5e9');
f1.get('nusample').setValue('0.4374');
f1.get('rhosample').setValue('2600');
f1.get('Esample2').setValue('4.5e9');
f1.get('nusample2').setValue('0.354');
f1.get('rhosample2').setValue('1270');
f1.get('InitialTime').setValue('0');
f1.get('EndingTime').setValue('1e-4');
f1.get('TimeSampling').setValue('1e-7');
f1.get('AmplitudeSource').setValue('5e-3');

global Properties
Properties.Offset = 1;
Properties.FrequencySource = 1e6;
Properties.DurationSource = 1e-6;
Properties.Esample = 13.5e9;
Properties.nusample = 0.4374;
Properties.rhosample = 2600;
Properties.Esample2 = 4.5e9;
Properties.nusample2 = 0.354;
Properties.rhosample2 = 1270;
Properties.PiezoDensity = 2651;
Properties.InitialTime = 0;
Properties.EndingTime = 1e-4;
Properties.TimeSampling = 1e-7;
```

7.4.6. Function sleeve_gui_v2

```
function sleeve_gui

global cE_11

%-------------------------------------------------------------------------------------------------------------------------------
%-------------------------------------------------------------------------------------------------------------------------------
%We start by drawing the gui
f1=frame('COMSOL Multiphysics - Sensitive Sleeve 2D Layer A','size',[1100 750]);

p1=panel;
p1.setFill('horizontal');
p1.add(label('<html><b>Parameter</b>'),1,1);
p1.add(label('<html>Offset<sub>source</sub>'),2,1);
p1.add(label('<html>Amplitude<sub>source</sub>'),3,1);
p1.add(label('<html>Frequency<sub>source</sub>'),4,1);
p1.add(label('<html>Duration<sub>source</sub>'),5,1);
```

```
p1.add(label('<html><b>Value</b>'),1,2);
p1.add(textfield(12,'text','','tag','Offset'),2,2);
p1.add(textfield(12,'text','','tag','AmplitudeSource'),3,2);
p1.add(textfield(12,'text','','tag','FrequencySource'),4,2);
p1.add(textfield(12,'text','','tag','DurationSource'),5,2);

p1.add(label('<html><b>Unit</b>'),1,3);
p1.add(label('<html>Piezo Number'),2,3);
p1.add(label('<html>V'),3,3);
p1.add(label('<html>Hz'),4,3);
p1.add(label('<html>s'),5,3);

lte=hex2dec('2264');
p1.add(label('<html><b>Range of operation</b>'),1,4);
p1.add(label(['<html>(1 ', lte, ' Offset<sub>source</sub> ', lte,' 30)']),2,4);
p1.add(label(['<html>(0 ', lte, 'Amplitude<sub>source</sub> ', lte,' 10)']),3,4);
p1.add(label(['<html>(1 ', lte,' Frequency<sub>source</sub>', lte,' 10000)']),4,4);
p1.add(label(['<html>(1/(20*Frequency<sub>source</sub> ', lte, '
Duration<sub>source</sub> ', lte, '1/(2*Frequency<sub>source</sub>))']),5,4);

p1.addVSeparator(4,9,2);
p1.addBorder('Source parameters');

p4=panel;
p4.setFill('horizontal');
p4.add(label('<html><b>Parameter</b>'),1,1);
p4.add(label('<html>E<sub>sample</sub>'),5,1);
p4.add(label('<html>&nu<sub>sample</sub>'),6,1);
p4.add(label('<html>&rho<sub>sample</sub>'),7,1);

p4.add(label('<html><b>Value</b>'),1,2);
p4.add(textfield(12,'text','','tag','Esample'),5,2);
p4.add(textfield(12,'text','','tag','nusample'),6,2);
p4.add(textfield(12,'text','','tag','rhosample'),7,2);

p4.add(label('<html><b>Unit</b>'),1,3);
p4.add(label('<html>Pa'),5,3);
p4.add(label('<html>1'),6,3);
p4.add(label('<html>kg/m<sup>3</sup>'),7,3);

p4.add(label('<html><b>Range of operation</b>'),1,4);
p4.add(label(['<html>(6 (Collagen) ', lte, ' E ', lte,' 1000000 (Diamond))']),5,4);
p4.add(label(['<html>(-1 &lt; &nu &lt; 1/2, isotropic range) ']),6,4);
p4.add(label(['<html>(1 ', lte, ' &rho ', lte,' 13600 (Mercury))']),7,4);

p4.addVSeparator(4,9,2);
p4.addBorder('First Layer''s Material properties');
```

```
p2=panel;
p2.setFill('horizontal');
p2.add(label('<html><b>Parameter</b>'),1,1);
p2.add(label('<html>E<sub>sample</sub>'),5,1);
p2.add(label('<html>&nu<sub>sample</sub>'),6,1);
p2.add(label('<html>&rho<sub>sample</sub>'),7,1);

p2.add(label('<html><b>Value</b>'),1,2);
p2.add(textfield(12,'text','','tag','Esample2'),5,2);
p2.add(textfield(12,'text','','tag','nusample2'),6,2);
p2.add(textfield(12,'text','','tag','rhosample2'),7,2);

p2.add(label('<html><b>Unit</b>'),1,3);
p2.add(label('<html>Pa'),5,3);
p2.add(label('<html>1'),6,3);
p2.add(label('<html>kg/m<sup>3</sup>'),7,3);

p2.add(label('<html><b>Range of operation</b>'),1,4);
p2.add(label(['<html>(6 (Collagen) ', lte, ' E ', lte,' 1000000 (Diamond))']),5,4);
p2.add(label(['<html>(-1 &lt; &nu &lt; 1/2, isotropic range) ']),6,4);
p2.add(label(['<html>(1 ', lte, ' &rho ', lte,' 13600 (Mercury))']),7,4);

p2.addVSeparator(4,9,2);
p2.addBorder('Second Layer''s Material properties');

p3=panel;
p3.setFill('horizontal');
p3.add(button('Solve','tag','solvebutton'),1,1);
p3.add(button('Default Values','tag','defbutton'),1,2);

p7=panel;
p7.setFill('horizontal');
p7.add(label('<html><b>Quantity</b>'),1,1);
p7.add(label('<html>Initial Time'),2,1);
p7.add(label('<html>Ending time'),3,1)
p7.add(label('<html>&DELTA(t)'),4,1);

p7.add(label('<html><b>Value</b>'),1,2);
p7.add(textfield(12,'text','','tag','InitialTime'),2,2);
p7.add(textfield(12,'text','','tag','EndingTime'),3,2);
p7.add(textfield(12,'text','','tag','TimeSampling'),4,2);

p7.add(label('<html><b>Unit</b>'),1,3);
p7.add(label('<html>s'),2,3);
p7.add(label('<html>s'),3,3);
p7.add(label('<html>s'),4,3);
```

```
p7.addVSeparator(5,8,2);
p7.addBorder('Time Sampling');

p6=panel;
p6.setFill('horizontal');
p6.add(label('tag','image','image',imageicon(which('logo.GIF'))),1,1);
p6.add(label('tag','image','image',imageicon(which('IPElogo.GIF'))),1,2);
p6.add(label('tag','image','image',imageicon(which('HeriotWatt.GIF'))),1,3);

left=panel;
left.add(p1,1,1,'horizontal');
left.add(p4,2,1,'horizontal');
left.add(p2,3,1,'horizontal');
left.add(p7,4,1,'horizontal');
left.add(p3,5,1,'horizontal');
%left.add(p5,6,1,'horizontal');
left.add(p6,7,1,'horizontal');
pref=left.getPreferredSize;
left.setMinimumSize(pref(1),pref(2));

f1.add(left,1,1);
f1.setWeight(1e6,1e6);
ax=axes('tag','axis');
ax.setVisible(false);
f1.add(ax,1,2,'both');
f1.add(label('tag','image','image',imageicon(which('SleeveLayerBilithic.gif'))),1,2);
f1.resetWeight;
setdefaults2(f1);

%-------------------------------------------------------------------------------------------------
-------------------------------------------------------------------
%-------------------------------------------------------------------------------------------------
-------------------------------------------------------------------
%We add here the listeners

f1.get('solvebutton').addActionListener('sleeve_al2');
f1.get('defbutton').addActionListener('sleeve_al2');
%f1.get('plottypebutton').addActionListener('sleeve_al2');

%-------------------------------------------------------------------------------------------------
-------------------------------------------------------------------
%-------------------------------------------------------------------------------------------------
-------------------------------------------------------------------
f1.show;

%sleeve_al(struct('source',{f1.get('defbutton')},'parent',{f1}));
```

```
%heatrod_al(struct('source',{f1.get('defbutton')},'parent',{f1}));
%heatrod_geom(f1);
```

BIBLIOGRAPHY

Aki and Richards (2002). Quantitative Seismology, Second Edition, University Science Books.
Al-Jabari, N. (2005). The development of two novel petrophysical techniques for measuring permeability and acoustic properties. Petroleum Engineering. Edinburgh, Heriot-Watt University. PhD.
Alkhalifah and Rampton (2001). "Seismic anisotropic in Trinidad: A new tool for lithology prediction." The leading edge.
Allen and Peddy (1993). Amplitude Variation with Offset: Gulf Coast Case studies. Tulsa, Oklahoma.
Anderson (1964). Dielectrics. 11 new fetter lane London EC4, Chapman and Hall LTD.
Ariffin, K. S. (2003). "Part I: Arang Batu."
Arnaud, Helbig, et al. (1999). "The Eight International Workshop on Seismic Anisotropy (8IWSA)." Geophysics 64(6): 1949-1955.
Arnsten (2007). "Validity of the long-wave approximation in periodically layered media." Geophysical Prospecting 55(1): 49-56.
Avseth, Mukerji, et al. (2005). Quantitative seismic interpretation; Applying Rock Physics Tools to Reduce Interpretation Risk. Cambridge, Cambridge University Press.
Bakke and Ursin (1998). "Thin-Bed AVO Effect." Geophysical Prospecting 46: 571-587.
Bakulin, Mateeva, et al. (2007). "Virtual source applications to imaging and reservoir monitoring." The leading edge.
Banik (1987). "An effective anisotropy parameter in transversely isotropic media." Geophysics 52(12): 1654-1664.
Barnes and Zener (1940). "Letters to the Editor." Physical Review 58.
Barton (2007). Rock Quality, Seismic Velocity, Attenuation and Anisotropy.
Bayuk, Ammerman, et al. (2007). "Elastic moduli of anisotropic clay." Geophysics 72(5): D107-D117.
Beard and Lowe (2003). "Non-destructive testing of rock bolts using guided ultrasonic waves." International Journal of Rock Mechanics & Mining Sciences 40: 527-536.
Berryman, Grechka, et al. (1999). "Analysis if Thomsen parameters for finely layered VTI media." Geophysical Prospecting 47(6): 959-978.
Biondi (2006). 3D Seismic Imaging.
Biryokov, Gulyaev, et al. (1995). Surface Acoustic Waves in Inhomogeneous Media, Springer.
Blangy (1994). "AVO in transversely isotropic media - An overview." Geophysics 59(5): 775-781.
Blitz (1967). Fundamentals of Ultrasonics. London, Butterworths.
Bloch, E. Deeb, et al. (2003). "Seismic Facies Analysis for Fracture Detection: a Powerful Technique." Society of Petroleum Engineers.
Boley and Weiner (1967). Theory of Thermal Stresses.
Botet (1996). Physique des ondes.
Boulanger and Hayes (1998). "Poisson's Ratio for Orthorhombic Materials." Journal of Elasticity 50: 87-89.
Bourbie, Coussy, et al. (1987). Acoustics of Porous Media, Gulf Publishing Company.

Brady and Brown (2006). Rock Mechanics for underground mining, third edition, Springer.
Bratek, Bratek, et al. (2002). "Properties and structure of different rank anthracites." Fuel 81: 97-108.
Brekhovskikh, L. M. (1980). Waves in Layered Media, Second Edition.
Brown and Korringa (1975). "On the dependence of the elastic properties of a porous rock on the compressibility of the pore fluid." Geophysics 40(4): 608-616.
Buchanan (1986). "The scattering of SH-Channel waves by a fault in a coal seam." Geophysical Prospecting 34: 343-365.
Buchanan, Jackson, et al. (1983). "Attenuation and anisotropy of channel waves in coal seams." Geophysics 48(2): 133-147.
Cady (1946). Piezoelectricity, McGraw-Hill Book Company, Inc.
Carcione (1999). "Effects of Vector attenuation on AVO of offshore reflections." Geophysics 64(3): 815-819.
Carcione (2001). Wave Fields in Real Media: Wave propagation in Anisotropic, Anelastic and Porous Media, Elsevier Science.
Carcione, Helle, et al. (1998). "Effects of attenuation and anisotropy on reflection amplitude versus offset." Geophysics 63(5): 1652-1658.
Castagna and Backus (1999). Offset-Dependent Reflectivity Theory and Practice of AVO Analysis Society of Exploration Geophysicists.
Castagna and Backus (1999). Offset-Dependent Reflectivity Theory and Pratice of AVO Analysis, Society of Exploration Geophysics.
Castagna and Smith (1994). "Comparison of AVO indicators:A modeling study." Geophysics 59: 1849-1855.
Castagna and Swan (1997). "Principles of AVO crossplotting." The leading edge.
Castagna, Swan, et al. (1998). "Framework for AVO gradient and intercept interpretation." Geophysics 63: 948-956.
Catuneanu (2006). Principles of sequence stratigraphy.
Causse, Riede, et al. (2007). "Amplitude analysis with an optimal model-based linear AVO approximation: Part II - Field example." Geophysics 72(3): C71-C79.
Causse, Riede, et al. (2007). "Amplitude analysis with an optimal model-based linear AVO approxiumation: Part I - Theory." Geophysics 72(3): C59-C69.
Claerbout (1985). Imaging the Earth's Interior. Oxford, London, Edinburgh, Boston, Palo Alto, Victoria, Blackwell Scientific Publications.
Clarke, Chambers, et al. (1961). "A Marine Geophysical Survey of the Undersea Coalfields of Northumberland, Cumberland and Durham." The Mining Engineer.
Coffeen (1984). Interpreting Seismic Data. Tulsa, Oklahoma, , Pennwell Books.
Curtis, Gerstoft, et al. (2006). "Seismic Interferometry-turning noise into signal." The leading edge.
Daley and Hron (1979). "Reflection and Trasmission coefficients for seismic waves in ellipsoidally anisotropic media." Geophysics 44(1): 27-38.
Domenico (1974). "Effect of water saturation on seismic reflectivity of sand reservoirs encased in shale." Geophysics 39(6).
Domenico (1976). "Effect of Brine-Gas mixture on velocity in an unconsolidated sand reservoir." Geophysics 41(5): 882-894.
Domenico (1977). "Elastic properties of unconsolidated porous sand reservoirs." Geophysics 42(7): 1339-1368.
Domenico (1984). "Rock litohlogy and porosity determination from shear and compressional wave velocity." Geophysics 49(8): 1188-1195.

Duffaut and Landro (2007). "Vp/Vs ratio versus differential stress and rock consolidation-A comparison between rock models and time-lapse AVO data." Geophysics 72(5): C81-C94.
Dulhunty and Penrose (1951). "Some relations between density and rank of coal." Fuel 30: 109-113.
Dutta, Mukerji, et al. (2007). "Rock Physics modelling constrained by sequence stratigraphy." The leading edge.
Dvorkin (2007). "Self-similarity in rock physics." The leading edge: 946-950.
Edlmann (2001). A new methodology for predicting the geo-mechanical properties of clastic reservoir rocks. Petroleum Engineering. Edinburgh, Heriot-Watt University. PhD.
Edwards, Asten, et al. (1985). "P-SV wave scattering by coal-seam inhomogeneities." Geophysics 50(2): 214-223.
Fertig and Muller (1978). "Computations of synthetic seismograms for coal seams witht the reflectivity method." Geophysical Prospecting 26: 868-883.
Fertig and Muller (1979). "Approximate Diffraction Theory for Transparent Half-Planes With Application to Seismic-Wave Diffraction at Coal Seams." Journal of Geophysics 46: 349-367.
Franklin (1948). "A note on the true density, chemical composition and structure of coals and carbonized coals." Fuel XXVII(2).
Franklin (1948). "A study of the fine structure of Carbonaceous solids by measurements of true and apparent densities: Part I. Coal."
Franklin (1949). "A strudy of the fine structure of Carbonaceous solids by measurements of true and apparent densities."
Franklin (1951). "Crystalline growth in graphitizing and non-graphitizing carbons."
Franklin (1956). "Homogeneous and Hererogeneous Graphitization of Carbon." Nature.
Galloway and Hobday (1983). Terrigenous Clastic Depositional Systems: Applications to Petroleum, Coal, and Uranium Exploration, Springer-Verlag.
Galperin (1985). Vertical seismic profiling and its exploration potential. Dordracht/Boston/Lancaster/Tokyo, D Reidel Publishing Company.
Galvin, Gurevich, et al. (2007). "Fluid-dependent shear-wave splitting in a poroelastic medium with conjugate fracture sets." Geophysical Prospecting 55: 333-343.
Gardner, Gardner, et al. (1974). "Formation velocity and density-the diagnostic basin for stratigraphic traps." Geophysics 39(6): 770-780.
Geldart and Sheriff (2004). Problems in Exploration Seismology and their solution.
Gentzis, Deisxman, et al. (2007). "Geomechanical properties and permaeability of coals from the Foothills and Mountain regions of western Canada." Coal Geology 69: 153-164.
Gercek (2007). "Poisson's ratio values for rocks." International Journal of Rock Mechanics & Mining Sciences 44: 1-13.
Gik (1982). "Effect of layers with anomalous seismic wave velocity on the image of objects." Geologiya i Geofizika 23(2): 116-122.
Gik (1995). "Introduction of static corrections according to information on spectrum reflected waves." Russian Geology and Geophysics 36(5): 116-119.
Gik (1996). "Experimental laboratory study of anisotropy for thin-layered media." Russian Geology and Geophysics 37(5): 94-107.
Gik (1997). "Physical modelling for travel of seismic waves in porous and fractured media." Russian Geology and Geophysics 38(4): 848-858.

Gik (1998). "Physical modeling of the effect of fracturing and porosity of rocks on the ratio of the velocities of shear and compressional seismic waves." Russian Geology and Geophysics 39(8): 1132-1142.
Gochioco (1990). "Seismic Surveys for coal exploration and mine planning." The leading edge.
Gochioco (1991). "Tuning effect and interference reflections from thin beds and coal seam." Geophysics 56(8): 1288-1295.
Gochioco (1998). "Short Note: Shallow VSP work in the U.S. Appalachian coal basin." Geophysics 63(3): 795-799.
Gochioco (2002). "Recent roel of geophysics in U.S. coal and CBM development." The leading edge.
Gochioco (2004). "Coal, geophysics, U.S. power generation, and mine safety." The leading edge.
Gommesen, Fabricius, et al. (2007). "Elastic Behaviour of North Sea Chalk: A well-log study." Geophysical Prospecting 55: 307-322.
Gonzalez and Mavko "Automatic detection of data inconsistencies for AVA analysis; Bootstrap and LMS regression."
Graff (1975). Wave motion in elastic solid.
Gray "Elastic Inversion for Lame Parameters."
Grechka (2007). "Multiple cracks in VTI rocks: Effective properties and fracture characterization." Geophysics 72(5): D81-D91.
Grechka and Kachanov (2006). "Effective Elasticity of fractured rocks: A snapshot of the work in progress." Geophysics 71(6): W45-W58.
Grechka and Rojas (2007). "On the ambiguity of elasticity measurements in layered rocks." Geophysics 72(3): D51-D59.
Greenhalgh (2006). "Numerical study of seismic scattering and waveguide excitation in faulted coal seams." Geophysical Prospecting 55: 185-198.
Greenhalgh, Suprajitno, et al. (1986). "Shallow seismic reflection investigations of coal in the Sydney Basin." Geophysics 51(7): 1426-1437.
Gregory (1976). "Fluid saturation effects on dynamic elastic properties of sedimentary rocks." Geophysics 41(5): 895-921.
Guion, P. D., N. L. Banks, et al. (1995). "The Silkstone (Westphalian A) from the east Pennines, England: implications for body genesis." Journal of the Geological society 152: 819-832.
Haase "Approximation Errors in AVO-Analysis and Inversion."
Hadden and Chew (1981). "Ultrasonics in Determining characteristics of Coal." Ultrasonics Symposium.
Hagedoorn, J. G. The collected work of J.G.HAGEDOORN.
Halliday, Curtis, et al. (2007). "Interferometric surfsce-wave isolation and removal." Geophysics 72(5): A69-A73.
Harbaugh, Davis, et al. (1995). Computing Risk for Oil Prospects: Principles and Programs, Pergamon.
Harman (1984). "High Resolution Seismic Reflection Techniques Applied in Coalfields: Cook Colliery, Queensland - A case History." Exploration Geophysics 15: 220-228.
Henry, G. (1994). Geophysique des bassins sedimentaires.
Hilterman (1975). "Amplitudes of seismic waves - a quick look." Geophysics 49(5): 745-762.
Hippel, v. (1954). Dielectrics and Waves. Boston London, Artech House.

Hogan (2006). "How to combine errors."
Homand-Etienne and Houpert (1989). "Thermally Induced Microcracking in Granites: Characterization and Analysis." Int. J. Rock. Mech. Min. Sci. & Geomech. Abstr. 26(2): 125-134.
Hood (1991). "Short Note: A simple method for decomposing a fracture-induced anisotropy." Geophysics 56(8): 1275-1279.
Hornby, Schwartz, et al. (1994). "Anisotropic effective-medium modeling of the elastic properties of shales." Geophysics 59(10): 1570-1583.
Hovem (1995). "Acoustic waves in finely layered media." Geophysics 60(4): 1217-1221.
Hutchins (1986). "Mechanisms of pulsed photoacoustic generation." Can. J. Phys. Vol. 64.
Hutchins, Young, et al. "Laser-generated waves for the investigation of porous solids."
Jaeger, J. C. and N. G. W. Cook (1979). Fundamentals of Rock Mechanics, Third Edition. LONDON.
Jaeger, J. C., N. G. W. Cook, et al. (2007). Fundamentals of Rock Mechanics, Fourth Edition, Blackwell.
Jilek (2000). "Approximate reflection coefficients of PS-waves in anisotropic media." SEG 2000 Expanded Abstract.
Johansen, Ruud, et al. (2004). "Effect of grain scale aligment on seismic anisotropy and reflectivity of shales." Geophysical Prospecting 52: 133-149.
Johnston (1987). "Physical properties of shale at temperature and pressure." Geopysics 52(10): 1391-1401.
Jolivet (1997). La deformation des continents.
Juhlin and Young (1993). "Short Note: Implications og thin layers for amplitude variation with offset (AVO) studies." Geophysics 58(8): 1200-1204.
Keho, Lemanski, et al. (2001). "The AVO hodogram: Using polarization to identify anomalies." The leading edge: 1214-1224.
Kenter, Braaksma, et al. (2007). "Acoustic behaviour of sedimentary rocks: Geologic properties versus Poisson's ratio." The leading edge.
Kessler and Kosloff (1991). "Elastic wave propagation using cylindrical coordinates." Geophysics 56(12): 2080-2089.
Kim, Wrolstad, et al. (1993). "Effects of transverse isotropy on P-wave for gas sands." Geophysics 58(6): 883-888.
King, Myer, et al. (1986). "Experimental studies of the elastic-wave propagation in a columnar-jointed rock mass." Geophysical Prospecting 34: 1185-1199.
Knox (1954). The Economic Geology of the Fife Coalfields. Department of scientific and industrial research. Edinburgh, Edinburgh University. B.Sc.
Krevelen, v. (1993). COAL, third completely revised edition. Amsterdam, London, New York, Tokyo, Elsevier.
Krevelen, V., Chermin, et al. (1959). "Chemical Structure and Properties of Coal XXIV - Sound Velocity and Fraction of Aromatic Carbon." Fuel 38: 483-488.
Kruger, Saenger, et al. (2007). "A numerical study on reflection coefficients of fractured media." Geophysics 72(4): D61-D67.
Kuster and Toksoz (1974). "Velocity and attenuation of seimic waves in two-phase media: Part I. Theoretical formulations." Geophysics 39(5).
Kuster and Toksoz (1974). "Velocity and attenuation of seismic waves in two-phase media: Part II. Experimental results." Geophysics 39(5): 607-618.

Kuwahara, Ito, et al. (1997). "Crustal heterogeneity as inferred from seismic coda wave decomposition by small-aperture array observation." Physics of the Earth and Planetary Interiors 104: 247-256.
Labuz and Bridel (1993). "Reducing frictional constraint in compression testing through lubrification." Int. J. Rock. Mech. Min. Sci. & Geomech. Abstr. 20: 451-455.
Lancaster and Whitcombe "Fast-track coloured inversion."
Landau and Lifshitz (1959). Theory of elasticity.
Lange and Almoghrabi (1988). "Lithology discrimination for thin layers using wavelet signal parameters." Geophysics 53(12): 1512-1519.
Lapreste (2002). Aide-memoire MATLAB.
Laubach, Schultz-Ela, et al. "Differential compaction of interbedded sandstone and coal."
Li (1976). "The anisotropic behaviour of Poisson's Ratio, Young's Modulus, and Shear Modulus in Hexagonal Materials." Phys. stat. sol. 38: 171-175.
Li, Dai, et al. (2007). "Converted-wave imaging in anisotropic media: theory and case studies." Geophysical Prospecting 2007(55): 345-363.
Li, Schott, et al. (1995). "Frequency-dependent Q-Estimation of Love-Type channel waves and the application of Gkorrection to seismograms." Geophysics 60(6): 1773-1789.
Lin and Phair (1993). "AVO Tuning." 63rd Annual International Meeting, Soc. of Expl. Geophys.: 727-730.
Liner and Fei (2007). "The Backus number." The leading edge.
Liu, Anderson, et al. (1976). "Velocity dispersion due to anelasticity; implications for seismology and mantle composition." Geophys. J. R. ast. Soc. 47: 41-58.
Liu, Crampin, et al. (1992). "Modelling channel waves with synthetic seismograms in an anisotropic in-seam seismic survey." Geophysical Prospecting 40: 513-540.
Liu and Schmitt (2003). "Amplitude and AVO responses of a single thin bed." Geophysics 68(4): 1161-1168.
Lubbe and Worthington (2006). "A field investigation of fracture compliance." Geophysical Prospecting 54: 319-331.
Lyman, G. (2007). "Wanted- a few good men: The war for talents comes to the mining industry." The leading edge.
Ma and Morozov "The exact Elastic Impedance as a Ray-path and Angle of Incidence Function."
Mahob and Castagna (2002). "AVO hodograms and polarization attributes." The leading edge.
Mahob and Castagna (2003). "AVO Polarization and hodograms: AVO strength and polarization product." Geophysics 68(3): 849-862.
Mari, Glangeaud, et al. (2001). Traitement du signal pour geologues et Geophysiciens, prospection sismique 1. Paris.
Mari, Glangeaud, et al. (2001). Traitement du signal pour Geologues et Geophysiciens: Techniques de base 2, Publications de l'Institut Francais du Petrole.
Maron (1987). Numerical Analysis: A Practical Approach.
Marsal (1987). Statistics for Geoscientists, Pergamon Press.
Martinez (1993). "Wave propagation effects on amplitude variation with offset measurements: A modeling study." Geophysics 58(4): 534-543.
Marton (1981). Ultrasonics, Academic Press.
Mason (1992). "Surface-to-borehole fault imaging in a buried horizontal waveguide-An experimental study in the southern North Sea." Geophysics 57(4): 532-442.

Maultzsch, Horne, et al. (2003). "Effects of an anisotropic overburden on azimuthal amplitude analysis in horizontal transverse isotropic media." Geophysical Prospecting 51: 61-74.

Mavko, Mukerji, et al. (1995). "Predicting stress-induced velocity anisotropy in rocks." Geophysics 60(4): 1081-1087.

Mazumdar (2007). "Poisson Dampening factor." The leading edge: 850-852.

McBeth and Schuett (2007). "The stress dependent elastic properties of thermally induced microfractures in aeolian Rotrliegend sandstone." Geophysical Prospecting 2007(55): 323-332.

McDonald, Angona, et al. (1958). "Attenuation of Shear and Compressional waves in Pierre Shales." Geophysics XXIII(3): 421-438.

Mehta, Bakulin, et al. (2007). "Improving the virtual source method by wave field separation." Geophysics 72(4): V79-V86.

Miller, Saenz, et al. (1992). "Feasibility of CDP seismic reflection to image structures in a 220-m deep, 3-m thick coal zone near Palau, Coahuila, Mexico." Geophysics 57(10): 1373-1380.

Misaghi, Landro, et al. (2007). "Overburden complexity and repeatability of seismic data: Impacts of positioning errors at the Oseberg field, North Sea." Geophysical Prospecting 55: 365-379.

Morgans and Terry (1958). "Measurements of the Static and Dynamic Elastic Moduli of Coal." Fuel 37: 201-209.

Muskat "The reflection of longitudinal wave pulses from plane parallel plates."

Muskat "The seismic wave energy reflected from various types of stratified horizons."

Muskat (1938). "The reflection of longitudinal wave pulses from plane parallel plates." 198-218.

Muskat and Meres (1939). "The seismic wave energy reflected from various types of stratified horizons." 149-155.

Muskat and Meres (1940). "Reflection and Transmission coefficients for plane waves in elastic media." Geophysics V(2): 115-148.

Muskat and Meres (1950). "Reflection and transmission coefficients for plane waves in elastic media." Geophysics V(2): 115-148.

Newendorp, P. D. (1975). Decision Analysis for Petroleum Exploration. Tulsa, Oklahoma, Pennwell Publishing Company.

Norris and Sinha (1993). "Weak elastic anisotropy and the tube wave." Geophysics 58(8): 1091-1098.

Nowacki, W. (1963). Dynamics of Elastic Systems. LONDON.

Nowak, Swan, et al. (2008). "Quantitative thickness estimates from the spectral response of AVO measurements." Geophysics 73(1): C1-C6.

Orlov, Gik, et al. (1983). "Modelling of the effct of a kimberlite pipe on a seimic wave field." Geologiya i Geofizika 24(3): 95-102.

Ostrander (1984). "Plane wave reflection coefficients for gas sands at non normal angles of incidence." Geophysics 49: 1637-1648.

Paige (2008). "A retrospective on my ADEMA effort."

Pedersen, Ursin, et al. (2007). "Wide-Angle phase-slowness approximations VTI media." Geophysics 72(4): S177-S185.

Peng, Chen, et al. (2006). "Factors facilitating or limiting the use of AVO for coal-bed methane." Geophysics 71(4): C49-C56.

Pietsch and Slusarckyk (1992). "The application of high resolution seisimics in Polish coal mining." Geophysics 57(1): 171-180.

Pomerol, Abrielle, et al. (1997). Elements de Geologie.
Postma (1955). "Wave propagation in a stratified medium." Geophysics XX(4): 780-806.
Quinquis (2000). Le traitement du signal sous Matlab. Paris.
Rai and Hanson (1988). "Shear-wave velocity anisotropy in sedimentary rocks: a laboratory study." Geophysics 53(6): 800-806.
Randall, Rose, et al. (1939). "Intercrystalline Thermal Currents as a Source of Internal Friction." Physical Review 56.
Randall and Zener (1940). "Internal Frisction of Aluminium." Physical Review 58.
Rao (1997). "In-fibre Bragg grating sensors." Meas. Sci. Technol. 8: 355-375.
Riedel and Theilen (2001). "AVO investigations of shallow marine sediments." Geophysics 2: 198-212.
Rippon, J. (1998). Variations in tectonic style and setting in British coalfields, University of Keele. PhD thesis.
Ross and Kinman (1995). "Nonbright-spot AVO; two examples." Geophysics 60: 1398-1408.
Rutherford and Williams (1989). "Amplitude-versus-offset." Geophysics 54(6): 680-688.
Ruzzene and Scarpa (2003). "Control of Wave Propagation in Sandwich Beams with Auxetic Core." Journal of intelligent Material systems and Structures: 443-453.
Ryan-Grigor (1997). "Empirical relationships between transverse isotropy parameters and Vp/Vs: Implications for AVO." Geophysics 62(5): 1359-1364.
Ryan-Grigor (1998). "Empirical relationships between anellipticity and Vp/Vs in shales: Potential applications to AVO studies and anisotropic seismic processing." 1998 SEG Expanded Abstracts.
Sadd, M. H. (2005). Elasticity: Theory, Applications, and Numerics.
Sams and Andrea (2001). "The effect of clay distribution on the elastic properties of sandstones." Geophysical Prospecting 49: 128-150.
Sams, Neep, et al. (1997). "The measurement of velocity dispersion and frequency-dependent intrinsic attenuation in sedimentary rocks." Geophysics 62(5): 1456-1464.
Sayers and Dean (2001). "Azimuth-dependent AVO in reservoirs containing non-orthogonal fracture sets." Geophysical Prospecting 49: 100-106.
Scarpa, Ciffo, et al. (2004). "Dynamic properties of high structural integrety auxetic open cell foam." Smart Materials and Structures 13: 49-56.
Schoenberg and Helbig (1997). "Orthorhombic media: Modeling elastic wave behaviour in a vertical fractued earth." Geophysics 62(6): 1954-1974.
Schoenberg and Sayers (1995). "Seismic anisotropy of fractured rock." Geophysics 60(1): 204-211.
Schuyer, Dijkstra, et al. (1954). "Chemical Structure and Properties of Coal VII - Elastic Constant." Fuel 33: 409-418.
Scott (1987). Coal and Coal-bearing strata: Recent Advances, The Geological Society.
Seeman and Horowicz (1983). "Vertical seismic profiling: Separation of upgoing and downgoing acoustic waves in a stratified medium." Geophysics 48(5): 555-568.
Shapiro, Zien, et al. (1994). "A generalized O'Doherty-Anstey formula for waves in finely layered media." Geophysics 59(11): 1750-1762.
Shen and Li (2004). "A combined geological, geophysical and Rock Mechanics Approach to Naturally Fractured Reservoir Characterization and Its Applications." Society of Petroleum Engineers SPE 90275.

Shuey (1985). "A simplification of the Zoeppritz equations." Geophysics 50(4): 609-614.
Sick, Muller, et al. (2003). "Amplitude corrections for randomly distributed heterogeneities above a target reflector." Geophysics 68(5): 1497-1502.
Simmons and Backus (1994). "AVO Modelling and the locally converted wave." Geophysics 59(9): 1237-1248.
Sinha and Kostek (1996). "Stress-induced azimuthal anisotropy in borehole flexural waves." Geophysics 61(6): 1899-1907.
Sinha, Simsek, et al. (2006). "Elastic-wave propagation in deviated wells in anisotropic formations." Geophysics 71(6): D191-202.
Stach, Mackowsky, et al. (1982). Stach's Textbook of Coal Petrology, Third revised and enlarged edition. BERLIN-STUTTGART.
Stein and Wysession (2003). An introduction to Seismology, Earthquakes and Earth Structure.
Stovas (2007). "Phase Velocity approximation in finely layered sediments." Geophysics 72(5): T57-T59.
Stovas and Arntsen (2006). "Vertical propagation of low frequency waves in finely layered media." Geophysics 71(3): T87-T94.
Stovas and Ursin (2007). "Equivalent time-average and effective medium for periodic layers." Geophysical Prospecting.
Swan (1991). "Amplitude-versus-offset measurement errors in a finely layered medium." Geophysics 56(1): 41-49.
Szabo (1981). "A representative Poisson's ratio for Coal." Int. J. Rock. Mech. Min. Sci. & Geomech. Abstr. 18: 531-533.
Szilard (1982). Ultrasonic Testing.
Szwilski (1984). "Determination of the anisotropic Elastic Moduli of Coal." International Journal of Rock Mechanics & Mining Sciences 21(1): 3-12.
Takemura, Golshani, et al. (2003). "Preferred orientaitions of open microcracks in granite and their relation with anisotropic elasticity." International Journal of Rock Mechanics & Mining Sciences 40: 443-454.
Tatham and McCormack (1998). Multicomponent Seismology in Petroleum Exploration.
Terry (1959). "The Dependence of the Elastic Behaviour of Coal on the Microcrack Structure." Fuel XXXVIII(2): 125-146.
Thomsen (1986). "Weak elastic anisotropy." Geophysics 51(10): 1954-1966.
Tiersten (1969). Linear Piezoelectric Plate Vibrations. New York, Plenum Press
Timur (1977). "Temperature dependence of compressional and shear wave velocities in rocks." Geophysics 42(5): 950-956.
Ting (2004). "Very Large Poisson's Ratio with a Bounded Transverse Strain in Anisotropic Elastic Materials." Journal of Elasticity 77: 163-176.
Ting and Chen (2005). "Poisson's ratio for anisotropic elastic materials can have no bounds." Q. Jl Mech. Appl. Math. 58(1): 73-82.
Tiwari and McMechan (2007). "Effects of incomplete parametrization on full-wavefield viscoelatstic seismic data for petrophysical reservoir properties." Geophysics 72(3): o9-o17.
Tsuneyama and Mavko (2007). "Elastic-Impedance analysis constrained by rock-physics bounds." Geophysical Prospecting 2007(55): 289-306.
Tsvankin (1997). "Reflection moveout and parameter estimation for horizontal transverse isotropy." Geophysics 62(2): 614-629.

Upadhyay (2004). Seismic Reflection Processing, with special Reference to Anisotropy.
Ursin (1983). "Review of elastic and electromagnetic wave propagation in horizontally layered media." Geophysics 48(8): 1063-1081.
Ursin and Ekren (1995). "Robust AVO Analysis." Geophysics 60(2): 317-326.
Ursin, S. (2002). "Reflection and transmission responses of a layered isotropic viscoelastic medium." Geophysics 67(1): 307-323.
Vandenbroucke and Largeau (2007). "Kerogen origin, evolution and structure." Organic Geochemistry 38(5): 719-833.
Vernik and Liu (1997). "Velocity anisotropy in shales: A petrophysical study." Geophysics 62(2): 521-532.
Vogelaar and Smeulders (2007). "Extension of White's layered model to the full frequency range." Geophysical Prospecting 55(5): 685-695.
Wang (2000). Variable grid-size and time-step finite difference method for seismic froward medeling and reverse-time migration. Departmen of Geology and Geophysics, University of Utah. PhD.
Wang (2002). "Seismic anisotropy in sedimentary rocks, part 1: A single-plug laboratory method." Geophysics 67(5): 1415-1422.
Wang (2002). "Seismic anisotropy in sedimentary rocks, part 2: Laboratory data." Geophysics 67(5): 1423-1440.
Wang, Rudolph, et al. (2007). "An analytical model of the mechanical properties of bulk coal under confined stress." Fuel 86: 1873-1884.
Weimer and Davis (1996). Applications of 3D Seismic Data to Exploration and Production.
Whitcombe (2002). "Short note: Elastic impedance normalization." Geophysics 67(1): 60-62.
Whitcombe, C., Reagan, Redshaw (2002). "Extended elastic impedance for fluid and lithology prediction." Geophysics 67(1): 63-67.
Whitcombe, F. (2001). "The AIGI crossplot as an aid to AVO analysis and calibration." SEG San Antonio 2001 Expanded Abstract.
Widmaier, Shapiro, et al. (1996). "AVO correction for scalar waves in the case of a thinly layered reflector overburden." Geophysics 61(2): 520-528.
Wilfrid (1961). Coal. LONDON, EDWARD ARNOLD (PUBLISHERS) LTD.
Woodcock and Strachan (2000). Geological History of Britain and Ireland.
Worthington (1894). "An introduction to geophysical tomography." First Break.
Wright (1987). "Short Note: The effects of transverse isotropy on reflection amplitude versus offset." Geophysics 52(4): 564-567.
Yancey (2006). Analysis and Application of Coal Seam Seismic Waves for detection and Abandonned Mines. Blacksburg, Faculty of the Virginia Polytechnic Institute. Master of Science in Geoscience.
Yilmaz (2001). Seismic Data Analysis.
Young and Hutchins (1987). "Measuring anisotropy in rocks using laser-generated ultrasound." Geophys. J. R. ast. Soc. 91: 501-516.
Yu, Vozoff, et al. (1993). "The influence of confining pressure and water saturation on dynamic elastic properties of some Permian coals." Geophysics 58(1): 30-38.
Zener (1937). "Internal Friction in Solids." 1937 52.
Zener (1938). "Internal Friction in Solids: II.General Theory of Thermoelastic Internal Frictions." Physical Review.

Zener (1941). "Theory of hte Elasticity of Polycrystals with Viscous Grain Boundaries." Physical Review 60.

Zener (1948). Elasticity and Anelasticity of Metals. Chicago Illinois.

Zener, Otis, et al. (1938). "Internal Friction in Solids: III.Experimetal Demonstration of Thermoelastic Internal Friction." Physical Review 53.

Zhu and Tsvankin (2006). "Plane-wave propagation in attenuative transversely isotropic media." Geophysics 71(2): P.T17-P.T30.

Zhu, Tsvankin, et al. (2007). "Physical modeling and analysis of P-wave attenuation anisotropy in transversely isotropic media." Geophysics 72(1): D1-D7.

Zhu, Tsvankin, et al. (2007). "Effective attenuation anisotropy of thin-layered media." Geophysics 72(5): D93-D106.

Zimmerman "An Effective New Method of Amplitude-versus-Offset Analysis for Marine Data."

Zoeppritz (1919). "Uber Reflexion und Durchgang seismicher Wellen durch Unstetigkeitsflachen." Gottinger Nachrichten 1: 66-84.

Zwieltering and v. Krevelen (1954). "Chemical Structure and Properties of Coal." Fuel 33: 331-337.